Time-lapse seismic inversion for pressure and saturation in clastic reservoirs

Christophe Ribeiro

Submitted for the Degree of Doctor of Philosophy

Heriot-Watt University

Institute of Petroleum Engineering

February 2006

Abstract

A new petro-elastic-based methodology to invert for reservoir pressure and saturation changes in clastic reservoirs is presented. The technique is based on an extensive petro-elastic analysis of reservoir sandstones from the North Sea and the Gulf of Mexico. Ultrasonic measurements from the literature and from the rock physics database at the Heriot-Watt Institute of Petroleum Engineering are used. From this analysis, two independent elastic properties are selected to represent the effect of pressure and saturation on the rock: the shear modulus, which is dependent only on pressure changes, and a newly derived parameter (called the saturation modulus), which is dependent only on change in fluid saturants. These two moduli are demonstrated to exhibit a higher degree of orthogonality in term of pressure and saturation variations than any of the other elastic properties (i.e. P-wave velocity, S-wave velocity, bulk modulus), consequently minimizing possible interference between the properties caused by these production effects. Rock physics relationships are derived to link changes in shear and saturation modulus to changes in pore pressure and fluid bulk modulus. In this dissertation, fluid bulk modulus is the preferred attribute to represent the effect of saturation, since it does not involve any assumption regarding the fluid distribution (e.g. homogeneous or heterogeneous mixtures).

A methodology is developed to obtain pore pressure and fluid bulk modulus estimates via time-lapse seismic inversion of shear and saturation moduli and the use of the calibrated rock physics relationships. The seismic inversion is rendered possible by the introduction of a new form for the P-wave reflectivity and elastic impedance. Following the inversion of multi-angle near, mid and far elastic impedance stacks from a baseline and a repeat survey, the shear and saturation moduli changes are inverted and converted to pore pressure and fluid bulk modulus changes. The proposed methodology is tested on a reservoir model study based on the Ainsa turbidite channel complex from the southern Pyrénées (Spain). The high accuracy of the estimated reservoir changes is assessed by comparison to the output from the dynamic flow simulator. In addition, an uncertainty analysis is carried out to determine the reliability of the estimates. In this study, the errors originate from the rock

physics approximations (the uncertainty in the fitting procedure) and also from the seismic attributes (shear and saturation moduli). A sensitivity study shows that the largest factor affecting the uncertainty of the final results given a constant known geology is errors in the seismic attributes; this is followed by errors in the pressure model, and errors in approximating the changes in saturation. The uncertainty analysis is implemented by assuming an independent and dependent set of controlling parameters in the pressure and saturation relations. The latter approach reduced the standard deviation of the production estimates by including the cross-coupling between parameters. The new methodology is also further validated by an application to the Palaeocene turbidite sandstone of the Foinaven field, west of Shetland. Cautious cross-matching and pre-conditioning of the time-lapse seismic data are applied to obtain high repeatability of the 4D stratigraphic elastic impedance inversion results. Predicted pore pressure and fluid bulk modulus changes from the flow simulator show an excellent correlation with the estimated results, and suggest possible updates to the static reservoir model.

Acknowledgements

I would like to thank Colin MacBeth, Patrick Corbett and Pierre Lanfranchi for giving me the opportunity to study at the Heriot-Watt Institute of Petroleum Engineering. I have felt privilege to study in such a multi-disciplinary environments that introduced me to many notions of petroleum engineering and reservoir management. During these three years, I have appreciated the supervision and support of my supervisor Colin MacBeth who enthusiasm in the project kept my motivation running during this tough but rewarding experience. I am also grateful to Patrick Corbett for encouraging me to follow several courses and the Spanish field trip, which truly change my vision on reservoir geology and management.

This project was financially supported by the Compagnie Générale de Géophysique (CGG). I would like to thank Pierre Lanfranchi for maintaining a continuous interaction between the company and I. I am also thankful to Olivier Kirstetter, Bernard Deschizeaux, Yahn Freudenreich, Cyrille Reiser, Philippe Doyen and all members of CGG's staff that offer me their help and advice. I would also like to thank Karl Stephen and Martin Landrø for reviewing my thesis and their constructive comments.

Trevor Ricketts and Martin Towns from BP are also acknowledged for their assistance and feedback during the project. I am also grateful to the partners of the Foinaven field, BP, Marathon Oil and Marubeni North Sea Limited for granting permission to publish the real data result and Schlumberger for allowing the use of Eclipse.

The encouragements of Alex Bertrand, Margarita Corzo, Neil Hoghson my coffee mates and many others students and staff at Heriot-Watt have been invaluable.

Finally, I would like to thank my friends in Britain, ainsi que ma famille et amis en France for their moral support et inestimable soutien.

Last but not least, I am truly indebted to Ann for her endless support, patience and love during these three years.

List of figures

List of tables

Chapter 1

Introduction

In the last decade, the use of seismic monitoring (4D) has greatly increased, and oil companies have shown their commitment to this technology (Marsh *et al.*, 2003; De Waal and Calvert, 2003), as confirmed by its more systematic application. Time-lapse seismic is now an integrated part of reservoir management strategy, and has proved its ability to improve reservoir understanding. The relatively low cost of this technology also makes it really attractive, especially in the deep water of the Gulf of Mexico or west of the Shetland Isles, where drilling operations or well interventions are costly. In some fields, like Foinaven and Schiehallion (west of Shetland), which are developed from subsea installations, the only source of information for monitoring production effects is 4D seismic, since PLT (Production Logging Tool) data are too expensive to acquire. The surveillance of this type of field relies entirely on 4D seismic, even if permanent pressure gauges or tracers are increasingly employed (Clifford, 2005). The application of time-lapse seismic has evolved a great deal over recent years, as evidenced by the frequent technical sessions and special workshops that are organized every year by the Society of Exploration Geophysicists (SEG) or the European Association of Geoscientists and Engineers (EAGE). In the past, the applications of seismic monitoring were predominantly focused on the tracking of fluid contacts and movements (i.e. gas-cap expansion, water sweep); discrimination between lithology and fluid effects; and identification of pressure compartment and reservoir connectivity. These qualitative sources of information were then exploited to update reservoir models and ultimately improve the prediction from the flow simulator. The growth of seismic reservoir monitoring has brought new technical challenges to the industry, in order to improve and enlarge the existing portfolio of this technology. In fact, the advance in acquisition (i.e. stearable streamers, full-wave field recording devices, permanent sensors), survey design (i.e. 4D dedicated acquisition),

seismic processing (i.e. specific 4D workflow) and integration between contractors and oil companies (i.e. in-house processing and R&D teams) have improved the repeatability and quality of the data, and paved the way for new applications. Time-lapse seismic is now being used in more challenging reservoirs, such as the carbonate fields of the Middle East, in order to monitor the steam-flooding process required for the extraction of heavy oils. Permanent down-hole geophones are used to acquire vertical seismic profiles (VSPs) in an active and also a passive mode, in order to record micro-seismic events induced by reservoir stress changes due to hydrocarbon production (Dasgupta, 2004). Thanks to the ability of new recording systems to characterize near-surface velocity variations, 4D monitoring has shifted onshore. Nine-component (9C) repeated land seismic surveys are now acquired, and have the potential to understand complex fracture networks and hydrocarbon migration, as in the Rulison field (Jackson *et al.*, 2004), and the potential to monitor CO_2 flooding as in the Weyburn field (Terrell *et al.*, 2002). The added value from seismic reservoir monitoring for field development is undeniable, and will only increase as it evolves towards a real-time integration of this technology with engineering data in fields such as Valhall (Barkved *et al.*, 2004), where ocean-bottom cables (OBC) are deployed to acquire seismic data on a trimestrial basis. Besides this, research has now moved towards the more quantitative aspects of 4D, by attempting to estimate hydrocarbon-production-related changes directly from seismic data. However, in most cases, seismic amplitude changes are not only due to variation in fluid saturation, pore pressure or even compaction, but to a combination of these effects. The goal of distinguishing between pore pressure and fluid saturation effects is the Holy Grail of 4D seismic, and has been the subject of many papers. Being able to accurately separate these two production effects would have an unquestionable impact on the management of a field, and particularly on the production and injection strategy. For example, pore pressure monitoring can allow reliable compartmentalization and connectivity interpretation of a reservoir in order to plan infill drilling. Additionally, it can also assist in assessing the strength and pressure support provided by an aquifer, in order to avoid the placement of an unnecessary injection facility. Pore pressure maintenance in an oil/water system is also of primary importance in order to limit the amount of gas coming out of solution, and ultimately to prevent the formation of a

gas cap. In reservoirs where the initial pore pressure is already close to the bubble-point pressure, any misinterpretation between pressure and saturation effects can lead to an imprecise choice of production or injection rates. In many cases, fluid saturation effects are incorrectly assumed to be the controlling factor in the 4D signatures, leading to an inaccurate estimation of hydrocarbon saturation, especially in the vicinity of injectors, where pressure variations produce significant amplitude changes. Improvements in oil saturation estimation can be beneficial for the monitoring of the water front and the determination of the producing interval within a reservoir. The independent estimation of pore pressure and fluid saturation, which are also two products from the reservoir flow simulation, allows a direct comparison between attributes derived from the seismic and engineering domains. These production attributes could be used in a 4D seismic history matching workflow in order to directly constrain the predictions from the fluid flow simulator with the seismically derived dynamic properties. Modifications of the reservoir model can also be made to improve the agreement between the flow simulation results and the seismically derived production estimates, and ultimately to increase reservoir performance and oil recovery. Following the development of pressure and saturation discrimination techniques, subsequent applications are also emerging, such as the estimation of fluid-flow properties (MacBeth, 2004; Vasco, 2004). This tendency increases the need for highly reliable separation of pressure and saturation effects, for instance, to improve the prediction of permeability and transmissibility (Almaskeri and MacBeth, 2005). The separation of pressure and saturation effects has mainly been tackled by means of rock-physics-based techniques (Brevik, 1999; Tura and Lumley, 1999; Landrø, 2001), and it is only recently that engineering approaches using production, pressure and PVT data, have been developed (He *et al.*, 2004; MacBeth *et al.*, 2004). Due to the dual dependency of seismic amplitude on pressure and saturation variations, these techniques require constraints from the rock physics or the engineering domains – depending on which route is favoured. These constraints involve mainly the derivation of approximate relationships between seismic amplitudes and production effects. These approximations represent the foundation of all methodologies, and need to be robust in order to stand any chance of success. However, the complexity of the fluid pressure and saturation sensitivity

of clastic reservoirs makes it difficult to determine these relations, since they might differ for different reservoir geological settings and production scenarios. As a result, proposed methodologies fail to meet the needs of the industry because of their restricted range of applicability. Despite some interesting work, many challenges remain before the issues of this subject can be fully addressed.

An academia–industry research collaboration between the Compagnie Générale de Geophysique (CGG) and the Heriot-Watt Institute of Petroleum Engineering, initiated the work presented in this dissertation. The aim of the project is to develop an accurate seismic method for monitoring changes in fluid pressures and saturations inside a producing hydrocarbon reservoir and between well locations. The study focuses on a variety of clastic reservoir rocks, and therefore offers a new technique applicable to a large variety of reservoirs. A detailed petro-elastic analysis of reservoir sandstones is carried out in order to precisely quantify their pressure and saturation dependency and ultimately improve upon existing techniques by obtaining highly accurate relationships between seismic attributes and production effects. This analysis includes the investigation of key elements such as the effects of clay content, porosity and core damage on the stress-sensitivity of sandstones, in order to strengthen the rock-physics basis of the proposed method. Steps are also made towards a more explicit inversion of pressure and saturation attributes from 4D seismic, in an effort to reduce the possible ambiguities that could occur between production estimates. For the purpose of characterizing fluid saturation effects, in this dissertation, fluid bulk modulus is preferred over hydrocarbon saturation. Assumptions about the saturation distribution (i.e. homogeneous or heterogeneous) can lead to erroneous production estimates – particularly in highly heterogeneous reservoir rocks.

This thesis is subdivided into seven chapters. Chapter 2 gives a general overview of the existing techniques used to discriminate between pressure and saturation effects, and exposes the limitations of these techniques. Chapter 3 presents a detailed petro-elastic analysis of sandstone reservoirs, and introduces an original rock physics correlation in order to isolate fluid pressure and saturation changes. In Chapter 4, the link between elastic

rock properties and the seismic AVO response is made by developing newer forms for offset-dependent reflectivity and impedance. In Chapter 5, a new method to invert for pore pressure and fluid bulk modulus changes is tested on a reservoir model-based study. In Chapter 6, an independent separation of reservoir pressure and saturation is applied to the Palaeocene turbidite sands from the Foinaven field, west of Shetland. In the concluding chapter, Chapter 7, the main results from each chapter are discussed, and possible extensions of this work are proposed.

Chapter 2

Overview of techniques for pressure and saturation discrimination

The determination of reservoir dynamic properties (i.e. pressure and saturation changes) has become a popular topic of research, mainly due to the introduction of time-lapse seismic technology and to the impact that such reservoir properties estimates can have on field management – as seen in Chapter 1. From the literature, one can see that two trends are discernible to independently estimate pressure and saturation effects: rock-physics- and engineering-based approaches. The rock-physics-based method aims to relate changes in the elastic properties of a rock measured in the laboratory, to time-lapse changes in seismic attributes. In these methods, the definition of the pressure- and saturation-sensitivity models is a key step, as well as the calibration of these models from the ultrasonic to the seismic-frequency domains. Another tendency that has emerged recently is the integration of production data in the separation of pressure and saturation effects. The production data can be seen as a way of constraining the previous rock-physics-based techniques, or can also be used independently to estimate production effects. In this chapter, the most recent developments in pressure and saturation inversion are discussed.

2.1 Rock-physics-based methodology

Brevik (1999) developed an inversion procedure to invert for pressure and saturation changes in a reservoir by minimizing the misfit between observed and modelled time-lapse changes in seismic amplitude and travel-time. A rock physics model is defined as linking production-related changes to seismic properties. By applying the technique to a synthetic case study, Brevik showed that reliable estimates could be obtained by using two independent seismic observations (i.e. P- and S-wave travel-times), and demonstrated that interdependence between these observations (i.e. P-wave travel-time and the ratio of S- to P-wave travel-time) bring instability in the inversion process. The use of seismic amplitude rather than travel-time, and its application to real data, is not discussed in his paper or reported in the literature. However, an attempt is made to study the sensitivity of the pressure and saturation estimates to errors in the measured travel-times. In 1999, Landrø introduced a method to discriminate between these production effects, based on the derivation of rock physics approximations relating pressure and saturation effects to density, P- and S-wave velocities. These approximations are then used to rearrange the P-wave reflectivity formulation to obtain pressure and saturation variations as a function of the change in AVO (amplitude versus offset) attributes (i.e. intercept and gradient defined in section 4.2.1). The reflectivity formulations and AVO concept are presented in Chapter 4. A pressure-sensitivity model for P- and S-wave velocity changes is derived from ultrasonic laboratory measurements. Figure 2.1 shows the second-order approximation linking relative change in P-wave velocity to variation in effective stress (i.e. effective pressure). It should be noted that the effect of pressure on the density term is relatively small for most consolidated sandstones (c.f. section 3.1.3) and assumed to be negligible when using this technique. Furthermore, linear approximations are derived for the density (ρ), P- (α) and S-wave (β) velocities as a function of water saturation. Figure 2.2 presents the calibrated saturation-sensitivity model obtained for the relative change in P-wave velocity as a function of water saturation. In summary, relative variations in seismic properties are represented by a first-order approximation for the saturation effect and a second-order approximation for the pressure effect as follows:

$$\frac{\Delta V_P}{V_P} = k_\alpha \Delta S + l_\alpha \Delta P + m_\alpha \Delta P^2 \tag{2.1}$$

$$\frac{\Delta V_S}{V_S} = k_\beta \Delta S + l_\beta \Delta P + m_\beta \Delta P^2 \tag{2.2}$$

$$\frac{\Delta \rho}{\rho} = k_\rho \Delta S \tag{2.3}$$

where ΔS and ΔP stand for the change in oil saturation and effective pressure, respectively. The k_α, k_β, k_ρ, l_α, l_β, m_α and m_β are the fitting parameters derived from ultrasonic laboratory measurements as in Figures 2.1 and 2.2.

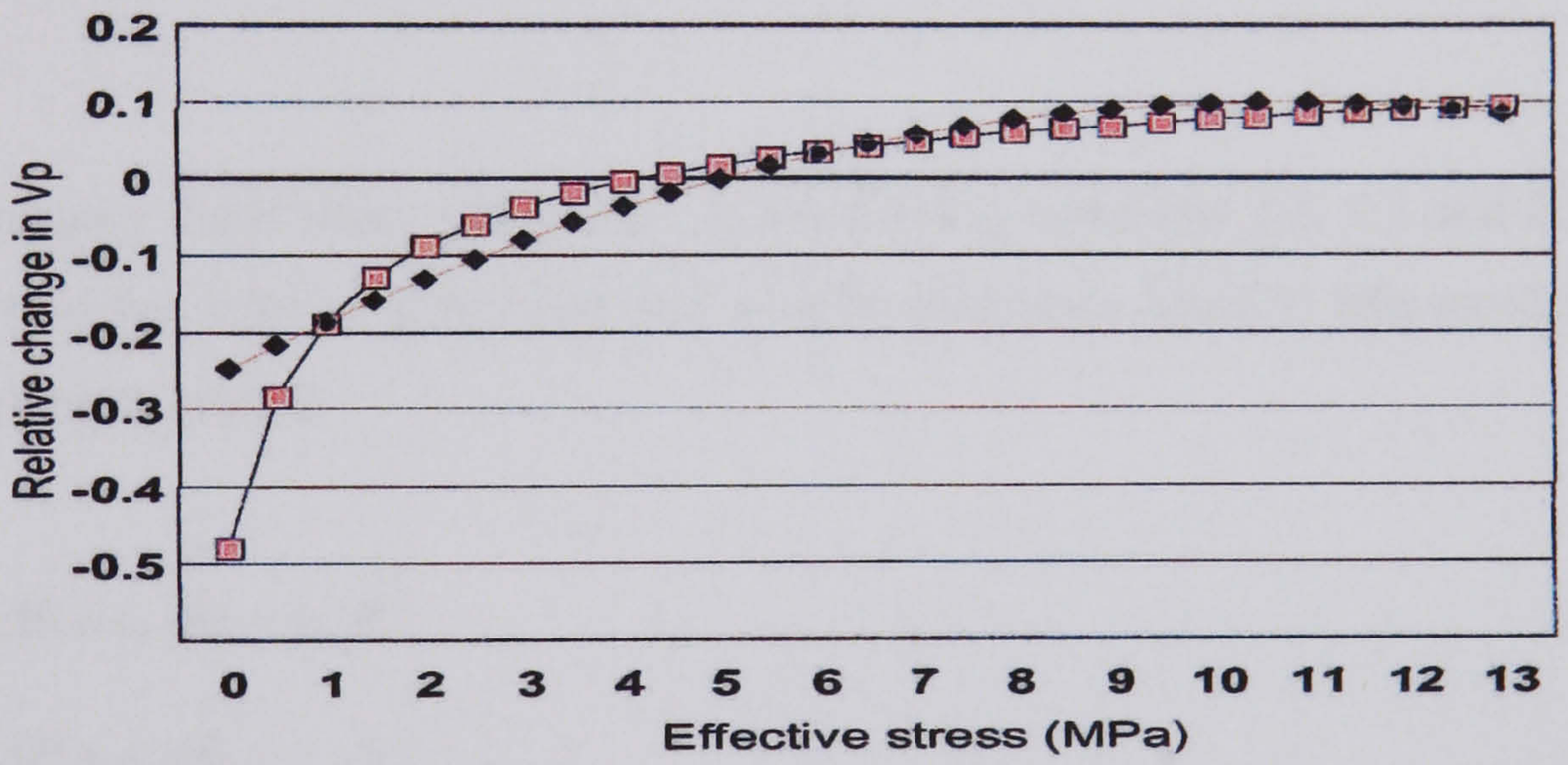

Figure 2.1: Relative change in P-wave velocity as a function of effective pressure (squares) for a typical calibrated Gassmann model. A linear fit (diamonds) is used to approximate the change of V_p due to water saturation (from Landrø, 2001).

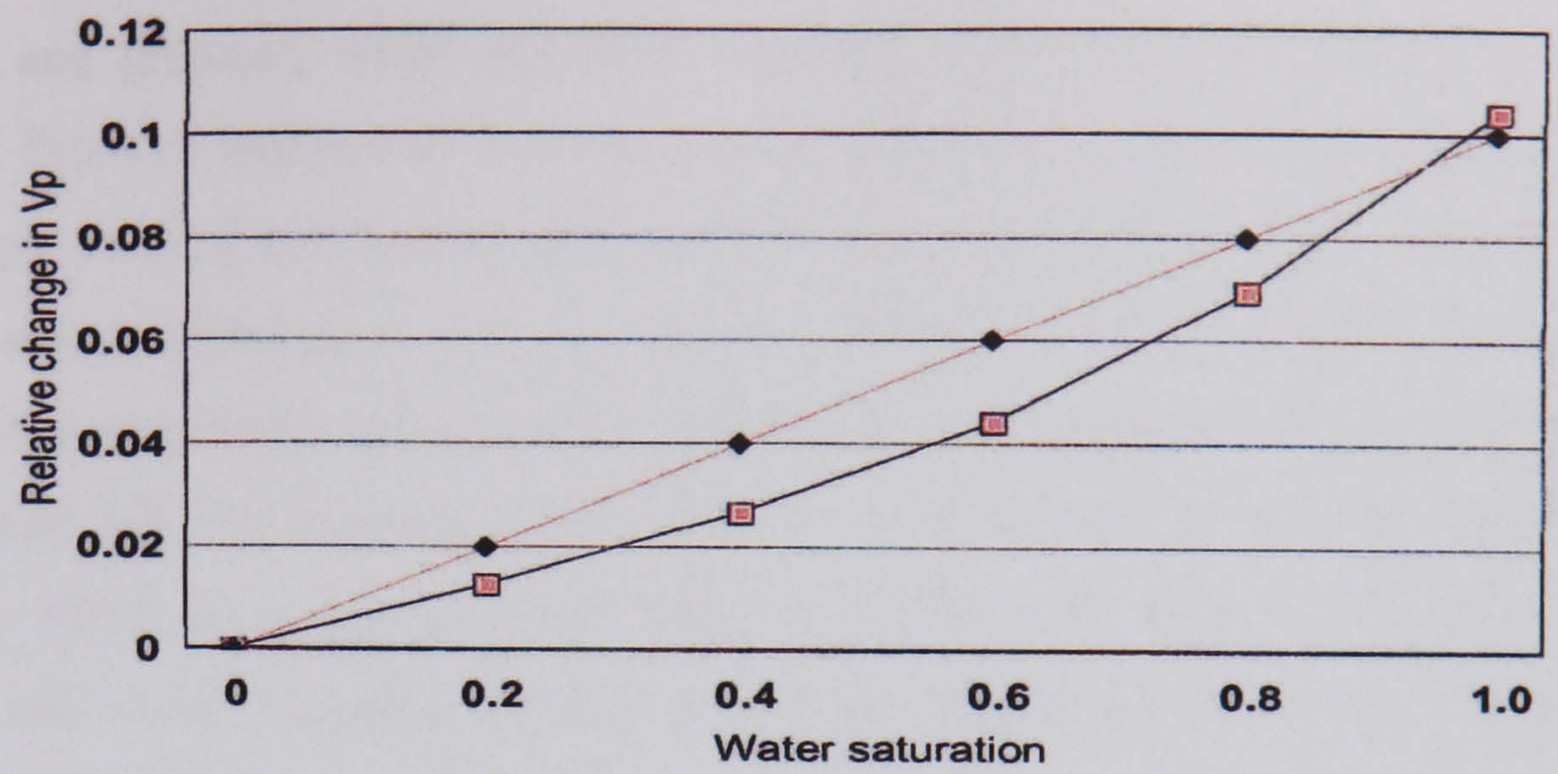

Figure 2.2: Relative changes in P-wave velocity as a function of water saturation (squares). Changes are relative to the initial pressure of the reservoir (i.e. 5 to 6 MPa). A second-order fit (diamonds) is used to represent the relationship between V_p and effective pressure (from Landrø, 2001).

By rearranging the P-wave reflectivity equation using equations 2.1, 2.2 and 2.3, Landrø showed (Landrø, 2001) that pressure and saturation changes could be expressed as follows for an oil/water system:

$$\Delta S \approx c_1 \Delta R_0 + c_2 \Delta G \tag{2.4}$$

$$\Delta P \approx c_3 \Delta R_0 + c_4 \Delta G \tag{2.5}$$

where ΔP, ΔS, ΔR_0 and ΔG are the changes in effective pressure, oil saturation, intercept and gradient, respectively. The coefficients c_1, c_2, c_3 and c_4 can be deduced from the empirical parameters k_α, k_β, k_ρ, l_α, l_β, m_α and m_β. To obtain these results, all relative changes in seismic properties must to be small; a velocity ratio V_P/V_S equal to 2 is chosen; and the assumption for small angles ($\sin^2\theta \approx \tan^2\theta$) is made. The method was tested on the Gullfaks field, Norwegian Sea, by deriving AVO attributes from near- and far-offset stacks rather than pre-stack gather analysis, in order to reduce the contamination by noise from the estimated intercept and gradient changes. Figure 2.3 shows a seismic section of change in

intercept and gradient, where an AVO anomaly is visible at the Top Cook formation interface. From an analysis of 29 core plugs, pressure and saturation sensitivity models for density (ρ), *P*- (V_P) and S-wave (V_S) velocities were derived, leading to the derivation of the following coefficient $c_1 = 8$, $c_2 = 8$, $c_3 = 23$ and $c_4 = -35$ in equations 2.4 and 2.5. Figure 2.4 shows the resulting pressure and saturation changes for the same seismic section as in Figure 2.3. An increase in pore pressure is observable at the Top Cook formation interface, which is caused by water injection in this area. Figure 2.5 presents the pore pressure and fluid saturation maps from the Top formation interface. It is notable that saturation changes follow the original oil–water contact closely, while pore pressure variations give an indication of the nature of some faults that can be interpreted as sealing. However, in the northern part of the map, anomalies are visible in the water zone, which are attributed to leakage between the pressure and saturation attributes since no fluid effect is expected in this area. The methodology above relies on AVO attributes that are known to be highly sensitive to noise (Cambois, 2000) and this is likely to reduce the quality of the production estimates. Furthermore, a total of five rock physics approximations are necessary for this technique: approximations which increase the error in the estimates and ultimately the possibility of cross-talk between pressure and saturation domains. The choice of a constant velocity ratio might also be the cause of the cross-talk, since it is a function of these production effects. In fact, the velocity ratio V_P/V_S is mostly dependent on pressure changes and varies only slightly with saturation (Stovas and Landrø, 2004). However, Landrø's method is straightforward to implement if the appropriate rock physics data are available, which makes it an attractive candidate for pressure and saturation discrimination.

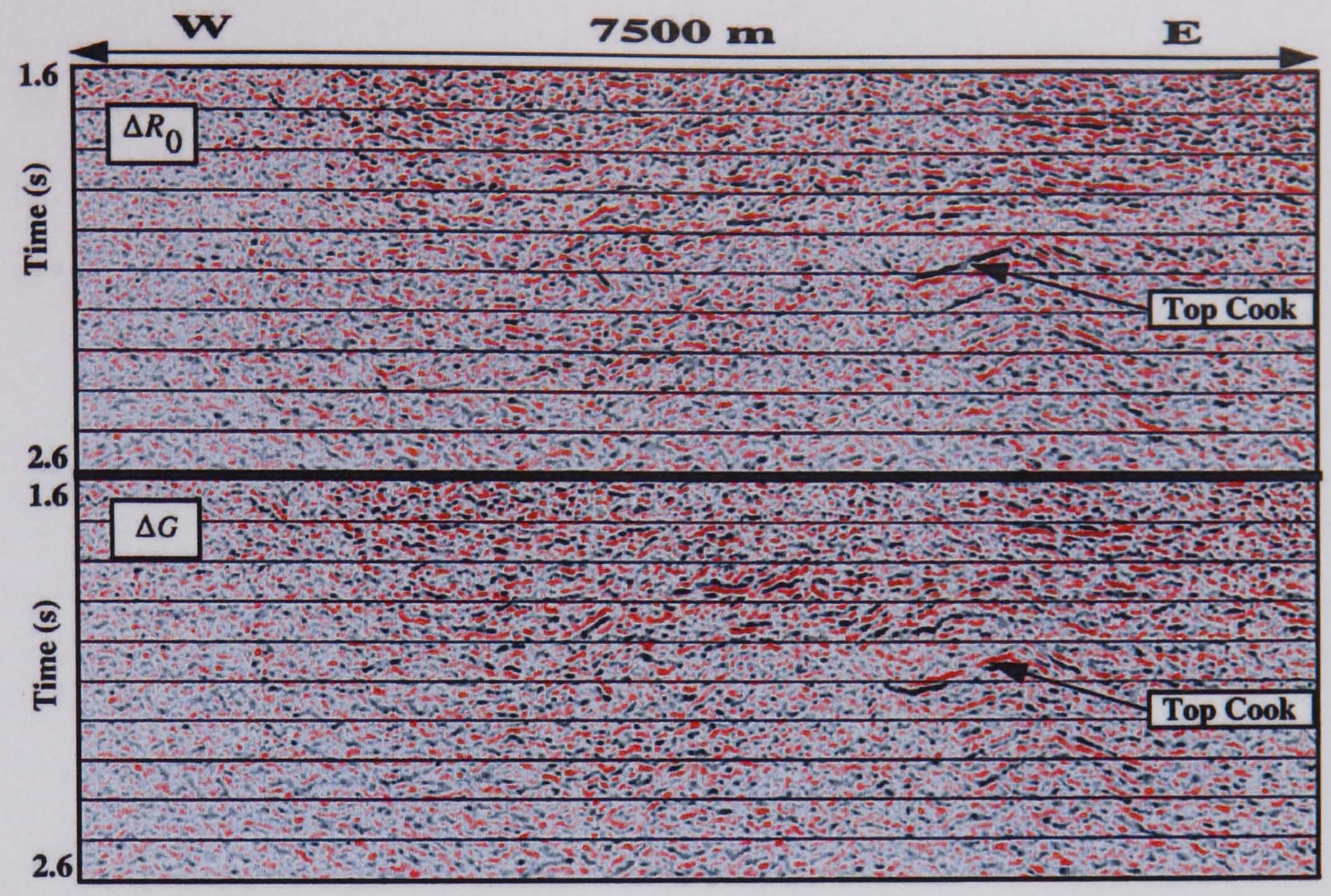

Figure 2.3: Changes in intercept *(ΔR_0)* and gradient *(ΔG)* for a seismic profile from the Gullfaks field. AVO products are computed between the baseline survey (1985) and a repeat survey (1996) based on the near- and far-offset stacks. AVO anomalies are observable at the Top Cook formation interface (from Landrø, 2001).

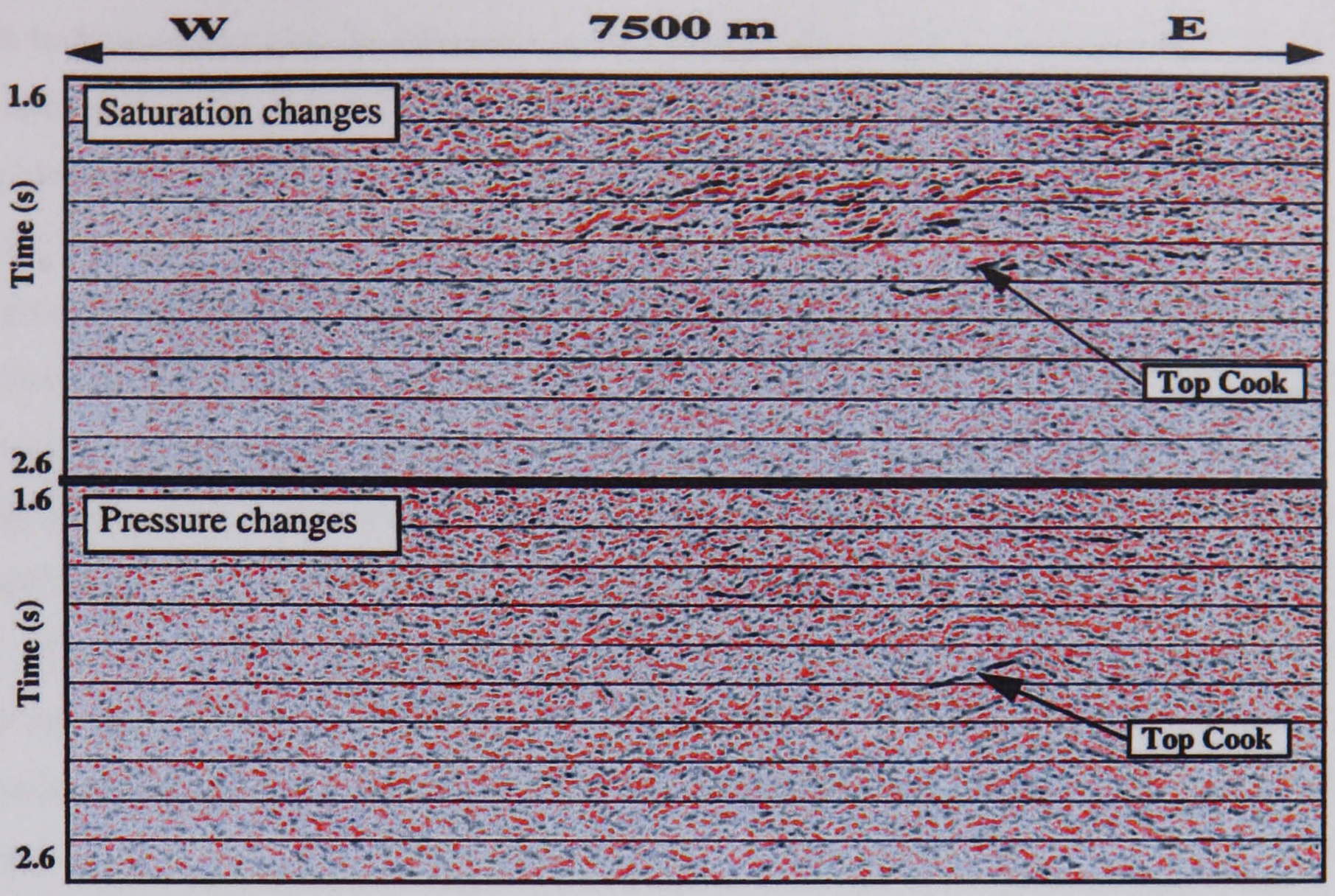

Figure 2.4: Oil saturation and pore pressure estimates obtained for the same seismic profile as in Figure 2.3. A large increase in pressure is visible at the Top Cook formation interface. This pressure anomaly is caused by water injection in this part of the reservoir (from Landrø, 2001).

Figure 2.5: Map view of the saturation (left) and pressure (right) attributes at the Top formation interface. The original oil–water contact (OOWC) is shown on both maps (red curve). The distribution of the pressure changes appears to be controlled by the faults, while the saturation anomalies follow the OOWC in the western part of the display (from Landrø, 2001).

This technique can also be extended to multicomponent marine data (Landrø *et al.*, 2003) by rearranging the PS reflectivity formulation. In 2001, two enhancements to Landrø's method were proposed (Meadows, 2001). One of them is the formulation of pressure and saturation changes in terms of relative changes in P- and S-wave impedances, in order to improve the reliability of the input seismic attributes of the method compared to the intercept and gradient. The second one is the derivation of a second-order approximation between velocities and saturation, which is more realistic than the linear one. The first modified method appears to be comparable to the original technique, while the second modified method improves the estimation of the saturation changes. In both cases, leakages are still observed from the pore pressure to the fluid saturation domains. However, it appears that the integration of time-lapse travel-time in addition to amplitudes might be a promising way to improve the production estimates (Landrø *et al.*, 2001). Landrø (2002) presented a deterministic uncertainty analysis of his methodology by using both 4D amplitude and travel-time. He demonstrated the potential of the 4D travel-time for reducing the uncertainty in the pressure and saturation estimates. Later, Veire *et al.* (2003) incorporated Landrø's approach into a Bayesian framework, and, using a synthetic example, showed the ability of their stochastic inversion to estimate pressure and saturation together with direct information on the uncertainty in the estimates.

Tura and Lumley (1999) presented a technique to estimate pressure or saturation when only one of these effects dominates the reservoir. They showed by cross-plotting time-lapse P- and S-impedances that saturation tends to cluster along the P impedance axis, while pressure changes cluster along the S-impedance axis. In the case of the combined effect of pressure and saturation, the points roughly follow the diagonal of the cross-plot. The clustering makes it possible to identify areas where changes in pressure only, saturation only, or a combination of both have occurred after remapping of the cross-plot amplitudes to their original location in the seismic domain. An additional calibration procedure applied to these amplitudes with production and rock physics data provides quantitative estimates of pore pressure and water saturation. An extension of this method (Lumley *et al.*, 2003) is possible by cross-plotting any set of attributes containing P- and S-wave information as

previously, and defining a pressure and saturation axis (Figure 2.6). Then, a coordinate transformation that can be linear or non-linear (depending on the definition of the axis), is applied to convert the data from the seismic (ΔA_p, ΔA_s) domain to the pressure and saturation (ΔP_p, ΔS) domain.

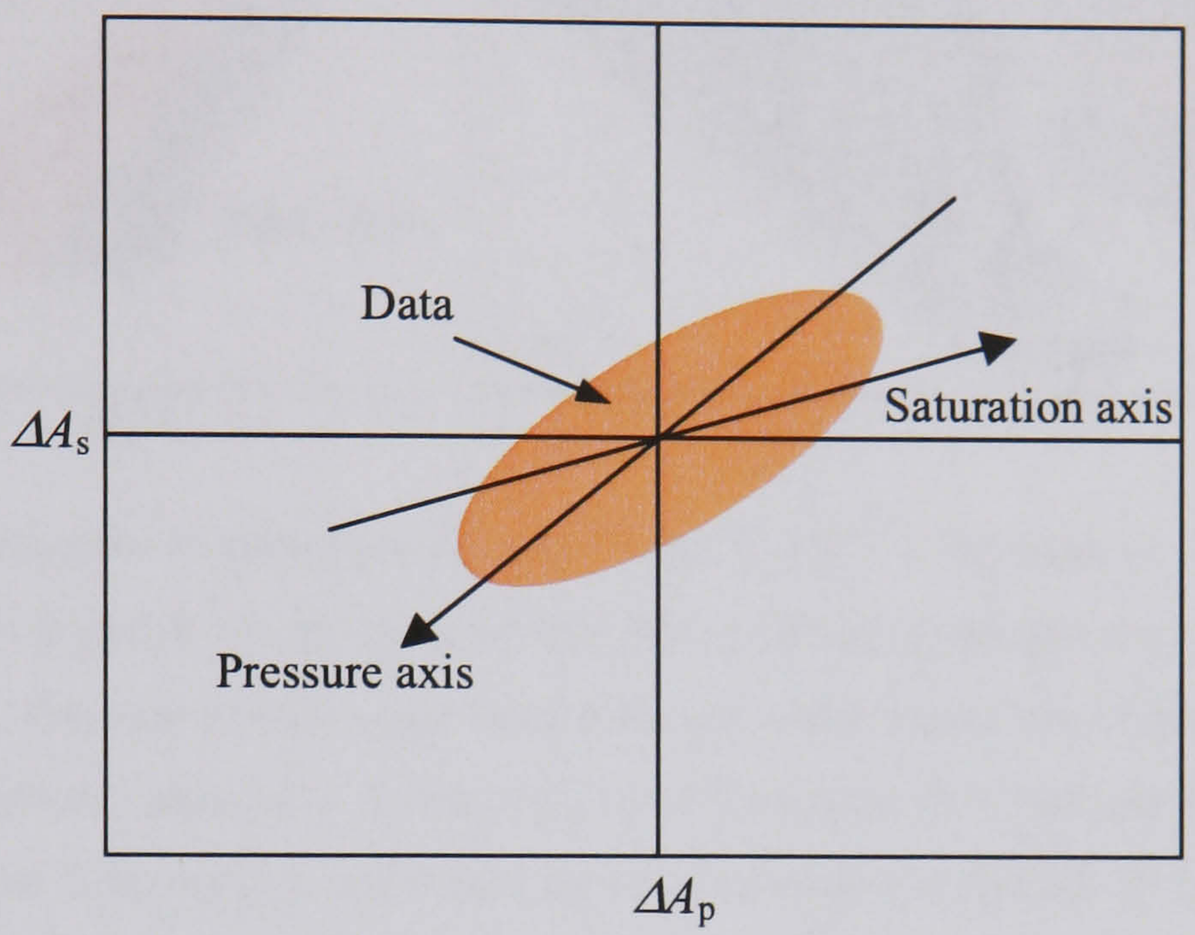

Figure 2.6: Illustration of the cross-plot of two seismic attributes ΔA_p (P-wave dominated) and ΔA_s (S-wave dominated). The pressure and saturation axes are determined by rock physics modelling. It should be noted that these axes can be non-linear or even different in each quadrant of the cross-plot, since the rock, for example, responds differently to a pressure increase or decrease.

In order to be quantitative, this method requires a calibration of the seismic attributes (i.e. ΔP_p and ΔS) to time-lapse saturation logs and bottom-hole pressure data. Cole *et al.* (2002) introduced qualitative and quantitative techniques, which are based on rock physics forward modelling, and, once again, a cross-plot of time-lapse impedances. After a dedicated rock physics analysis (Meadows *et al.*, 2002), modelled P- and S-wave impedances are cross-plotted in order to identify four quadrants where different scenarios of pore pressure, water and gas saturation changes occurred, as in Figure 2.7a. By cross-plotting the real P- and S-impedances on to the previous cross-plot it is possible to colour-code the seismic data as a function of the different production scenarios, as presented in Figure 2.7b.

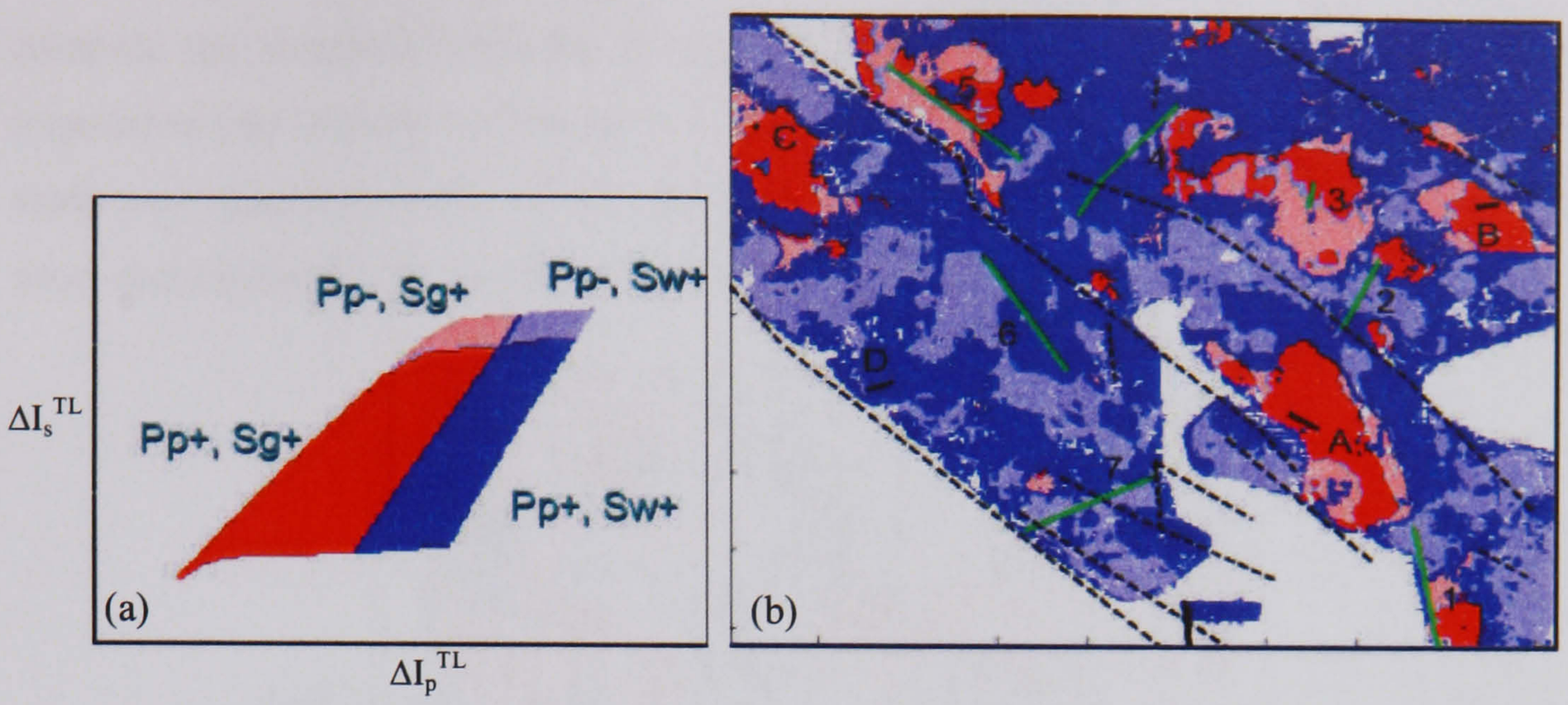

Figure 2.7: (a) Cross-plot of time-lapse P- (ΔI_p^{TL}) and S- (ΔI_s^{TL}) impedances, illustrating that pore pressure and fluid saturation can be grouped into four different quadrants (i.e. different scenarios). P_p, S_g, S_w stand for the pore pressure, gas saturation and water saturation, respectively, while the + and – signs represent an increase or decrease in these quantities. (b) Qualitative pressure/saturation scenario maps of the Schiehallion field obtained after relating the real 4D P- and S-impedances to the corresponding pressure/saturation scenario defined in (a). Injectors, producers and faults are shown by black, green and dotted black lines (from Cole *et al.*, 2002).

In order to make the technique quantitative, all possible P- and S-impedance values are forward-modelled to obtain a finer grid of the 4D impedance cross-plot. A 3D cube, containing pairs of P- and S-impedance-changes as a function of pore pressure, saturation and porosity changes, is forward-modelled. Then, a picking procedure is applied to select the pressure/saturation scenario corresponding to the real P- and S-impedance changes within the volume. The picking can be constrained by a priori porosity information from the reservoir model or an average reservoir value to reduce the number of pressure/saturation scenarios. Figure 2.8 shows the resulting pore pressure and water saturation maps. Pressure variations appear to correlate with the position of the wells, while unrealistic changes are observed at several injectors where increases in water saturation are not visible. This is attributed to rock damage occurring in the vicinity of the injectors. This could also be due to inaccuracy in the derivation of the rock physics model affecting the definition of the pressure and saturation axis. Furthermore, there is an opportunity to

compute the standard deviation for the production estimates, since a given P- and S-impedance pair is likely to provide several pressure and saturation scenarios. This real case study was carried by using 4D P- and S-impedance as discriminating attributes, but might show more potential for an alternative pair of seismic attributes.

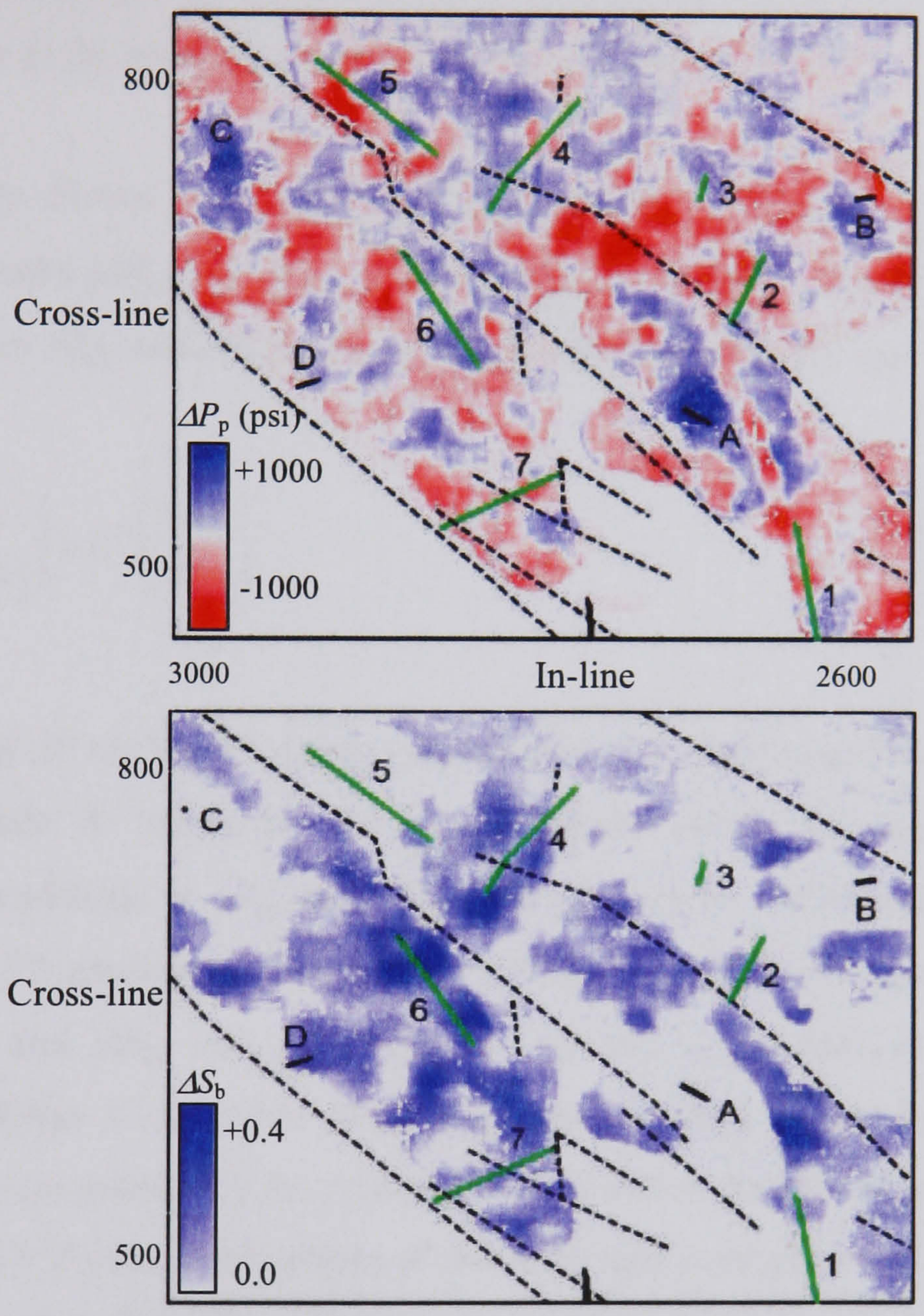

Figure 2.8: Quantitative pore pressure (top) and water saturation (bottom) maps derived from the second method (see the text) proposed by Cole *et al.* (2002). Pore pressure increase can be observed in the vicinity of injectors, while decrease is noticeable near most producers. Despite rather large changes in the pore pressure near injectors (A, B and C), no variations in water saturation are visible. In fact, improbable gas saturation increases (not shown here) are estimated at these locations. Injectors, producers and faults are shown by black, green and dotted black lines (from Cole *et al.*, 2002).

Alvarez *et al.* (2002) showed that time-lapse changes in P- and S-impedances are not the ideal attributes to discriminate between pressure and saturation. They classified the discriminating power of different pairs of attributes (i.e. P- and S-wave velocities, P- and S-impedances, Poisson ratio and P-impedance, and fluid factor and AVO gradient), and demonstrated that the time-lapse fluid factor and the AVO gradient cross-plot offer a better orthogonality of the pressure and saturation axis (as in Figure 2.6).

More recently, Stovas and Landrø (2004) proposed a methodology combining PP and PS time-lapse stacks (ΔR_{pp} and ΔR_{ps}) to independently estimate pressure and fluid effects. The inversion from ΔR_{pp} and ΔR_{ps} to pressure and saturation changes can be expressed as:

$$\begin{pmatrix} \Delta S \\ \Delta P/P_0 \end{pmatrix} = B^{-1} \begin{pmatrix} \Delta R_{pp} \\ \Delta R_{ps} \end{pmatrix} \tag{2.6}$$

where ΔS and ΔP are the 4D saturation and pressure changes, and P_0 is the initial effective pressure, while B represents the transformation matrix depending on pressure and saturation. In addition to ΔR_{pp} and ΔR_{ps}, different pairs of AVO attributes (i.e. intercept, PP gradient and PS gradient) were tested in the same inversion procedure as in equation 2.6, and showed that ΔR_{pp} and ΔR_{ps} offer the optimal discrimination. Furthermore, it was demonstrated that a maximum offset angle for the stack should be selected in order to minimize the uncertainty in the production estimates in the inversion of the matrix system in equation 2.6. Further applications of this technique were proposed by Stovas and Landrø (2004) to analyse the effect of net-to-gross ratio (N/G) on the discrimination on the previous production effects, and by Stovas *et al.* (2004) to separate between N/G and saturation. Looking towards an integration of seismic with other geophysical surveillance methods, Hoversten *et al.* (2003) presented a method combining cross-well seismic and electromagnetic (EM) data. Predictions of pore pressure, water saturation and CO_2 gas/oil ratio are made for a reservoir undergoing CO_2 flooding.

2.2 Engineering-based methodology

MacBeth *et al.* (2004) introduced a method to calibrate 4D seismic attribute difference to production data from injector and producer wells, in order to estimate pore pressure and fluid saturation. The method is divided into two steps. First, the 4D signal is processed to reduce spurious noise only keeping a genuine time-lapse signature. To achieve this, a threshold is defined so that the 4D signal agrees with the well activity within the reservoir. In the second step, this thresholded 4D signal is calibrated to well data. A linear approximation for the 4D signal is used (equation 2.7), and the coefficients a and b are derived from two repeated surveys by solving the linear system (equations 2.8 and 2.9).

$$\overline{\Delta A} \approx a\overline{\Delta S_o} + b\overline{\Delta P} \tag{2.7}$$

where $\overline{\Delta A}$ is the pore volume average of the seismic attribute changes, while $\overline{\Delta S_o}$, $\overline{\Delta P}$ are the average oil saturation and pore pressure changes in the entire reservoir, as determined from production data. Equation 2.7 is valid for any attributes sensitive to pressure and saturation (i.e. offset stacks, AVO attributes, impedance, instantaneous frequency, phase or time-shifts).

$$\overline{\Delta A_{12}} \approx a\overline{\Delta S_{12}} + b\overline{\Delta P_{12}} \tag{2.8}$$

$$\overline{\Delta A_{13}} \approx a\overline{\Delta S_{13}} + b\overline{\Delta P_{13}} \tag{2.9}$$

where the subscripts (1,2) and (1,3) stand for the time-lapse difference between the first (2) and second repeat (3) survey with the baseline survey (1). The main assumption in this technique is that sufficient production changes have occurred between each survey, and that the coefficients a and b are time-invariant. Two pairs of coefficients (a, b) and (c, d) are computed from two different seismic attributes (i.e. A and B) in order to allow for separation of pore pressure and saturation changes by inversion of equations 2.10 and 2.11.

$$\Delta A(x,y) = \hat{a}\Delta S_o(x,y) + \hat{b}\Delta P(x,y) \tag{2.10}$$

$$\Delta B(x,y) = \hat{c}\Delta S_o(x,y) + \hat{d}\Delta P(x,y) \tag{2.11}$$

where $\hat{a}$, $\hat{b}$, $\hat{c}$ and $\hat{d}$ are estimates from above. It should be noted that the seismic attributes should be relatively uncorrelated, to avoid the use of redundant information in the inversion. This approach was tested on a turbidite sand from the Schiehallion field, west of Shetland. Recently, Floricich *et al.* (2005) improved the previous method by deriving the coefficients *a*, *b*, *c* and *d* at the wells, instead of using a regional calibration procedure, in the process reducing the necessary number of repeat surveys. They also carried out a multi-attribute analysis to select the most suitable seismic attributes (e.g. restricted angle stacks, elastic impedances, intercept-gradient products, instantaneous frequency or phase) for the inversion and extraction by principal component analysis (PCA) of two independent attributes in terms of pressure and saturation. From these new attributes, pore pressure and fluid saturation are estimated by solving equations 2.10 and 2.11. Figure 2.9 shows an example of the application of this technique to a Jurassic reservoir from the North Sea. It should be noted that this approach could be extended by taking into account for the spatial variation of the parameters $\hat{a}$, $\hat{b}$, $\hat{c}$ and $\hat{d}$. This could be achieved by deriving the parameters at various wells and interpolating between the wells or by using a derivation coupled to reservoir flow simulation outputs. A reservoir model-based inversion process was presented (He *et al.*, 2004) in which pressure and saturation estimates were updated from an initial fixed reservoir model until convergence was reached between modelled and real seismic impedances. This technique can be assimilated to a pressure-saturation seismic history matching. The impedances are computed via petro-elastic modelling, and the initial pressure and saturation model is derived from a flow simulation or from production data. The main feature of this inversion is the engineering constraints that are applied during the update of the production attributes. In fact, the attributes have to conform to the material balance law, PVT data, irreducible fluid saturation and bubble point pressure. Furthermore, constraints on the nature of the aerial distribution of the pore pressure are also considered. This technique was applied successfully to a synthetic case and a real field study (Draugen

field, North Sea). It should be noted that the comparison between modelled and real seismic impedance implies an upscaling step that might affect the quality of the final inversion products.

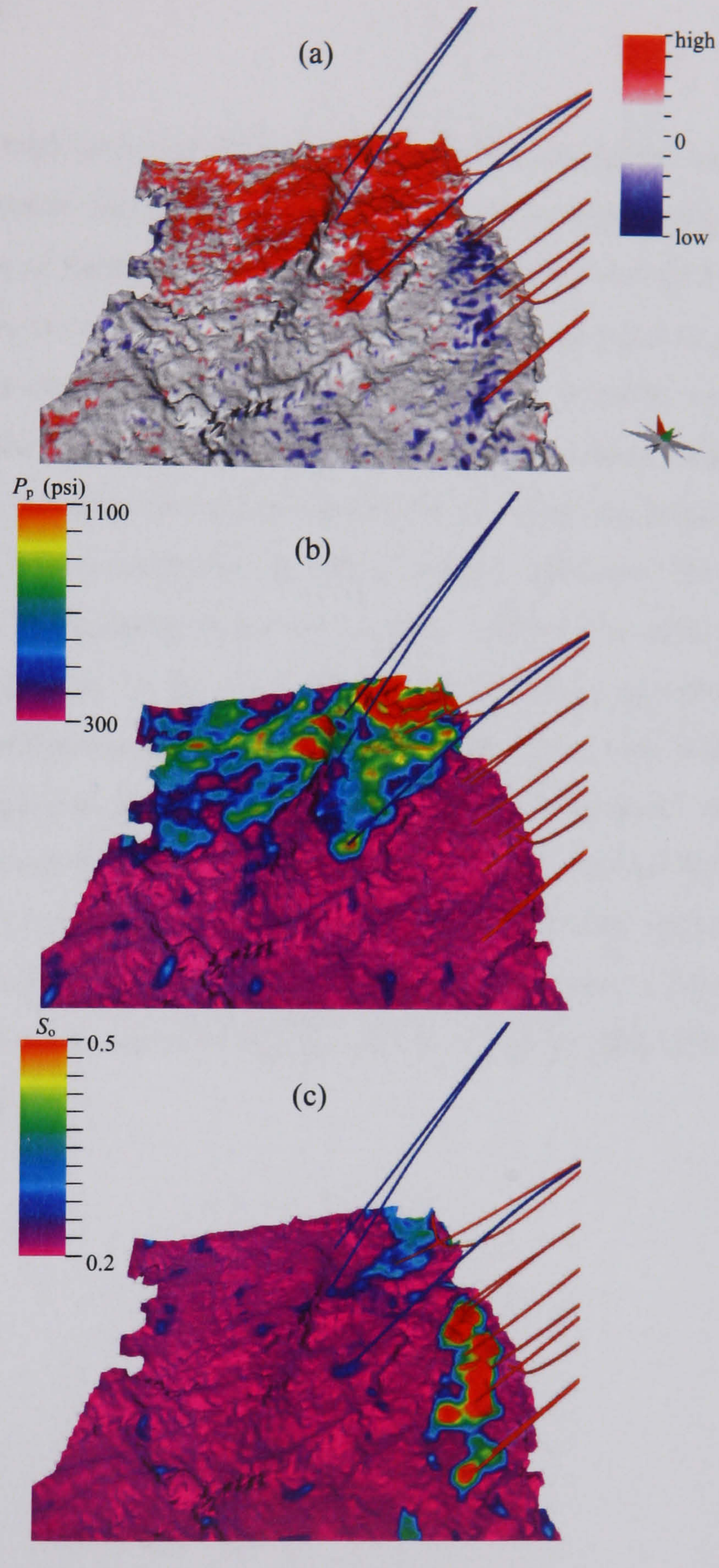

Figure 2.9: (a) Seismic amplitude difference between the baseline and the repeat survey. (b) P50 (50% confidence level) map of pore pressure changes. (c) P50 map of oil saturation changes. Blue and red lines denote the producer and injector wells (from Floricich *et al.*, 2005).

2.3 Conclusions

A critical aspect of the rock physics method presented in this chapter is the accuracy of the models used to characterize the pressure and saturation sensitivity of the reservoir rock. Prior to any application of these methods, the petro-elastic behaviour of the rock needs to be fully understood, in order to identify the controlling parameters (e.g. clay content, porosity variations, core damage effect and fluid distribution). Suitable models have to be derived in order to take into account these factors and to obtain reliable production estimates. Furthermore, the actual techniques assume a homogeneous mixture of fluid, and might therefore under- or over-estimate the effect of fluid saturation. However, the rock physics methodologies (particularly those of Landrø, 1999a; Tura and Lumley, 1999) appear to be the most popular so far. The integration of engineering constraints into the discrimination of pressure and saturation effects provides an opportunity to derive estimates that can honoured independent source of information. Techniques based solely on engineering data have been found to be as reliable as rock physics methods. In addition, they offer the prospect of cross-validation of pressure and saturation estimates originating from the geophysical and engineering domains. A feature common to both approaches is the need for seismic attributes, which are highly sensitive to production effects and, to some extent, are non-interfering.

Chapter 3

Petro-elastic analysis of sandstone reservoirs

The present study focuses on clastic rocks, which make up most petroleum systems, and which are also more predictable in term of geometry and structure than carbonates. A good understanding of the rock and fluid physics within the reservoir is a key element in any reservoir characterization project aimed at qualitative or quantitative interpretation. In the case of discrimination of pore pressure and fluid saturation effects, it is of primary interest to fully understand how the rock's elastic properties respond to those effects. However, elastic properties appear to be affected in a complicated way by both reservoir pressure and fluid saturation – themselves depending on fluid composition, confining pressure, temperature, pore shape distribution, pore aspect ratio, fluid distribution and clay content (Wang, 2000). In the first part of this chapter, I will focus on the pressure and saturation sensitivity of reservoir sandstone, while defining the main factors affecting their behaviour. In the second part, based on a petro-elastic analysis carried out on a variety of reservoir sandstones, two rock physics attributes will be introduced: both acting independently in term of pressure and saturation effects. Finally, the derivation of pore pressure and fluid saturation changes from those two attributes will be presented.

3.1 Stress-sensitivity of reservoir sandstone

Prior to starting this section, it is important to state some basic definitions regarding the composition of sandstones. In geophysics or engineering in general, a sedimentary rock is assumed to be composed of a matrix and pores. A more detailed representation, as found in geology, describes a sedimentary rock as a mixture of grains, matrix, cement and pores. This definition accounts for the depositional history of the rock, where the grains are detrital particles forming the framework, and the matrix is made up of finer particles deposited within the framework at the same period of time. On the other hand, the cement is of post-depositional origin and is formed from minerals that have grown at the grains' surfaces or contacts. Finally, the definition of pores is common to both geological and engineering interpretation – being the voids containing the hydrocarbons. The framework or dry-frame of sandstone will refer to the engineering definition, but, in later sections, the geological definition is also used to consider the different parts of the framework and their effect on the stress-sensitivity of the rock.

3.1.1 An introduction to pressure

Figure 3.1 introduces the terminology for pressure (Bruce and Bowers, 2002) used in this chapter. *Pore pressure* (P_p), also known as formation pressure, is the pressure of the fluid in the pore space of the rock. The *hydrostatic pressure* is the pressure due to a column of water, so, for a rock in which the pores are connected all the way up to the surface, the pore pressure is equal to the pressure exerted by the weight of the overlying fluids. When the pore pressure is greater than the hydrostatic pressure, the excess pressure is referred to as *overpressure* (Carcione and Helle, 2002). The *confining* or *overburden pressure* (P_c) is the pressure exerted by the weight of the overlying rocks, including the pore fluids. Pore pressure and confining pressure have opposite effects on the rock. A confining pressure increase will firstly close the low-aspect-ratio pores (flat pores and cracks), followed by closure of the high-aspect-ratio pores (rounded pores), resulting in an overall stiffening of the rock matrix. In contrast, a pore pressure increase will have an opposite effect as it will re-inflate the matrix.

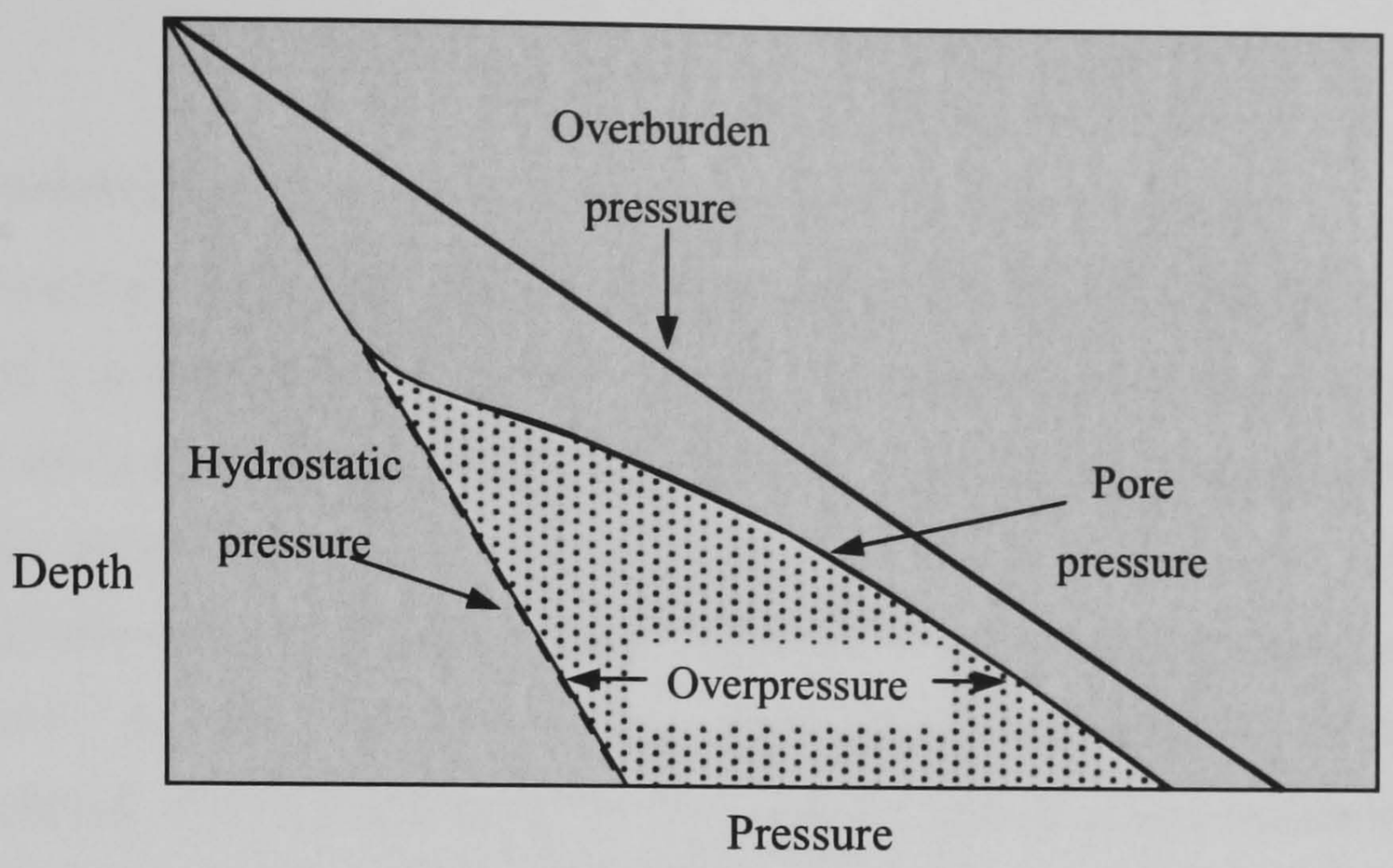

Figure 3.1: Schematic pressure–depth plot, where the different pressure terminologies are illustrated. The amount of overpressure is defined as the deviation between the pore and hydrostatic pressure trends.

Since both pressures have opposite effects on most elastic properties (Zimmerman, 1991), it is possible to express the pressure dependence by a single variable, called the *effective pressure* (P_e). This concept was first introduced by Terzaghi (1936). The effective pressure has the following form (Christensen and Wang, 1985):

$$P_e = P_c - nP_p \tag{3.1}$$

where P_e is the effective pressure, P_c is the confining pressure, P_p is the pore pressure, and n is known as the effective stress coefficient or coefficient of internal deformation. The effective stress coefficient is often set to unity and, in that case, the effective pressure is simply equivalent to a difference of confining and pore pressures, which is called the *differential pressure* (P_d). The effective stress coefficient is generally an unknown, usually lying between 0 and 1, but its limitations for the estimation of the pore pressure are addressed in section 3.3.3.

3.1.2 Prediction of the dry-frame pressure sensitivity of sandstone

A Understanding the pressure dependencies of elastic properties

It is common knowledge that the stress-sensitivity of a reservoir sandstone depends on the textural properties of the rock. For example, in a high-porosity unconsolidated sandstone (i.e. a shallow-marine reservoir) stress-sensitivity will be large compared to that of a low-porosity consolidated sandstone (i.e. a deep-water reservoir). However, this should not be considered as a rule of thumb, because other factors tend to either reduce stress-sensitivity (i.e. clay content), increase it (i.e. micro-crack concentration) or both (i.e. sand composition, texture and distribution). As a generalization, elastic properties will be highly stress-sensitive at low confining pressure until the stress-sensitivity comes close to zero at high confining pressure. In other words, elastic properties (i.e. shear modulus, bulk modulus, V_s, V_p) will increase rapidly at low confining pressure and then reach a characteristic plateau at high confining pressure (Figure 3.2). In 4D feasibility studies, the position of this plateau will determine the stress-sensitivity of the reservoir under study. If, for example, the initial confining pressure is high, the reservoir will have a low stress-sensitivity, and it is likely that 4D changes caused by pressure variations will be under the noise level of the seismic data. If the initial pressure is low to moderate, it is likely that seismic monitoring will be successful, particularly if looking at pore pressure increases rather than pressure depletion. Special care needs to be taken when predicting sandstone pressure-sensitivity, because the accuracy of the pressure laws will drive the reliability of the 4D feasibility study or the ability to discriminate between production effects.

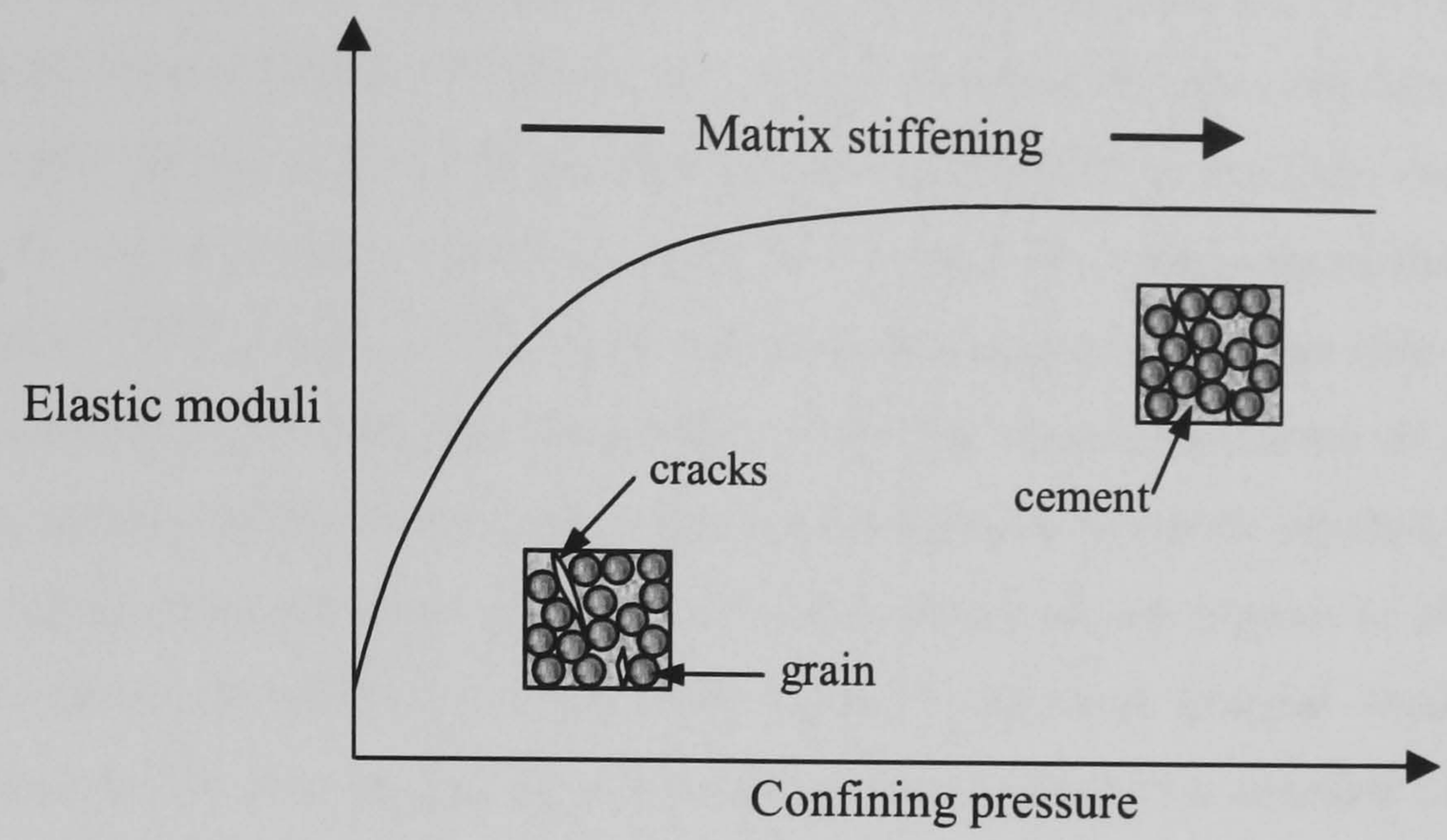

Figure 3.2: Typical pressure dependence of elastic moduli. Under confining pressure loading, all the internal weaknesses of the rock (grain–grain contacts, micro-cracks or regions of discontinuities) close, resulting in an increase in elastic moduli.

There are various ways to model the dry-frame stress-sensitivity of a rock. One approach is to idealize the porous granular rock as a random packing of identical spherical particles, and to use contact theory in order to express the effective elastic moduli of the medium (Mindlin, 1949; Digby, 1981; Walton, 1986). The problem of including spherical particles of different sizes was also dealt with by Brandt (1955), in order to compute the effective bulk modulus only. Models based on contact theory are mainly relevant to unconsolidated systems (Bachrach *et al.*, 2000), even if effective elastic moduli of consolidated systems can be computed by including the effects of cements and asperities at the contact region (Murphy *et al.*, 1991). A second approach is to use effective medium theory to model elastic properties by inserting cavities of varying shapes into the rock matrix, such as ellipsoidal inclusions (Kuster and Töksöz, 1974). In this framework, both dry and fluid-saturated effective elastic properties can be computed by adequately setting the inclusions' modulus. An inherent limitation of the previous methods is the requirement for specific parameters that are generally unknown and need to be estimated. This probably explains why it is common practice in the industry to derive empirical relationships (for example,

Eberhart-Phillips *et al.*, 1989) between elastic properties and effective stress directly from laboratory measurements. However, the empirical approach does not have any physical basis, and it fails to explain the mechanical process involved in the stress-sensitivity of any materials. An alternative approach uses the concept of excess-compliance (Sayers and Kachanov, 1995; Sayers, 2002) to derive semi-empirical relationships able to describe the stress-sensitivity of sandstones (MacBeth, 2004). The stress dependence of the rock matrix (grains, intra-granular detritus and cement) is assumed to be due to internal discontinuities, such as grain–grain contacts, micro-cracks, clay content or any regions of internal damage. In fact, the stress-sensitivity of the rock related to all those internal weaknesses can be accounted for by introducing the excess-compliance, which is a function of the confining pressure loading the rock. At high confining pressures, the rock matrix, which is a homogeneous isotropic elastic medium, will have a finite given compliance, while the excess-compliance will tend to zero because only the incompressible pore space remains and all internal weaknesses are closed. Then, as pressure is released, excess-compliance is formed, due to the opening of cracks and weakening of grain–grain contacts.

B A stress-sensitivity model

MacBeth (2002) proposed compliance-based laws for the dry-frame pressure sensitivity of sandstone, using the concept of excess-compliance. It is important to note that the theoretical bases behind the derivation of those stress-sensitivity formulations are accurate for a homogeneous isotropic elastic medium. Here, two preliminary results from MacBeth (2004) are shown, in order to illustrate where the excess-compliances act on the elastic properties.

$$\kappa(P_c) = \frac{\kappa_\infty}{1 + \kappa_\infty Z_N(P_c)} \tag{3.2}$$

and

$$\mu(P_c) = \frac{\mu_\infty}{1 + \mu_\infty \left(4Z_N(P_c) + 6Z_T(P_c)\right)/15} \tag{3.3}$$

where μ_∞ and κ_∞ are the high-pressure asymptotes for the shear and bulk moduli, respectively. The total normal Z_N and tangential Z_T compliances represent the normal and tangential excess-compliances resulting from the amount of discontinuities present in the rock. It can be observed that the bulk modulus is sensitive to normal compliance only while the shear modulus will depend on both normal and tangential compliances. By making the assumption that the compliances or combination of compliances are decreasing exponentially as a function of confining pressure, he showed that the resulting equations for the bulk modulus and the shear modulus are the sigmoidal functions:

$$\kappa(P_c) = \frac{\kappa_\infty}{1 + E_\kappa e^{-\frac{P_c}{P_\kappa}}} \tag{3.4}$$

and

$$\mu(P_c) = \frac{\mu_\infty}{1 + E_\mu e^{-\frac{P_c}{P_\mu}}} \tag{3.5}$$

Note that the parameters μ_∞, κ_∞, E_κ, E_μ, P_μ and P_κ control the behaviour of the moduli. The asymptotes μ_∞, κ_∞ give the modulus of the rock in its high-pressure state; it should be noted that the asymptotic behaviour is only valid for high pressure relevant to laboratory measurements, but might break down at very high pressure due to inelastic deformation. P_μ and P_κ represent the rate of pressure increase, and give an insight into the nature of the internal discontinuities of the rock. Finally, the overall variation in elastic moduli κ and μ is given by:

$$S_\kappa = \frac{\kappa_\infty - \kappa(0)}{\kappa_\infty} = \frac{E_\kappa}{1 + E_\kappa} \tag{3.6}$$

and

$$S_\mu = \frac{\mu_\infty - \mu(0)}{\mu_\infty} = \frac{E_\mu}{1 + E_\mu} \tag{3.7}$$

The parameters S_κ and S_μ must be greater than zero but less than unity. The exponential term controlling the dependence of pressure on the elastic properties can also be found in empirical relationships such as those described by Eberhart-Phillips *et al.* (1989). Shapiro (2003) presented a derivation of the Eberhart-Phillips pressure relationships for the velocities, bulk and shear moduli, using theoretically and empirically based assumptions. Starting with the same idea as Shapiro, i.e. separating porosity in a compliant and stiff part and assuming that the compressibility depends mainly on changes in compliant porosity, one can show (Appendix A) that the bulk and shear moduli take similar forms to those in equations 3.4 and 3.5. One can show by analogy between equations 3.4–3.5 and A.5–A.6 that:

$$P_\kappa = P_\mu = \frac{\partial \phi_{co}}{\partial C_d} \tag{3.8}$$

where ϕ_{co} stands for the compliant porosity and $C_d = 1/\kappa_d$ for the dry compressibility of the rock. Equation 3.8 shows that the parameters P_μ and P_κ are related to the gradational change of compliant porosity cause by compressibility changes. However, it should be mentioned that the derivation of equation 3.8 contained many approximations, so the previous statement should be viewed as a possible way to give a physical meaning to P_μ and P_κ, rather than a definite result. Another observation is that the parameters P_μ and P_κ in equation 3.8 are identical. This was also observed in the work of Eberhart-Phillips, but it will be shown later that the bulk and shear moduli generally display a distinct rate of pressure increase. In section 3.1.3, a more detailed description of the physical meaning of the stress-sensitivity parameters is presented, based on laboratory experiments.

3.1.3 Analysis of laboratory data

In this study, ultrasonic measurements of compressional- and shear-wave velocities as a function of confining pressure are available for 25 room-dry cores from a Palaeocene turbidite sandstone from the Foinaven field, west of the Shetland Isles. Furthermore, porosity and permeability measurements as a function of confining pressure are also included. Dry bulk modulus, κ_d, and shear modulus, μ_d, are obtained using the following relations:

$$V_P = \sqrt{\frac{\kappa_d + 4/3\,\mu_d}{\rho_d}} \tag{3.9}$$

$$V_S = \sqrt{\frac{\mu_d}{\rho_d}} \tag{3.10}$$

where V_p stands for the P-wave velocity, V_s for the S-wave velocity, and ρ_d is the dry-frame density computed from the weight and volume of the cores. Stress-sensitivity parameters were computed individually for each core sample, by fitting equations 3.4 and 3.5 using a least-squares procedure (Table 3.1). Clay content, porosity and density of all core samples are presented in Table 3.2. Figure 3.3 shows typical results obtained from the least-squares fitting of the sigmoidal functions to the elastic moduli values derived from the laboratory measurements. The correlation coefficients are greater than 0.8 for all samples. It can be seen that the compliance-based models reproduced accurately the dry-frame pressure-sensitivity of the Palaeocene sandstone.

Sample number	κ_∞ (GPa)	E_κ	P_κ (MPa)	μ_∞ (GPa)	E_μ	P_μ (MPa)
1	8.82	0.94	7.29	6.24	1.84	4.76
2	8.53	0.40	2.51	7.00	0.83	7.08
3	10.22	0.81	8.36	6.34	1.14	5.43
4	11.72	0.29	12.06	7.49	1.17	3.81
5	15.71	1.18	8.55	12.06	1.04	8.25
6	9.36	0.48	4.65	6.66	0.78	7.21
7	8.52	1.86	5.13	6.37	1.64	4.89
8	10.17	1.09	4.97	8.26	1.28	6.53
9	10.15	0.54	5.86	8.65	1.13	5.79
10	10.67	0.28	4.54	8.57	1.15	6.12
11	9.76	0.92	3.36	8.09	1.07	9.07
12	8.36	0.80	4.50	6.47	1.49	6.12
13	14.78	1.20	7.07	10.36	1.66	6.02
14	13.49	0.83	3.77	10.27	1.11	7.25
15	12.65	5.85	1.58	11.24	1.00	8.97
16	16.28	1.31	5.34	14.35	1.16	9.06
17	14.52	1.33	4.31	13.88	1.01	8.73
18	7.04	1.59	4.33	5.82	1.63	6.67
19	8.95	1.58	5.33	5.87	1.38	6.87
20	7.02	0.30	9.31	6.06	1.81	5.72
21	8.01	0.97	6.13	6.54	0.77	7.44
22	6.56	0.26	5.50	5.63	1.60	6.56
23	6.13	0.31	3.41	5.94	0.85	8.04
24	11.59	1.32	5.34	10.41	1.60	11.28
25	12.63	1.29	5.24	9.29	1.25	8.87

Table 3.1: Stress-sensitivity parameters for the 25 samples from the Foinaven database. These parameters are obtained by least-squares fitting of equations 3.4 and 3.5 to the laboratory measurements made on room-dry sandstone plugs. Confining pressure in the laboratory experiments ranged from 4 to 34 MPa.

Sample number	Clay content (%)	Porosity (%)	Density (g/cm^3)
1	4	30.7	1.89
2	4	29.8	1.92
3	13	29.8	1.87
4	8	26.8	1.96
5	7	20.9	2.15
6	6	28.8	1.89
7	10	27.3	1.88
8	4	26.3	1.94
9	2	27.6	1.93
10	6	25.9	1.96
11	6	28.2	1.92
12	2	30.7	1.85
13	4	20.6	2.08
14	9	23.7	2.09
15	0	22.6	2.06
16	1	19.0	2.18
17	4	18.1	2.20
18	9	32.7	1.85
19	3	31.1	1.85
20	5	30.6	1.85
21	17	28.7	1.90
22	10	32.8	1.80
23	12	30.4	1.83
24	3	26.6	1.97
25	14	24.9	2.06

Table 3.2: Clay content, porosity and density of the 25 core samples from the Foinaven database. Clay content is obtained by Fourier transform infrared mineralogy.

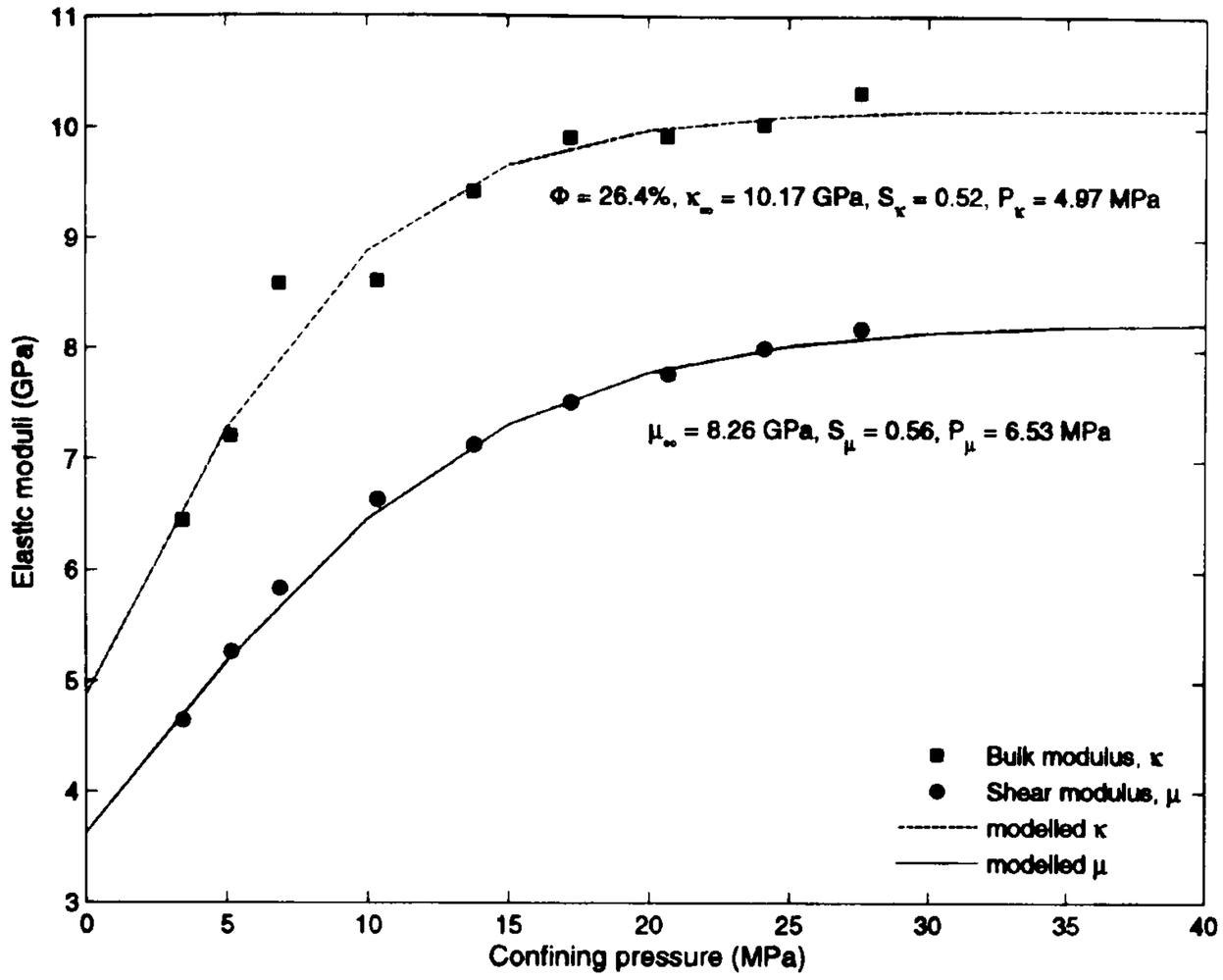

Figure 3.3: Representative fits of a core sample from the Foinaven database. Data points are shown by the symbols, while the lines stand for the least-squares fitting solution of equations 3.4 and 3.5. Fit parameters are provided below each curve.

In an effort to obtain results that are as general as possible, stress-sensitivity parameters from different depositional systems (MacBeth, 2004) are also included. Data from a Cretaceous shallow-marine rock outcrop, consisting of a sequence of clean, disaggregated, loosely consolidated and well-cemented Lochaline sandstones, are considered (Kirstetter, 2001). Data from various reservoir rocks, including a gas-producing sandstone reservoir in the Cooper Basin, Australia (Khaksar *et al.*, 1999a), Palaeocene Forties sandstones from the Nelson Field (UKCS), clean Rotliegend sandstones from the Southern Gas Basin (Freund, 1992), and clean Gulf Coast Miocene sands (Gregory, 1976). For the sake of clarity, averaged elastic properties (Table 3.3) and stress-sensitivity parameters (Table 3.4) over the available cores are presented separately. In the conversion from velocities to elastic moduli, a constant value of density measured at standard conditions (14.6 psi) is used for the Foinaven database. For the data taken from the literature, density measurements as a function of the confining pressure are used when available. However, Figure 3.4 shows that

the assumption of a constant density value insensitive to confining pressure loading is fulfilled. In fact, density variations of less than 3% are observed for the loosely consolidated Lochaline and consolidated Rotliegend sandstones, while changes of up to 9% are visible for the anomalous high-porosity disaggregated Lochaline sandstone.

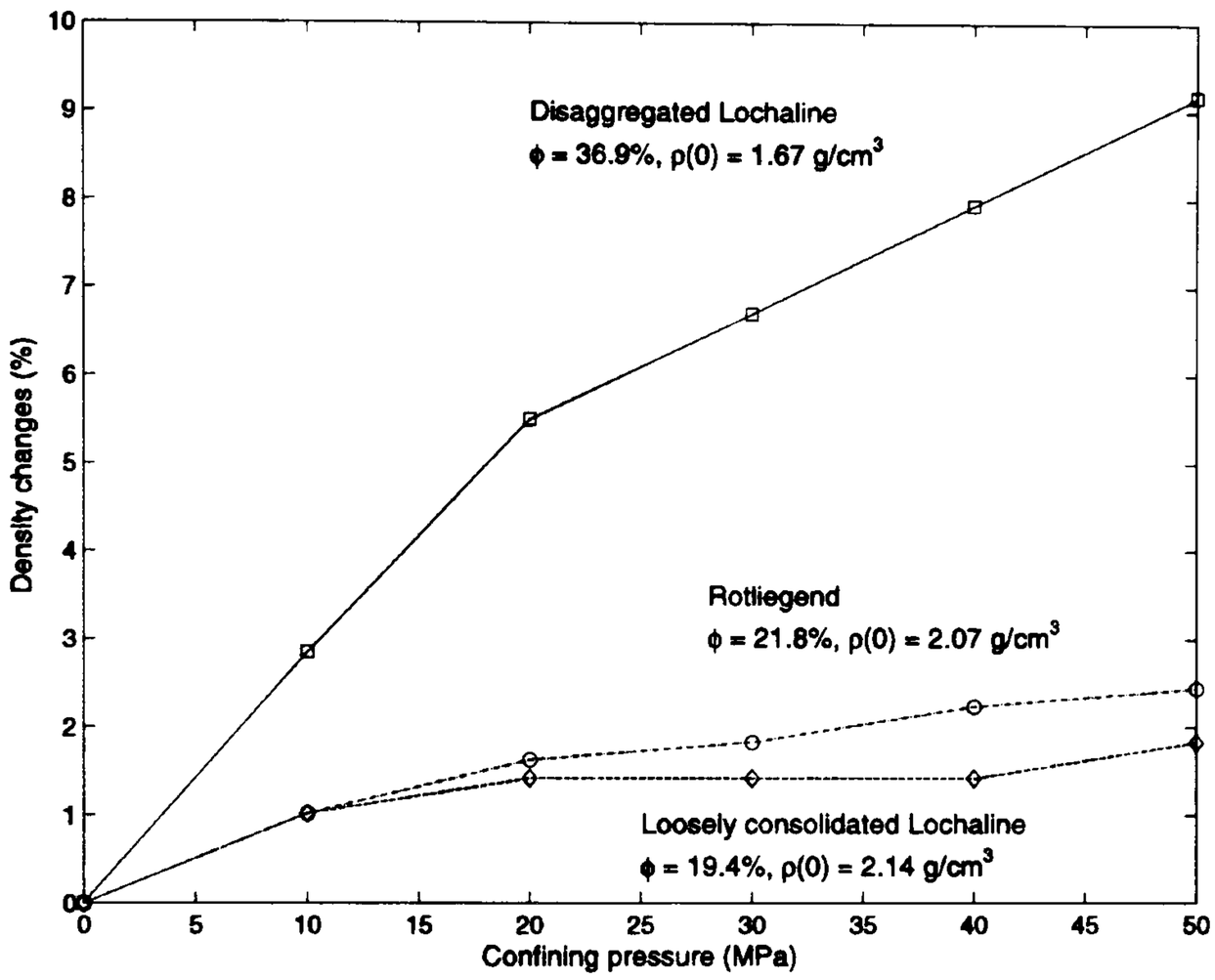

Figure 3.4: Measurements of the percentage variation in density versus confining pressure for two outcrop sandstones (loosely consolidated and disaggregated Lochaline) and a reservoir sandstone (Rotliegend). The pressure dependence of density is small, except for the anomalous disaggregated Lochaline.

Outcrop sandstones	V_p (km/s)	V_s (km/s)	ρ_d (g/cm^3)	ϕ (%)	V_p/V_s
Loosely consolidated Lochaline	3.67	2.22	2.17	18.0	1.65
Disaggregated Lochaline	0.97	0.64	1.64	37.1	1.51
Well-cemented Lochaline	4.88	2.77	2.52	5.0	1.76
Reservoir sandstones					
Forties (Nelson)	1.82	1.13	2.00	25.4	1.61
Rotliegend (southern North Sea)	2.28	1.51	2.08	23.6	1.51
Cooper Basin	2.69	1.74	2.26	13.2	1.55
Miocene (Gulf coast)	2.46	1.84	1.99	21.7	1.34

Table 3.3: P-wave velocity (V_p), S-wave velocity (V_s), density (ρ_d), porosity (ϕ), and velocity ratio (V_p/V_s) are listed for three different outcrop sandstones (top rows) and four different reservoir sandstones (bottom rows).

Outcrop sandstones	S_κ	S_μ	P_κ (MPa)	P_μ (MPa)	κ_∞ (GPa)	μ_∞ (GPa)
Loosely consolidated Lochaline	0.57	0.59	6.14	7.75	13.89	16.85
Disaggregated Lochaline	0.79	0.75	14.85	15.20	3.05	2.70
Well-cemented Lochaline	0.07	0.39	4.49	6.94	36.79	31.68
Reservoir sandstones						
Forties (Nelson)	0.65	0.67	7.12	6.78	9.15	7.75
Rotliegend (southern North Sea)	0.64	0.57	9.82	13.54	12.41	10.99
Cooper Basin	0.61	0.63	15.08	11.53	18.63	18.44
Miocene (Gulf coast)	0.75	0.53	9.55	23.24	12.40	14.30

Table 3.4: Stress-sensitivity parameters for the dry bulk modulus (S_κ, P_κ, κ_∞) and for the shear modulus (S_μ, P_μ, μ_∞) are listed for three different outcrop sandstones (top rows) and four different reservoir sandstones (bottom rows). These parameters are obtained by least-squares fitting of the functions in equations 3.4 and 3.5 to laboratory measurements.

Figure 3.5 presents representative fits obtained for four different reservoir sandstones. Dry bulk modulus (Figure 3.5, top) and shear modulus (Figure 3.5, bottom) are displayed, and showed that the data are grouped according to their porosity. In fact, the low-porosity Cooper Basin sandstone stands out from the other sandstone reservoirs, which lie in the same range of porosity. Even if those sandstones (Forties, Rotliegend, Gulf Coast) have approximately the same porosity, some variability in their behaviour can be observed with increasing confining pressure. This variability can be explained by different degrees of cementation or consolidation of the rock, but also by different mineralogy (amount of clay, quartz or other minerals), petrophysical properties (rock fragments), complex pore geometry, and also the concentration of micro-fractures. The stress-sensitivity parameters provide some insight into interpreting the pressure dependence of the rock. For example, it can be observed that the asymptote at high-pressure κ_∞ or μ_∞ seems to be correlated with porosity (the asymptote value increases with decreasing porosity). The S_κ or S_μ provides the maximum variation of the elastic modulus from initial ($P_c = 0$) to high-pressure states, giving an indication of the overall stress-sensitivity of the rock. Finally, the microcrack-closure stress, which plays a major role into the stress-sensitivity behaviour, can be related to the parameters P_κ and P_μ.. P_κ or P_μ give an indication on the dynamic of the elastic modulus changes with confining pressure; a small value will correspond to a high stress-sensitivity at low confining pressure, leading to a quick ascent towards the high-pressure plateau; while a large value will represent a more regular stress-sensitivity along the pressure path. This observation is in accordance with equation 3.8 relating P_κ and P_μ to the gradational change of compliant porosity ϕ_c due to the compressibility changes. A large P_κ and P_μ will correspond to a regular decrease of ϕ_c with decreasing compressibility, while a small P_κ and P_μ will refer to a steep reduction of ϕ_c, with the first reduction of compressibility followed by a small decrease thereafter. In order to extend the interpretation of the stress-sensitivity parameters and study the effects of cementation and consolidation (the two main diagenetic processes affecting reservoir rocks), data from three Lochaline sandstone outcrop samples are selected: a clean, well-cemented sandstone (5% porosity); a loosely consolidated, uncemented sandstone (18% porosity) with pressure-dissolution sutures at the grain–grain contacts preventing it from falling apart; and, finally,

a manually disaggregated and recombined sandstone (37% porosity). Figure 3.6 shows how the amount of excess-compliance can be related to the degree of cementation and consolidation of the rock. A progression – from disaggregated, to loosely consolidated – to well cemented, represents a decrease in the concentration of compliant area, leading to a poorer stress-sensitivity for the sandstones. In fact, an increase in S_κ, S_μ, P_κ and P_μ is observed from the well-cemented to disaggregated samples, showing an increase in the overall stress-dependence and gradational changes of modulus with confining pressure. The stress-sensitivity appears to be smaller for a rock that has been through a cementation process rather than a consolidation process. This is expected, since it might be easier to break down the dry-frame of consolidated samples (which have pressure-solution contacts) rather than cemented samples, in order to accommodate for the increase in pressure loading. All the previous observations made on the stress-sensitivity parameters for the reservoir rocks are also valid for the outcrop rocks.

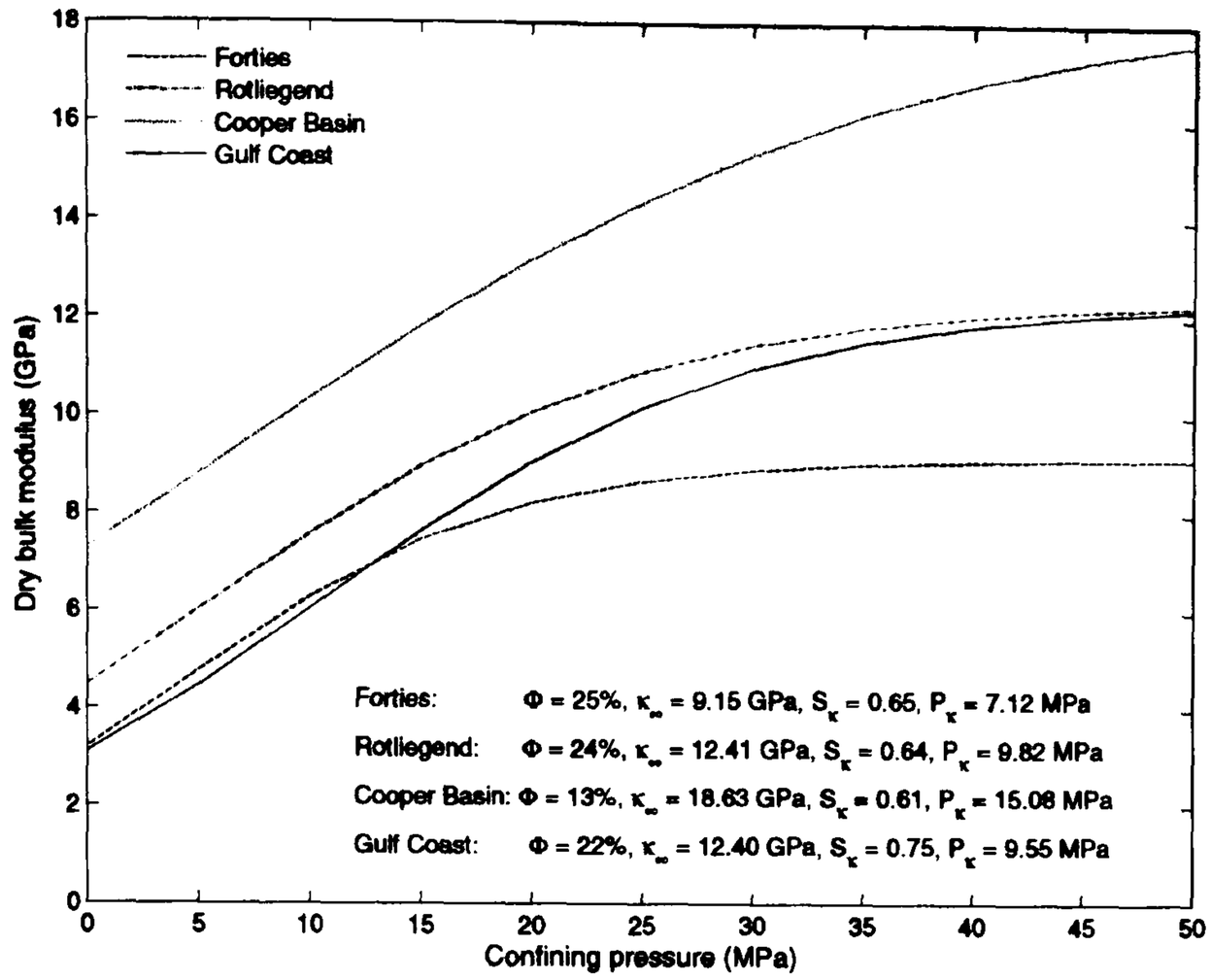

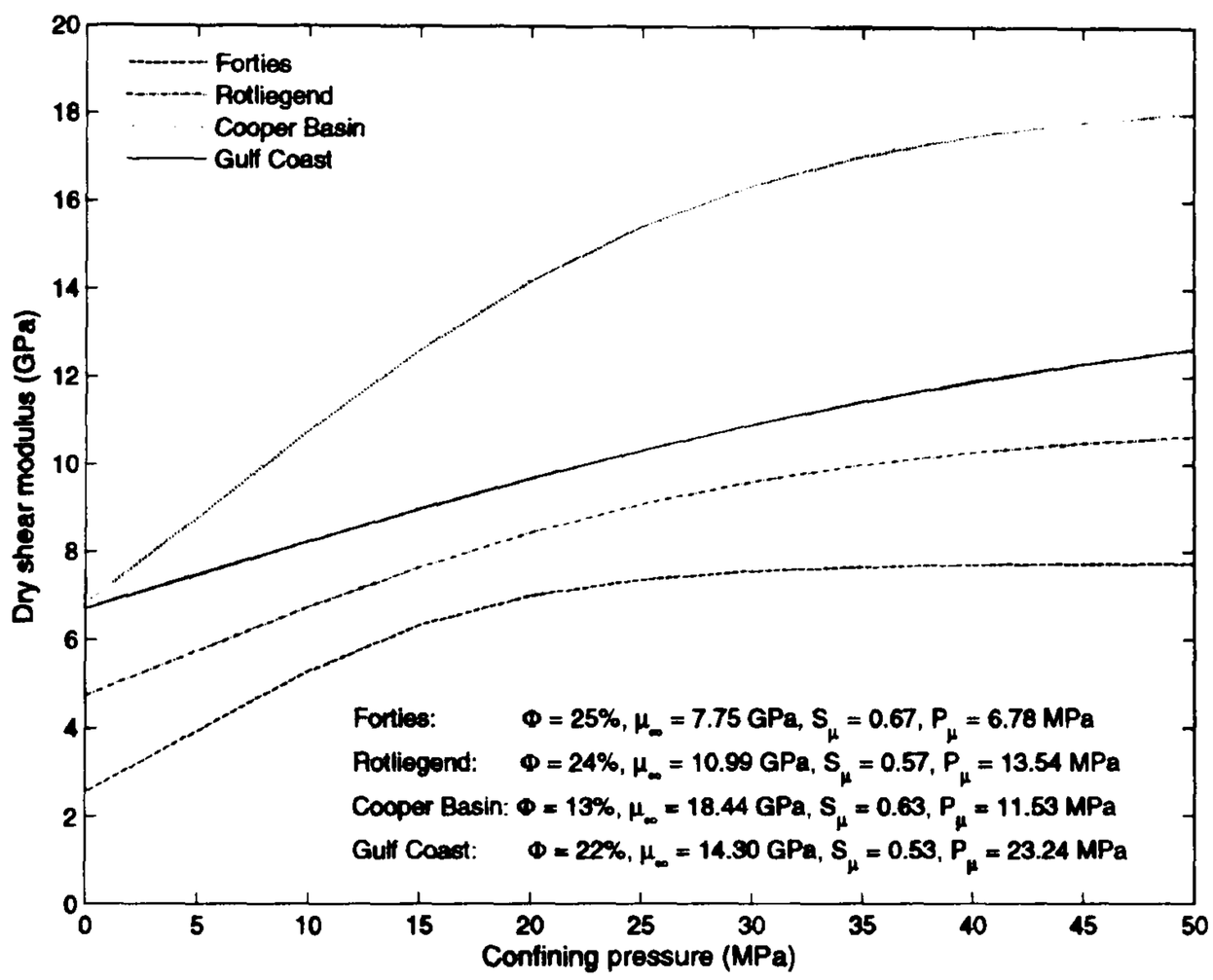

Figure 3.5: Pressure dependence of the dry bulk modulus (top) and shear modulus (bottom) for the reservoir sandstones shown in Table 3.3. Least-squares fit parameters are provided for each modulus and reservoir sandstone. Each curve represents the stress-sensitivity model obtained after least-squares fitting.

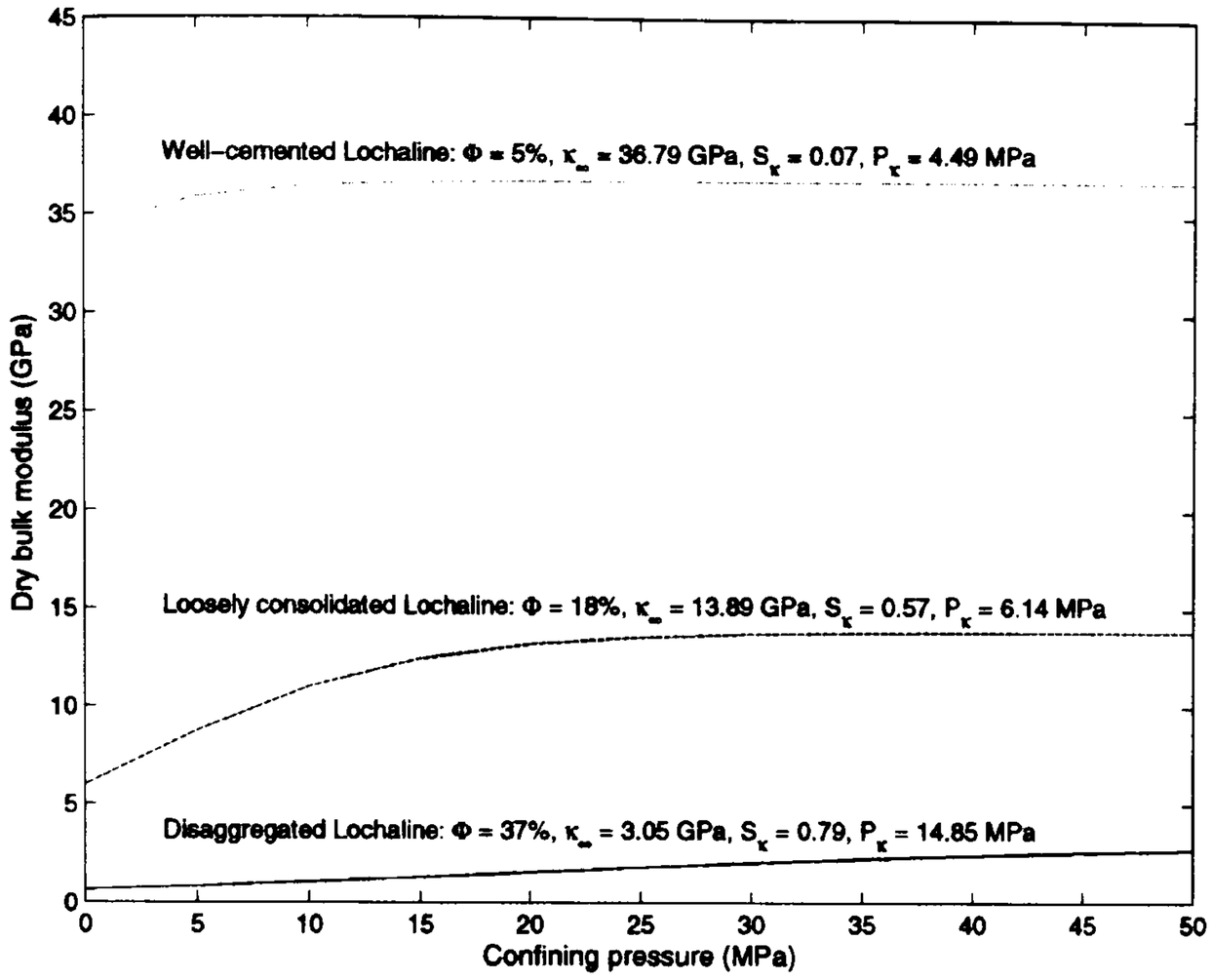

Figure 3.6: Pressure dependence of the dry bulk modulus (top) and shear modulus (bottom) for the same sandstones in three different diagenetic settings. Least-squares fit parameters are provided for each modulus and outcrop sandstone. Each curve represents the stress-sensitivity model obtained after least-squares fitting.

3.1.4 Effect of porosity and clay content

Different parameters (like pore aspect ratio, pore distribution, presence of illitic fragments) can affect the elastic properties of a rock, but it appears that porosity and clay content are the most influential parameters. However, in the models derived in the previous section, their dependence does not appear explicitly in equations 3.4 and 3.5. Several authors have developed empirical relationships (Han *et al.*, 1986; Eberhart-Phillips *et al.*, 1989), which are explicitly a function of porosity and clay content, but act independently of the stress. Marion *et al.* (1992) developed a geometrical sand–clay model for interpreting elastic properties versus clay content in consolidated sandstones. More recently, Xu and White (1995) proposed a velocity model attributing the effect of clay to the difference of pore geometry and pore aspect ratio between sand- and clay-related pores, but still did not consider the impact of clay and porosity on the stress-sensitivity. It can be expected that these two parameters have an effect on the microstructures of the sandstone, and so influence the stress-sensitivity. In the following section, the porosity variation due to the reduction of the pore space under pressure loading (Kirstetter, 2002) and the thermal effect on the dry-frame of the rock (Zhang and Bentley, 1999) are assumed to be negligible in the first approximation for consolidated and well-cemented sandstones.

A Porosity effect

It can be observed from Figure 3.6 that the porosity in sandstone will decrease with the degree of consolidation or cementation of the rock. This is in accordance with the general statement that the porosity of sandstones decreases with depth. Therefore, a number of stress-sensitivity parameters in equations 3.4 and 3.5 should correlate with porosity. From the Foinaven database, it can be concluded that the parameters P and E do not correlate with porosity, while the high-pressure asymptote shows a clear linear correlation with porosity (Figure 3.7 – top row). These conclusions are in accordance with the results from MacBeth (2004) for the range of porosity studied here. However, at lower porosity (less than 15%) P and E exhibit a linear correlation with porosity.

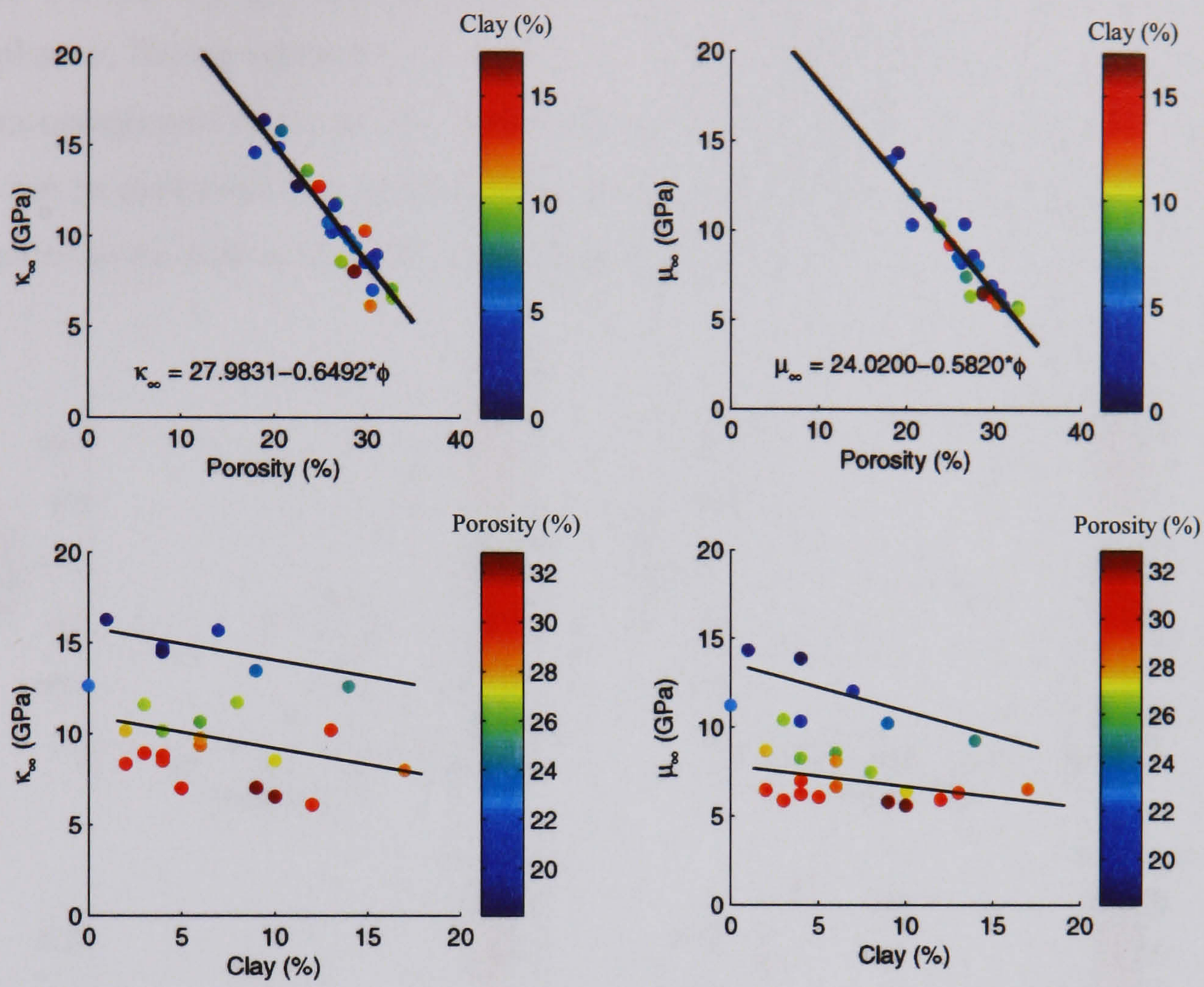

Figure 3.7: Plots of the high-pressure asymptote parameters κ_∞ and μ_∞ as a function of both measured porosity (top) and clay fraction (bottom) for the Foinaven database. Points are colour-coded according to the percentage of the second parameter. Lines represent least-squares fits of the data, showing the relationship between κ_∞ and μ_∞ versus porosity, while trend-lines correspond to possible variations with clay content.

Recently, MacBeth and Ribeiro (2005) rewrote equations 3.4 and 3.5 as:

$$\kappa(P_c) = \frac{\kappa_\infty}{1 + \kappa_\infty F_\kappa e^{-\frac{P_c}{P_\kappa}}} \tag{3.11}$$

and

$$\mu(P_c) = \frac{\mu_\infty}{1 + \mu_\infty F_\mu e^{-\frac{P_c}{P_\mu}}} \tag{3.12}$$

where F_κ and F_μ are directly proportional to the total (pressure-dependent) excess-compliance. Fitting equations 3.11 and 3.12 to the Foinaven database, an increase in the excess-compliance with porosity is observed for F_μ but not for F_κ (Figure 3.8 – top row). This can be explained by a larger amount of excess-compliances in the tangential direction compared to the normal direction (equations 3.2 and 3.3).

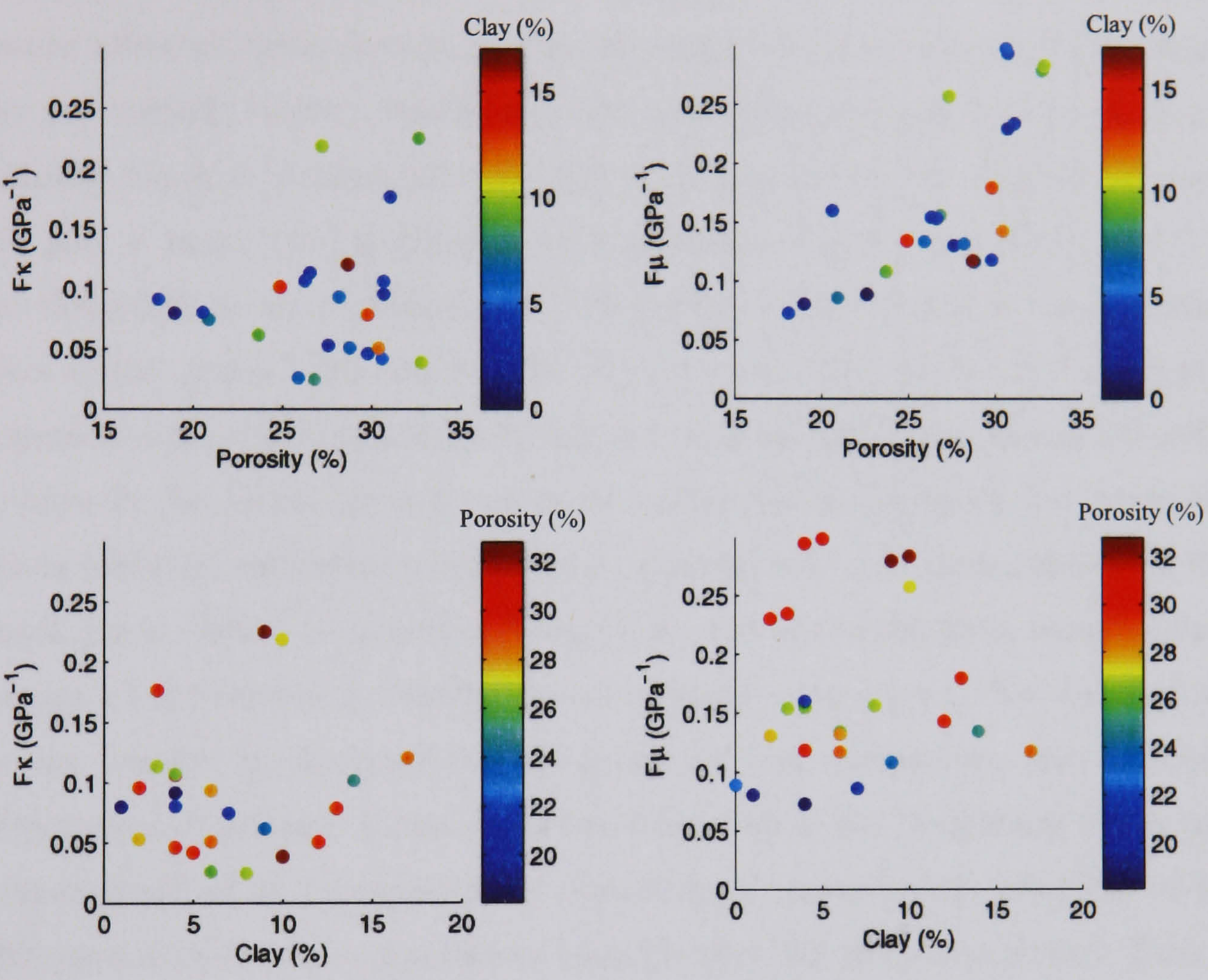

Figure 3.8: Plots of the total excess-compliances F_κ and F_μ as a function of both measured porosity (top) and clay fraction (bottom) for the Foinaven database. Points are colour-coded according to the percentage of the second parameter.

B Clay cements

It is generally accepted that increasing the clay content will tend to decrease velocities, bulk and shear modulus by softening the rock-frame. A small amount of clay can dramatically weaken the grain contacts, and, in the process, it significantly reduces the elastic properties

(Han, 1986). There are four main types of clay: kaolinite, illite, montmorillonite and chlorite, which all have different characteristics. Kaolinite grows as accordion-shaped crystals (Figure 3.9, A) and destroys the porosity of the rock, but does not affect the permeability to such an extent. However, illite forms fibrous crystals (Figure 3.9, B) growing radially from the grain surface. This fibrous clay obstructs the throat passages and so diminishes the permeability without changing the porosity. Montmorillonite has a dramatic effect on permeability, because its lattice structure (Figure 3.9, C) can absorb water and expand. Finally, chlorite is a ferromagnesian-rich clay mineral (Figure 3.9, D) principally found in volcaniclastic sandstone. It appears that the location of these clays could play a major role in affecting rock properties (Sams and Andrea, 2001). Firstly, stress-dependent or stress-independent clay particles that are part of the framework can replace quartz grains while maintaining the pore space characteristics. This type of clay distribution is referred to as structural clay, and includes framework, interstitial and laminar clay deposits. Secondly, the clay can be pore-related, with clay particles coating the grain surfaces (chlorite, montmorillonite or illite); growing across the pore space from the edges of sand grains (illite); or generally filling pores and cementing grain contacts (kaolinite). This type of distribution is referred to as a dispersed clay deposit. The distribution of the clay can depend on the conditions at deposition, on compaction, and diagenesis (i.e. kaolinitization of feldspar minerals, for example). Due to the complexity of the geological processes involved in the formation or deposition of clay minerals, MacBeth and Ribeiro (2005) developed a micro-mechanical classification for shaly sandstones. Their models (equations 3.12 and 3.13) describe the impact of clay on the stress sensitivity of sandstone, regardless of the type of clay, since many possible geological scenarios and depositional settings can lead to the same class of mechanical behaviour. Figure 3.7 (bottom row) shows that by dividing the Foinaven database into porosity subsets, there is a linear correlation of κ_∞ and μ_∞ with clay content. This dependence appears to be clear at higher porosity. On the other hand, only marginal dependences between excess-compliances and clay content are observable in Figure 3.8 (bottom row). This example from the Foinaven field gives a good example of the difficulty of quantifying the effect of clay content in sandstone. Alterations of elastic properties due to clay are observable, but cross-validation with other sandstones is

required to draw a definite conclusion due to the scatter of the present data. Using a more comprehensive database, MacBeth and Ribeiro (2005) came to a similar conclusion by suggesting that a more detailed database is required in order to carefully study the petrology of the sandstone and to define all external factors affecting the stress-sensitivity of the rock properties.

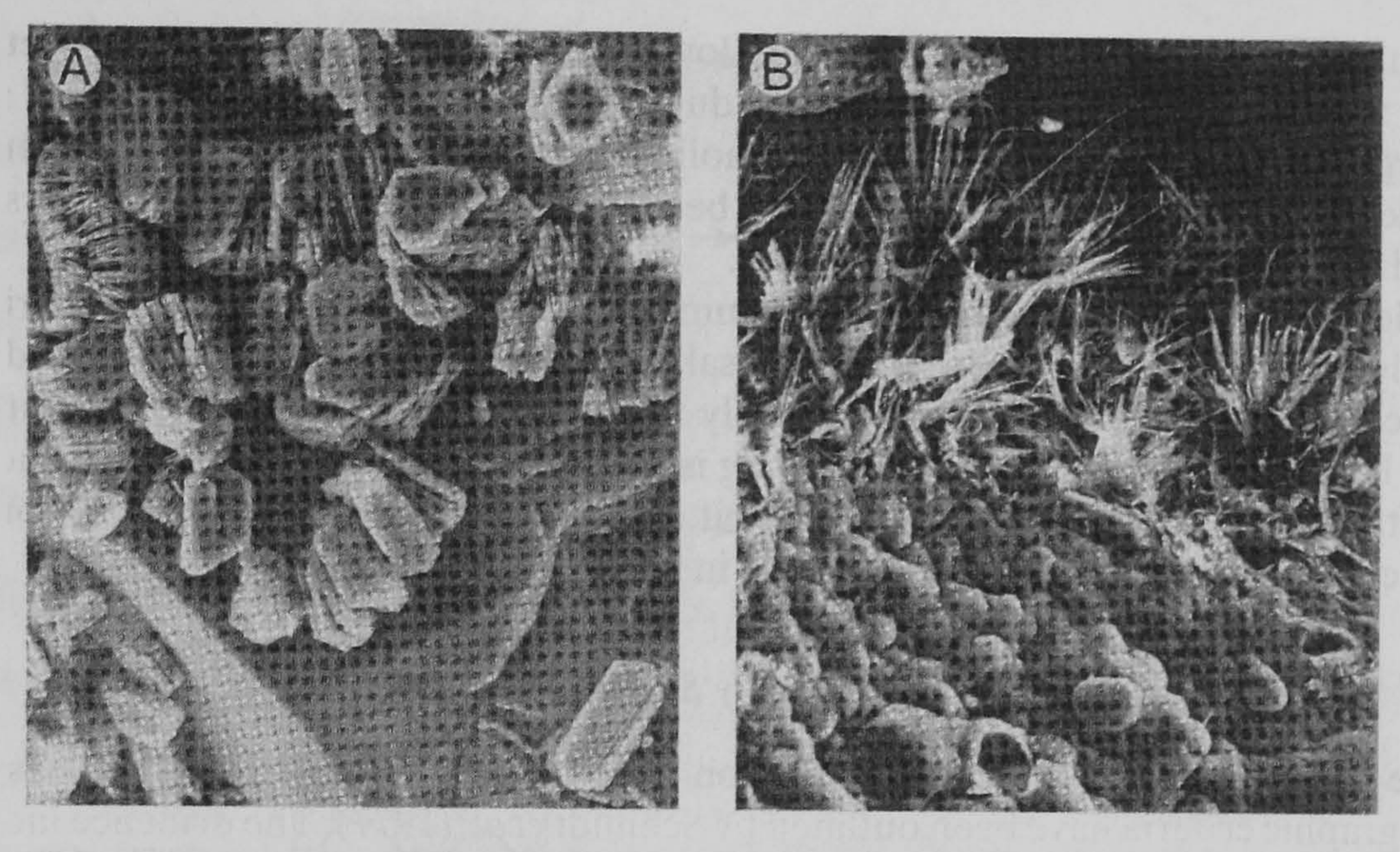

Figure 3.9: Scanning electron micrographs illustrating the main types of clay present in sandstone (from Selley, 2000). (A) kaolinite 'accordion' crystals. (B) Fibrous crystals of illite. (C) Flaky crystals of montmorillonite. (D) Chlorite clay cement.

3.1.5 Core damage effects

A core recovered from a reservoir formation is released from the *in situ* stress state present in the subsurface. First, the vertical stress diminishes as the core approaches the surface, and then the horizontal stress is released when the core is extracted from the formation. In this process, the core is prone to mechanical deformation, leading to the formation of micro-cracks, softening or even breaking of grain–grain contacts. Figure 3.10 illustrates the formation of micro-cracks at the grain surface due the extraction of a rock sample. When the core is reloaded to its initial stress state for the laboratory analysis, the resulting velocity measurements do not match the *in situ* velocity, which indicates that irreversible damage has occurred in the rock. The effect of stress changes on velocities has been simulated for synthetic core samples (Holt *et al.*, 1996; Fjaer and Holt, 1999), and shows a permanent velocity reduction between core-damaged and virgin rock samples. These core-damage effects can have different sources, due to the anisotropic nature of the stress releases that annealed the closure of micro-cracks during reloading, or due to the breaking of grain bonds (i.e. reduction of the cementation). The main point is that laboratory measurements will lead to an increase in the stress-sensitivity of the rock compared to the *in situ* formation. However, in the studies mentioned above, the process of cementation used may not fully mimic the diagenetic history of a real rock, and might overestimate the effect of stress release. Velocity estimation from rock physics models derived from these measurements will not necessarily agree with seismic estimates, and the models should be corrected appropriately. In Chapter 6, this issue will be further discussed and a possible correction of core-damage effects will be introduced.

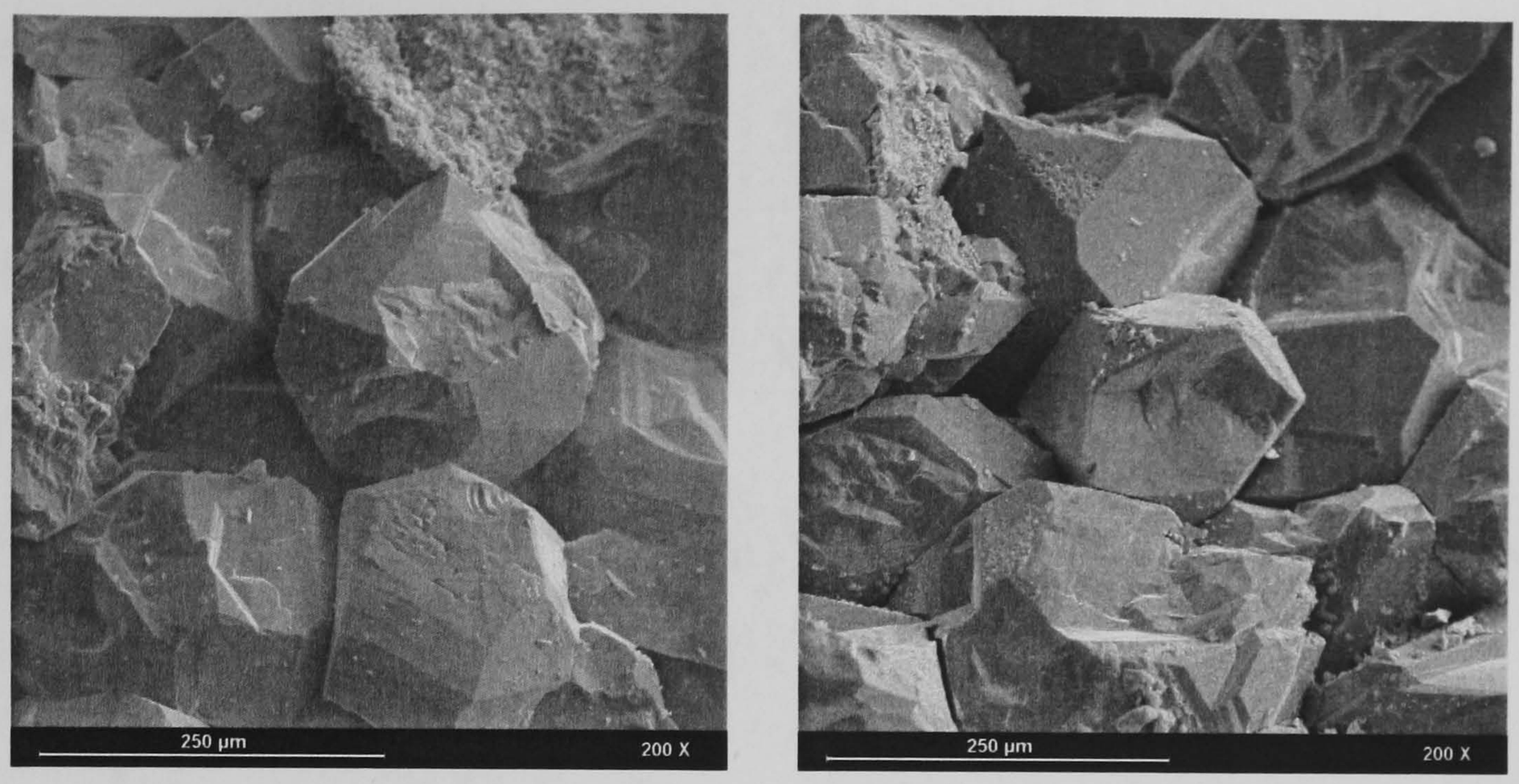

Figure 3.10: SEM (Scanning Electron Microscopy) image showing two Fontainebleau sandstone samples (from Stendahl, 2001). Left: abundant quartz cement and an open pore network, and in the upper part a micro-porous clay aggregate. Right: micro-cracks along grain contacts, generated during sample extraction.

3.2 Fluid saturation sensitivity of sandstone

Density and elasticity of reservoir sandstone *in situ* are not only sensitive to effective pressure, but are also sensitive to the nature and distribution of the saturants filling up the pore space. It is thus important to be able to predict the effect of fluid substitution on the dry-frame elastic properties of sandstone. To do so, Gassmann's relations are commonly used.

3.2.1 Gassmann's relations

Gassmann (1951) derived relations for calculating the bulk modulus (κ_s) and the shear modulus (μ_s) of a fluid-saturated porous rock. The saturated bulk modulus is computed from the bulk modulus of the rock-forming mineral, κ_m, the dry-frame, κ_d, and pore fluid, κ_f, using equation 3.13. The pore fluid can be a single phase of brine, oil or gas, or a

mixture of these fluids. Under the assumption given by Gassmann, the shear modulus of the rock is not affected by the pore fluid, and remains constant under fluid substitution (equation 3.14), and the density of the saturated rock is given by equation 3.15. Berryman (1999) demonstrated that the shear modulus' insensitivity to fluid substitution is an exact result – and not an assumption, as frequently stated in the literature.

$$\kappa_s(P_e,\text{sat}) = \kappa_d(P_e) + \frac{\left(1-\frac{\kappa_d(P_e)}{\kappa_m}\right)^2}{\frac{\phi}{\kappa_f(P_p,\text{sat})} + \frac{1-\phi}{\kappa_m} - \frac{\kappa_d(P_e)}{\kappa_m^2}} \tag{3.13}$$

$$\mu_s = \mu_d \tag{3.14}$$

where, ϕ, κ_m, and κ_f are the rock porosity, the mineral bulk modulus, and the fluid bulk modulus, respectively.

$$\begin{aligned}\rho_d &= \rho_m(1-\phi)\\ \rho_s &= \rho_m(1-\phi)+\rho_f\phi\end{aligned} \tag{3.15}$$

where ρ_d and ρ_s are the dry and fluid-saturated density of the rock, respectively. The symbols ρ_m and ρ_f are the matrix and pore fluid densities. In Gassmann's equation, the mineral bulk modulus represents the moduli of the minerals making up the rock. If the mineralogy of the rock is known, an effective mineral modulus can be computed by averaging. It should be noted that the Gassmann's relations are only valid at sufficiently low frequencies (less than 100 Hz), and will be less accurate for higher frequencies (sonic and ultrasonic measurements). This is because the pore fluid requires a sufficiently long elapsed time to reach equilibrium, because of the pore-pressure gradient induced by waves

propagating through the pores. The basic assumptions for Gassmann's equation, which are generally fulfilled for sandstone reservoir rocks, are that:

1) The rock (both the matrix and the frame) is macroscopically homogeneous.
2) All the pores are interconnected or communicating.
3) The pore fluid is frictionless.
4) The rock–fluid system under study is closed.
5) The pore fluid does not interact with the solid in a way that would modify the properties of the frame.

In the application of equation 3.13, the dry-frame bulk modulus is derived using the rock physics model described in section 3.1.3. However, when fluid substitution is applied to core measurements, it is important during a laboratory experiment not to overdry the samples (Smith *et al.*, 2003) and to preserve the amount of water that is part of the rock-frame. If this is not done, then velocity measurements will be overestimated and fluid substitution results will be rendered irrelevant. The fluid bulk modulus, κ_f, can be calculated using the Reuss average (Reuss, 1929):

$$\frac{1}{\kappa_f} = \frac{S_b}{\kappa_b} + \frac{S_g}{\kappa_g} + \frac{S_o}{\kappa_o} \qquad (3.16)$$

$$S_o + S_b + S_g = 1$$

where κ_o, κ_g and κ_b are the bulk moduli of oil, gas and brine, respectively, and S_o, S_g, and S_b are the oil, gas and brine saturations, respectively. Equation 3.17 implies that the pore fluid is uniformly distributed into the pore space. The bulk density ρ_f of the fluid mixture is calculated by:

$$\rho_f = S_b\rho_b + S_g\rho_g + S_o\rho_o \qquad (3.17)$$

where ρ_b, ρ_g, and ρ_o are the bulk densities of brine, gas, and oil, respectively. The expressions from Batzle and Wang (1992), used to compute the pore fluid modulus and densities, are presented in Appendix B. These pore fluid properties are dependent on the composition, temperature and pressure of the pore fluid (Table 3.5).

Brine salinity (ppm)	18,000
Temperature (°C)	60
Gas gravity	0.6
Oil gravity (API)	27.69
Overburden pressure (MPa)	45

Table 3.5: Fluid characteristics and reservoir conditions used in the Batzle and Wang (1992) correlations for pore fluid properties.

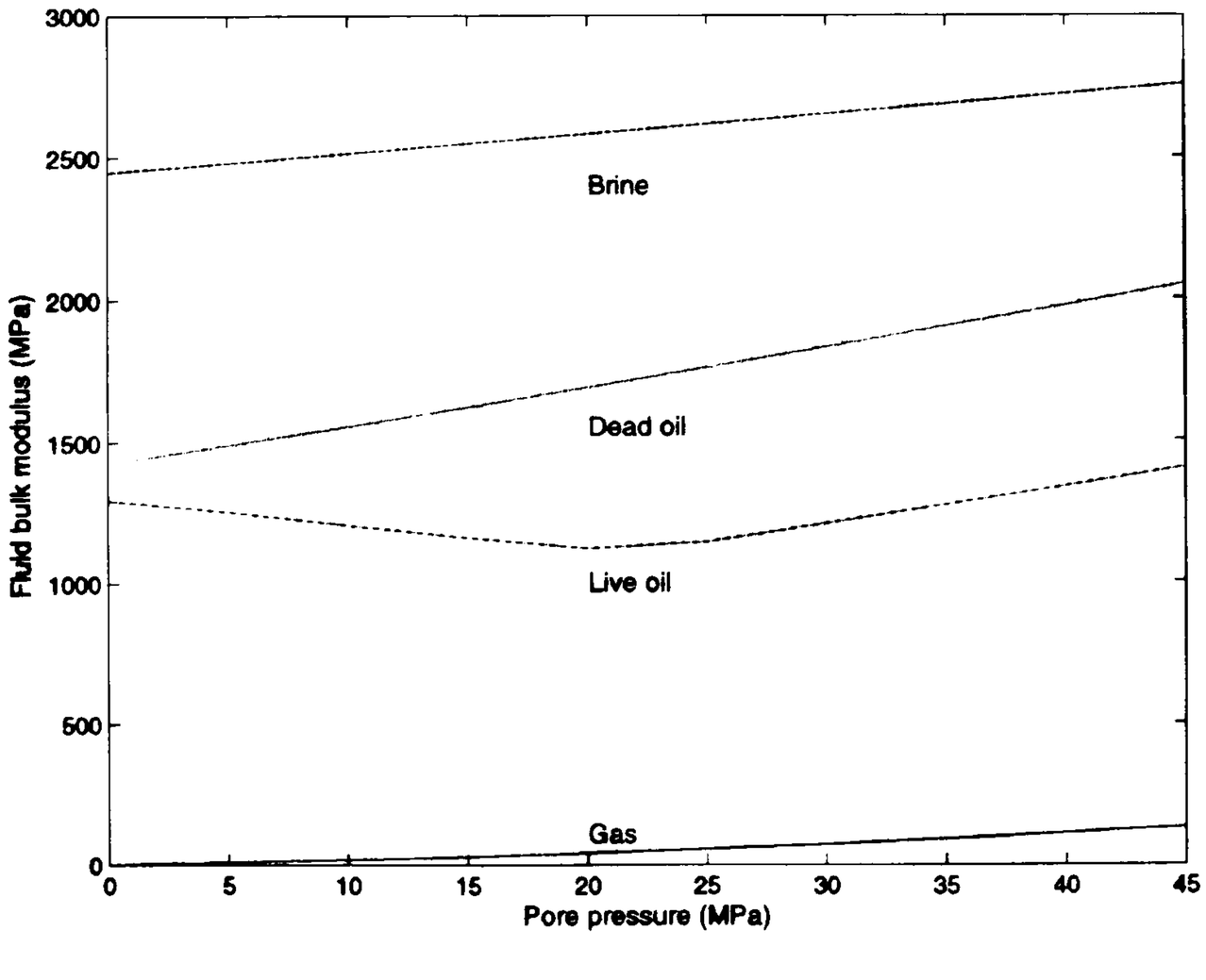

Figure 3.11: Fluid bulk modulus of gas, live oil, dead oil and brine phases as a function of pore pressure. Moduli of all fluids increase with pore pressure, except for live oil below the bubble point pressure (P_b = 20 MPa).

Figure 3.11 presents the fluid bulk moduli of a single phase of live oil, dead oil, brine and gas as a function of pore pressure. The fluid bulk modulus of dead oil, brine and gas increase with pore pressure, with the exception of the live oil, which decreases below bubble point pressure due to gas coming out of solution. Because the gas phase has a very small modulus compared to the other fluids, it can be expected from equation 3.16 that a small amount of gas will have a dramatic effect on the mixture modulus. In fact, Figure 3.12 shows the fluid bulk modulus of three homogeneous mixtures mimicking a pre-production scenario S1 (S_o = 75%, S_b = 25%) and two post-production scenarios S2 (S_o = 30%, S_b = 70%) and S3 (S_o = 30%, S_b = 65%, S_g = 5%). In the following, the oil phase is chosen to be live oil, unless otherwise stated. It can be observed that κ_f is predicted to increase due to the production of hydrocarbons, because brine (high κ_f) is replacing oil (low κ_f) in the reservoir. On the other hand, when a small amount of gas (5%) is added to the mixture, then a dramatic decrease occurs, and the resulting κ_f post-production becomes smaller than in the pre-production case. When reservoir pressure drops below the bubble point and gas comes out of solution, the gas phase is the predominant factor in the mixture bulk modulus. The estimated seismic velocities using Gassmann's relations in fluid-saturated porous rock are only valid if the fluid mixture (brine, oil, and gas) is uniformly distributed at a very small scale. If the fluid distribution is heterogeneous at a larger scale (i.e. patchy saturation), then the seismic velocities obtained using the previous approach will lead to an underestimation of the velocities (Mavko and Mujerki, 1998; Dvorkin *et al.*, 1999). An alternative to estimate seismic velocities in the case of patchy saturation (Domenico, 1976) is to use the Voigt average (Voigt, 1928) instead of the Reuss average for the fluid bulk modulus:

$$\kappa_f = S_b\kappa_b + S_o\kappa_o + S_g\kappa_g \tag{3.18}$$

Figure 3.13 illustrates the resulting κ_f, assuming homogeneous (Reuss average) and heterogeneous (Voigt average) mixtures. The Reuss average represents the lower bound of the fluid bulk modulus, while the Voigt average represents the upper bound at the

laboratory scale. It should be noted that the effect of irreducible saturation is not included into the Voigt average; therefore the fluid bulk modulus is overestimated. In fact, Sengupta and Mavko (2003) show that a modification of the Voigt average allows to take into account for residual oil and connate water saturations, which are considered as homogeneous at the seismic scale. The modified Voigt average is illustrated on Figure 3.13. However, the assumption of homogeneous irreducible saturation distribution is not always fulfilled as connate water is sometimes found heterogeneously distributed (Morrow and Melrose, 1991). Other prediction methods exist to estimate the effect of changing pore fluid on elastic properties. Kuster–Töksöz theory (1974), as described in section 3.1.2.A, can be used for fluid substitution, and can lead to better results at the high frequency laboratory scale in the case of fracture-like pores (Capello de P. and Batzle, 1997).

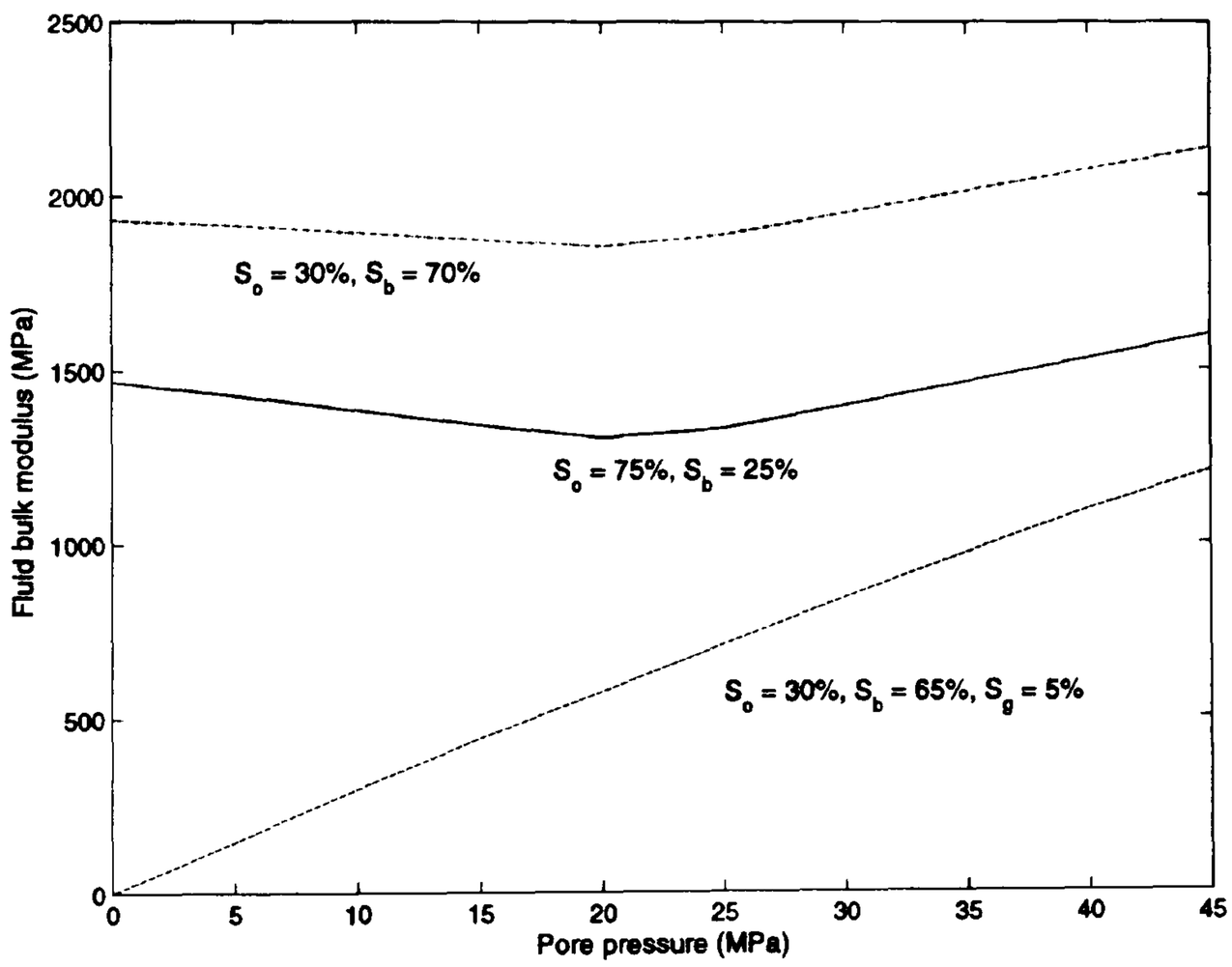

Figure 3.12: Fluid bulk moduli of three homogeneous mixtures as a function of pore pressure. A pre-production scenario S1 (S_o = 75%, S_b = 25%) and two post-production scenarios S2 (S_o = 30%, S_b = 70%) and S3 (S_o = 30%, S_b = 65%, S_g = 5%) are considered.

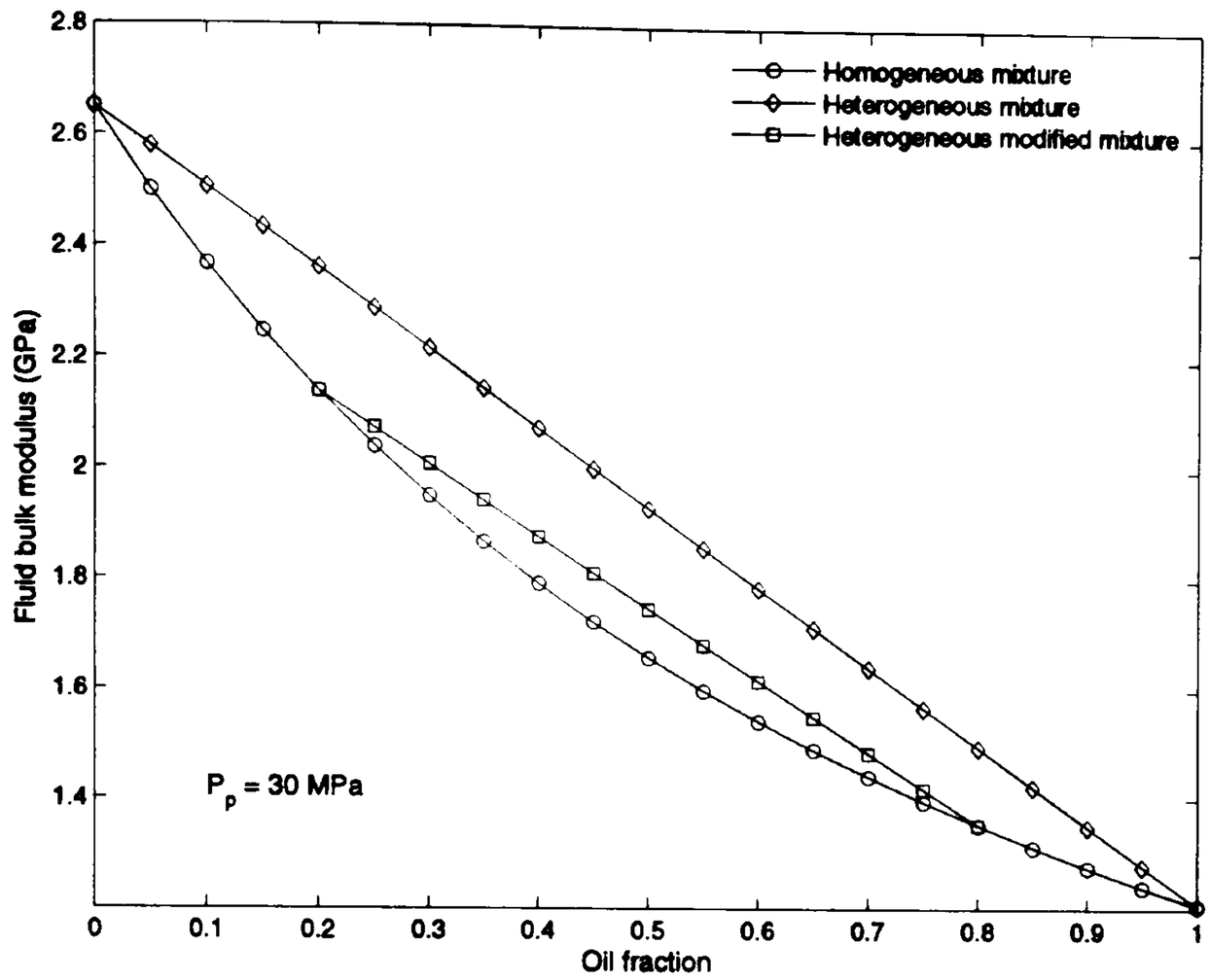

Figure 3.13: Fluid bulk moduli of homogeneous and heterogeneous mixtures of live oil/brine as a function of oil fraction. The plot corresponds to a pore pressure of 30 MPa.

3.2.2 Fluid saturation effects on elastic properties

The effect of fluid saturation on elastic wave velocities in porous media has been studied in detail by many authors (Wyllie *et al.*, 1958; King, 1966; Gregory, 1976). S-wave and P-wave velocities behave differently to pore fluid saturation changes. For example, if the pore fluid is brine or oil, then P-wave velocity will increase, while S-wave velocity will decrease. However, these changes are generally small and difficult to observe, due to the coupling of the bulk and shear modulus in the formula for the determination of the velocities (equations 3.9 and 3.10). In fact, from equation 3.13 one can note that the saturated bulk modulus is a more intuitive indicator of saturation effect than velocities. Figure 3.14 illustrates the effect of fluid saturation (single phase) on the dry bulk modulus pressure model derived from the Foinaven core sample (Figure 3.3). Single phases (100% saturation) of gas, live oil and brine are considered. Fluid properties are computed using the Batzle and Wang expressions (Appendix B) with the fluid characteristics and reservoir conditions from Table 3.5. It can be observed that at 20 MPa differential pressure, the dry

bulk modulus increases 46% for brine saturation, 22% for oil saturation, and 1% for gas saturation. The brine phase has the larger effect on the dry bulk modulus, followed by the oil phase and the gas phase. These observations agree with the fluid compressibilities, which increase from the gas to the brine phase. It can also be noted that the effect of gas saturation on the bulk modulus at high differential pressure (low pore pressure) is small but becomes non-negligible at low differential pressure. However, the assumption of single-phase fluid saturation gives a good insight into the behaviour of the bulk modulus, although it is far from the reality.

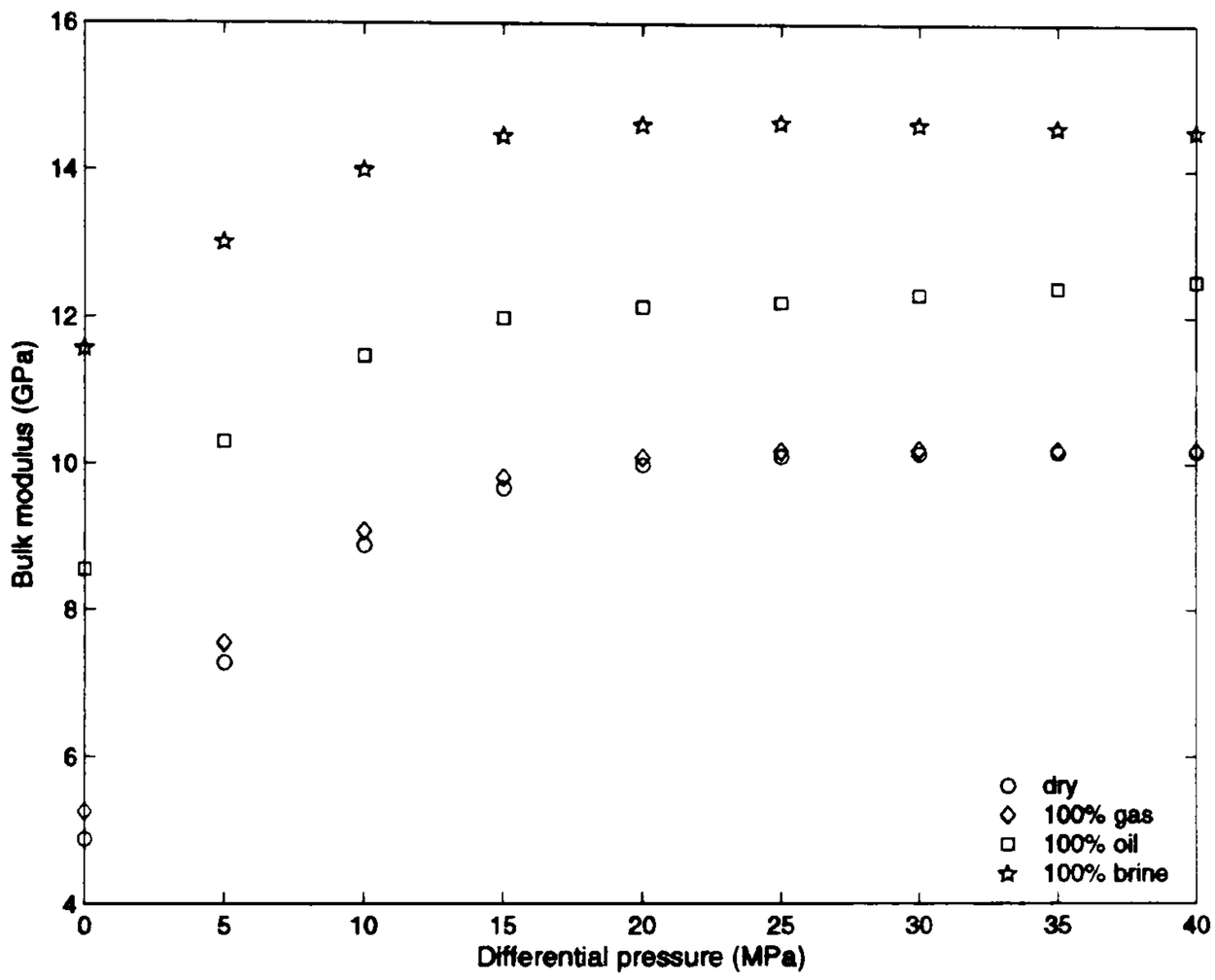

Figure 3.14: Effect of fluid saturation on the dry bulk modulus pressure model derived from the Foinaven core sample (Figure 3.3). Single phases of gas, live oil and brine saturation are used for the fluid substitution. Bulk modulus is plotted against differential pressure, where pore pressure is being changed only.

Figure 3.15 uses the same homogeneous mixtures as in Figure 3.12. The largest effect on the dry bulk modulus is observed for the post-production scenario S2, followed by the pre-production scenario S1. This means that production of hydrocarbon in an oil/brine system will increase the initial saturated bulk modulus of the rock. On the other hand, post-production scenario S3 shows that the presence of a small amount of gas (S_g = 5%)

produced a large decrease in the saturated bulk modulus. The saturated bulk modulus of this post-production scenario is smaller than in the pre-production scenario, meaning that the production of hydrocarbon with gas coming out of solution will decrease the initial saturated bulk modulus. In the case of scenario S3, it can be emphasized that the saturated bulk modulus will tend towards the dry bulk modulus at high differential pressure (i.e. low pore pressure). In fact, the gas phase controls the general behaviour of the mixture, and so the mixture compressibility tends to zero at low pore pressure as for a single phase of gas. In the previous example, a homogeneous mixture was considered, but, in the case of patchy saturation, a heterogeneous mixture might be more appropriate. In order to illustrate the effect of using a homogeneous or heterogeneous mixture for fluid substitution, the previous dry bulk modulus is saturated mathematically using fluid bulk moduli computed from the Reuss average (homogeneous assumption) and the Voigt average (heterogeneous assumption). Figure 3.16 shows the resulting saturated bulk modulus for a range of oil fractions in an oil/brine system. For low-frequency seismic, the patchy and homogeneous fluid saturation represent the upper and lower bounds of the saturated bulk modulus, respectively. Mavko and Mujerki (1998) show that these two bounds for patchy and homogeneous saturation can be calculated using Gassmann's relations with the Voigt and Reuss effective fluid modulus averages. This is an important result that can be used to bracket saturated bulk modulus values when no a priori knowledge is available on the degree of patchiness of the reservoir rock. Even if the saturated bulk modulus is affected in a complex way by fluid distribution and gas saturation, it can give a good indication of the state of saturation of the rock.

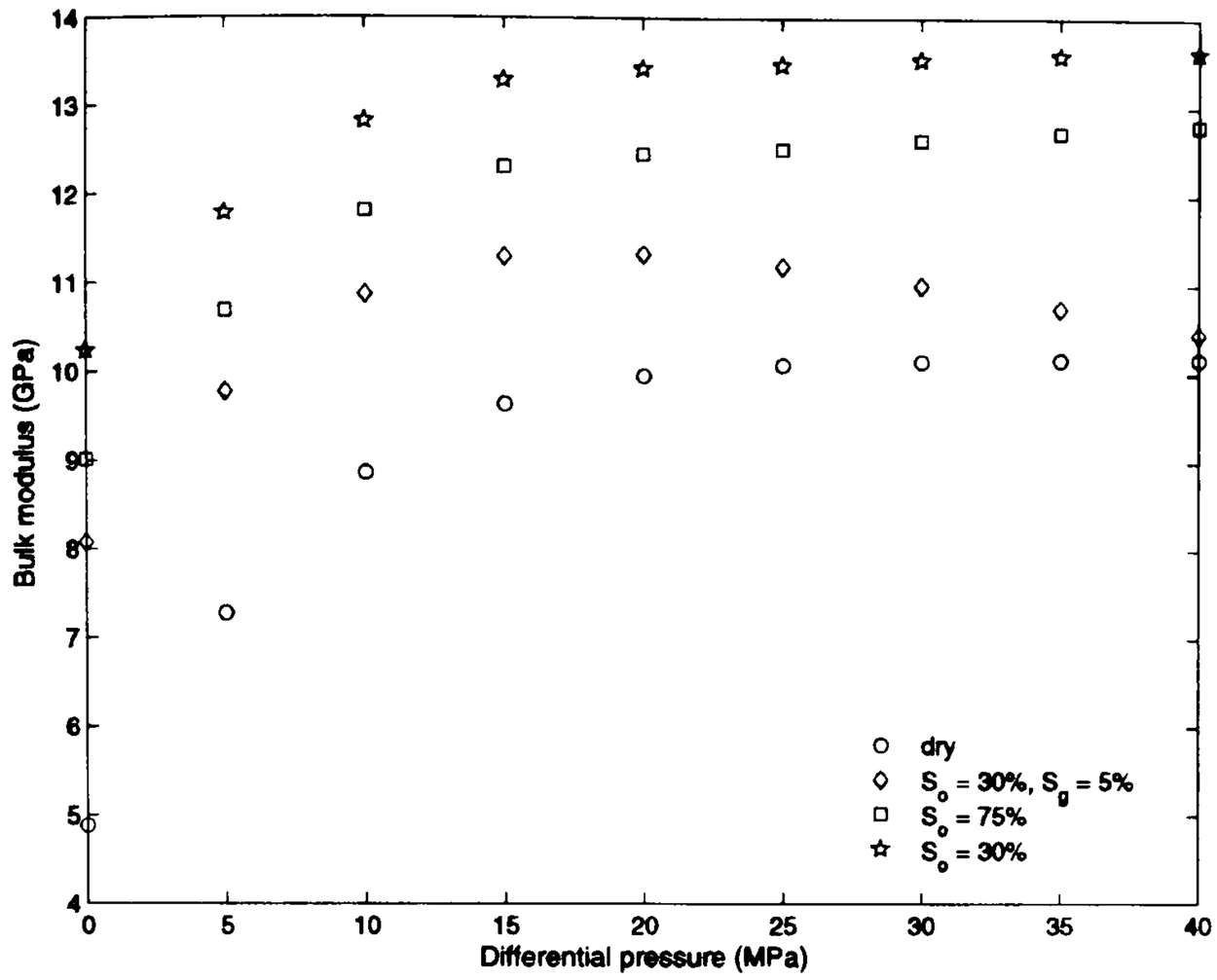

Figure 3.15: Effect of fluid saturation on the dry bulk modulus pressure model derived from the Foinaven core sample (Figure 3.3). A pre-production scenario S1 (S_o = 75%, S_b = 25%) and two post-production scenarios S2 (S_o = 30%, S_b = 70%) and S3 (S_o = 30%, S_b = 65%, S_g = 5%) are considered. Bulk modulus is plotted against differential pressure, where pore pressure is being changed only.

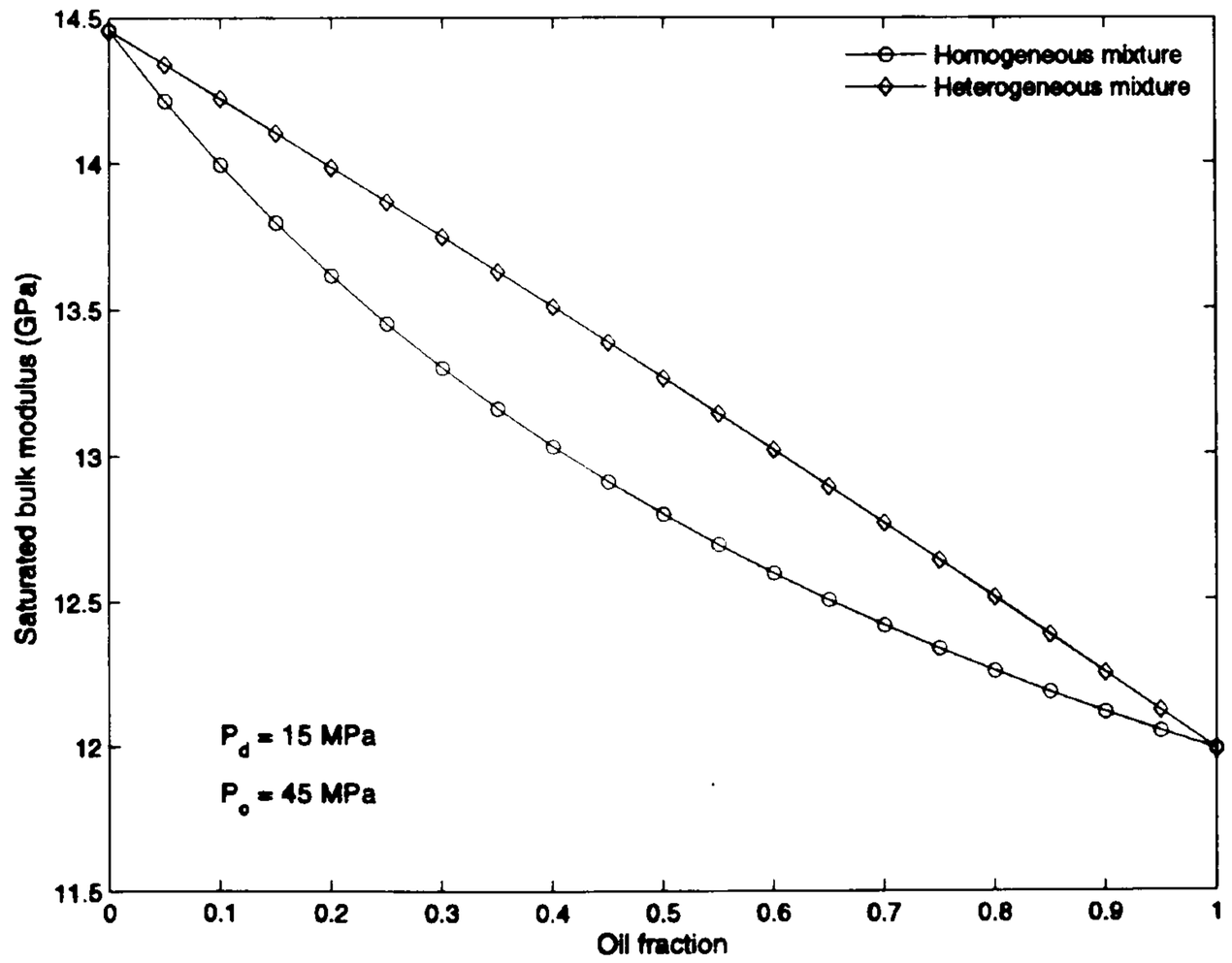

Figure 3.16: Saturated bulk modulus is plotted against oil fraction at a differential pressure of 15 MPa. Homogeneous (Reuss average) and heterogeneous (Voigt average) mixtures of live oil/brine are considered.

3.3 Discrimination between pressure and saturation effects

3.3.1 Rock physics relationships

It is well recognized that the velocity ratio V_p/V_s is a lithology indicator that is used to discriminate between reservoir and non-reservoir rocks (Wang, 2000). Based on the previous statement and on equation 3.19, one can see that the ratio of the bulk modulus to the shear modulus is just an offset version of the velocity ratio and also depends on the rock lithology.

$$\frac{\kappa_s}{\mu_d} = \frac{V_p^2}{V_S^2} - \frac{4}{3} \tag{3.19}$$

Figure 3.17 presents a cross-plot of dry bulk modulus against shear modulus for the Foinaven database. An excellent correlation can be observed between the two moduli, where the scattering of the data is attributed to the variation in mineralogy between samples. The κ_d/μ_d ratio is independent of confining pressure and porosity changes. This linear relationship was also observed in clastic granular rocks by Castagna *et al.* (1993) and Wang (2000), where the shear and bulk moduli are found to be approximately equal to each other. More recently, Smith *et al.* (2003) showed that the κ_d/μ_d ratio is dependent on the nature of the rock: from 1 for clean sandstones to 2–3 for shaly sandstones. If the mineralogy of the reservoir sandstone does not vary much in the field, then it can be concluded that a single value for the κ_d/μ_d ratio is representative of a field, as shown in Figure 3.17 for the Foinaven example. On this figure, it can be observed that the linear fit does not cross at the origin, as it would be expected following the Hertz-Mindlin theory for an unconsolidated sandstone at zero confining pressure. This can be attributed to the degree of consolidation and cementation of the rock. This interesting relationship between bulk and shear moduli has been used in the estimation of shear-wave velocities (Han and Batzle, 2004).

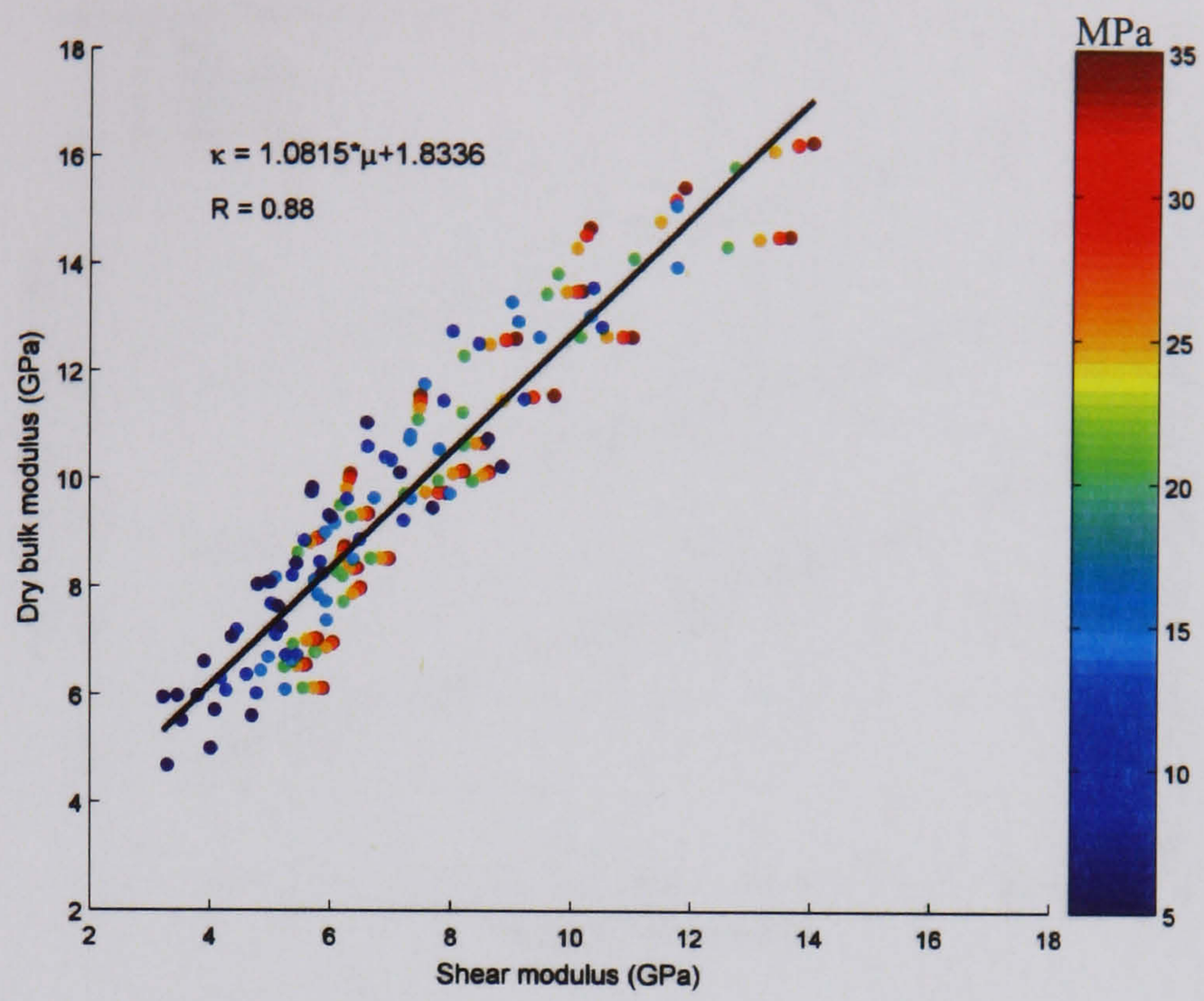

Figure 3.17: Cross-plot of the dry bulk modulus against the shear modulus for the Foinaven database. Points correspond to confining pressures of 5, 10, 15, 20, 25 and 35 MPa. A linear relationship with a correlation coefficient of 0.88 is derived by least-squares fitting between the two moduli.

Ribeiro and MacBeth (2004) took advantage of the insensitivity of the shear modulus to fluid substitution in the κ_d/μ_d cross-plot, and showed that the saturation effect impacts only the intercept of the linear correlation, while the slope remains constant. Assuming single-phase fluid saturation, it can be shown that a linear trend-line having the same slope can be fitted equally well through each saturation state. However, the trends are derived up to a differential pressure of 30 MPa, since a degradation of the correlation is observed at higher differential pressure (Figure 3.18 – shaded area). Table 3.6 shows that this upper pressure limit is realistic for most sandstone reservoirs.

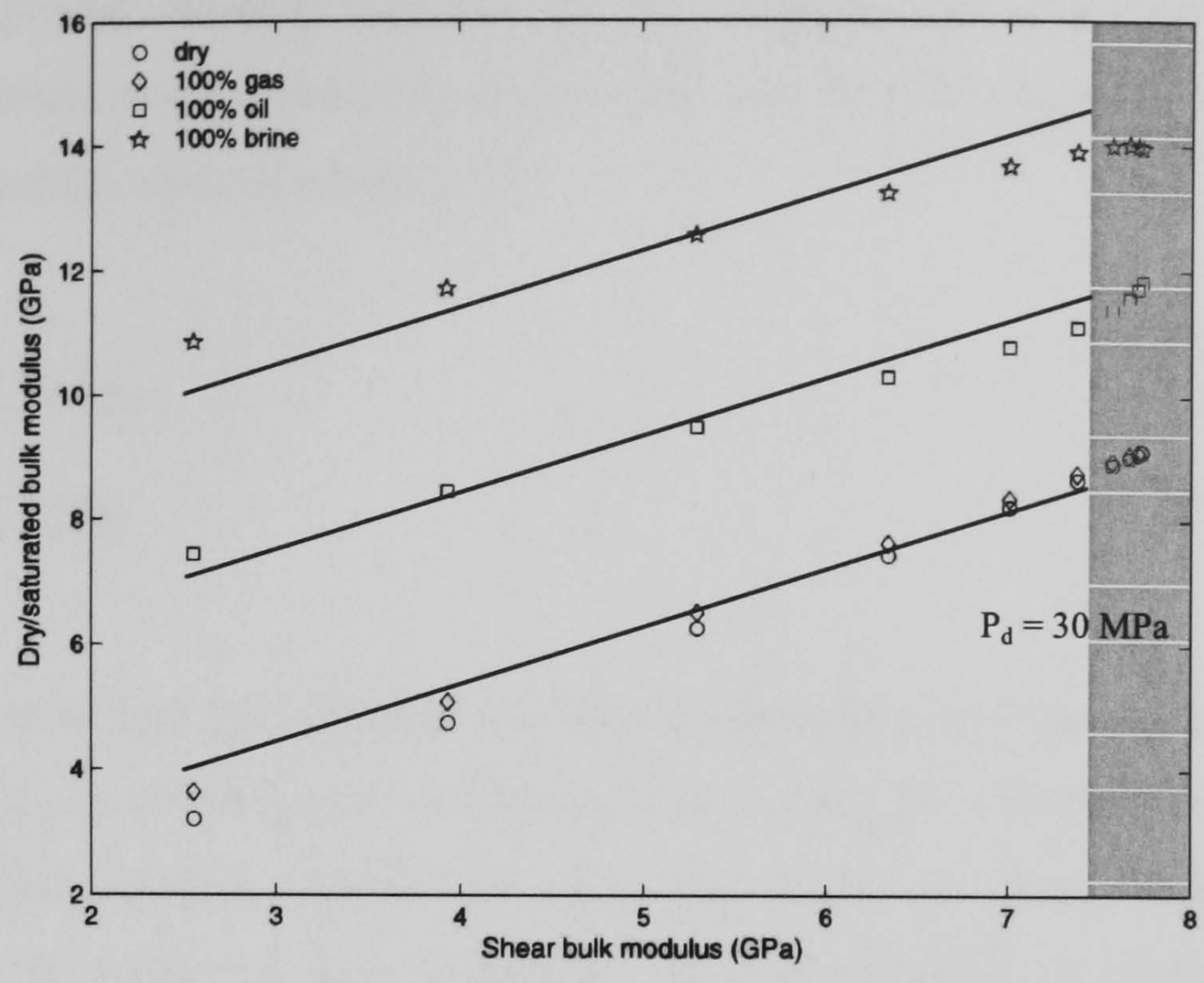

Figure 3.18: Bulk modulus plotted against shear modulus for the Forties sandstone. Four different saturation states are displayed (dry, fully water-saturated, fully gas-saturated and fully oil-saturated). Linear trend-lines with a common slope are plotted for each saturated case.

Field	Effective Pressure (MPa)
Nelson	16.7
Foinaven	17.5
Magnus	4.8
Fulmar	15.6
GOM (Tura *et al.*, 1999)	19.2
GOM (Lumley *et al.*, 1997)	26–32
Indonesia (Lumley *et al.*, 1997)	1–3
West Africa (Lumley *et al.*, 1997)	12–26
Gullfaks	5-6

Table 3.6: Effective pressures for selected sandstone reservoirs. All are generally less than 30 MPa.

From this simplified example, one can derive a relationship (equations 3.20 and 3.21) isolating saturation and pressure effects into two non-interfering attributes: the saturation modulus (χ_s) and the shear modulus (μ_d):

$$\kappa_d = \chi_d + b\mu_d \tag{3.20}$$

$$\kappa_s = \chi_s + b\mu_d \tag{3.21}$$

It can be observed that the robustness of the relationship from equation 3.21 persists in more realistic cases (Figure 3.19 to Figure 3.22). Using the mixtures from the previous section to mathematically saturate the reservoir sandstones from Table 3.4, a linear correlation for all reservoir rock, regardless of their saturation is derived, providing a common single slope. It should be noted that the slope b varies for the different sandstones and becomes larger as the difference between the parameters S_κ and S_μ increases (c.f. Figure 3.5). Then, vertical bulk modulus shifts are applied to accurately match each saturation state. Table 3.7 shows that the correlation coefficients for all the reservoirs are generally greater than 0.95, and that equation 3.21 is valid for all reservoir sandstones. Furthermore, the robustness of equation 3.21 is higher for an oil/brine system, and degrades slightly in the presence of gas. For all reservoir sandstones, averaged standard deviations of 2%, 2% and 5% are obtained for the intercept of the linear fit in the pre-production S1, post-production S2 and S3, respectively. Additionally, by assuming an heterogeneous mixture, the same conclusion can be drawn even if a slight increase of the parameter b is noted due to a different behaviour of gas saturation between the Reuss and Voigt average (Figure 3.23). An increase of the saturated bulk modulus is also observed cause by the increase of fluid bulk modulus in the heterogeneous case (c.f. Figure 3.16). The separation of pressure and saturation effects in this rock physics context constitutes the foundation of the petro-elastic-based approach to estimate pore pressure and fluid bulk modulus from repeated seismic data (Ribeiro and MacBeth, 2004). Equation 3.21 is valid only for the static case, and does not provide any insight into the dynamic changes of pressure and saturation. In the following section, explicit expressions to estimate those changes are introduced.

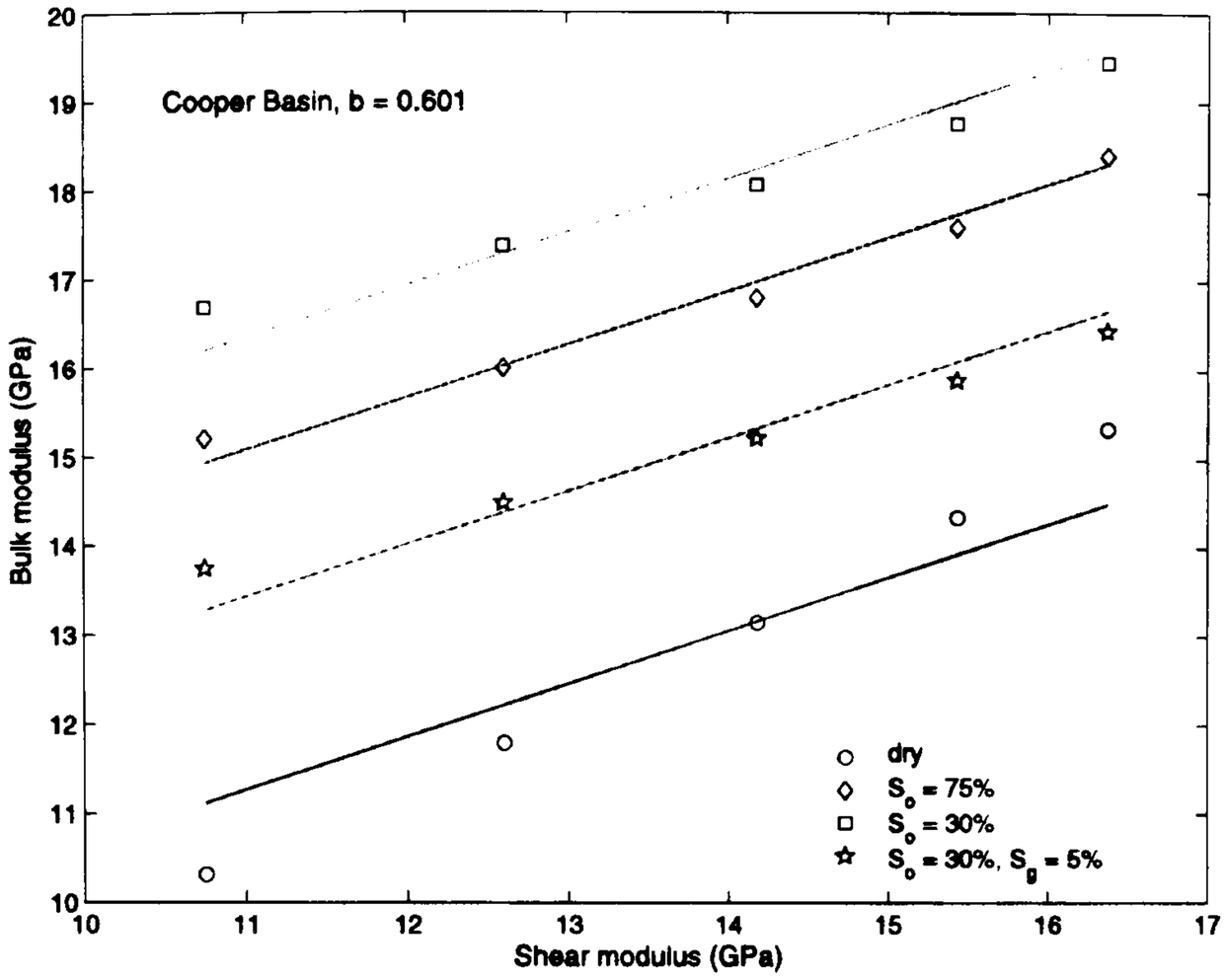

Figure 3.19: Bulk modulus plotted against shear modulus for the Cooper Basin sandstone. Four different saturation states are displayed (dry; pre-production S1; post-production S2 and post-production S3). Least-squares fits computed with a parameter b = 0.601 are shown for each saturation case. Homogeneous mixtures of fluids are considered.

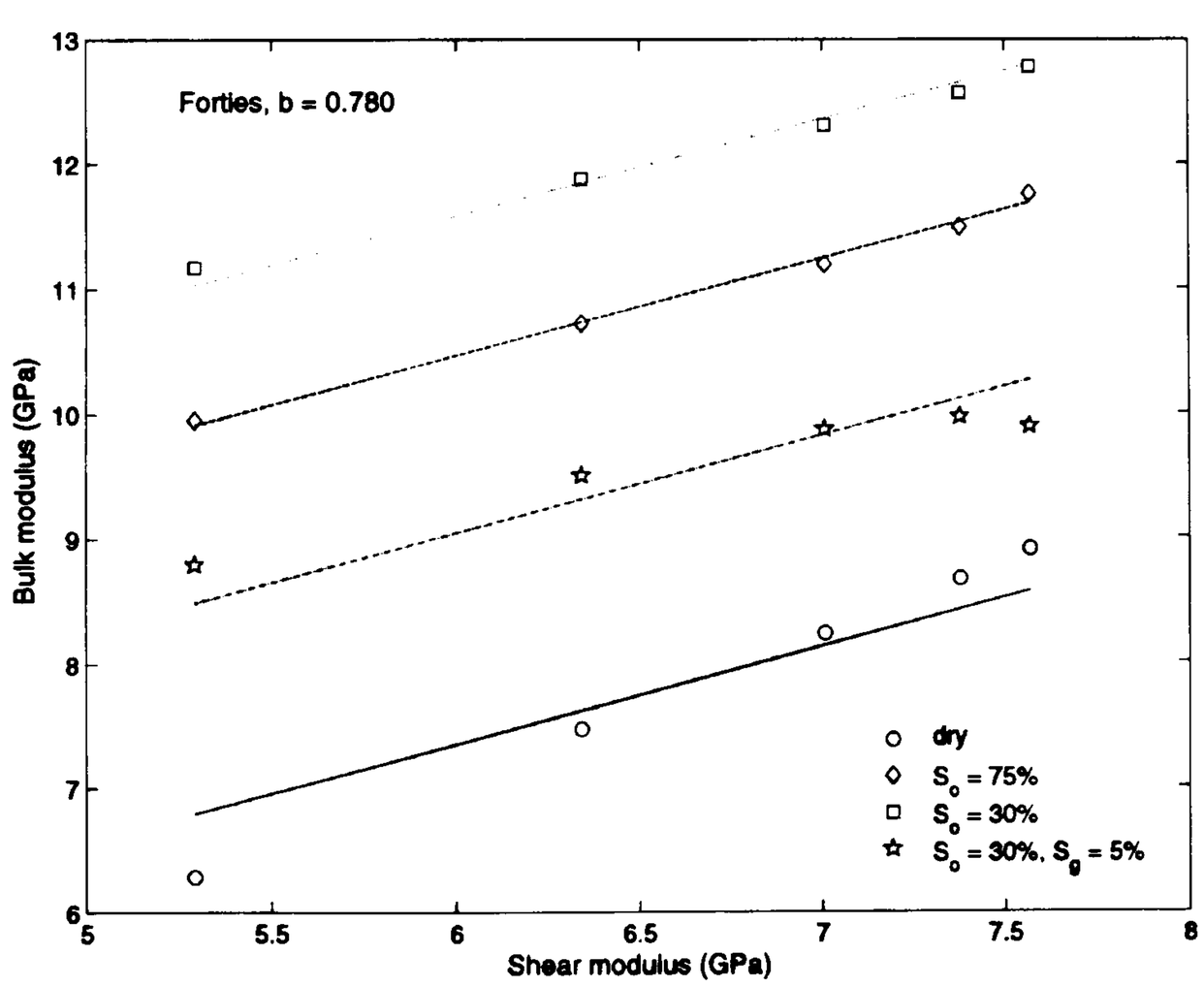

Figure 3.20: Bulk modulus plotted against shear modulus for the Forties sandstone. Four different saturation states are displayed (dry; pre-production S1; post-production S2 and post-production S3). Least-squares fits computed with a parameter b = 0.780 are shown for each saturation case. Homogeneous mixtures of fluids are considered.

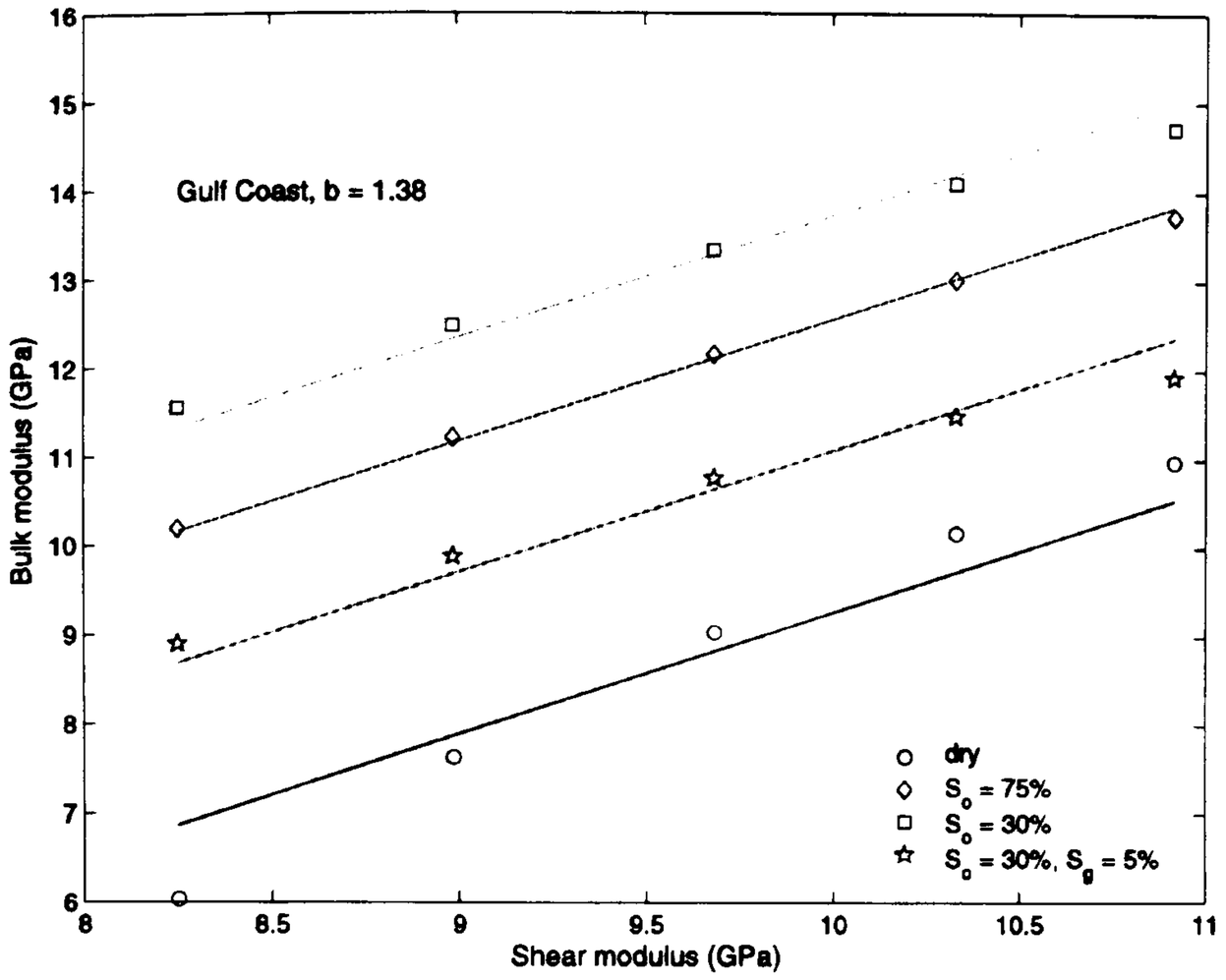

Figure 3.21: Bulk modulus plotted against shear modulus for the Gulf Coast sandstone. Four different saturation states are displayed (dry; pre-production S1; post-production S2 and post-production S3). Least-squares fits computed with a parameter b = 1.380 are shown for each saturation case. Homogeneous mixtures of fluids are considered.

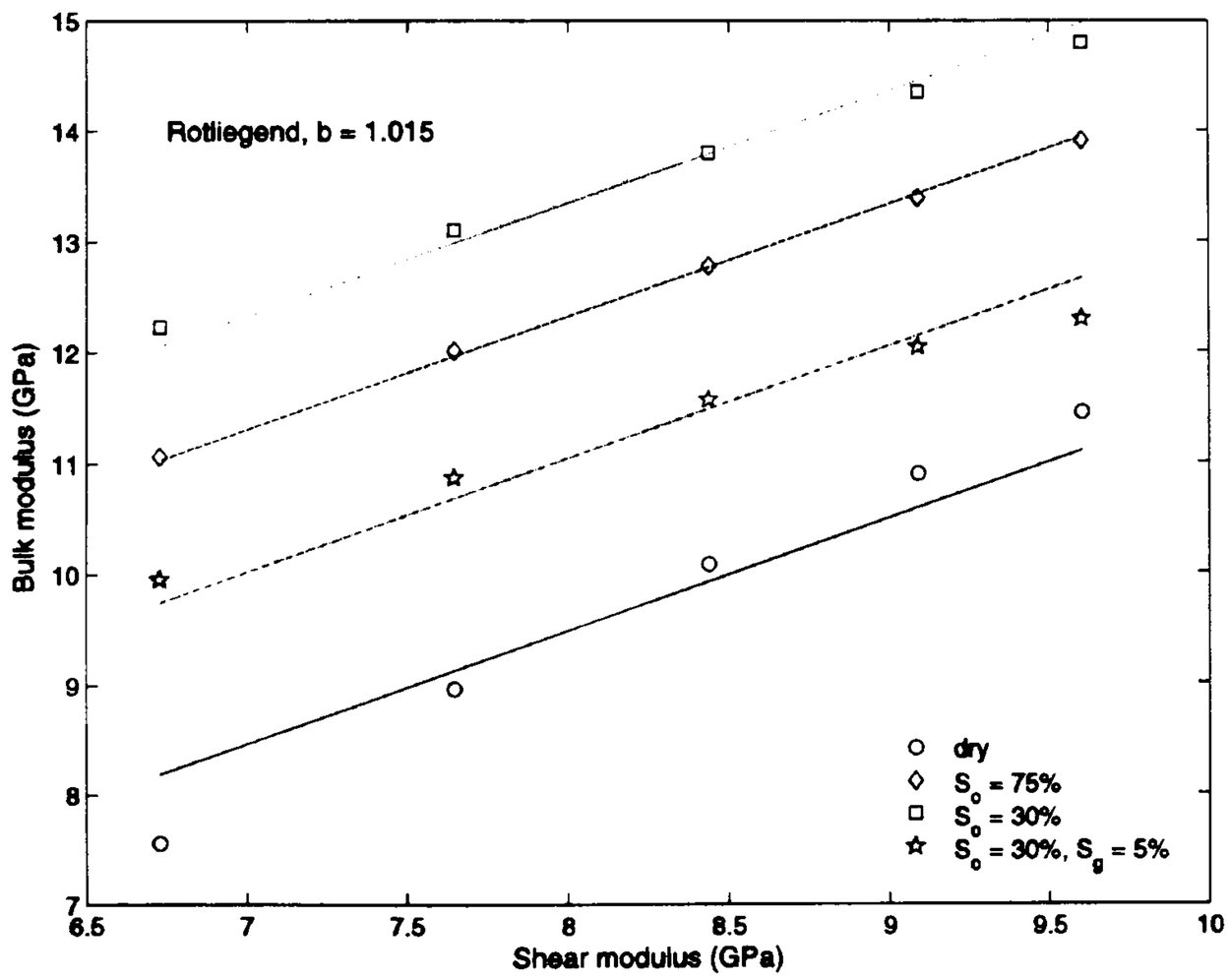

Figure 3.22: Bulk modulus plotted against shear modulus for the Rotliegend. Four different saturation states are displayed (dry; pre-production S1; post-production S2 and post-production S3). Least-squares fits computed with a parameter b = 1.015 are shown for each saturation case. Homogeneous mixtures of fluids are considered.

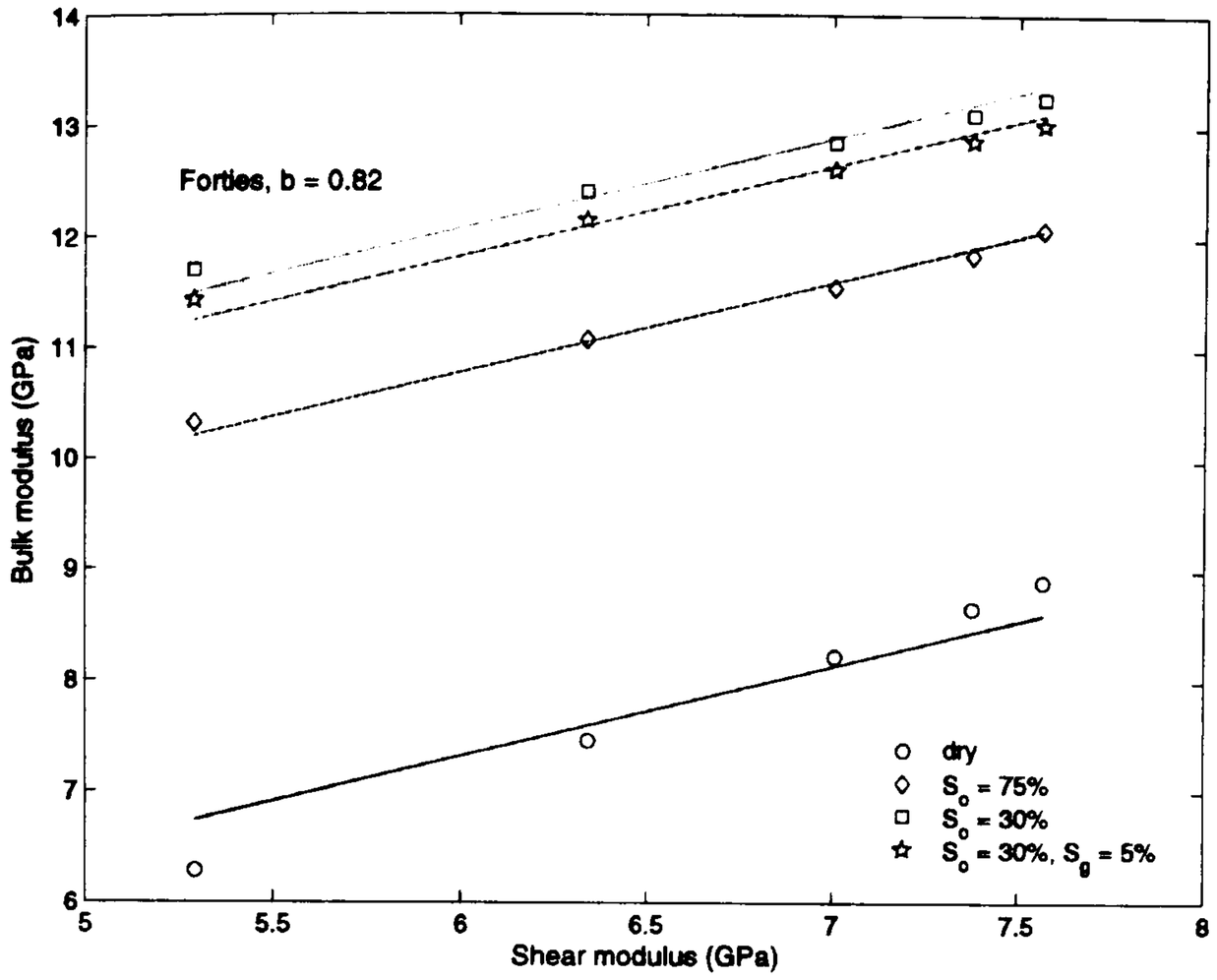

Figure 3.23: Bulk modulus plotted against shear modulus for the Forties sandstone. Four different saturation states are displayed (dry; pre-production S1; post-production S2 and post-production S3). Least-squares fits computed with a parameter b = 0.82 are shown for each saturation case. Heterogeneous mixtures of fluids are considered.

	Cooper	Forties	Gulf Coast	Rotliegend
Dry	0.892	0.896	0.925	0.932
Pre-production S1	0.978	0.994	0.997	0.998
Post-production S2	0.926	0.980	0.972	0.980
Post-production S3	0.926	0.687	0.950	0.935

Table 3.7: Correlation coefficients corresponding to the fits of equations 3.20 and 3.21 to the four different saturation states (dry, pre-production S1, post-production S2 and S3) for the Cooper Basin, Forties, Gulf Coast and Rotliegend sandstones.

3.3.2 Dynamic fluid bulk modulus changes

The fluid bulk modulus is the preferred attribute to estimate saturation changes because it does not involve any assumption about the degree of patchiness of the reservoir. Furthermore, from the estimated fluid bulk modulus changes and an appropriate averaging law, the different saturations can be retrieved for patchy (Reuss average), and homogeneous (Voigt average), fluid distributions. Mavko and Mukerji (1995) showed that Gassmann's relation (equation 3.13) could be written exactly as follows:

$$\left(\kappa_s + \frac{4}{3}\mu_d\right) = \left(\kappa_d + \frac{4}{3}\mu_d\right) + \frac{\phi}{\phi_c} R_c \tag{3.22}$$

where R_c is the Reuss average of the pore fluid and mineral moduli, evaluated at a special porosity $\phi_c = \phi/(1-\kappa_d/\kappa_m)$, called critical porosity, which is a constant:

$$\frac{1}{R_c} = \frac{\phi_c}{\kappa_f} + \frac{1-\phi_c}{\kappa_m} \tag{3.23}$$

Considering the insensitivity of the shear modulus to fluid saturation, equation 3.22 can be reformulated into equation 3.24:

$$\kappa_s = \kappa_d + \frac{\phi}{\phi_c} R_c \tag{3.24}$$

Since the fluid bulk modulus is much smaller than the mineral modulus ($\kappa_f \langle\langle \kappa_m$), $R_c \approx \kappa_f/\phi_c$. Furthermore, for most consolidated sandstones, the fluid bulk modulus is also much smaller than the dry bulk modulus, $\kappa_f \langle\langle \kappa_d$. Under these assumptions, equation 3.24 can be rewritten as:

$$\kappa_s \approx \kappa_d + \frac{\phi}{\phi_c^2}\left(\kappa_f\right)_{\text{patchy/uniform}} \tag{3.25}$$

where the fluid bulk modulus is obtained from equation 3.16 or 3.18. This approximation is more accurate when the rock is well consolidated or even cemented, because of the assumption, $\kappa_f \langle\langle \kappa_d$. Equation 3.25 shows that the resulting saturated bulk moduli for patchy and uniform saturation follow the same mathematical expression, and only differ by the choice of the fluid bulk modulus averaging law. Then, by substitution of equations 3.20 and 3.21 into 3.25, it can be demonstrated that:

$$\Delta\chi_s = \chi_{sII} - \chi_{sI} \approx \frac{\phi}{\phi_c^2}\left[\left(\overline{\kappa_f}\right)_{II} - \left(\overline{\kappa_f}\right)_{I}\right]_{\text{patchy/uniform}}$$

$$\Delta\kappa_f \approx \frac{\phi_c^2}{\phi}\Delta\chi_s \tag{3.26}$$

where χ_{sI} and χ_{sII} stand for the saturation modulus at times I and II, respectively. κ_{fI} and κ_{fII} stand for the fluid bulk modulus at times I and II, respectively. This last approximation is equivalent to neglecting the effect of pore pressure on the fluid bulk modulus changes, since it has been established that the saturation modulus is independent of pressure. To validate this result, the fluid bulk modulus changes are computed for the different production scenarios presented in Table 3.8.

	ΔS_o	ΔS_g
S1–S2 (live oil)	45%	0%
S1–S3 (live oil)	45%	5%
S1′–S2′ (dead oil)	45%	0%

Table 3.8: Oil (ΔS_o) and gas (ΔS_g) saturation changes between the pre-production scenario S1 (S_o = 75%, S_b = 25%) and the two post-production scenarios S2 (S_o = 30%, S_b = 70%) and *S*3 (S_o = 30%, S_b = 65%, S_g = 5%). Post-production scenarios S1' and S2' equivalent to S1 and S2 are also defined for dead oil.

In the case of a homogeneous fluid distribution, Figure 3.24 shows that the fluid bulk modulus changes are only slightly dependent on pore pressure for a two-phase system containing brine and live or dead oil. However, in the presence of gas, the changes are highly related to the pore pressure changes. This observation agrees with the larger standard deviation in χ_s noticed in the previous section for gas-saturated rocks. Figure 3.25 is an equivalent display to Figure 3.24, but in this case for a heterogeneous fluid distribution. For a heterogeneously distributed fluid, the fluid bulk modulus changes appear to be independent of pore pressure in all scenarios. It can be concluded that equation 3.26 is valid in the first approximation in a reservoir sandstone saturated with a homogeneous or heterogeneous mixture of fluids. However, in the presence of gas, the approximation breaks down, as the pressure dependence of the gas phase dominates the overall behaviour of the fluid bulk modulus changes.

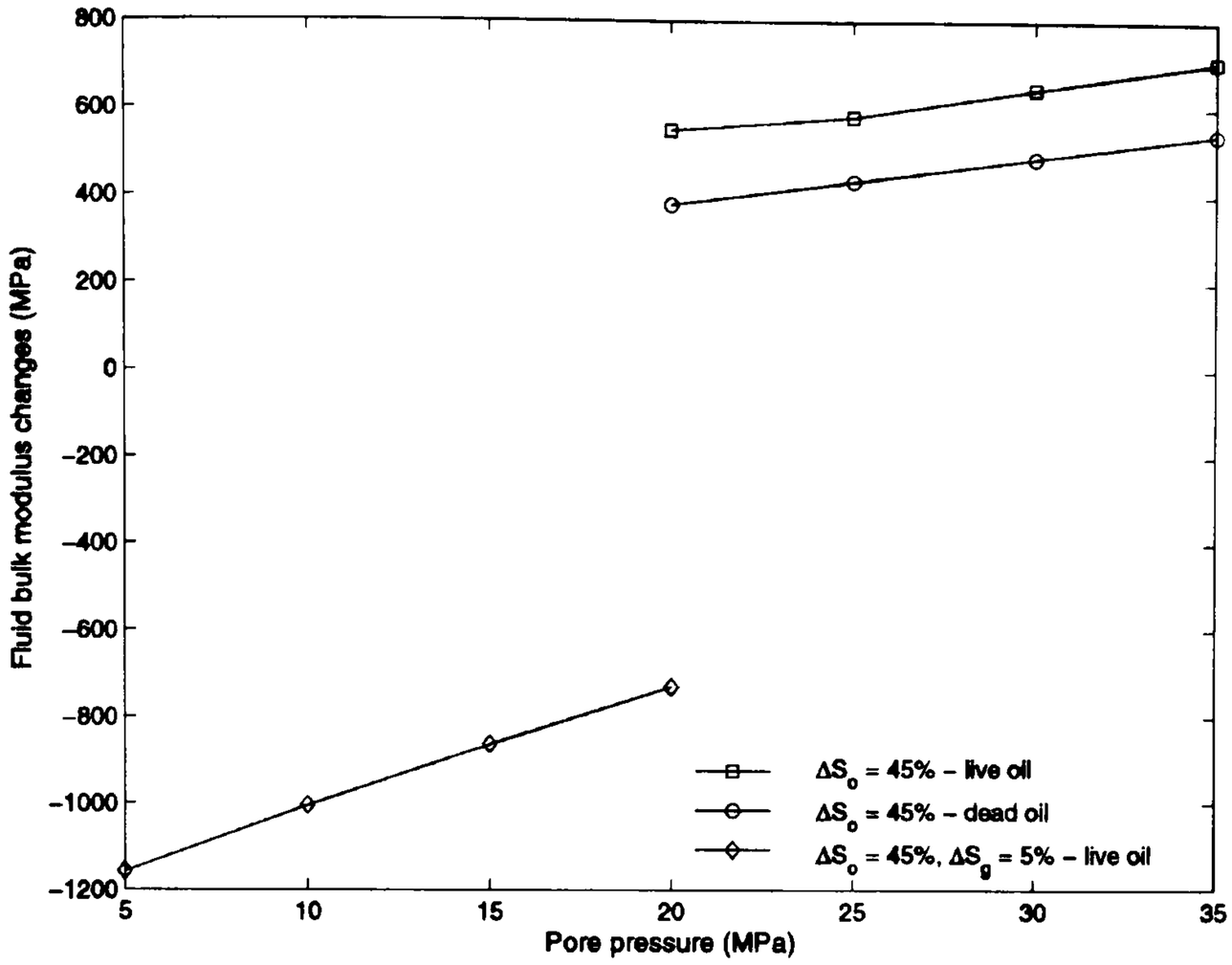

Figure 3.24: Fluid bulk modulus changes for the production scenario presented in Table 3.8. An initial pore pressure of 20 MPa, equal to the bubble point pressure, and a homogeneous fluid distribution are assumed.

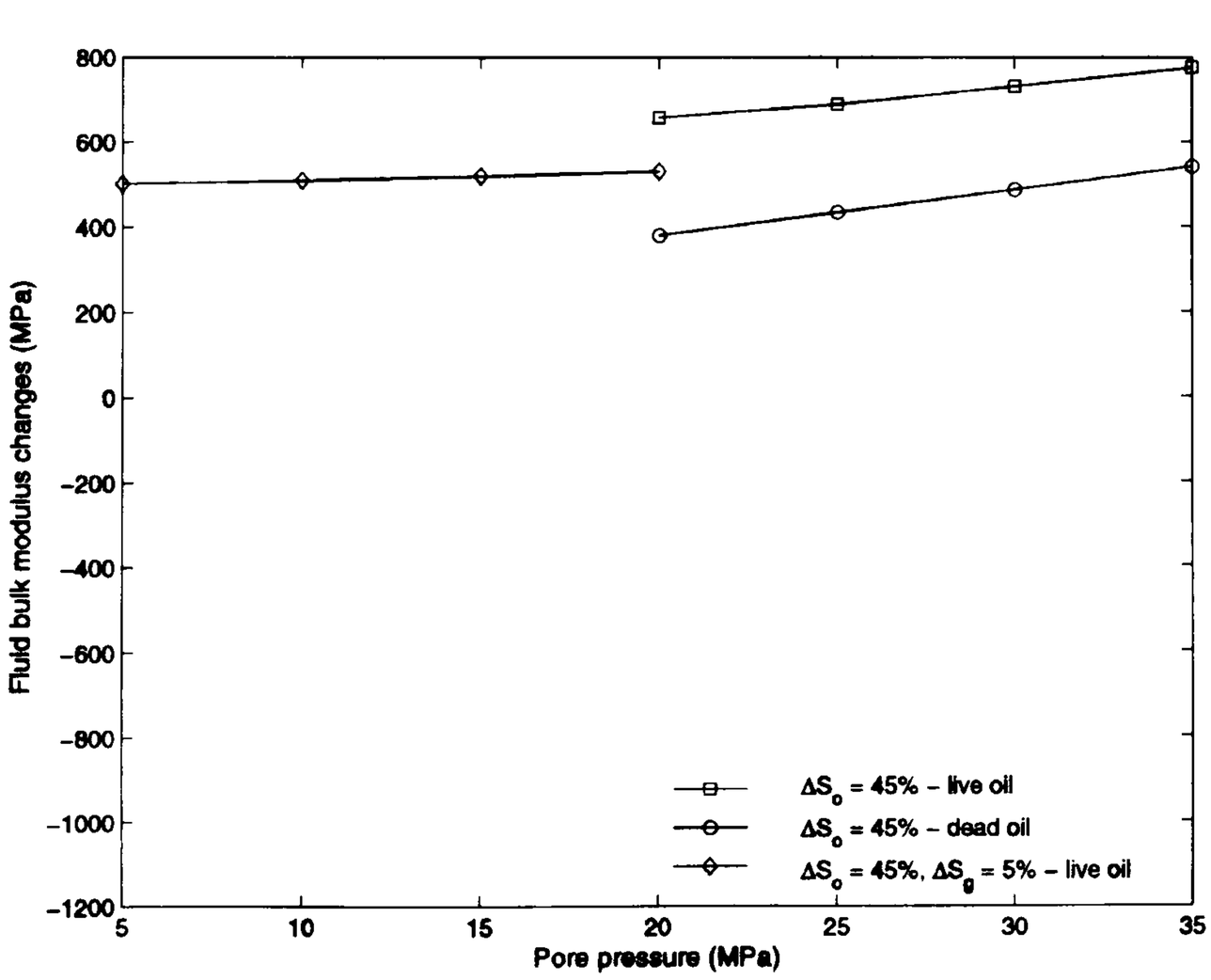

Figure 3.25: Fluid bulk modulus changes for the production scenario presented in Table 3.8. An initial pore pressure of 20 MPa, equal to the bubble point pressure, and a heterogeneous fluid distribution are assumed.

3.3.3 Dynamic pore pressure changes

In order to retrieve the pore pressure from the shear modulus, equation 3.5 is used. The resulting time-lapse pressure changes take the following form:

$$\Delta P_{\mathrm{p}} = -P_{\mu} \ln\left[\frac{\mu_{\mathrm{dII}}\left(\mu_{\infty} - \mu_{\mathrm{dI}}\right)}{\mu_{\mathrm{dI}}\left(\mu_{\infty} - \mu_{\mathrm{dII}}\right)}\right] \tag{3.27}$$

where μ_{dI} and μ_{dII} stand for the shear modulus at times I and II, respectively. It should be noted that in the derivation of equation 3.27, there is no distinction between the differential and effective pressure, meaning that the effective stress coefficient (equation 3.1) is set to unity. Biot (1941) shows that the effective stress coefficient is given by equation 3.28 and would vary from zero (i.e. hard rocks) to unity (i.e. soft rocks).

$$n = 1 - \frac{\kappa_s}{\kappa_m} \tag{3.28}$$

Several authors (Christensen and Wang, 1985; Prasad and Manghnani, 1997; Khaksar *et al.*, 1999b) have reported effective stress coefficients different from unity in drained and undrained sandstones. However, Gurevich (2004) showed that in theory the effective stress coefficient should be equal to unity in the drained case, which agrees with the results from Hofmann *et al.* (2004). In fact, there is no universal effective stress coefficient, and it will vary for each elastic property. Following the approach of Todd and Simmons (1972), the effective stress coefficient can be computed using equation 3.29, where A represents an elastic property.

$$n = 1 - \left[\partial A / \partial P_{\mathrm{p}}\right]_{P_{\mathrm{d}}} \left[\partial A / \partial P_{\mathrm{d}}\right]^{-1}_{P_{\mathrm{p}}} \tag{3.29}$$

Since wave velocity measurements as a function of varying pore pressure are not available from the Foinaven database, the results from Hofmann *et al.* (2004) are used. Figure 3.26 and Figure 3.27 show the effective stress coefficient computed from a brine-saturated clastic sample with a porosity of 13%. The effective stress coefficient for the bulk modulus is close to unity at low differential pressures, but then decreases with increasing pressure. The effective stress coefficient for the shear modulus is equal to unity at low differential pressure, and shows little variation when pressure increases. The effective stress coefficient for the rigidity remains nearly constant between 1 and 0.9 for a differential pressure varying from 0 to 70 MPa. From this rock physics-based result, it can be concluded that the assumption of a unit effective stress coefficient is reliable, as the shear modulus is used in the derivation of the pore pressure changes. In fact, at differential pressures lower than 30 MPa (which is the limit of applicability for equation 3.21), the effective stress coefficient for the shear modulus varies from 1.01 to 0.95.

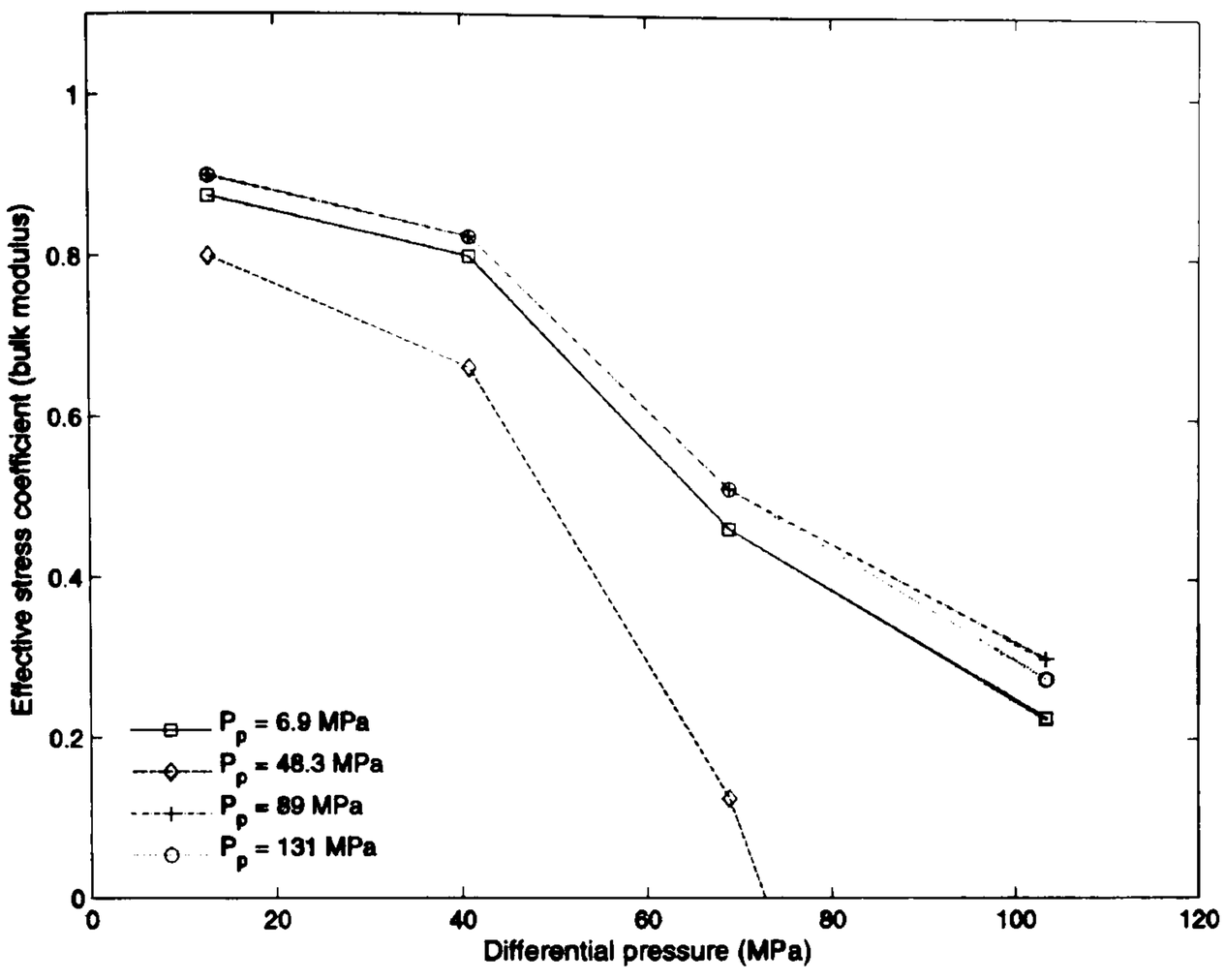

Figure 3.26: Effective stress coefficient for the bulk modulus as a function of differential and pore pressure (from Hofmann *et al.*, 2004).

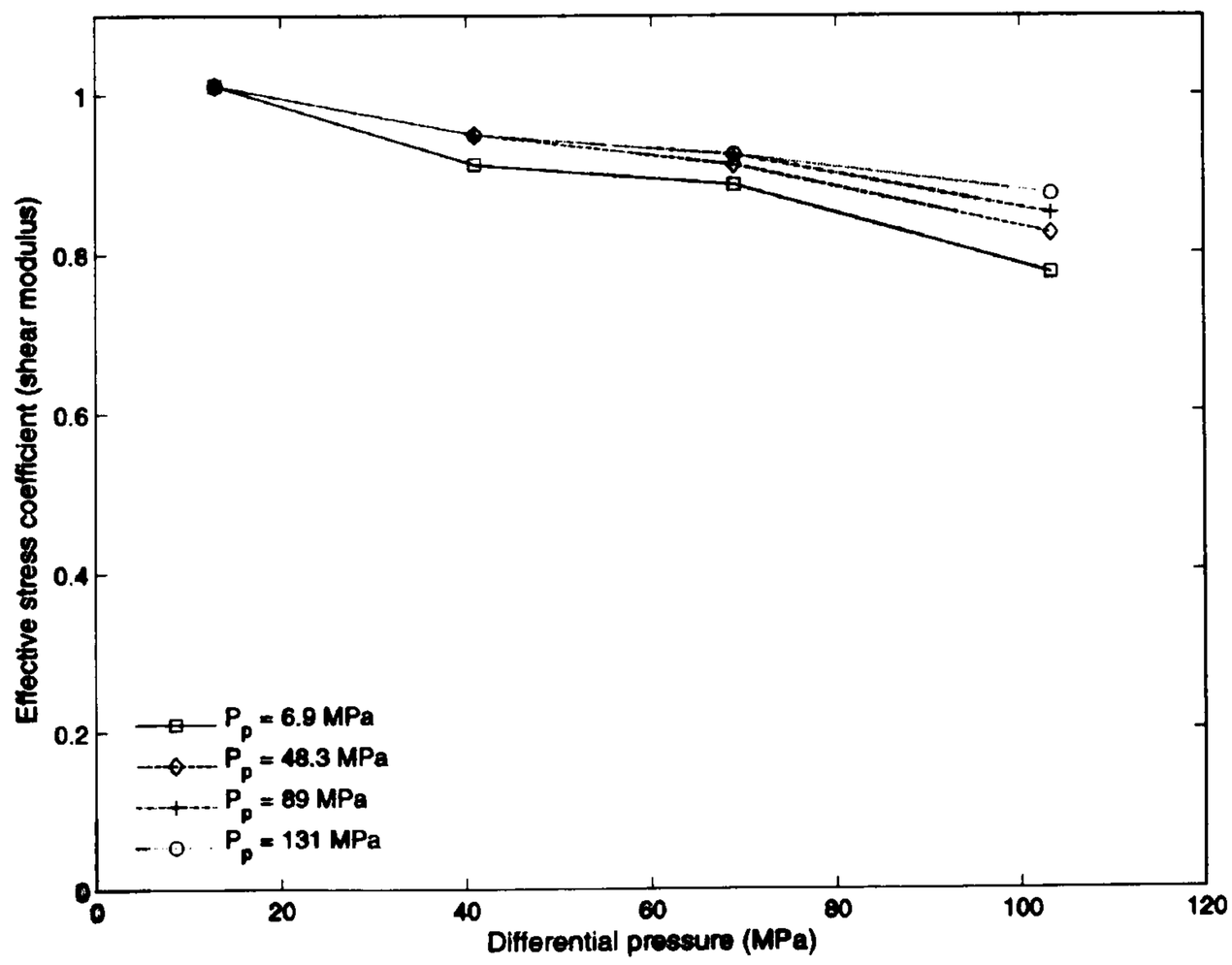

Figure 3.27: Effective stress coefficient for the shear modulus as a function of differential and pore pressure (from Hofmann *et al.*, 2004).

3.4 Conclusions

From this petro-elastic study, two rock physics attributes are identified. One is dependent on the pressure effect (shear modulus, μ_d) and the second is dependent on the fluid saturation effect (saturation modulus, χ_s). The relationships (equations 3.20 and 3.21) allow the separation of pressure and fluid-saturation effects and represent a general result that is tested on a variety of reservoir sandstones. The main factors possibly influencing the quality of the previous approximations are highlighted as being the clay content, the porosity, and core-damage effects. Explicit formulations (equations 3.26 and 3.27) to estimate pore pressure and fluid bulk modulus changes, are also obtained for uniformly and heterogeneously saturated sandstones. The rock physics relationships derived are shown to be robust, and form the basis of an independent pressure and saturation discrimination technique. In the next chapter, these relations are transformed into the seismic domain, in order to define how pressure and saturation attributes can be inverted from time-lapse seismic data.

Chapter 4

Rock physics interpretation of seismic reflectivity

The acquisition of time-lapse seismic data offers the opportunity to monitor production-related seismic-amplitude changes. These changes in reflected amplitude are directly dependent on the variations in the elastic properties of the reservoir rock, and show different responses with incidence angles. In order to interpret which of these changes are related to pressure and saturation effects, the petro-elastic behaviour of the reservoir rock needs to be fully understood. In the previous chapter, approximations were presented that allowed us to quantify the pressure and saturation effects at the rock physics level. To bridge the gap between the seismic and reservoir domains, these relations can be integrated with mathematical expressions that relate seismic reflection data to elastic properties at different incidence angles. The purpose is to reduce the ambiguity occurring between pressure and saturation variations in time-lapse seismic interpretation, by inverting for seismic attributes independent of those changes. In this chapter, a brief overview of seismic-wave propagation and geophysical terminology is presented. Then, the reflectivity and elastic impedance concepts are introduced and newer formulations developed, leading to an explicit separation of pressure and saturation effects. Finally, a 1D analysis based on well-log data is carried out in order to demonstrate the reliability of the shear and saturation modulus for identifying the pressure and saturation effects from seismic reflectivity.

4.1 Seismic-wave propagation

4.1.1 An overview

Seismic waves travelling in the subsurface induce elastic deformation of the rock along their propagation path by changing the stress field. These elastic deformations vanish after the elapsed time necessary for the rock to revert to its initial stress field. The ability of the rock to resist these stress changes is directly dependent on its characteristics. In the previous chapter, it was explained that compressional and shear stresses change the volume and the shape of the rock, respectively. The more the rock resists these changes, the higher the compressional or the shear velocities. Based on the different P-wave velocity, S-wave velocity or velocity ratio responses (Yilmaz, 2001) for different rock types, it is possible to distinguish between them and particularly to differentiate reservoir and non-reservoir rocks. Variations in the nature of the fluid saturating the pores will also change the velocities (cf. Chapter 3), and allow differentiation between various reservoir conditions. The use of seismic data for lithology and fluid prediction is not straightforward. Although S-wave and P-wave velocities can be measured directly in the laboratory or in well-bore holes, this is not the case with conventional seismic data. In fact, seismic data measure the reflected energy at all layer interfaces of the subsurface. In order to explain the mechanism involved in the acquisition of P-wave data, a layered medium composed of two infinite elastic half-spaces is considered. Figure 4.1 presents the partitioning of an incident P-wave at an interface, into its reflected P-wave (R_{pp}) and transmitted P-wave (T_{pp}) components. The angles of the incident, reflected, and transmitted waves follow Snell's law:

$$p = \frac{\sin\theta_1}{V_{p1}} = \frac{\sin\theta_2}{V_{p2}} \tag{4.1}$$

where:

V_{p1} = P-wave velocity in layer 1

V_{p2} = P-wave velocity in layer 2

θ_1 = incident P-wave angle

θ_2 = transmitted P-wave angle

p = ray parameter

The ratio of the reflected P-wave energy to that of the incident P-wave energy is defined as the P-wave reflection coefficient R_{pp} (θ_1). Zoeppritz (1919) derived a set of equations in order to determine the reflected and transmitted amplitudes for plane waves as a function of the angle of incidence and acoustic impedances. In the case of normal incidence, Zoeppritz's equations for the reflection coefficient take the simple form shown by equation 4.2.

$$R_{pp} = \frac{I_{p2} - I_{p1}}{I_{p2} + I_{p1}} = \frac{1}{2}\frac{\Delta I_p}{\bar{I}_p} \tag{4.2}$$

where:

I_{p2} = impedance of layer 2 = $\rho_2 V_{p2}$

ρ_2 = density of layer 2

I_{p1} = impedance of layer 1 = $\rho_1 V_{p1}$

ρ_1 = density of layer 1

ΔI_p and $\bar{I}_p$ are the difference and the average of impedance at the interface, respectively. However, Zoeppritz's equations in their general forms are not intuitive, and approximations are mostly used in the industry.

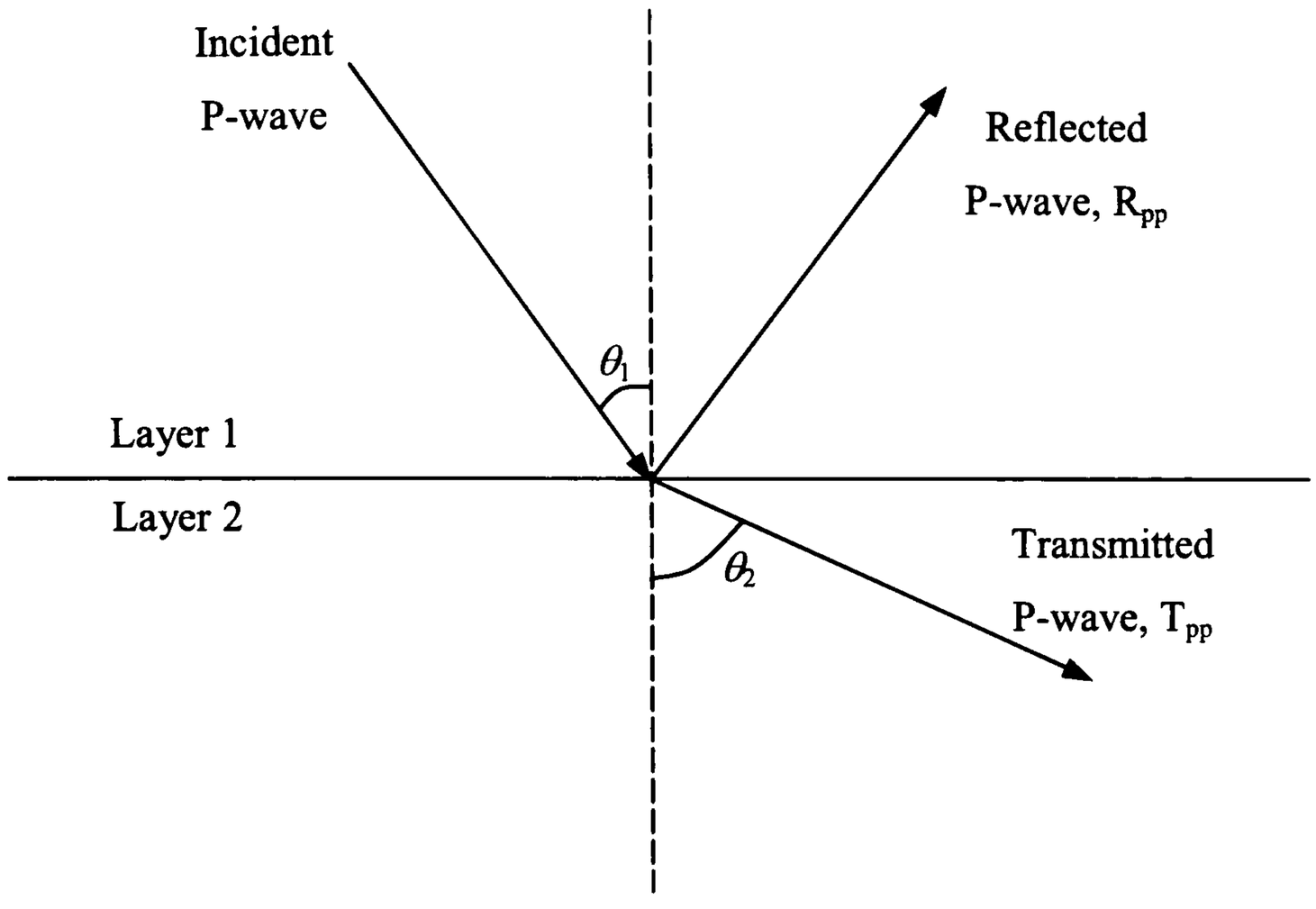

Figure 4.1: Partitioning of an incident P-wave into its reflected P-wave and transmitted P-wave components. The θ_1 and θ_2 stand for the incidence and transmission angles.

4.1.2 Amplitude variation versus offset

In the case of an offset-dependent reflection coefficient, Aki and Richards (1980) approximated Zoeppritz's equations in terms of changes in density, P-wave velocity and S-wave velocity (equation 4.3).

$$R(\theta) = \left[\tfrac{1}{2}\left(1 + \tan^2\theta\right)\right]\frac{\Delta V_p}{\overline{V}_p} - \left[4\frac{V_s^2}{V_p^2}\sin^2\theta\right]\frac{\Delta V_s}{\overline{V}_s} + \left[\frac{1}{2}\left(1 - 4\frac{V_s^2}{V_p^2}\sin^2\theta\right)\right]\frac{\Delta\rho}{\overline{\rho}} \qquad (4.3)$$

where:

$$\Delta V_p = V_{p2} - V_{p1}$$

$$\Delta V_s = V_{s2} - V_{s1}$$

$$\Delta\rho = \rho_2 - \rho_1$$

$$\overline{V_p} = \frac{V_{p1} + V_{p2}}{2}$$

$$\overline{V_s} = \frac{V_{s1} + V_{s2}}{2}$$

$$\overline{\rho} = \frac{\rho_1 + \rho_2}{2}$$

V_p stands for the P-wave velocity, V_s for the S-wave velocity, ρ for the density, and θ for the average of the incidence angle θ_1 and transmission angle θ_2. It should be noted that this equation is split into three parts: the first one relates to the change in P-wave velocity across the interface (i.e. the P-wave reflectivity); the second one relates to the change of S-wave velocity across the interface (i.e. the S-wave reflectivity); and the last one relates to the change of density across the interface. All these quantities: $\Delta V_p / \overline{V_p}$, $\Delta V_s / \overline{V_s}$ and $\Delta\rho / \overline{\rho}$ have to be small in order to satisfy the approximations made to lead to equation 4.3. It is important to note that the three terms of the previous equation are interdependent in terms of pressure and saturation, since V_p, V_s and ρ are also interdependent. Using reflection coefficients at a different angle of incidence makes it possible to invert for relative changes in P-wave and S-wave velocities if density is constrained (Smith and Gidlow, 1987). Direct hydrocarbon indicators derived from these attributes have demonstrated their potential to identify gas-saturated sandstones (Fatti *et al.*, 1994). However, this method is purely qualitative, as it detects S-wave and P-wave velocities that depart from a reference relation defined for a specific rock type (for example, the mudrock line of Castagna *et al.*, 1985). The reflectivity-coefficient equation 4.3 is also commonly known as the AVO (amplitude variation with offset) equation. In fact, equation 4.4 presents equation 4.3 rearranged in terms of increasing incidence angle, and gives all the meaning to the term AVO.

$$R(\theta) = \left[\frac{1}{2}\left(\frac{\Delta V_p}{\overline{V_p}} + \frac{\Delta\rho}{\rho}\right)\right] + \left[\frac{1}{2}\frac{\Delta V_p}{\overline{V_p}} - 4\frac{V_s^2}{V_p^2}\frac{\Delta V_s}{\overline{V_s}} - 2\frac{V_s^2}{V_p^2}\frac{\Delta\rho}{\overline{\rho}}\right]\sin^2\theta + \left[\frac{1}{2}\frac{\Delta V_p}{\overline{V_p}}\right]\left(\tan^2\theta - \sin^2\theta\right) \quad (4.4)$$

The first term in this equation is called the intercept or the acoustic impedance, and is independent of the incidence angle and directly related to equation 4.2. The second term is called the gradient, while the third term is only acting for an angle of incidence greater than 30 degrees – allowing a possible simplification of equation 4.4 by assuming $\tan^2\theta \approx \sin^2\theta$. Generally, the intercept, gradient or combinations of both (usually called fluid factors) are used as hydrocarbon indicators. Figure 4.2 presents the reflectivity, computed using the Aki and Richards (1980) approximation for a pre-production case ($S_b = 0.25$, $S_o = 0.75$, $P_d = 20$ MPa) and a post-production case ($S_b = 0.75$, $S_o = 0.25$, $P_d = 15$ MPa). The stress-sensitivity parameters of Figure 3.3 are used for the sand matrix, while constant velocities and density are assumed for the overlying shale properties ($V_p = 2900$ m/s, $V_s = 1600$ m/s and $\rho = 2.24$ g/cm^3). In this chapter, a mixture of live oil and brine is taken to have the same fluid characteristics and reservoir conditions as those presented in Table 3.5.

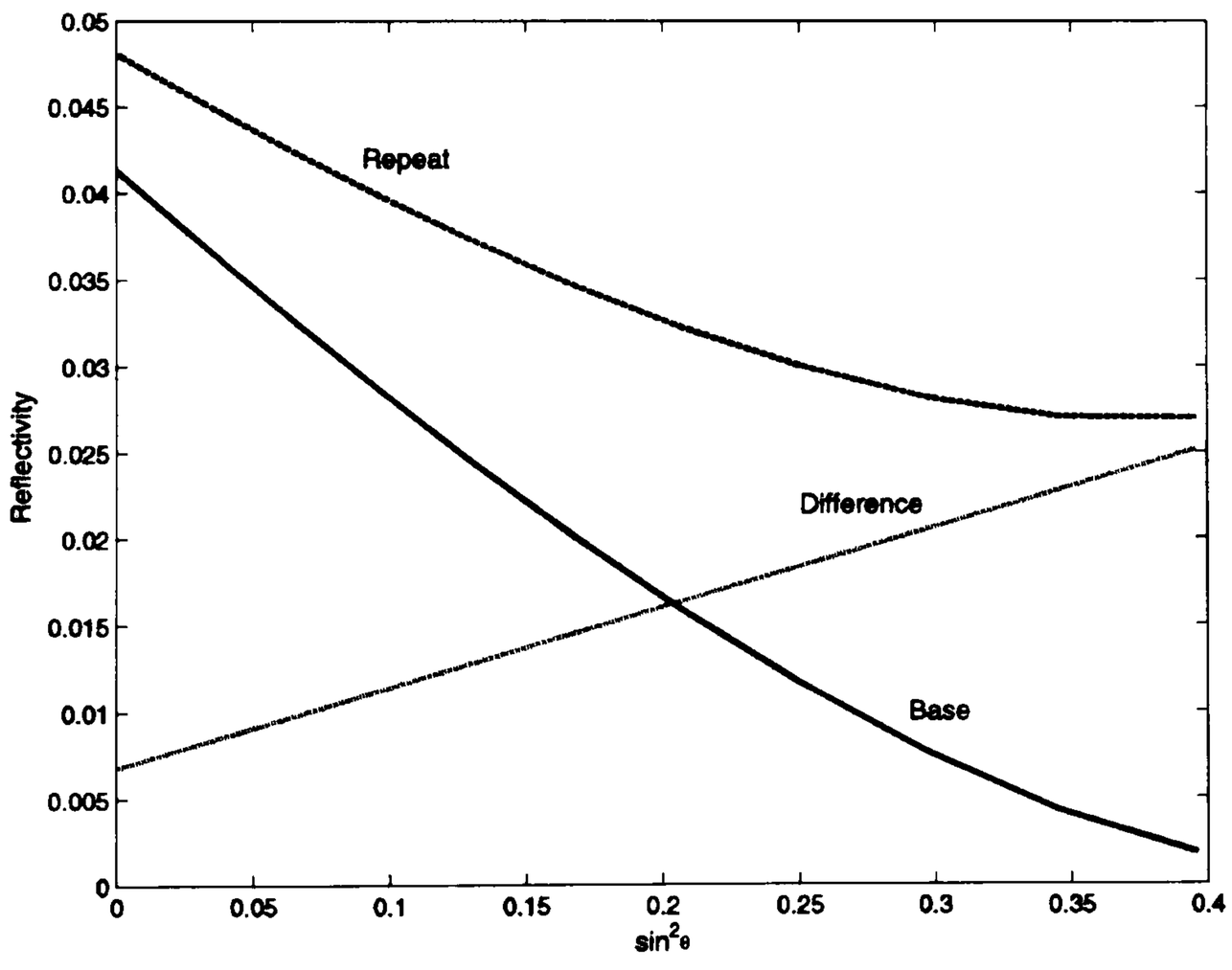

Figure 4.2: Reflectivity for a pre-production case (base: $S_b = 0.25$, $S_o = 0.75$, $P_d = 20$ MPa), and a post-production case (repeat: $S_b = 0.75$, $S_o = 0.25$, $P_d = 15$ MPa). The stress-sensitivity parameters of Figure 3.3 are used in this example. The reflectivity difference between the repeat and base scenarios is also plotted.

A decrease of 5 MPa in differential pressure occurs due to the injection of water. It should be noted that reflectivities for the post-production scenario are larger than the initial case, because of the higher contrast created between shale and brine-bearing sand. The reflectivities in the case of the oil-bearing or brine-bearing sands, both decrease with increasing angle up to 30° ($\sin^2\theta = 0.25$). Above this value, the reduction of the reflectivity eases, because of the third term in equation 4.4. Time-lapse reflectivity is also plotted for the previous example, and it can be observed that the difference between the repeat and base cases increases with offset. It seems that the pressure or fluid effects dominated the 4D signature at large offsets. From the low stress-sensitivity that can be observed in Figure 3.3 between the differential pressures of 20 and 15 MPa, it might be expected that the fluid-saturation effect is the dominating factor. However, the previous remark is only valid for low stress-sensitivity sandstones, since the effect of pressure for high stress-sensitivity rock might not be negligible. Over the last twenty years, numerous AVO approximations have been proposed (Shuey, 1985; Fatti *et al.*, 1994; Verm and Hilterman, 1995), leading to different kinds of hydrocarbon indicators – with the most popular being the intercept and gradient from the two-term AVO approximation of Shuey (1985). AVO cross-plotting has become common practice for highlighting the presence of hydrocarbons, and AVO classifications (Rutherford and Williams, 1989; Castagna and Swan, 1997) have been developed in order to categorize AVO anomalies as a function of sand types. Although AVO inversion is commonly used to extract AVO attributes from seismic data, Cambois (2000) emphasizes the sensitivity of the intercept and gradient to noise, and shows the possible unreliability of AVO attributes. The most damaging types of noise (Cambois, 2001) are: wavelet variation with offset (amplitude and phase); residual normal move-out; NMO stretching; inaccurate estimation of the incidence angle; organized noise (multiples, converted waves); and residual time shifts (i.e. cold-water statics). To obtain quantitative AVO attributes, all types of noise need to be optimally eliminated. Goodway *et al.* (1997) first introduced into AVO analysis, the use of Lamé's parameters: λ, μ and their products with density. The idea was to take full advantage of the physical meaning of those attributes (cf. section 3.3) when compared with the intercept and gradient, to improve lithology and pore-fluid discrimination. Later, Gray *et al.* (1999) reformulated the Aki and Richards

approximations in terms of changes in bulk modulus, Lamé's constants and shear modulus (equations 4.5 and 4.6).

$$R(\theta)=\left(\frac{1}{4}-\frac{1}{3}\gamma\right)(\sec^2\theta)\frac{\Delta\kappa(P,S)}{\overline{\kappa}(P,S)}+\gamma\left(\frac{1}{3}\sec^2\theta-2\sin^2\theta\right)\frac{\Delta\mu(P)}{\overline{\mu}(P)}+\left(\frac{1}{2}-\frac{1}{4}\sec^2\theta\right)\frac{\Delta\rho(P,S)}{\overline{\rho}(P,S)}$$

(4.5)

$$R(\theta)=\left(\frac{1}{4}-\gamma\right)(\sec^2\theta)\frac{\Delta\lambda(P,S)}{\overline{\lambda}(P,S)}+\gamma\left(\frac{1}{2}\sec^2\theta-2\sin^2\theta\right)\frac{\Delta\mu(P)}{\overline{\mu}(P)}+\left(\frac{1}{2}-\frac{1}{4}\sec^2\theta\right)\frac{\Delta\rho(P,S)}{\overline{\rho}(P,S)}$$

(4.6)

where:

$$\Delta\kappa=\kappa_2-\kappa_1$$

$$\Delta\mu=\mu_2-\mu_1$$

$$\Delta\rho=\rho_2-\rho_1$$

$$\overline{\kappa}=\frac{\kappa_1+\kappa_2}{2}$$

$$\overline{\mu}=\frac{\mu_1+\mu_2}{2}$$

$$\overline{\rho}=\frac{\rho_1+\rho_2}{2}$$

$$\gamma=\frac{V_s^2}{V_p^2}$$

$$\lambda=\kappa+\frac{2}{3}\mu$$

κ stands for the bulk modulus, ρ for the density, μ and λ for the Lamé's parameters. Equations 4.5 and 4.6 are more intuitive than equation 4.3, because they express reflection coefficients as a function of the elastic properties of the rock. It can be observed that the second term of the equations 4.5 and 4.6 are only dependent on pressure, while the two other terms are dependent on pressure and saturation. Although physical insight into the reflectivity approximations has increased during recent years and provided the potential to

distinguish between different lithologies and pore fluids (Goodway, 2001), none of the actual AVO attributes are solely dependent on pressure or saturation.

4.1.3 A new AVO approximation

It was shown in the previous chapter that two rock physics attributes could be used to isolate the pressure and saturation effects. Equation 3.21 introduced a new attribute: the saturation modulus, χ_s, dependent only on the pore fluid; along with the shear modulus, μ_d, which is dependent only on the pressure (Ribeiro and MacBeth, 2004). By substituting equation 3.21 into the Aki and Richards approximation (equation 4.3), a new reflectivity relation (equation 4.7) is derived as a function of relative changes in the previous attributes and also density.

$$R(\theta)=\left(\frac{1}{4}-\left(\frac{1}{3}+\frac{b}{4}\right)\gamma\right)(\sec^2\theta)\frac{\Delta\chi(S)}{\overline{\chi}(S)}+\gamma\left(\frac{1}{3}\sec^2\theta-2\sin^2\theta+\frac{b}{4}\sec^2\theta\right)\frac{\Delta\mu(P)}{\overline{\mu}(P)}+\left(\frac{1}{2}-\frac{1}{4}\sec^2\theta\right)\frac{\Delta\rho(P,S)}{\overline{\rho}(P,S)} \tag{4.7}$$

where:

$$\Delta\chi=\chi_2-\chi_1$$

$$\Delta\mu=\mu_2-\mu_1$$

$$\Delta\rho=\rho_2-\rho_1$$

$$\overline{\chi}=\frac{\chi_1+\chi_2}{2}$$

$$\overline{\mu}=\frac{\mu_1+\mu_2}{2}$$

$$\overline{\rho}=\frac{\rho_1+\rho_2}{2}$$

$$\gamma=\frac{V_s^2}{V_p^2}$$

where:

χ stands for the saturation modulus; μ for the shear modulus; ρ for the density; and b for the gradient of the rock physics relationship (equation 3.21).

It should be reiterated that the parameter b is independent of saturation. All relative changes in equation 4.7 are dependent only on pressure ($\Delta\mu/\overline{\mu}$) or saturation ($\Delta\chi/\overline{\chi}$ and $\Delta\rho/\overline{\rho}$). In fact, the relative change of density due to pressure in most consolidated sandstones is generally very small (approximately 1–2% for a dry rock). Therefore, the pressure dependence of the density term can be neglected. Furthermore, the third term in $\Delta\rho/\overline{\rho}$ is generally very small, and is often negligible in comparison with the two other terms. However, pressure or saturation variations might have a non-negligible effect on the density term in unconsolidated and carbonate rocks, which are beyond the focus of this thesis. Figure 4.3 shows a comparison between the reflectivity computed from equations 4.3 and 4.7 for the pre-production scenario of Figure 4.2. One can note that the accordance between the two approximations is good – in the process validating the new AVO formulation (equation 4.7).

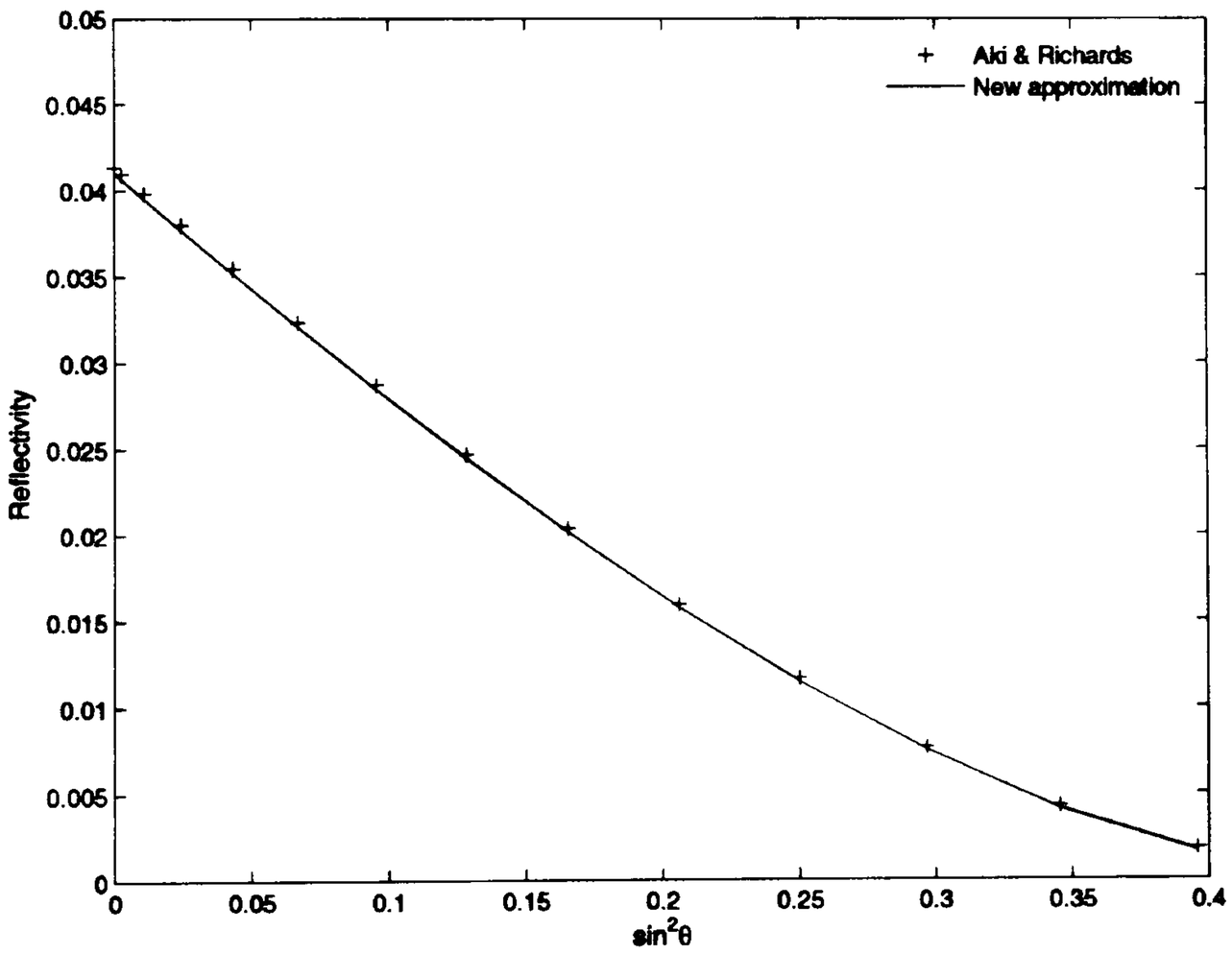

Figure 4.3: Comparison of the reflectivity computed from the Aki and Richards approximation (equation 4.3) and the new approximation (equation 4.7). Reflectivity from the pre-production case of Figure 4.2 shows a good agreement between both approximations.

The sensitivity to pressure and saturation of the reflectivity attributes from equations 4.4, 4.5, and 4.7 is analysed in order to define their discriminating capability. A pre-production scenario (S_b = 0.25, S_o = 0.75, P_d = 15 MPa) is considered, while the oil fraction varies from 0.75 to 0.25 and the differential pressure from 5 to 25 MPa (due to pore pressure changes) in a variety of post-production cases. Changes in time-lapse reflectivity attributes are computed for the different combinations of pressure and oil fraction changes. Figures 4.4, 4.5 and 4.6 show the resulting reflectivity changes cross-plotted as pairs: $\Delta V_s/\overline{V}_s$, $\Delta V_p/\overline{V}_p$, $\Delta\mu/\overline{\mu}$, $\Delta\kappa/\overline{\kappa}$, and $\Delta\mu/\overline{\mu}$, $\Delta\chi/\overline{\chi}$, respectively. It is noteworthy that the orthogonality between $\Delta V_s/\overline{V}_s$ and $\Delta V_p/\overline{V}_p$ in terms of pressure and saturation effects is poor, confirming that these attributes by themselves are not able to discriminate between pressure and saturation effects. In fact, the reflectivities vary with both production effects. On the other hand, an improved separation of pressure and saturation is noticeable on the cross-plot of $\Delta\mu/\overline{\mu}$ versus $\Delta\kappa/\overline{\kappa}$, even if the bulk modulus reflectivity is still dependent on both production effects. By cross-plotting $\Delta\mu/\overline{\mu}$ versus $\Delta\chi/\overline{\chi}$, a high degree of orthogonality is observed between the two reflectivities, meaning that the pressure and saturation effects are focused on two distinct axes. Furthermore, there is a noticeably higher sensitivity of $\Delta\chi/\overline{\chi}$ to saturation as compared to $\Delta\kappa/\overline{\kappa}$. Also apparent is the smaller dependence of $\Delta\chi/\overline{\chi}$ on pressure as compared to $\Delta\kappa/\overline{\kappa}$. The new formulation (equation 4.7) offers the opportunity to invert for the reflectivity of the shear modulus and saturation modulus, which emerge as the optimal seismic attributes to separate the pressure and saturation effects.

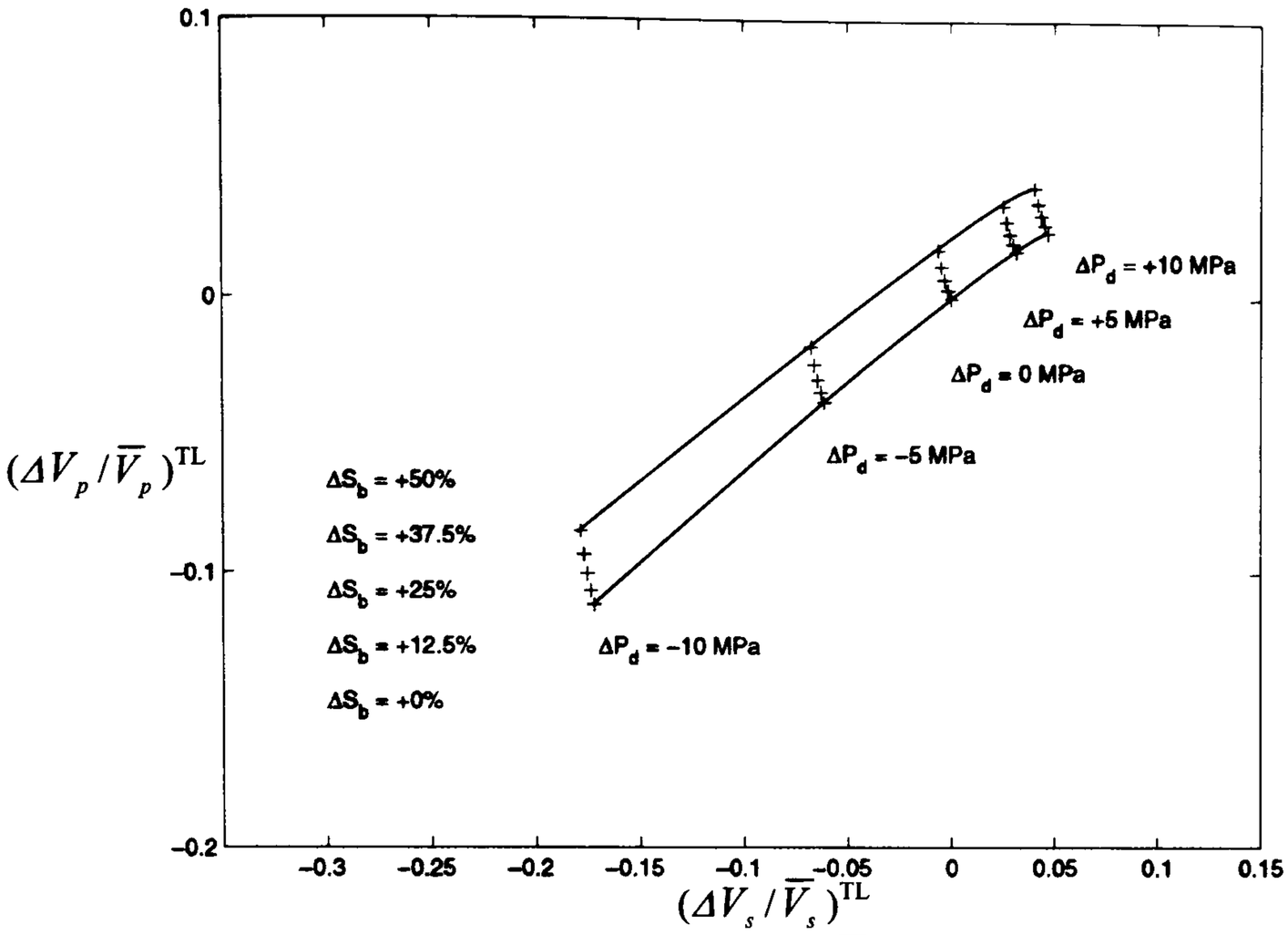

Figure 4.4: Analysis of the time-lapse P-wave $(\Delta V_p / \overline{V}_p)^{TL}$ and S-wave $(\Delta V_s / \overline{V}_s)^{TL}$ reflectivity dependence on pressure and saturation effects. An initial differential pressure of 15 MPa and an oil saturation of 75% are assumed. Changes in brine saturation, ΔS_b, and differential pressure, ΔP_d, are plotted.

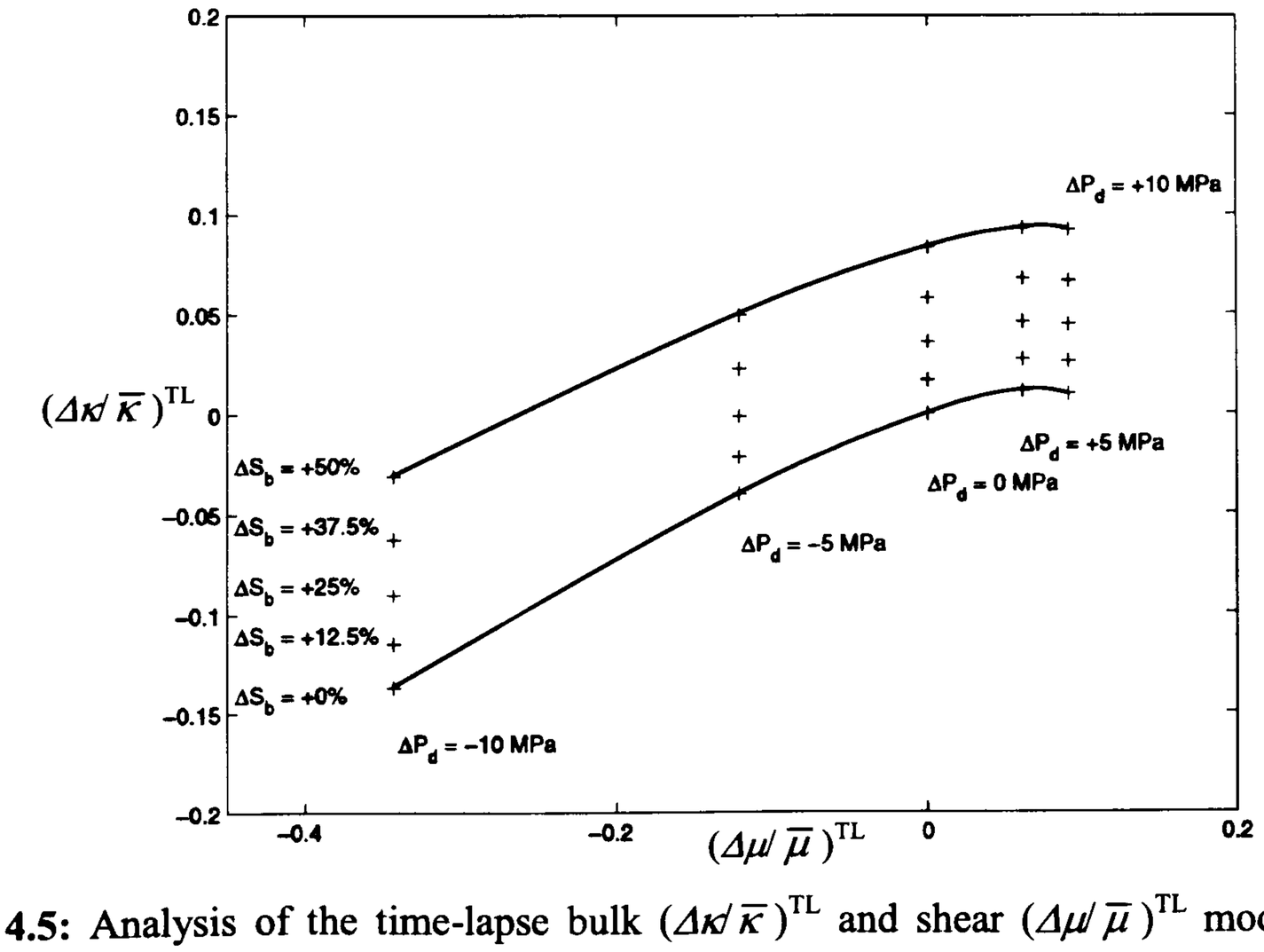

Figure 4.5: Analysis of the time-lapse bulk $(\Delta\kappa / \overline{\kappa})^{TL}$ and shear $(\Delta\mu / \overline{\mu})^{TL}$ modulus reflectivity dependence on pressure and saturation effects. An initial differential pressure of 15 MPa and an oil saturation of 75% are assumed. Changes in brine saturation ΔS_b and differential pressure ΔP_d are plotted.

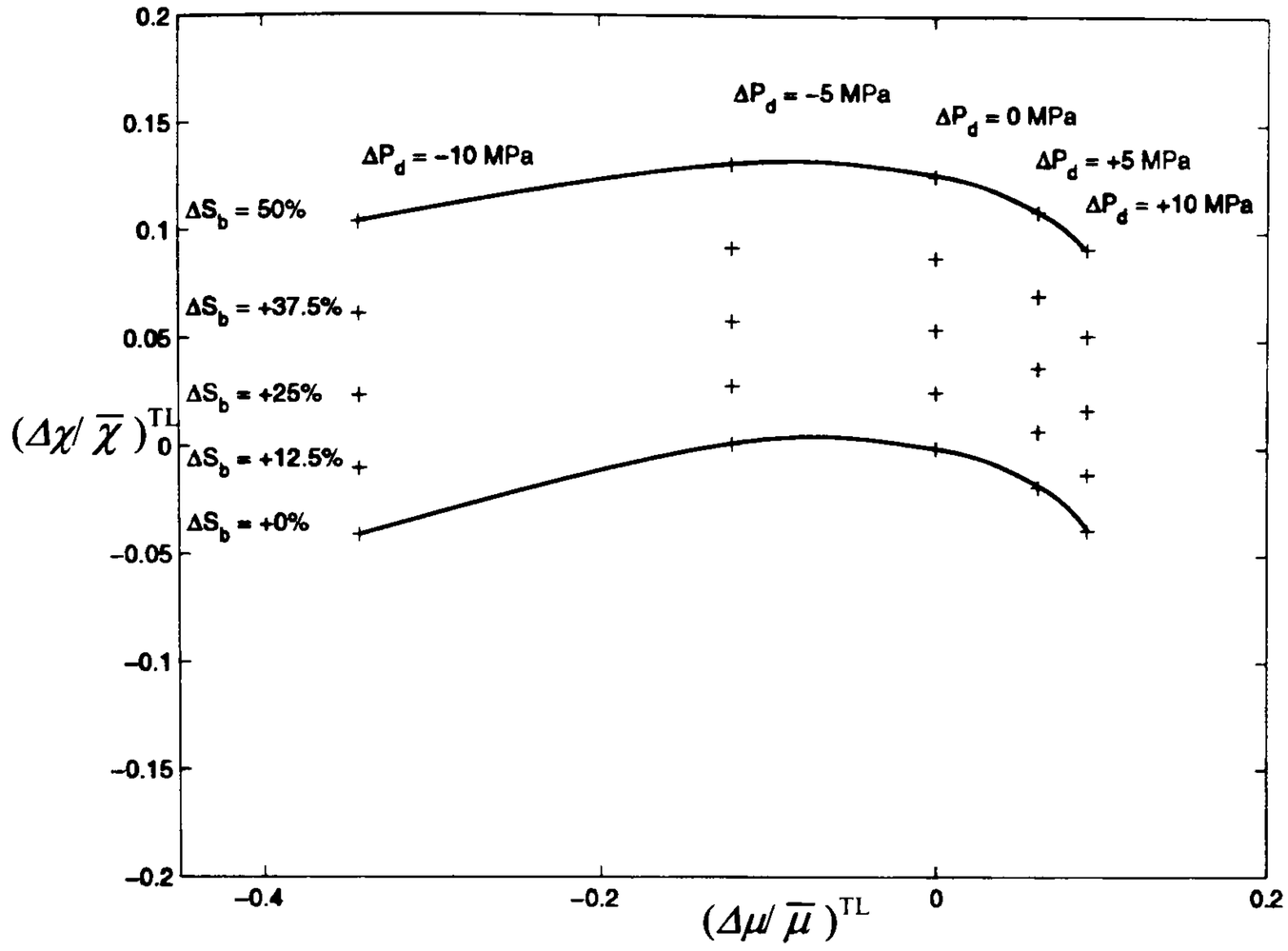

Figure 4.6: Analysis of the time-lapse saturation $(\Delta\chi/\overline{\chi})^{TL}$ and shear $(\Delta\mu/\overline{\mu})^{TL}$ modulus reflectivity dependence on pressure and saturation effects. An initial differential pressure of 15 MPa and an oil saturation of 75% are assumed. Changes in brine saturation ΔS_b and differential pressure ΔP_d are plotted.

4.2 Elastic impedance

It is shown (in equation 4.2) that the amplitudes of zero offset and intercept stacks relate to change in acoustic impedance (AI). Acoustic impedance values can be used to predict lithology and fluid content. However, with acoustic impedance only, it can be difficult in some cases to distinguish between different lithologies, for example, oil-bearing sand and brine-bearing sand show similar responses to acoustic impedance (Figure 4.7). In fact, acoustic impedance changes by 3% from oil- to brine-saturated sands. For real data, such a small change might not be distinguishable from the background noise of the seismic. Connolly (1999) developed the theoretical concept of elastic impedance (EI), which represents an extension of acoustic impedance at non-normal offset. Elastic impedance is a function of P-wave velocity, S-wave velocity, density, and incidence angles (equation 4.8).

$$EI(\theta) = V_p^{a1} V_s^{a2} \rho^{a3} \tag{4.8}$$

where:

$$\gamma = V_s^2 / V_p^2$$

$$a_1 = (1 + \tan^2 \theta)$$

$$a_2 = -8\gamma \sin^2 \theta$$

$$a_3 = (1 - 4\gamma \sin^2 \theta)$$

To relate seismic to elastic impedance, the stacked data must be some form of angle stack, rather than a constant range of offsets. This approach makes it possible to assess the AVO information in the data, and to determine elastic parameters that are more sensitive to fluid content than those using the normal offset. Figure 4.7 shows that elastic impedance has the potential to discriminate between oil-bearing sand and brine-bearing sand. Changes in impedance due to fluid substitution increase linearly with offset in this oil/brine example. A variation in brine saturation of 50% generates a change of 18% in elastic impedance at 30°, compared to the 3% previously mentioned at zero offset. This aspect of elastic impedance was first exploited to image pore fluid during the appraisal and development of the Foinaven field, west of Shetland.

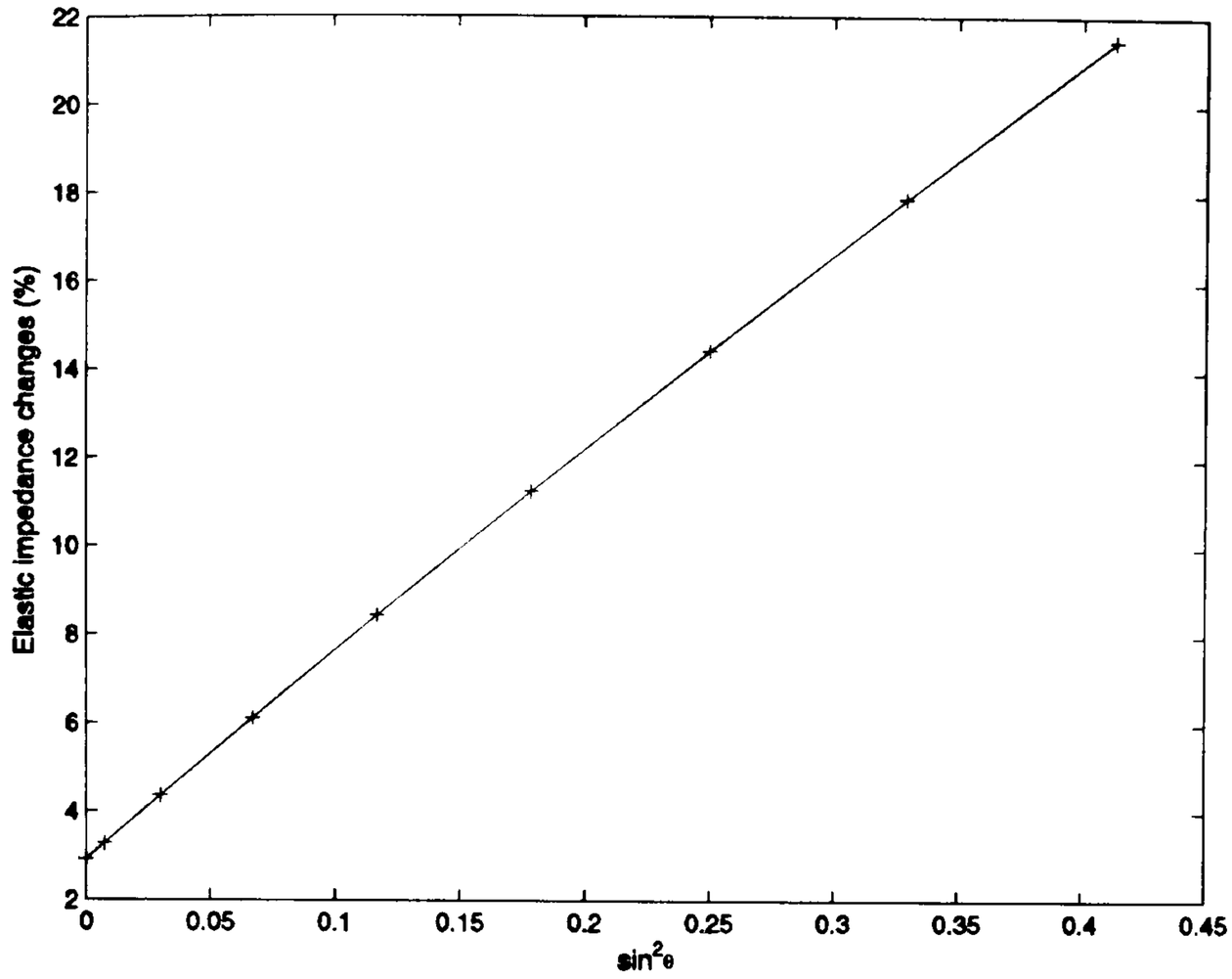

Figure 4.7: Time-lapse elastic impedance changes as a function of angle between a pre-production scenario ($S_b = 0.25$, $S_o = 0.75$, $P_d = 20$ MPa) and a post-production scenario ($S_b = 0.75$, $S_o = 0.25$, $P_d = 20$ MPa). A linear increase of elastic impedance changes with incidence angle is observed.

It can be observed that, by definition, the dimension of elastic impedance is angle dependent and will vary significantly from near to far offsets. To overcome this feature, different reflectivity approximations can be used (Verwest *et al.*, 2000), or a simple normalization can be applied to the elastic impedance formulation (Whitcombe, 2002). Normalized elastic impedance (NEI) takes the form shown by equation 4.9, and has the same dimensions as acoustic impedance.

$$NEI(\theta) = V_{p0}\rho_0\left[\left(\frac{V_p}{V_{p0}}\right)^{a1}\left(\frac{V_s}{V_{s0}}\right)^{a2}\left(\frac{\rho}{\rho_0}\right)^{a3}\right] \tag{4.9}$$

where V_{p0}, $V_{s0,}$ and ρ_0 stand for the reference P-wave velocity, S-wave velocity, and density, respectively. The exponent coefficients a_1, a_2 and a_3 are the same as those in equation 4.8. The reservoir cap rock – or even a type of sand – can be chosen as the

reference, depending on the purpose of the normalized elastic impedance analysis. Equation 4.9 allows the comparison of elastic impedance between various angles, which facilitates their interpretation. In an effort to improve lithology and fluid discrimination, Whitcombe *et al.* (2002) extended the work of Connolly by proposing a new form of elastic impedance, called the extended elastic impedance (EEI). By substituting $\tan\psi$ for $\sin^2\theta$ in equation 4.8, the conventional elastic impedance values can be extrapolated outside the physical range of $\sin^2\theta$, since the new variable ψ varies from –90° to +90°. EEI takes the following form after normalization:

$$NEEI(\psi) = V_{p0}\rho_0\left[\left(\frac{V_p}{V_{p0}}\right)^p\left(\frac{V_s}{V_{s0}}\right)^q\left(\frac{\rho}{\rho_0}\right)^r\right] \tag{4.10}$$

where:

$p = (\cos\psi + \sin\psi)$,

$q = -8\gamma\sin\psi$,

$r = (\cos\psi - 4\gamma\sin\psi)$,

$\tan\psi = \sin^2\theta$

Figure 4.8 presents an illustration of the use of EEI, where two seismic attribute maps corresponding to specific values of ψ are derived for the top reservoir of the Forties field, Central North Sea. The first map (left), labelled 'lithological impedance', relates to the shear modulus and emphasizes the depositional features of the reservoir. Sand channels can be clearly delineated. The second map (right), labelled 'fluid impedance', relates to the bulk modulus, and images the fluid properties within the channels.

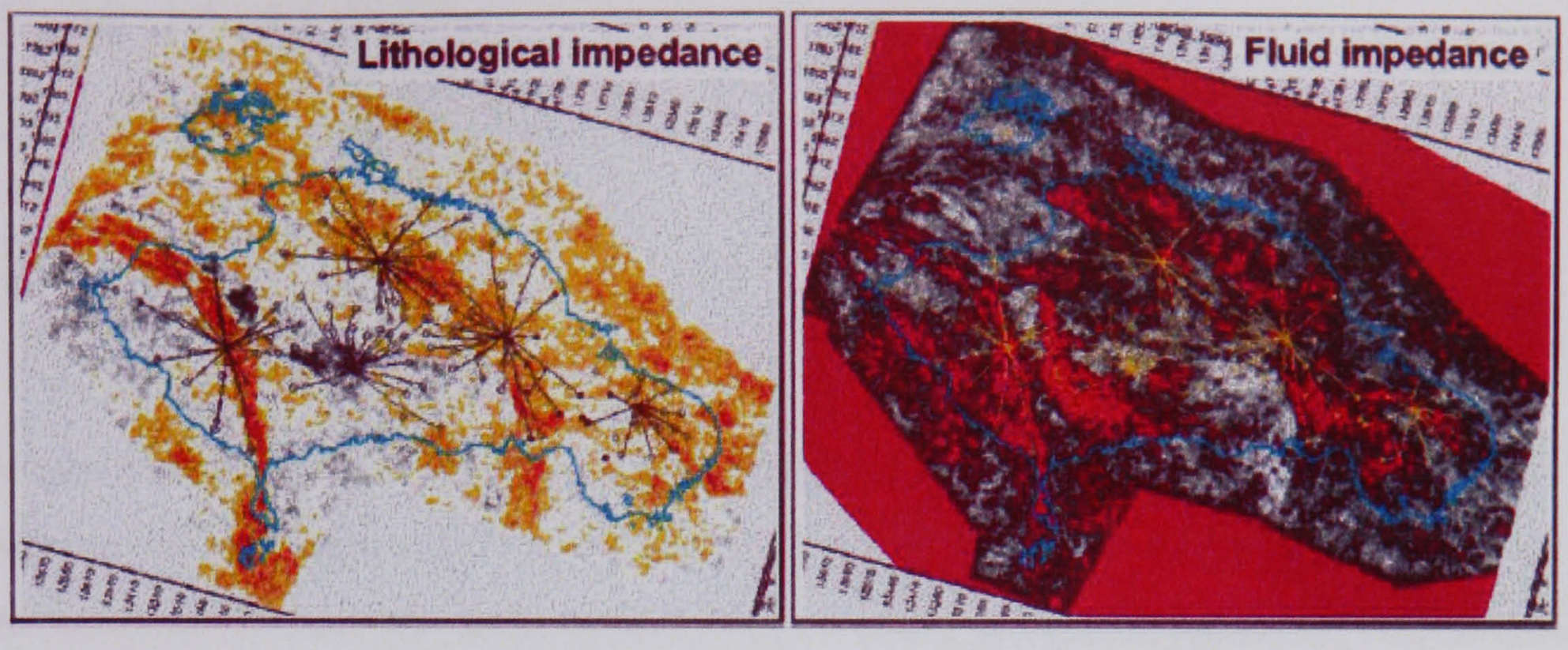

Figure 4.8: Bulk (fluid impedance) and shear (lithological impedance) modulus maps generated using EEI formulation for ψ= 12.4° and ψ=-51.3° , respectively. These maps were computed over a 25-ms window for the top reservoir in the Forties field, Central North Sea (from Whitcombe *et al.*, 2002).

Goodway (2001) introduced a qualitative lithology and fluid discrimination technique, based on the interpretation of suitable seismic attributes (i.e. $\mu\rho$ and $\lambda\rho$). He derived a Lamé formulation for elastic impedance, and defined elastic properties by appropriate combination of these impedances at different angles. Thanks to elastic impedance, absolute values of elastic parameter are accessible, which simplify the interpretation of seismic data. Following the approach of Connolly, the reflectivity equations presented in the previous section can also be expressed in an elastic impedance form. The new elastic impedance formulation (equation 4.11), called fluid elastic impedance (FEI), allows the estimation of elastic parameters, depending only on pressure or fluid saturation (Ribeiro and MacBeth, 2004).

$$FEI(\theta) = \chi^{c_1} \mu^{c_2} \rho^{c_3} \tag{4.11}$$

$$c_1 = \left[\frac{1}{2} - \left(\frac{2}{3} + \frac{b}{2}\right)\gamma\right]\sec^2\theta$$

$$c_2 = \gamma\left(\frac{2}{3}sec^2\,\theta - 4\,sin^2\,\theta + \frac{b}{2}sec^2\,\theta\right)$$

$$c_3 = \left(1 - \frac{1}{2}\sec^2\theta\right)$$

where χ stands for the saturation modulus; μ the shear modulus; ρ the density; and γ the inverse of the squared velocity ratio as defined in equation 4.8. This new formulation can be normalized in the same way as equation 4.9, in order to homogenize the dimension to a reference impedance (equation 4.12).

$$NFEI(\theta) = FEI_{ref}\left[\left(\frac{\chi}{\chi_0}\right)^{c_1}\left(\frac{\mu}{\mu_0}\right)^{c_2}\left(\frac{\rho}{\rho_0}\right)^{c_3}\right] \tag{4.12}$$

where χ_0, μ_0, ρ_0, and FEI_{ref} stand for the reference saturation modulus, shear modulus, density, and impedance, respectively. The parameters c_1, c_2, and c_3 refer to the exponent coefficients of equation 4.12. An insight into the effect of pressure and saturation changes on elastic impedance can be gained by plotting the exponent coefficients of equations 4.8 and 4.12 against incidence angles. In fact, from Figure 4.9, the effect of pressure and saturation cannot be interpreted, since the S-wave and P-wave velocities both depend on these effects. It can be noted that elastic impedances are dominated by P-wave velocity, and only at a large incidence angle does S-wave velocity contribute to the elastic impedance values. The contribution of the density decreases with increasing incidence angles. However, from Figure 4.10, the pressure and saturation changes can be interpreted via the exponent coefficients c_2 and c_1 of the shear and saturation moduli. The exponent coefficient of the saturation modulus increases with incidence angles, meaning that the effect of saturation is prominent at large incidence angles. On the other hand, the exponent coefficient for the shear modulus decreases with incidence angle, meaning that the effect of

pressure is prominent at small incidence angles, even if the saturation dependence from γ will slightly affect this coefficient. The contribution of the density decreases with incidence angle. From Figure 4.10, the significance of pressure and saturation effects as a function of incidence angles is illustrated thanks to equation 4.10. These conclusions are also valid for the angle-dependent coefficients of the reflectivity equations 4.3 and 4.7, since these coefficients are a scaled version of the elastic impedance ones.

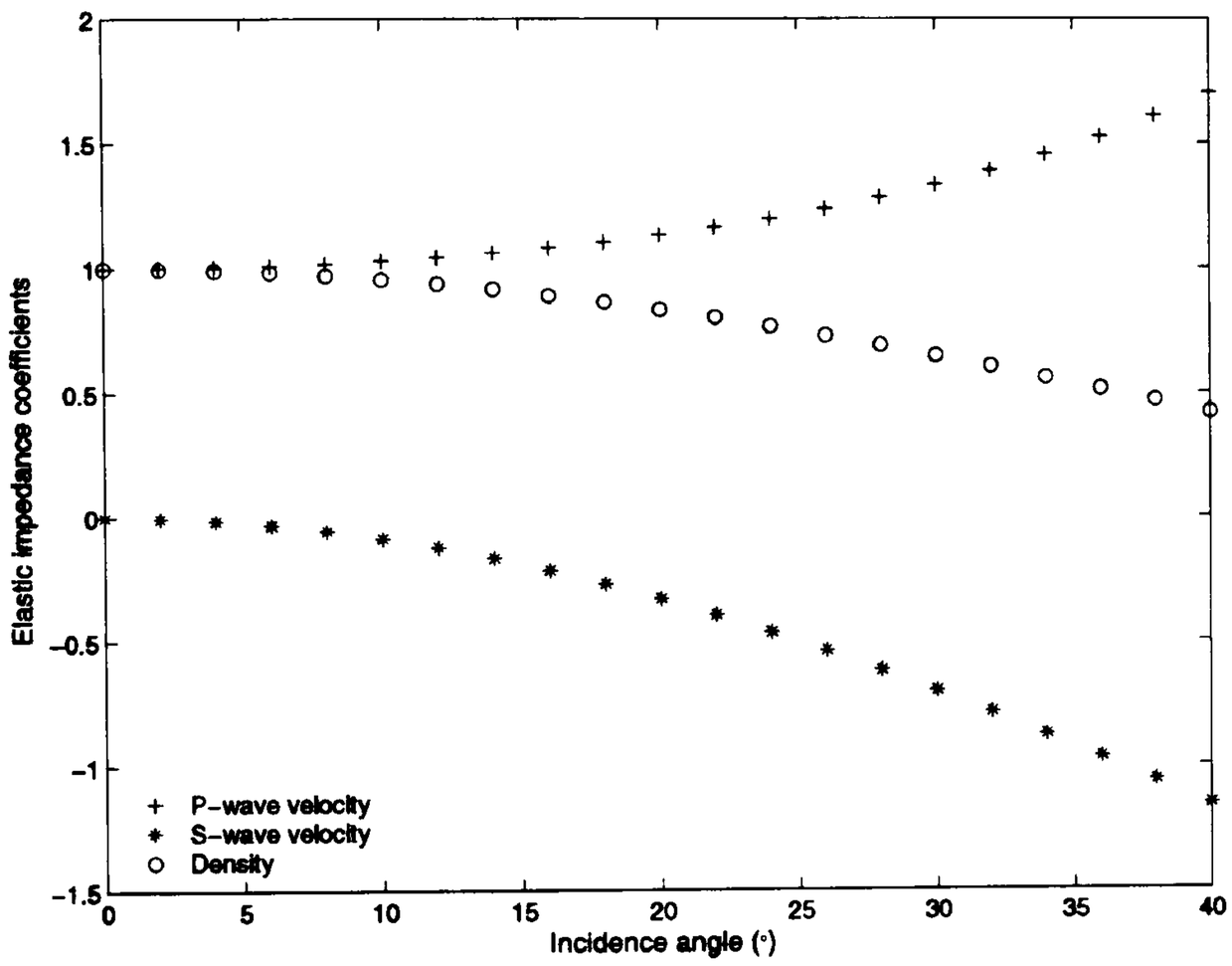

Figure 4.9: Exponent coefficients of equation 4.8, plotted against incidence angles. An average value of γ is assumed for the reservoir formation.

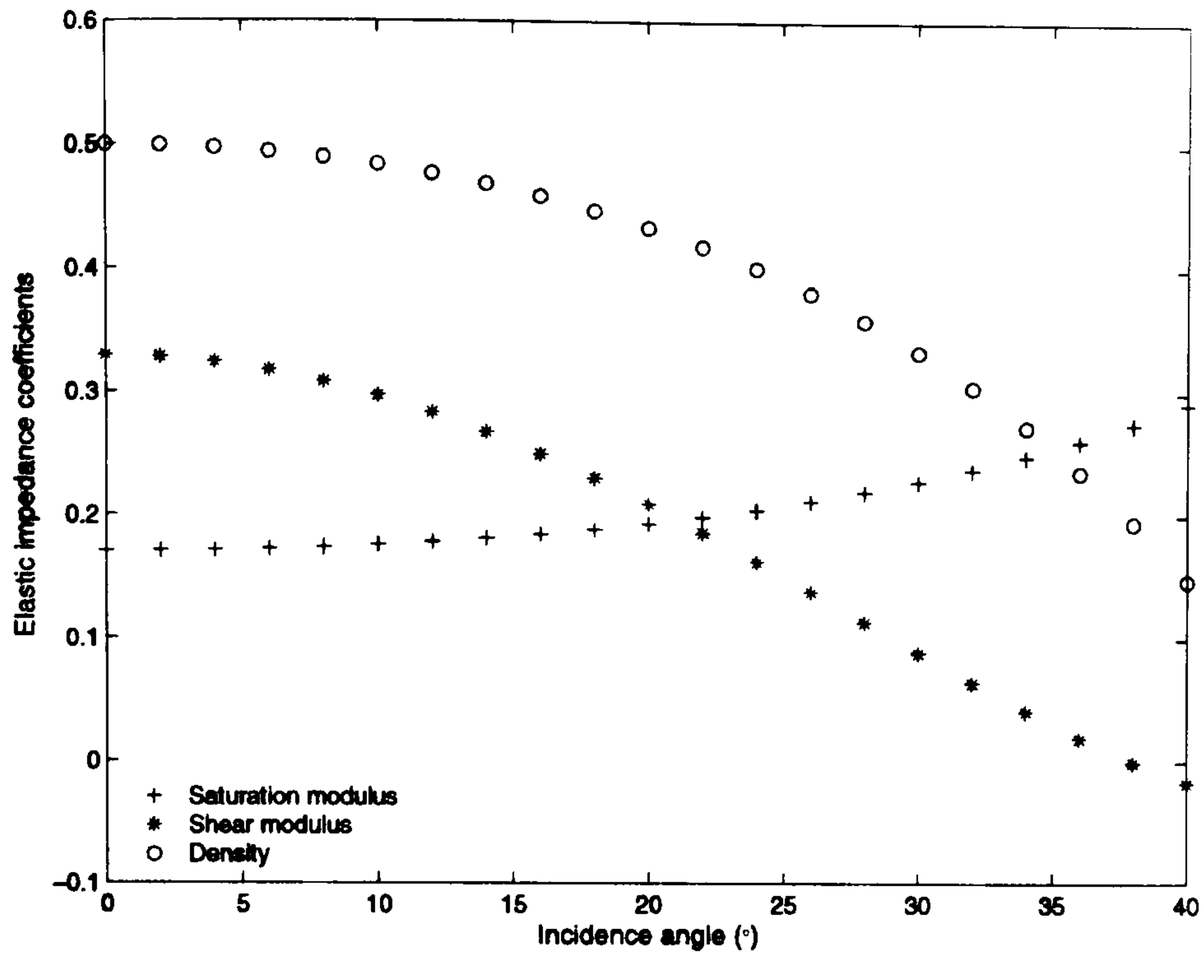

Figure 4.10: Exponent coefficients of equation 4.11, plotted against incidence angles. An average value of γ is assumed for the reservoir formation. The pressure effect appears to dominate at near angles while saturation effect takes over at the far angles.

Elastic impedance inversion is extremely popular because it simplifies the interpretation of production effects but also offers some solutions to the problems encountered by AVO analysis. For example, elastic inversion is less sensitive to misalignment and wavelet variations. In fact, EI inversion, and especially layer-based stratigraphic inversion (Gluck *et al.*, 1997), can be an alternative to AVO inversion. The process of inversion, which allows conversion of reflection amplitudes into absolute impedance values, has brought new benefits. The 3D elastic impedance volumes have a broader bandwidth that improves vertical resolution compared to seismic data. The integration of petrophysical properties and elastic impedance volumes can be more intuitive when used to support static or dynamic reservoir simulation. In Chapter 6, the process of elastic impedance inversion from seismic data will be fully covered and applied to real data.

4.3 Pressure and saturation effects on time-lapse data

To illustrate the combined effect of pressure and saturation changes due to hydrocarbon production on repeated seismic data, 1D petro-elastic modelling is carried out on a synthetic well design from a well of the Foinaven field, west of Shetland (Figure 4.11). The model is composed of two sand units: an upper reservoir situated between 2278 and 2322 ms, and a lower reservoir situated between 2352 and 2378 ms. Hydrocarbon is produced from the top reservoir, while water is injected in the lower reservoir. The layer of shale between the two sands is sealing. Two brine saturation and pressure profiles are used in order to mimic two different reservoir production stages. The upper reservoir shows an increase of brine saturation, due to the production of oil in the upper part of the sand. Differential pressure increases by 10 MPa, due to pore pressure depletion. The lower reservoir initially contained 25% of connate water, and brine saturation increases to 65% after water injection. The differential pressure drops by 10 MPa, due to an increase in pore pressure. It should be noted that the elastic impedance displayed in the following section corresponds to elastic impedance normalized using the upper oil sand at 15 MPa differential pressure as a reference. As before, the stress-sensitivity parameters of Figure 3.3 are used for the sand matrix, while constant velocities and density are assumed for the overburden and underburden shale properties (V_p = 2900 m/s, V_s = 1600 m/s and ρ = 2.24 g/cm^3).

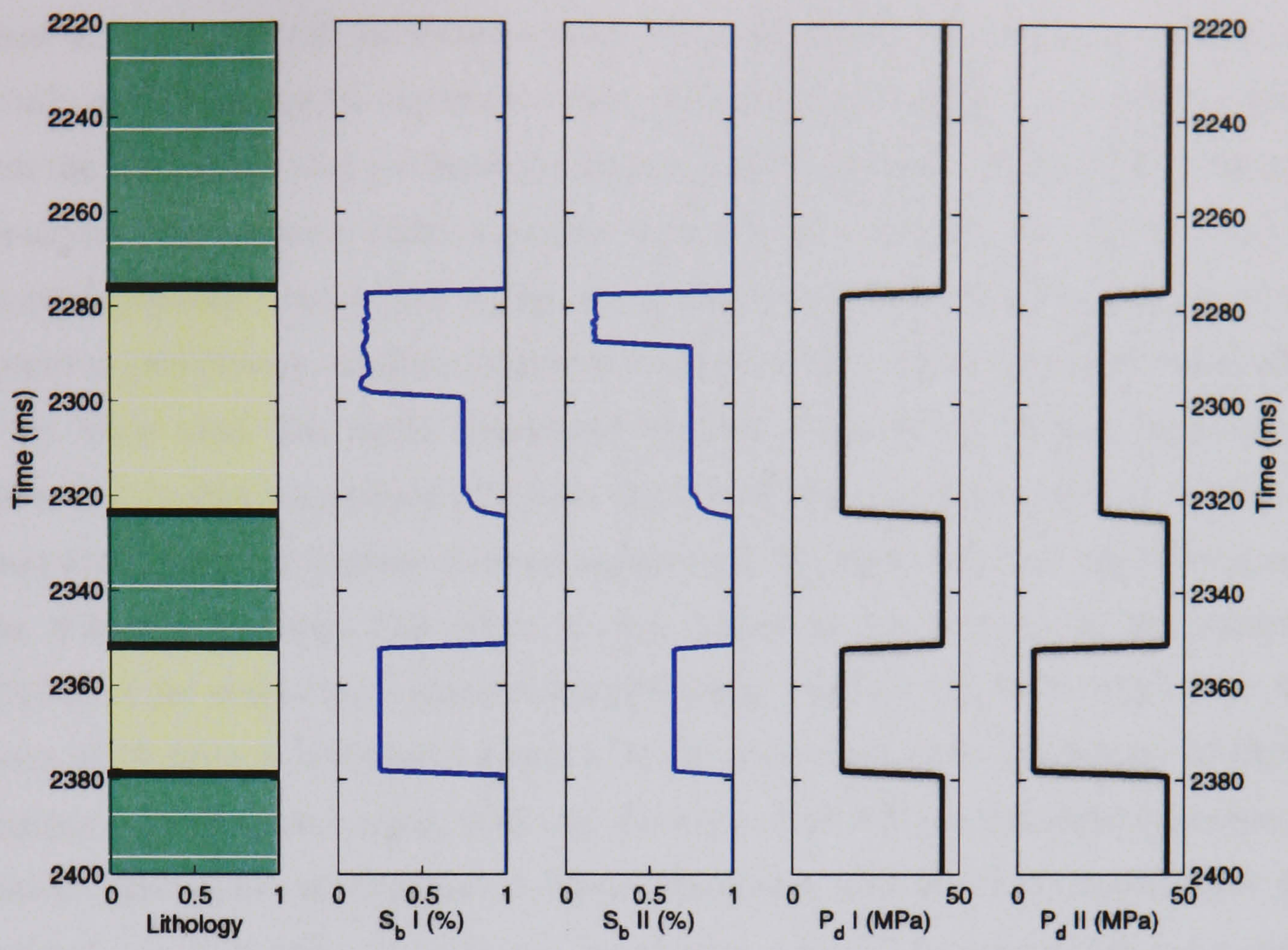

Figure 4.11: Characteristics of the synthetic well used for the 1D petro-elastic modelling. Logs are displayed in the following order, from left to right: lithology (green: shale, yellow: sand); brine saturation pre-production (S_b I); brine saturation post-production (S_b II); differential pressure pre-production (P_d I); and differential pressure post-production (P_d II). Connate water is set to 20% and 25%, and residual oil saturation is set to 25% and 35% in the upper and lower sand, respectively.

4.3.1 Time-lapse seismic signatures

Three scenarios (pressure changes only, saturation changes only and pressure/saturation changes) are considered in an effort to highlight the separate and combined effects of pressure and saturation variations in a reservoir. Figure 4.12 and Figure 4.13 present the resulting seismic and elastic impedance gathers in the case where only pressure changes are assumed. For both the base and repeated seismic gathers, the two reservoir units show a decrease or an increase of reflectivity with incidence angles, at the top and base sands, respectively. Furthermore, the oil–water contact is clearly visible and shows a slight

increase of amplitude with incidence angles. It can be seen on the time-lapse difference, especially at the near angles, that the increase of differential pressure in the upper reservoir stiffens the sand matrix and increases (or decreases) the amplitude at the top (or bottom) of the reservoir. The opposite effect is visible in the lower sand unit, due to a decrease of differential pressure. Due to the higher stress-sensitivity of sandstone to pressure-down compared to pressure-up, smallest amplitude changes can be noted in the upper sand rather than the lower sand. The elastic impedance displays (Figure 4.13) confirm the previous observations. In fact, an increase of elastic impedance with incidence angles is visible for the base case, due to an increase in brine saturation in the upper and lower sands compared to the reference oil-sand. This effect is also related to the increase in the exponent coefficient of the saturation modulus noted previously (Figure 4.10). In the repeat case, the increase of 10 MPa in differential pressure in the upper sand causes a decrease of elastic impedance with incidence angle, while the decrease of 10 MPa in differential pressure in the lower sand shows an increase of elastic impedance with incidence angle. Since the reference is set to 15 MPa, the term μ/μ_0 in equation 4.12 will be greater than unity in the upper sand and lower than unity in the lower sand, explaining the variations of impedance with incidence angle observed previously. The elastic impedance difference shows that impedance changes are larger in the lower sand compared to the upper sand. These results are expected, since the magnitude of the shear modulus decrease in the lower sand is much larger than its increase in the upper sand. It appears, as stated in the previous section 4.2, that pressure changes are less observable at large incidence angles.

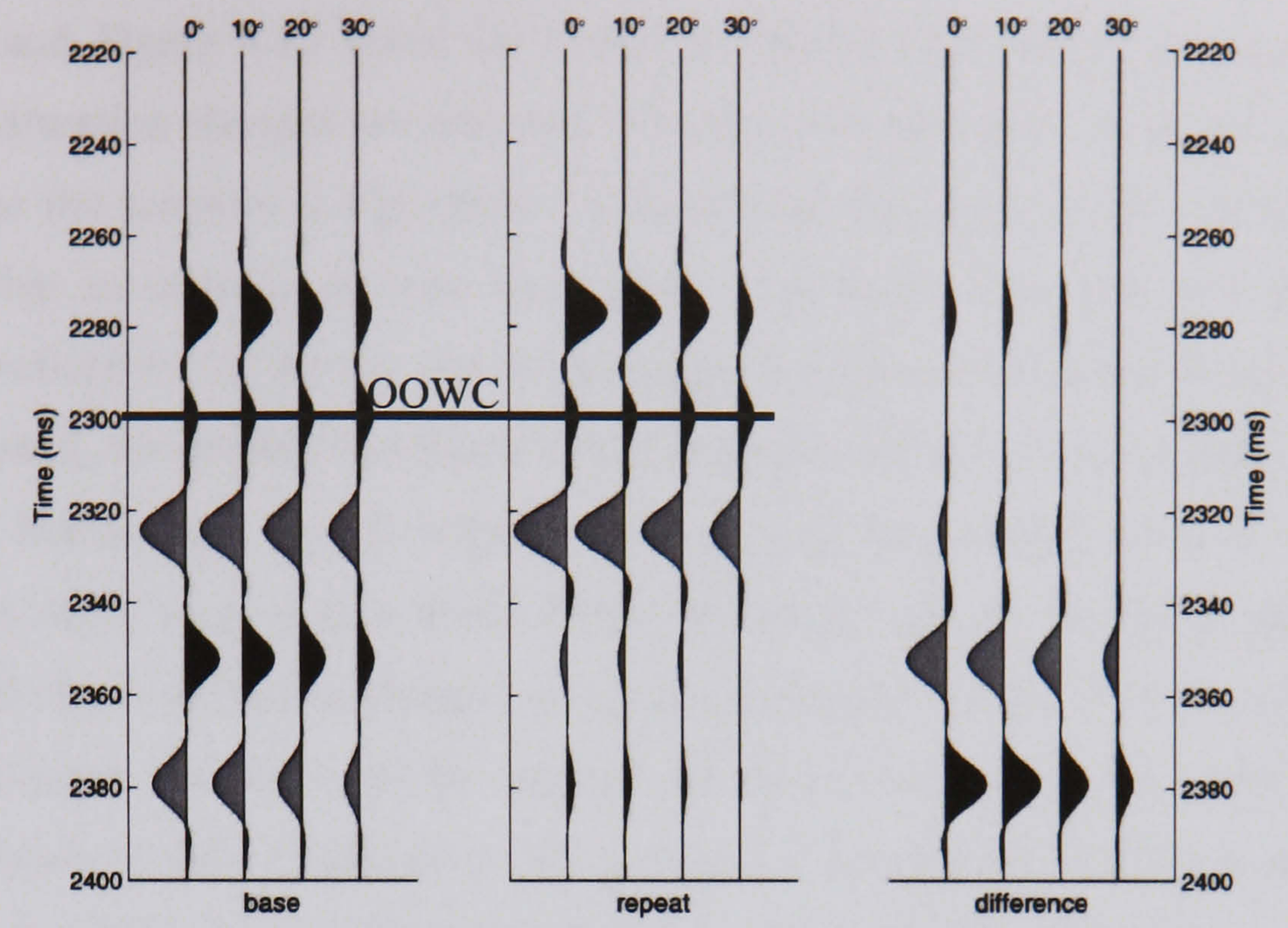

Figure 4.12: Synthetic seismic gathers for the base (pre-production) and repeat (post-production) scenario. Only pressure variations are taken into account, and the saturation profile S_b I (Figure 4.11) is considered. The base, repeat and difference gathers are displayed from left to right. For each gather, four different incidence angles are presented, from 0 to 30 degrees.

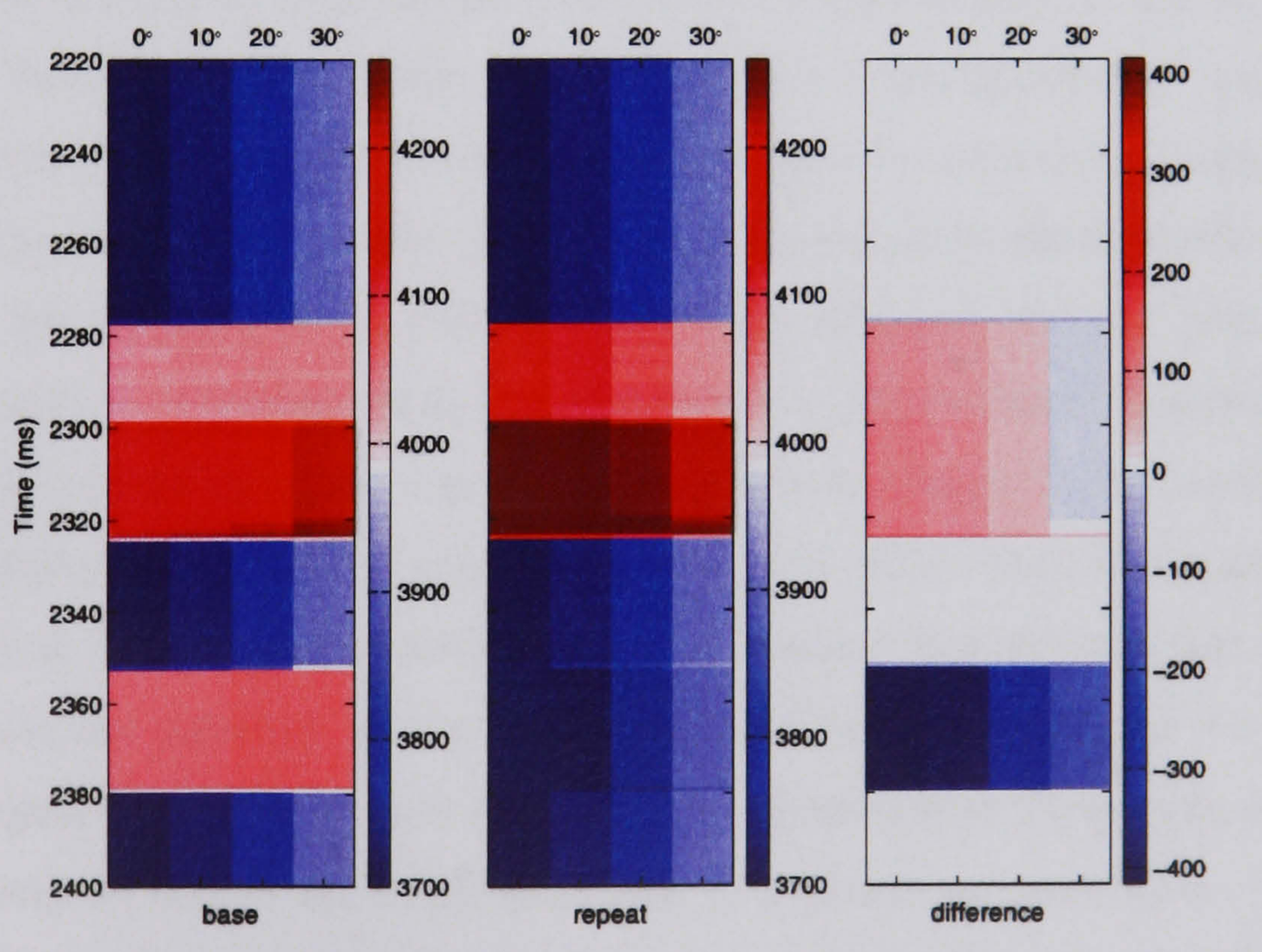

Figure 4.13: Synthetic elastic impedance gathers for the base (pre-production) and repeat (post-production) scenario. Only pressure variations are taken into account, and the saturation profile S_b I (Figure 4.11) is considered. The base, repeat and difference gathers are displayed from left to right. For each gather, four different incidence angles are presented, from 0 to 30 degrees.

Figure 4.14 and Figure 4.15 show the synthetic seismic and elastic impedance gathers where only saturation changes are assumed. The observations for the base case remain the same, because the scenario is equivalent to the previous example. In the repeat case, it is noteworthy that an increase in brine saturation in the lower sand increases the absolute value of the reflectivity at the top and bottom reservoir, but preserves the AVO behaviour. In the upper sand, the upward movement of the brine phase results in the interference of the top reservoir horizon and the oil–water contact, an interference that could be difficult to interpret from static seismic data alone. However, on the seismic amplitude difference, it can clearly be observed that no changes occur at the top and bottom of the upper sand, and that the time-lapse signatures of the original (OOWC) and moved oil–water (MOWC) contact are clearly visible. Furthermore, the increase of the absolute amplitude in the lower sand increases slightly with incidence angles. The elastic impedance displays, especially the elastic impedance difference (Figure 4.15), show that the effect of the brine saturation increases with incidence angles. This observation is in accordance with the behaviour of the saturation modulus exponent in Figure 4.10. From these two previous illustrations of the separate effects of pressure and saturation on seismic measurements, it can be concluded that the new formulation for elastic impedance offers a straightforward way to relate changes in shear and saturation modulus with changes in reflectivity amplitudes and impedances. The interpretation of the AVO behaviour in term of production effects is better defined. The last scenario deals with the combined effect of pressure and saturation changes. The seismic amplitude difference in Figure 4.16 shows that 4D signatures appear at the top and bottom of the upper sand due to the pressure changes. In the lower sand, the effects of pressure and saturation compete against each other. The 4D signature at low angles appears to be due to a smaller change of pressure than the one that is actually occurring, while the signature at the high angles vanishes. Interpretation of the elastic impedance (Figure 4.17) also leads to the same biased conclusion. Time-lapse data can be difficult to interpret, due to the combined effect of pressure and saturation – especially when these effects compete against each other. Also, it is apparent that the pore pressure depletion scenario might be difficult to observe if the rock is initially at a high differential pressure.

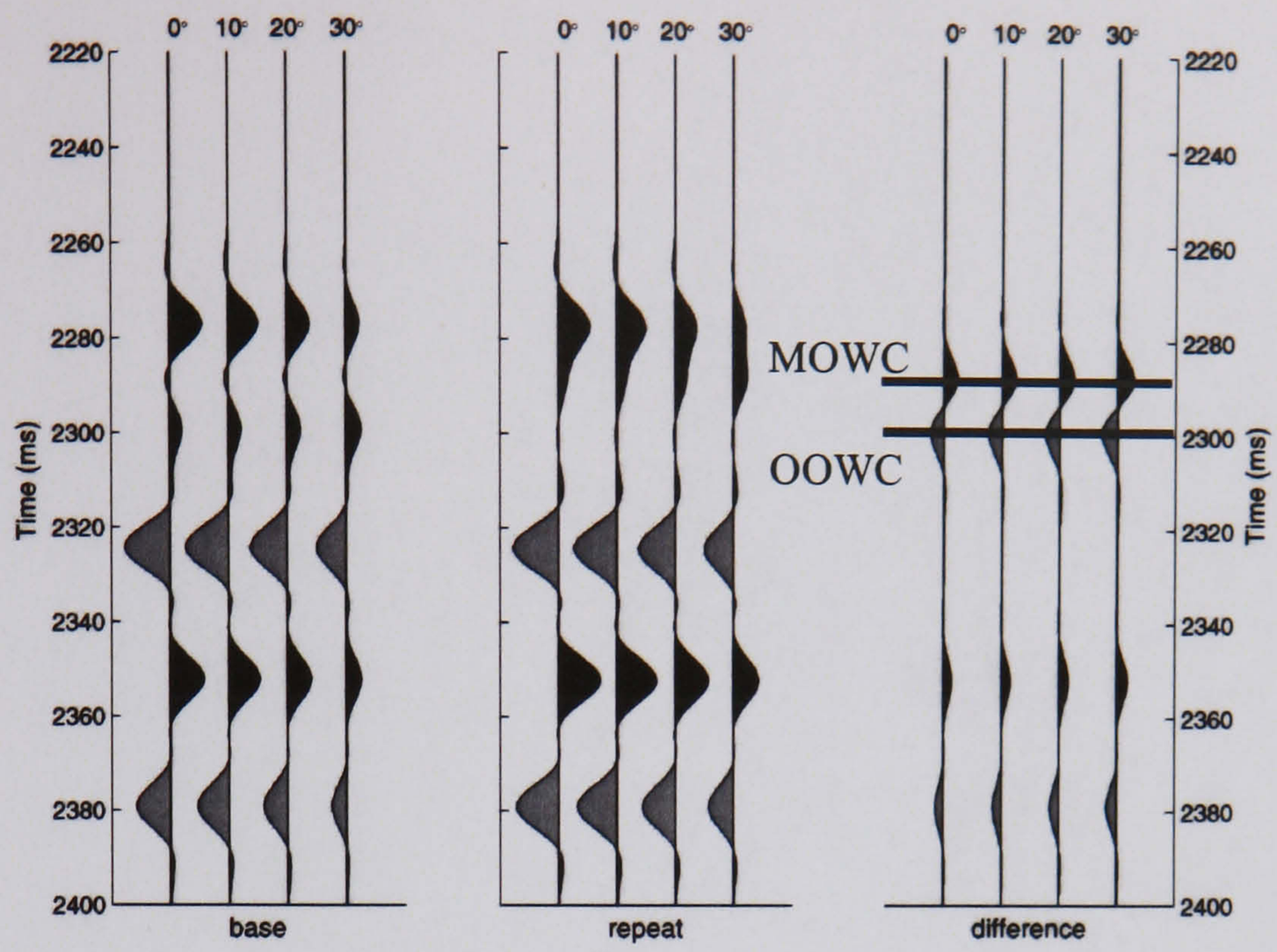

Figure 4.14: Synthetic seismic gathers for the base (pre-production) and repeat (post-production) scenario. Only saturation variations are taken into account, and the pressure profile P_d I (Figure 4.11) considered. The base, repeat and difference gathers are displayed from left to right. For each gather, four different incidence angles are presented, from 0 to 30 degrees.

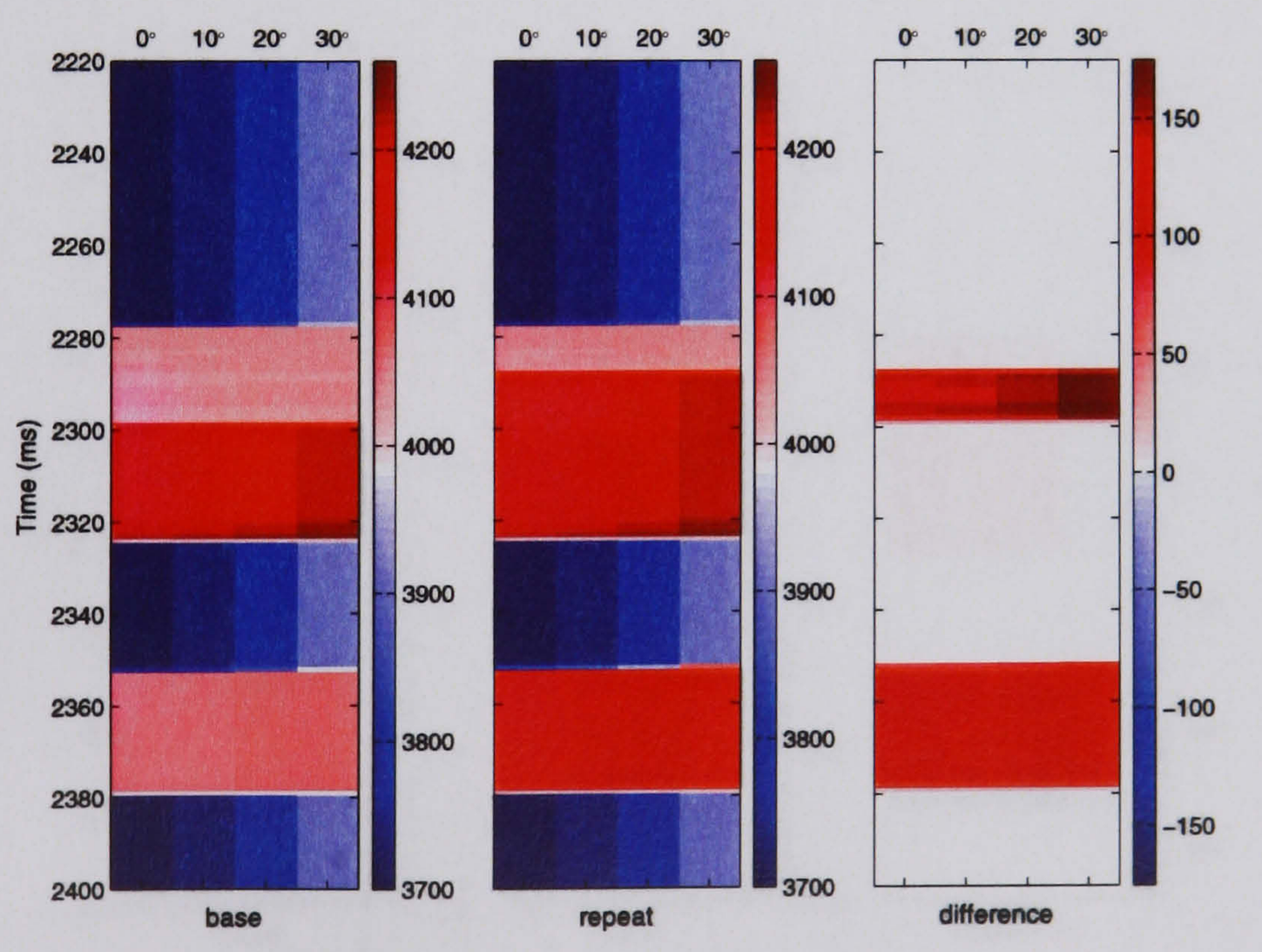

Figure 4.15: Synthetic elastic impedance gathers for the base (pre-production) and repeat (post-production) scenario. Only saturation variations are taken into account, and the pressure profile P_d I (Figure 4.11) considered. The base, repeat and difference gathers are displayed from left to right. For each gather, four different incidence angles are presented, from 0 to 30 degrees.

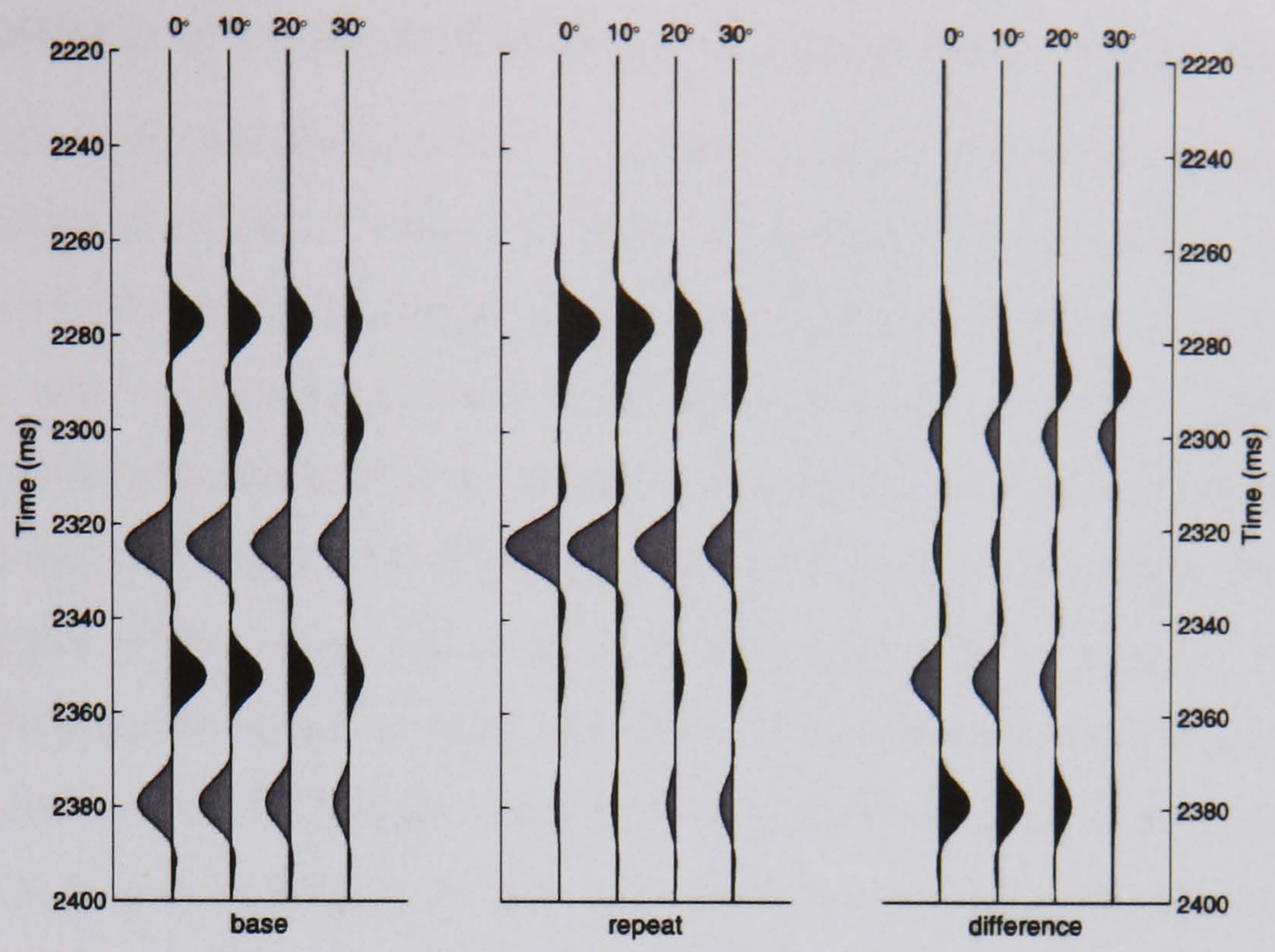

Figure 4.16: Synthetic seismic gathers for the base (pre-production) and repeat (post-production) scenario. Both pressure and saturation variations are taken into account. The base, repeat and difference gathers are displayed from left to right. For each gather, four different incidence angles are presented, from 0 to 30 degrees.

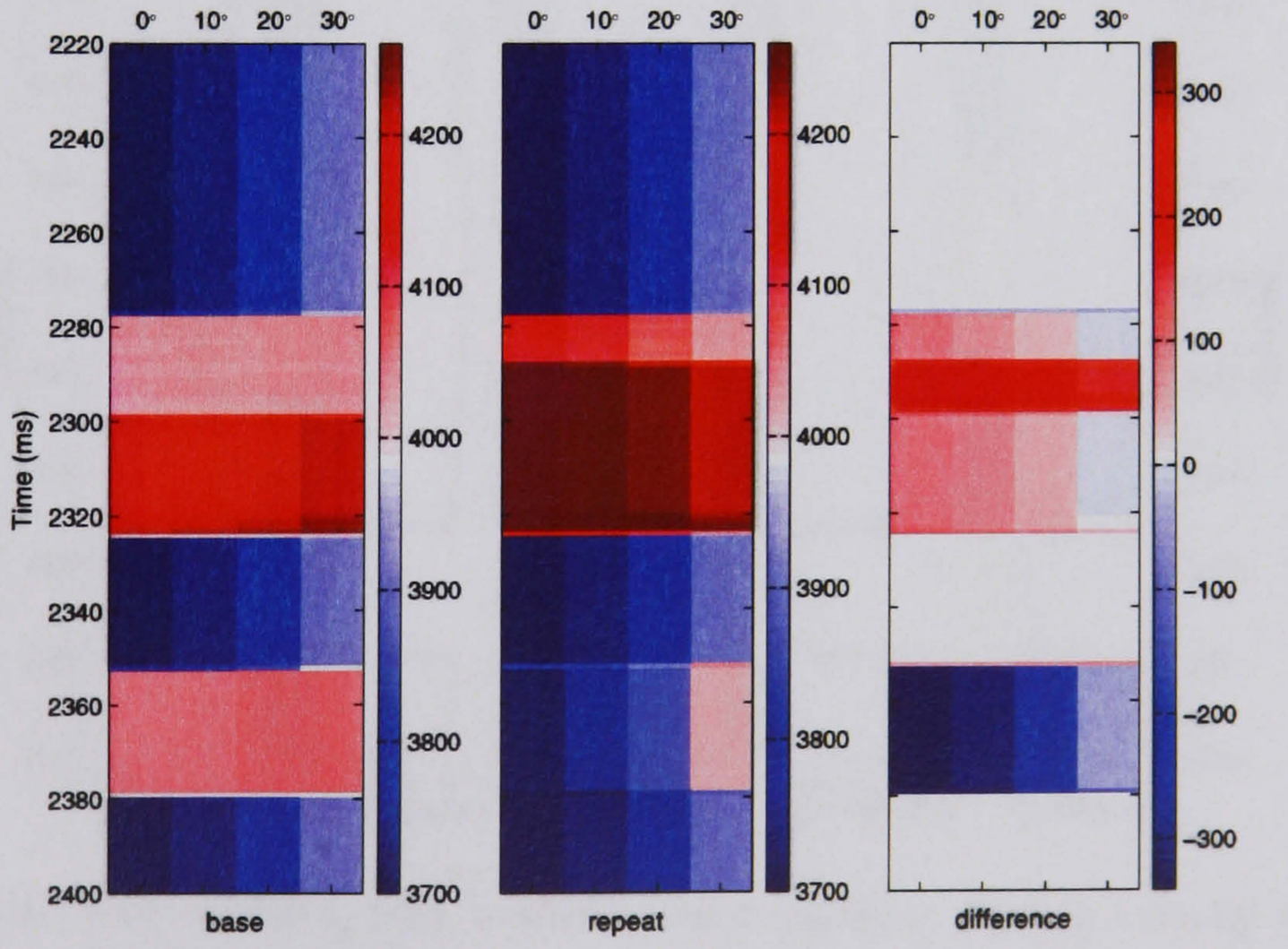

Figure 4.17: Synthetic elastic impedance gathers for the base (pre-production) and repeat (post-production) scenario. Both pressure and saturation variations are taken into account. The base, repeat and difference gathers are displayed from left to right. For each gather, four different incidence angles are presented, from 0 to 30 degrees.

4.3.2 Sensitivity of rock physics properties to pressure and saturation

It is shown that seismic amplitude or elastic impedance alone cannot be used to distinguish between pressure and saturation effects. In order to confirm the ability of the shear modulus and saturation modulus to differentiate between these effects, time-lapse changes in seismic properties (i.e. saturation modulus, bulk modulus, shear modulus, P-wave velocity and S-wave velocity) are computed for the three previous production scenarios. Figure 4.18 shows that the saturation modulus is less affected by pressure changes (less than 5%) than bulk modulus changes (15% when pressure decreases) when only pressure changes are considered. The shear modulus is more sensitive to the effect of pressure decrease (40% changes) than increase (10% changes only). Furthermore, P-wave and S-wave velocities are both sensitive to pressure changes, as shown by equations 3.9 and 3.10. From this display, one can note that the shear and saturation modulus are the most and least sensitive parameters to pressure, respectively.

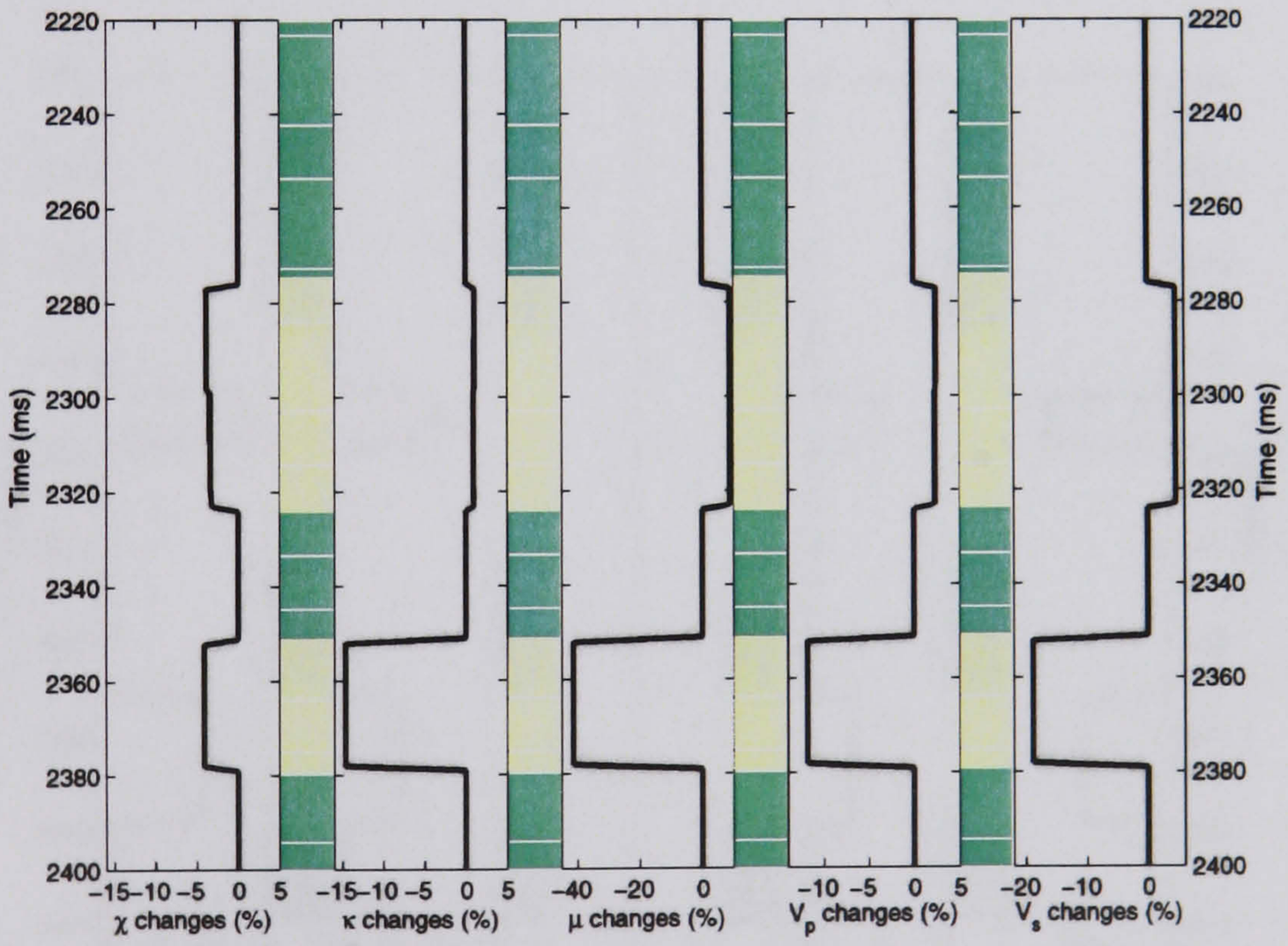

Figure 4.18: Saturation modulus, bulk modulus, shear modulus, P-wave velocity and S-wave velocity changes due to the effect of pressure changes only. Pressure profiles from Figure 4.11 are used.

On the other hand, when only saturation changes are assumed (Figure 4.19), it is noteworthy that the shear modulus remains constant and that the S-wave and P-wave velocities are slightly affected (less than 1%). S-wave velocity is responsive to saturation because of the contribution of the density term. As demonstrated by Figure 4.6, a better sensitivity of the saturation modulus to saturation effect can be observed (up to 15%) compared to the bulk modulus (up to 10%). Once more, Figure 4.20, which presents the combined effect of pressure and saturation on the rock properties, shows the inability of P-wave and S-wave velocities to distinguish between pressure and saturation changes. To some extent, the same conclusion can be reached for the shear and bulk moduli, since the bulk modulus values are biased by the pressure effect. In fact, the saturation changes in the lower sand are not interpretable from the changes in bulk modulus. The shear and saturation modulus stand as the optimum parameters to separate production effects. The amount of pressure leakage into the saturation modulus is small when compared to the bulk modulus.

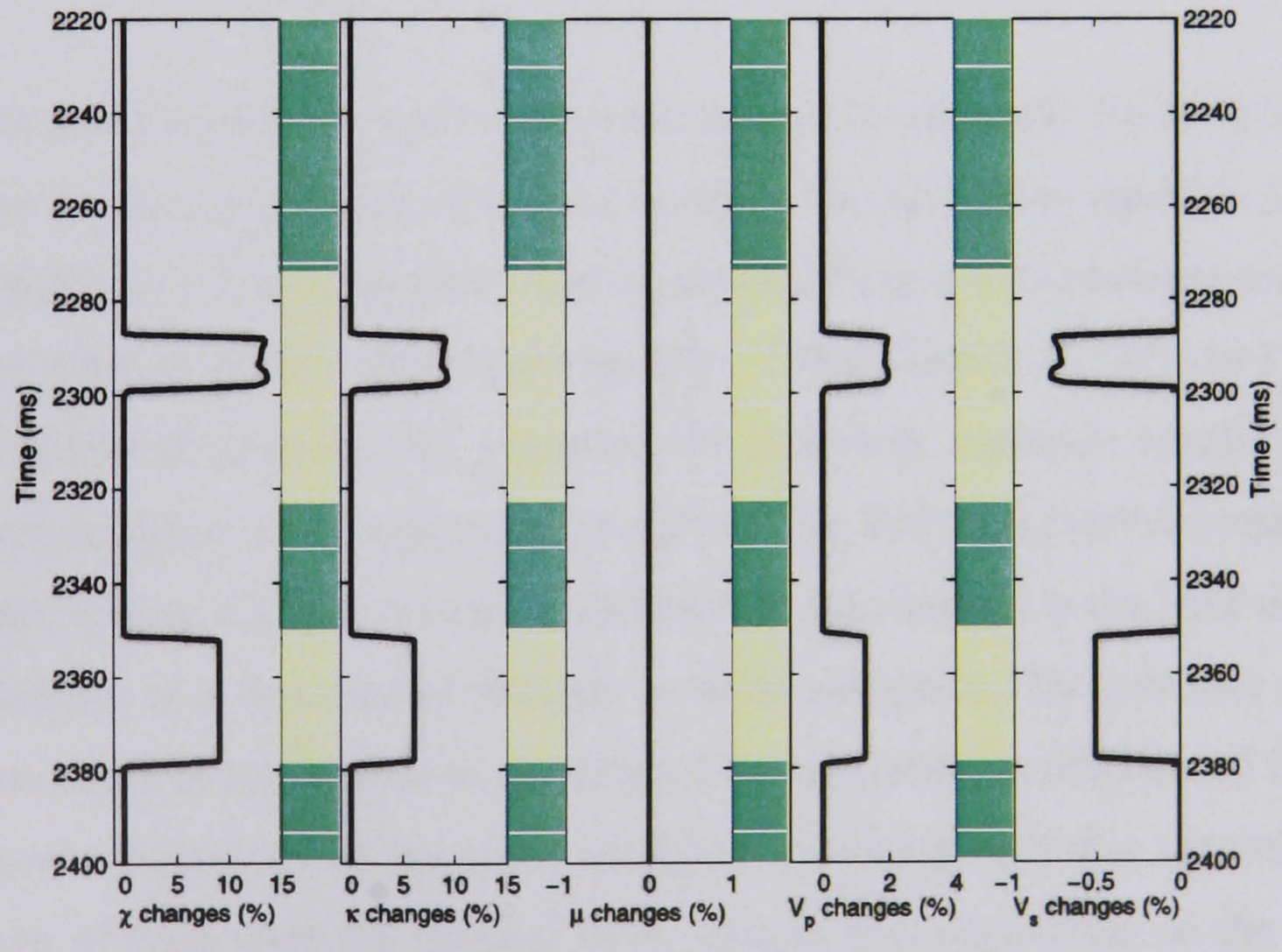

Figure 4.19: Saturation modulus, bulk modulus, shear modulus, P-wave velocity and S-wave velocity changes due to the effect of saturation changes only. Saturation profiles from Figure 4.11 are used.

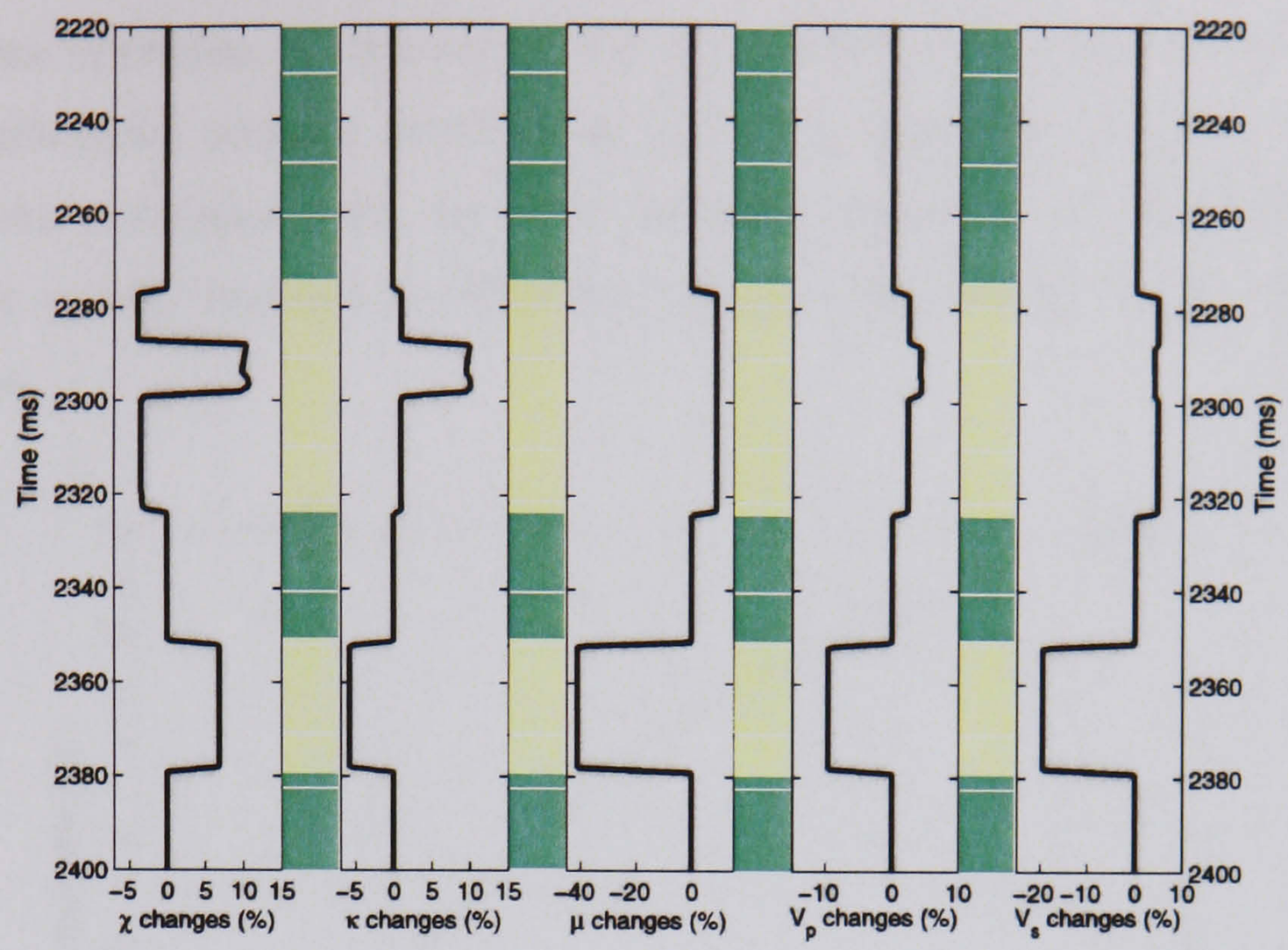

Figure 4.20: Saturation modulus, bulk modulus, shear modulus, P-wave velocity and S-wave velocity changes due to the combined effect of pressure and saturation changes. Saturation and pressure profiles from Figure 4.11 are used.

To further demonstrate the two previous statements, the example from Figure 4.5 and Figure 4.6 can be used to compute the shear modulus, the saturation modulus and the bulk modulus, at different states of pressure and saturation. Figure 4.21 presents the change of shear modulus relative to the initial condition (P_d = 15MPa and S_o = 75%) as a function of changes in differential pressure. As expected, all saturation scenarios overlie each other, since the shear modulus is, by definition, unaffected by fluid substitution (equation 3.14). Figure 4.22 and Figure 4.23 show equivalent displays for changes in the bulk modulus and saturation modulus as a function of changes in brine saturation. The pressure dependence on the bulk modulus is larger than in the case of the saturation modulus, and is correlated with the pressure behaviour of the shear modulus. A change in brine saturation of 25% gives a change of bulk modulus ranging from –9% to 5%, depending on the differential pressure variations. For the saturation modulus, values between 2% and 6% are observed. In order to summarize the degree of pressure leakage into the saturation attributes, Table 4.1 presents the relative change of bulk modulus and saturation modulus, assuming no

change in brine saturation. It can be noted that the pressure leakage for the bulk modulus is higher for differential pressure decrease (up to 12.8%) compared to increase (only 1%), because of the correlation with the shear modulus. However, the saturation modulus appears to be equally sensitive to differential pressure changes (up to 4%), regardless of their direction.

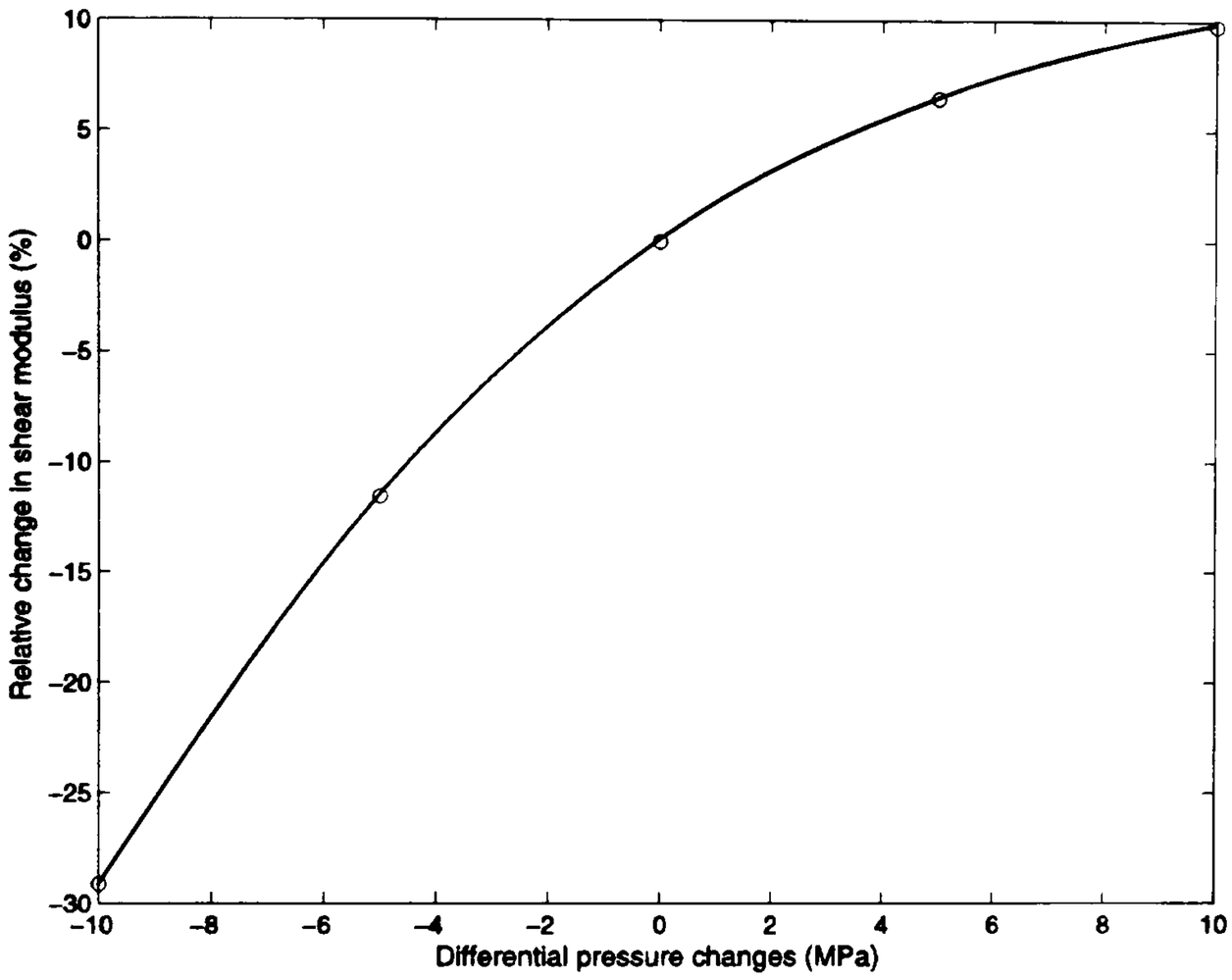

Figure 4.21: Changes in shear modulus relative to the initial scenario (P_d = 15 MPa and S_o = 75%) as a function of differential pressure changes, where pore pressure is being changed only. All the different saturation scenarios are superimposed on each other.

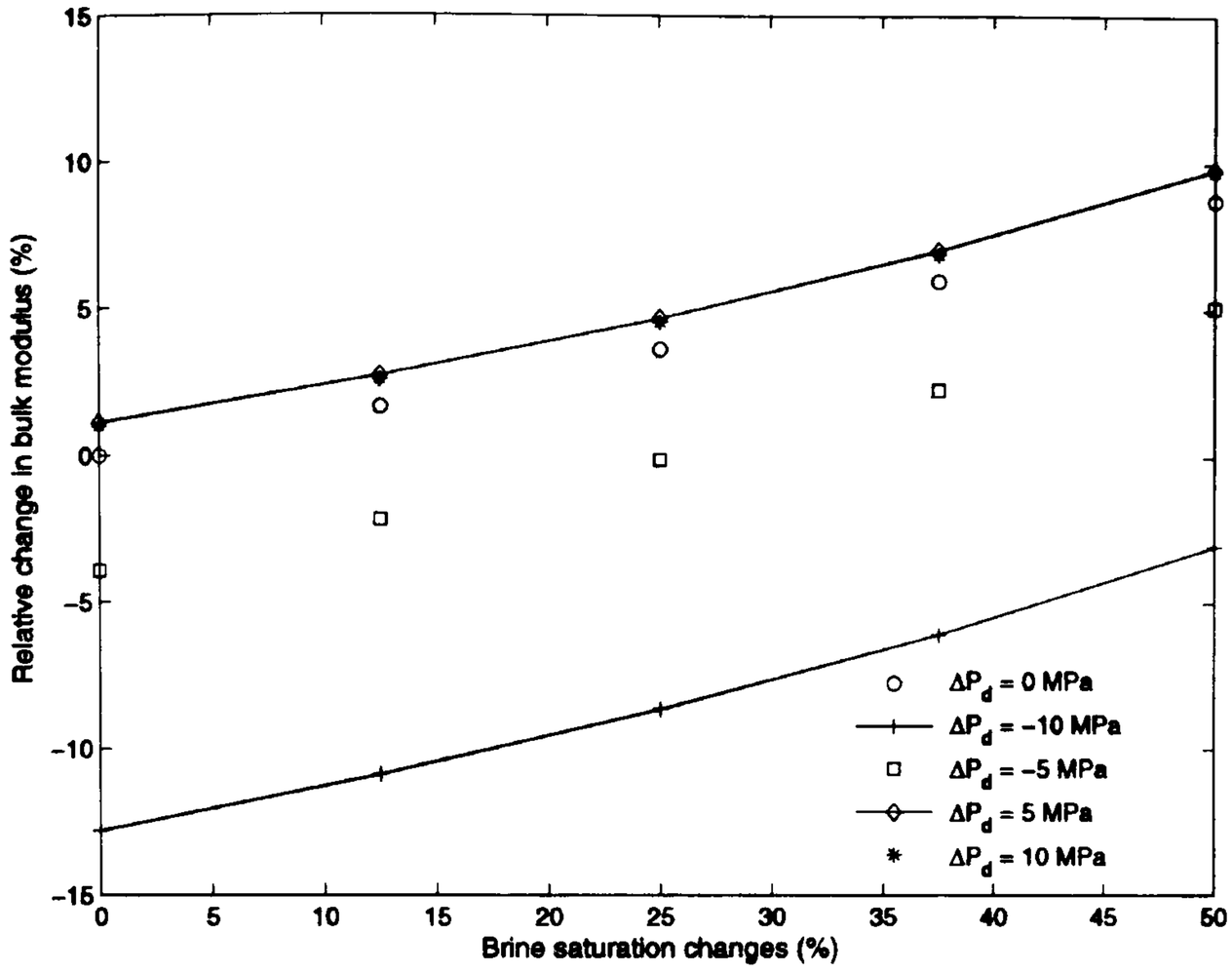

Figure 4.22: Changes in bulk modulus relative to the initial scenario (P_d = 15 MPa and S_o = 75%) as a function of changes in brine saturation. Differential pressure changes are provided for each set of points. Bulk modulus appears to be highly dependent on the magnitude of the differential pressure changes, where pore pressure is being changed only.

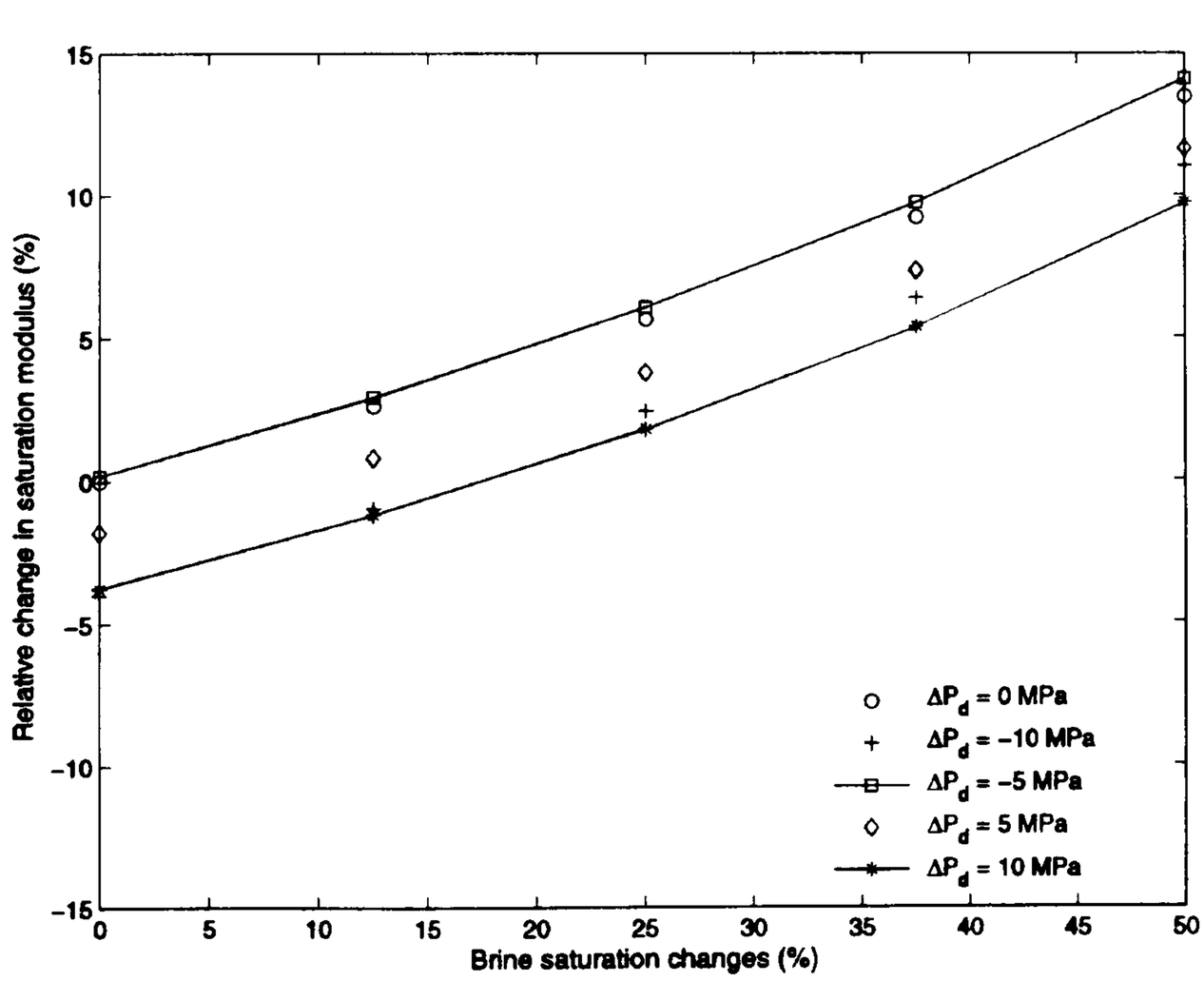

Figure 4.23: Changes in saturation modulus relative to the initial scenario (P_d = 15 MPa and S_o = 75%) as a function of changes in brine saturation. Differential pressure changes are provided for each set of points. The saturation modulus is slightly dependent on the magnitude of the differential pressure changes, where pore pressure is being changed only.

Differential pressure changes (MPa)	Relative bulk modulus changes due to P_d (%)	Relative saturation modulus changes due to P_d (%)
-10	-12.3	-4.0
-5	-3.9	0.2
0	0.0	0.0
5	1.1	-1.8
10	1.0	-3.7

Table 4.1: Relative changes in bulk and saturation modulus as a function of differential pressure, where pore pressure is being changed only. The pressure sensitivity due to pressure is higher for the bulk modulus than for the saturation modulus. Brine saturation remains constant in this case.

4.4 Conclusions

In this chapter, rock physics relationships derived in Chapter 3 are implemented, and new formulations for the AVO equation and elastic impedance are presented. These new approximations compare favourably with existing approximations, but, in addition, offer more insight into the interpretation of pressure and saturation effects on time-lapse seismic amplitudes and elastic impedances. The use of current seismic attributes to estimate pressure and saturation will lead to cross-talk occurring between the estimates. However, inversion for the shear and saturation modulus should provide the opportunity to optimally reduce the leakage between the estimates – thanks to their relatively greater independence in the pressure and saturation domain. In the next chapter, the estimation of pore pressure and fluid bulk modulus changes is carried out for a reservoir model-based study.

Chapter 5

A reservoir model-based study

The reservoir simulator is a tool that offers a way to link the engineering and geophysics domains. It enables us to interpret the observed 4D seismic changes in terms of pressure and saturation changes, and to obtain more insight into the spatial and temporal variation of these attributes. Reservoir simulation studies are useful for studying time-lapse feasibility (Khan *et al.*, 2000), and are generally preferred to the simple approach, where averaged reservoir changes are assumed. In this chapter, a reservoir model-based study (Figure 5.1) is carried out to model synthetic seismogram and elastic impedances in order to test a new methodology to discriminate between the pressure and saturation effects introduced in Chapter 3. The Ainsa II turbidite-filled channel complex (southern Pyrénées, Spain) is used as an analogue in this exercise. A 3D geological model is built in order to capture the main features of the turbidite channels. After dynamic flow simulation is run through the model, outputs (i.e. water saturation, pore pressure) are used through a petro-elastic transformation (MacBeth *et al.*, 2003), in order to derive the elastic properties of the reservoir rock. Synthetic seismogram and elastic impedances are then obtained, and are used to estimate pressure and saturation effects to be compared with the original outputs from the flow simulator. Finally, an uncertainty analysis is carried out in order to define the robustness of the proposed methodology. The uncertainties in the estimates are given in the cases where the error sources are correlated and uncorrelated.

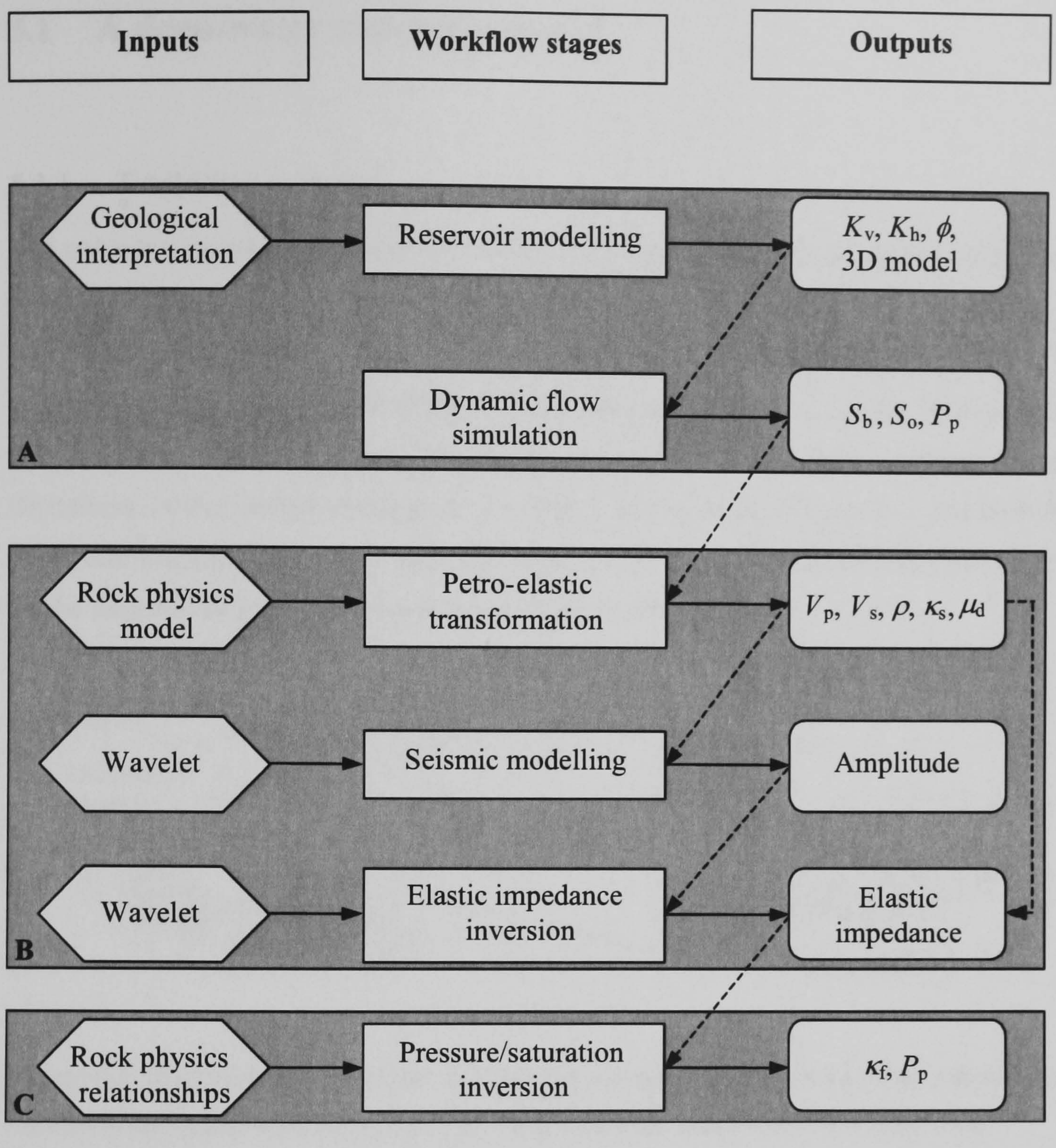

Figure 5.1: Flowchart of the reservoir model-based study. Part A involves the building of the 3D reservoir model from geological interpretation, which is flow simulated. Part B represents the simulator to seismic link. Outputs for the flow simulator (i.e. S_b and P_p) are input into a petro-elastic transformation in order to compute elastic properties (i.e. V_p, V_s, ρ, κ_S and μ_d). These properties are then used to model synthetic seismograms and elastic impedance. Part C corresponds to the separation of the pressure and saturation effects from elastic impedance, using the rock physics relationships introduced in Chapter 3. The dotted arrows stand for the process outputs necessary in subsequent stages.

5.1 A deep-water reservoir model

5.1.1 Turbidite systems

The concept of a turbidite is associated with deep-water sedimentation (Mutti, 2000). Most turbidite reservoirs are formed as a succession of graded beds consisting of sandstone/mudstone pairs – each bed being deposited by different turbidity currents. The argillaceous beds are deposited during the lower flow regime of the current, while the sand-rich beds are deposited during the upper flow regime – the latter resulting in rapid deposition. In the context of deep-sea fan depositional systems (Figure 5.2, modified from Mutti and Lucchi, 1972; Mutti and Ghibaudo, 1972), the turbidite currents form channels on the slope of the fan, following the mechanism described above.

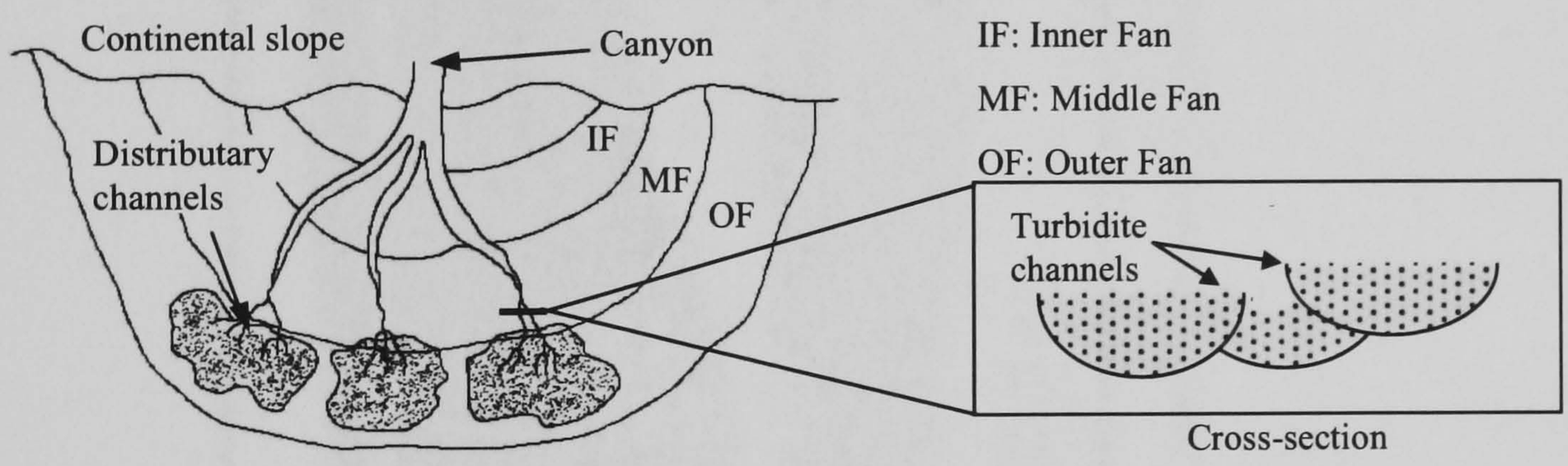

Figure 5.2: Illustration of a fan model and turbidite channels. The schematic cross-section presents a group of stacked sand channels, where the latest deposited channel erode the older ones.

5.1.2 Outcrop location and description

The Ainsa channel system, south-central Pyrénées, is a well-exposed, deep-marine sandy channelized fan system of late Eocene age (Gardiner, 2003). The Ainsa channel complex is one of the most famous submarine channel outcrops within Europe, and is often used as an analogue for deep-marine turbidite reservoirs. The channel complex is approximately 2000 metres long and 70 metres thick.

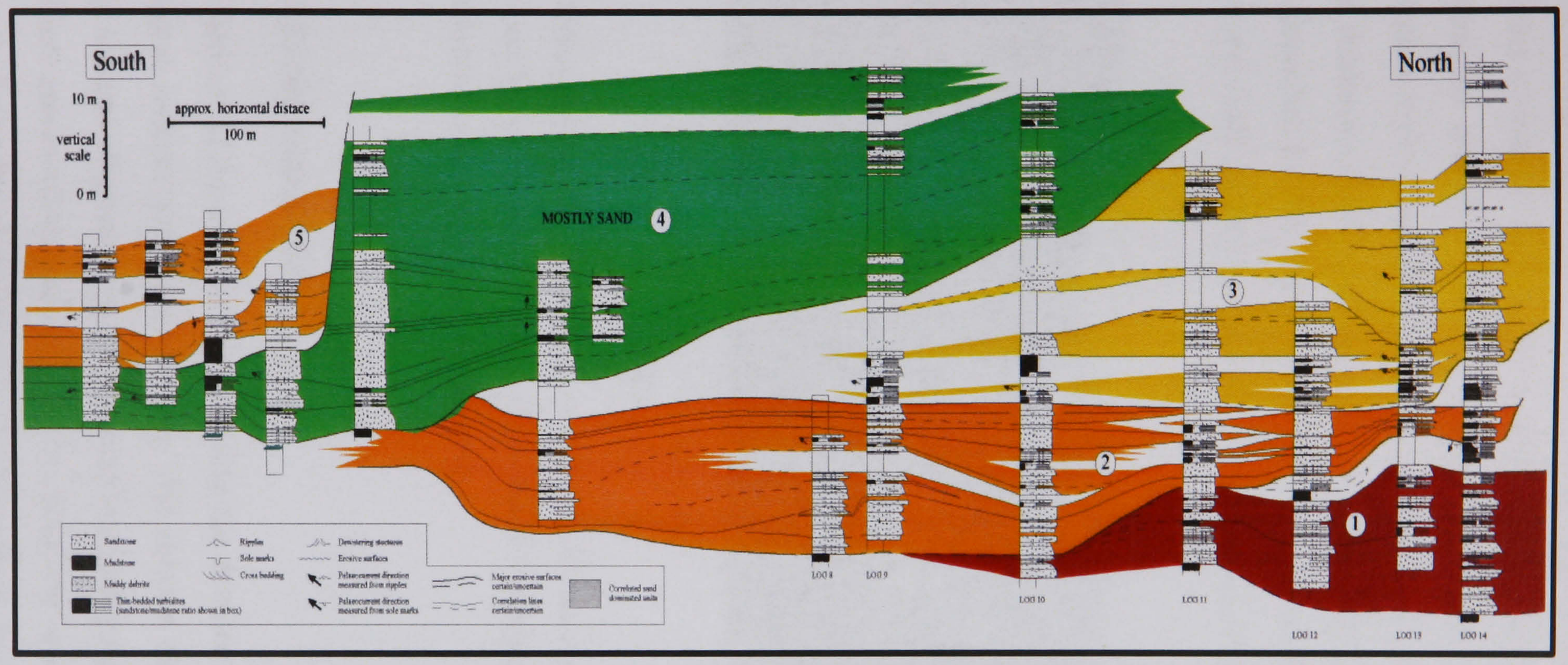

Figure 5.3: Bed correlation of the Ainsa II channel complex. Five turbidite channels, numbered from 1 to 5, are identified (from Clark, 1995).

From the bed correlation (Figure 5.3, see Clark, 1995) it can be seen that the Ainsa II channel complex consists of five stacked channels numbered from 1 to 5 on Figure 5.3. The channel dimensions are finer than the seismic resolution. In fact, the height of each individual channel varies from 10 to 30 metres, but a stack of these channels can reach up to 60 metres thickness in the central part of the outcrop (Figure 5.4). In Figure 5.4, the graded beds deposited by the different turbidity currents can be observed inside channel 4. Each of these individual beds (blue dotted lines) is separated by thin layers of mudstone.

Figure 5.4: Photograph of the western part of the Ainsa II outcrop (Courtesy of Gardiner, 2004). Channels 1, 4 and 5 are interpreted (red and yellow lines). The layering of the various sand deposits is clearly visible inside channel 4 (blue dotted lines).

5.2 Reservoir modelling

A 2D cross-section of the outcrop is built using the detailed bed correlation (Figure 5.3), and a geological interpretation made on-site. The sinuous channels are conceptualized in cross-section as semi-elliptical objects deposited in a background of sandy shale accounting for the erosional process (Stephen *et al.*, 2001). Since the aerial extension of the outcrop is not available to derive the characteristics of the channels in the direction perpendicular to

the 2D cross-section, wavelength and sinuosity amplitudes are assumed for each individual channel, in order to derive a 3D geological model (Figure 5.5).

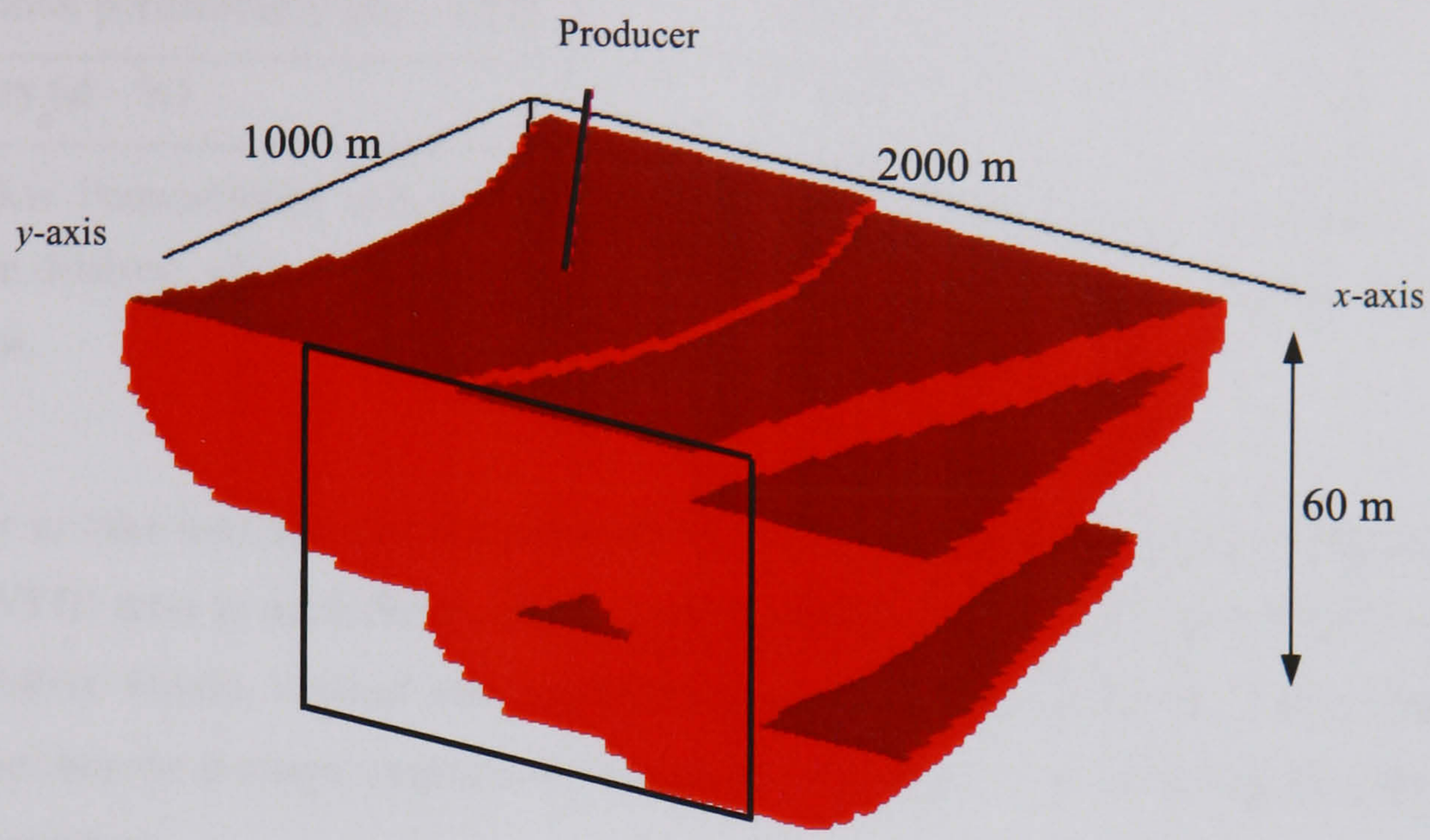

Figure 5.5: 3D geological model of the Ainsa II outcrop. The black area delineates the boundaries of the outcrop. The aerial characteristics of the channels are assumed along the *y*-axis, since no data are available to extend the model in that direction. The location of the producer to be used in the flow simulator is highlighted.

The dimensions of the model are as follows:

	Cell size (m)	**Number of cells**	**Dimension (m)**
x-direction	25	80	2000
y-direction	25	40	1000
z-direction	2	30	60

Prior to the reservoir flow simulation, petrophysical properties (porosity, absolute permeabilities) are assigned to each cell in each facies (sand and sandy shale). Values representative of the rock physics database from the Foinaven field are used for the sand and assumed for the shale (Johnston, 1987) to compute the petrophysical properties of the two facies (Table 5.1). Averaged vertical and horizontal permeabilities of 325 mD are obtained for core plugs with 24% averaged porosity.

	Sand	Shale
Vertical permeability (K_v – mD)	325	0.05
Horizontal permeability (K_h – mD)	325	0.05
Porosity (ϕ – %)	24	10

Table 5.1: Permeabilities and porosity for sand and shale. Sand values are derived from the Foinaven database, while shale porosity is assumed (Johnston, 1987) and permeability chosen to be fairly low.

In order to take into account the presence of amalgamation surfaces and different net-to-gross (NTG) ratio in each facies, the following approach is used (Stephen, 2002; MacBeth *et al.*, 2005). Firstly, vertical and horizontal permeability are computed using a harmonic and an arithmetic average, respectively (equations 5.1 and 5.2), considering only the net-to-gross variations.

$$K_h^{mix} = NTG * K_h^{sand} + (1 - NTG) * K_h^{shale} \tag{5.1}$$

$$\frac{1}{K_v^{mix}} = \frac{NTG}{K_v^{sand}} + \frac{1 - NTG}{K_v^{shale}} \tag{5.2}$$

Then the amalgamation ratio A (i.e. the fraction of shale removed) is included in the calculation of the vertical permeability using equation 5.3. Since many turbidite systems consist of sheet-like sandstone beds, the nature of the sand-on-sand contacts between individual beds will only affect the vertical permeability.

$$K_v^{mix2} = exp\left[A * ln\left(\frac{K_v^{sand}}{K_v^{mix}} \right) + ln\left(K_v^{mix} \right) \right] \tag{5.3}$$

Figure 5.6 presents the vertical permeability plotted against amalgamation ratio for the two facies of the model.

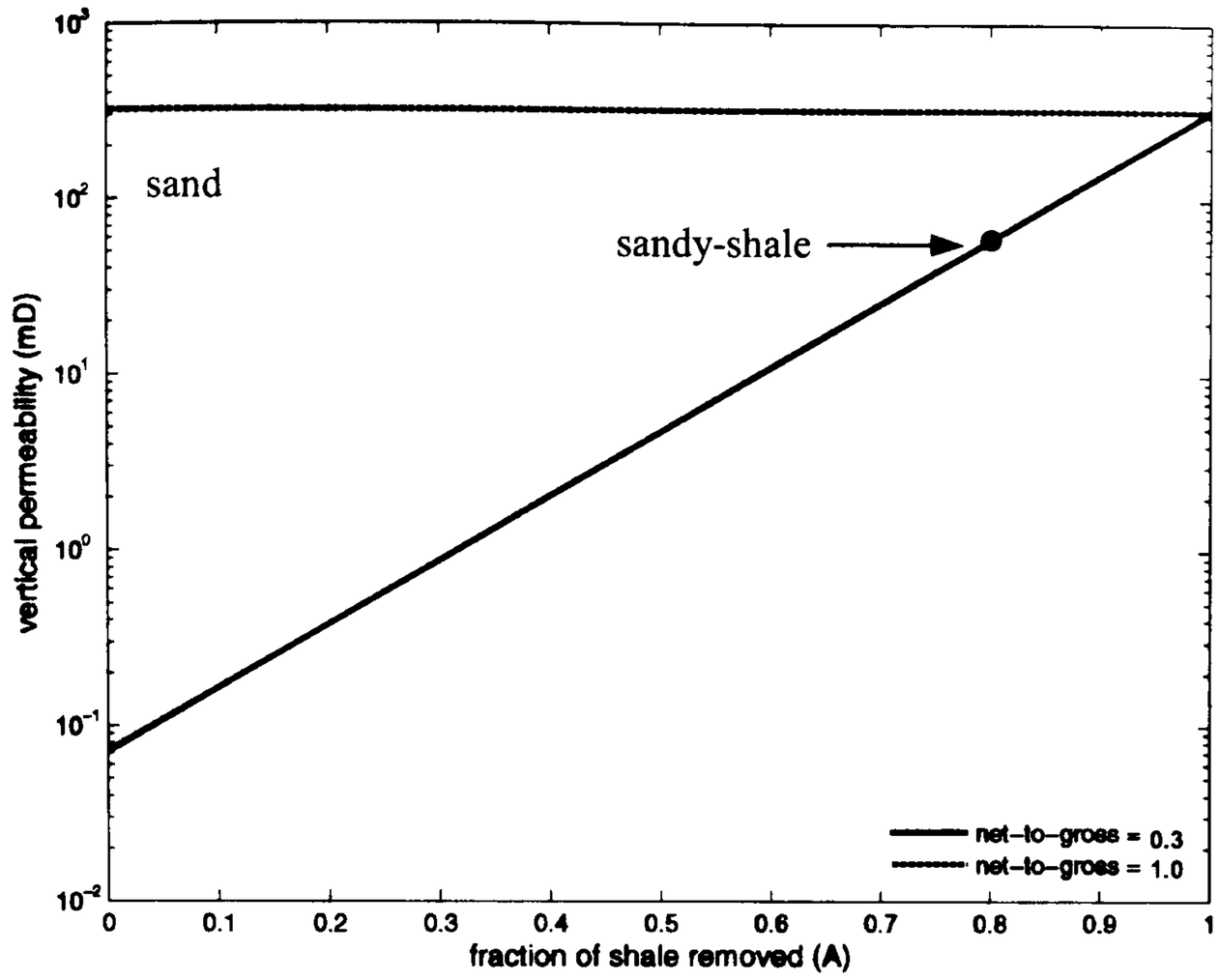

Figure 5.6: Plots of vertical permeability against amalgamation ratio for different net-to-gross ratios. Vertical permeabilities for the sand (A = 0) and sandy-shale (A = 0.8) are highlighted.

It can be observed that, with increasing amalgamation ratio, permeability barriers to vertical flow formed by argillaceous beds are removed and result in an increase of the vertical permeability. The sand exhibits a constant vertical permeability, since it contains no shale. In this study, the amalgamation ratios are equal to 0 and 0.8; and the net-to-gross ratios to 1 and 0.3 in the sand and sandy-shale facies, respectively. Furthermore, vertical permeability is also sensitive to sand lamination, grain-size distribution and granular sorting (Selley, 2000). In order to include this effect, vertical permeability is reduced by 70%, which corresponds to a low K_v/K_h ratio.

5.3 Dynamic reservoir simulation

For the purpose of the flow simulation, the Eclipse™ 100 black oil simulator is used on the geological model presented in section 5.2, and geomechanical effects are neglected. In fact, stress-sensitivity of porosity and absolute permeability are also neglected. Figure 5.7 and Figure 5.8 present porosity and permeability changes plotted against differential pressure, where the reference is fixed to 21 MPa, which is in the order of the initial differential

™: Eclipse is registered trademark of Schlumberger.

pressure in this study. It can be observed that the stress-sensitivity of porosity is less than 2.5% for the full range of pressure and can be considered negligible at this level of approximation. Overall absolute permeability from the Foinaven database appears to be much more stress-sensitive than porosity. If a change of 10 MPa in differential pressure is assumed (Figure 5.8), then it can be noted that the stress-sensitivity of permeability is less than 5% and can also be neglected. If large changes in pressure are expected, the stress-sensitivity of permeability can reach up to 9%, particularly if differential pressure decreases. A reduction or obstruction of the pore space network as differential pressure increases could be at the origin of the larger stress-sensitivity observed for the permeability. However, core damage occurring during the removal of the samples from their initial stress condition might be the cause of the large sensitivity of porosity and permeability observed at low differential pressure. The data used in these plots are derived from the Foinaven rock physics database and the stress-sensitivity results are believed to be representative of the Foinaven field and, some extent, to the west of Shetland area.

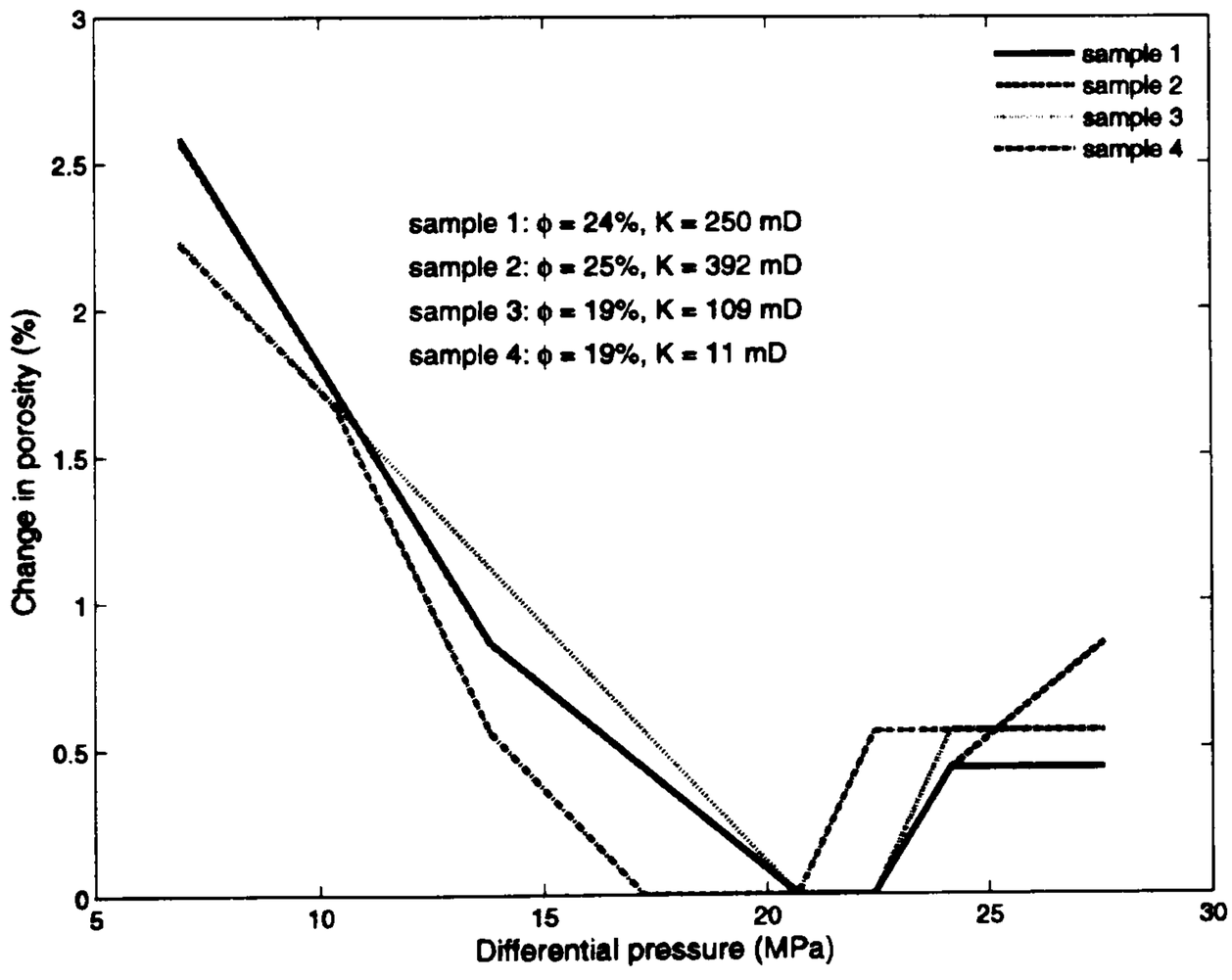

Figure 5.7: Sensitivity of porosity to differential pressure. Relative porosity changes are computed using a reference differential pressure of 21 MPa. Porosities and absolute permeabilities of the different core plugs are provided at the reference conditions. Porosity variations due to differential pressure changes appear to be minor.

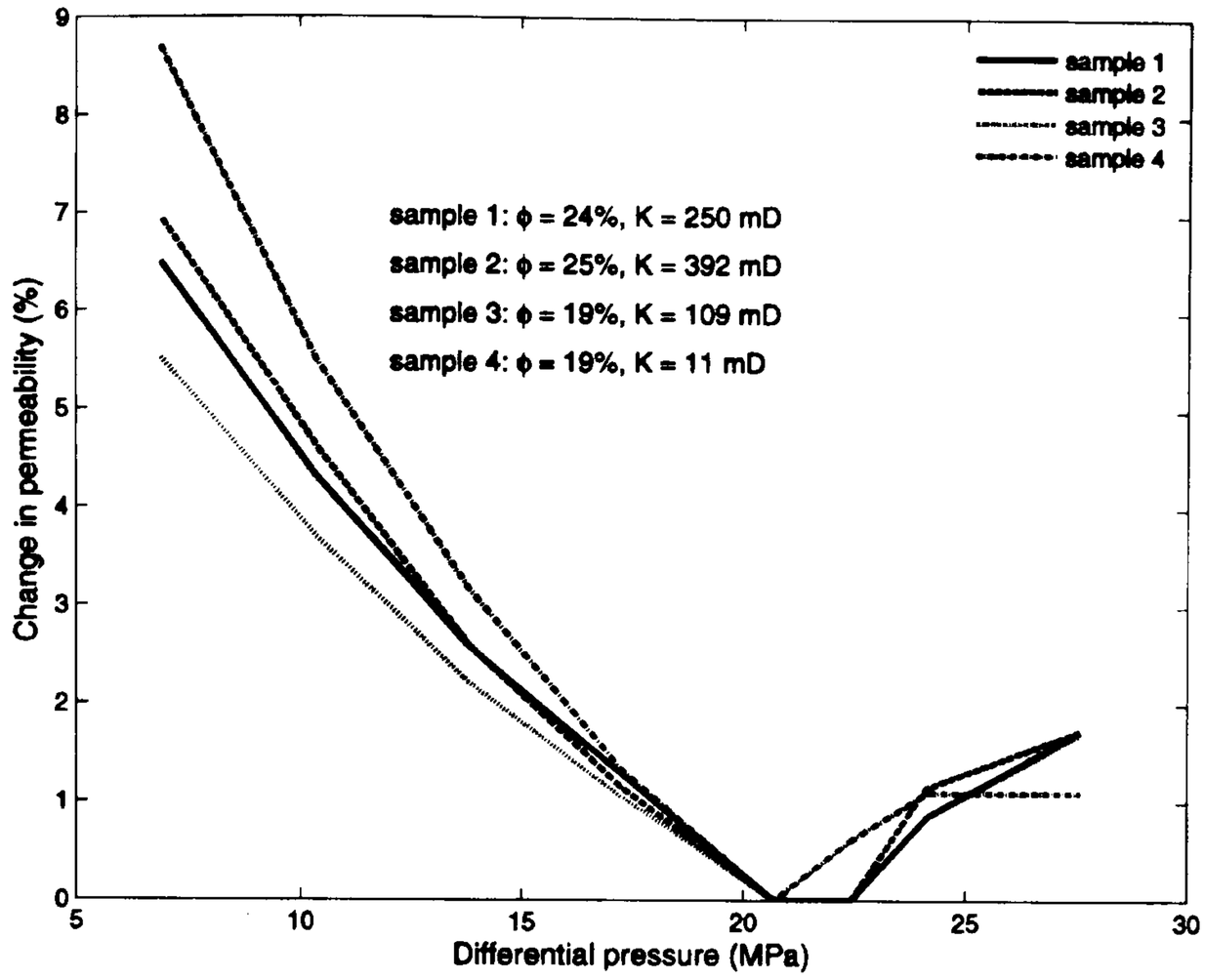

Figure 5.8: Sensitivity of absolute permeability to differential pressure. Permeability changes for each sample are computed using a reference differential pressure of 21 MPa. Porosities and absolute permeabilities of the different core plugs are provided at the reference conditions. For large changes in differential pressure, permeability can vary up to 9% from its initial value.

5.3.1 Reservoir setting and initial conditions

Although the lithostatic gradient varies with depth, most pressure versus depth plots use a default gradient of 1 psi/ft (Fetrl, 1976), which corresponds to a force exerted by a formation with an average bulk density of 2.31 g/cm^3. In the present case, the reservoir depth is equal to 7240 ft, which provides an overburden pressure of 49.9 MPa. In this study, the hydrocarbon recovery process is natural water drive with one producer where the assumed liquid volume rate target (300,000 stb/day) controls the production of fluids. The reservoir is in connection with an active aquifer having a porosity of 23% and permeability of 75 mD. In the flow simulation, an analytical aquifer of 500 m of thickness and 9000 m of radius is used. The main factor here is the relative size and mobility of the water of the aquifer relative to the size of the hydrocarbon accumulation (Dake, 1978). In fact, the drop in the reservoir pressure depends on the factor mentioned above, which is related to the

amount of pressure support provided by the aquifer. The initial oil–water contact is set at 7404 ft relative to the 7437 ft of the reservoir bottom, and the oil–gas contact lies far above the reservoir, to ensure that no free gas is present initially.

5.3.2 Relative permeability

In the present flow-simulation model, the reservoir and production setting are tuned in order to prevent the reservoir pressure dropping below the bubble point pressure, thus avoiding having any gas coming out of solution. The Eclipse programme requires the relative permeability and capillary pressure curves for the oil–water and oil–gas system to run the two-phase flow simulation. The relative permeability provided by the Foinaven field's operator describes the capability of the flow of one phase in the presence of another, and is shown in Figure 5.9 for the present oil–water system. In this simulation, it is assumed that the pressure difference between the non-wetting phase and the wetting phase is negligible.

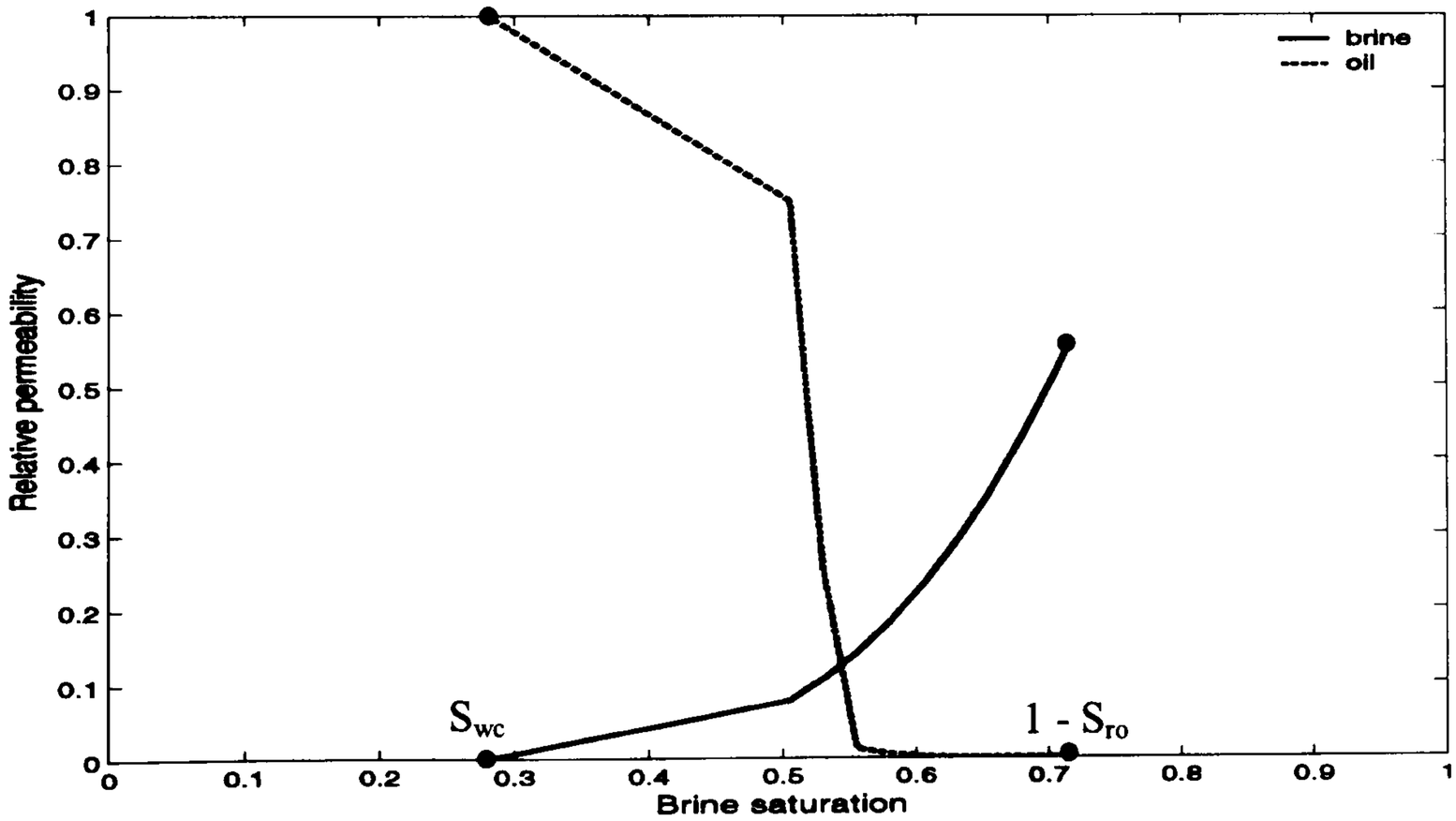

Figure 5.9: Relative permeability of brine and oil as a function of brine saturation. The S_{wc} and S_{ro} stand for the connate water saturation and the residual oil saturation. Relative permeabilities are normalised by the absolute permeability at connate water saturation.

5.3.3 Reservoir fluids

The reservoir fluids present in the system are oil and brine. Characteristics of the gas are also input to the flow simulator, but, since the pressure is not dropping below the bubble point pressure, there is no gas evolving in the system. The brine used for the flow simulation has a salinity of 18,000 ppm (parts per million). Its density is set to 1.018 g/cm^3 and compressibility to 3.13×10^{-6} psi^{-1} under standard conditions (ambient temperature 15.6°C and atmospheric pressure). The hydrocarbon is set to be a live oil with a specific gravity of 27.69 API. The American Petroleum Institute (API) developed a non-linear relationship (equation 5.4) to classify different types of oil (Archer and Wall, 1986). SG stands for the specific oil gravity relative to water at 60°F.

$$API = \frac{141.5}{SG} + 131.5 \tag{5.4}$$

The oil density is set to 0.898 g/cm^3, and its compressibility to 1.0×10^{-5} psi^{-1} under standard conditions. The bubble point pressure of this live oil is around 22 MPa. Since the oil phase remains in its undersaturated state during the whole of the simulation, the gas properties are not presented.

5.3.4 PVT properties

For the flow simulation, the following PVT properties are required as input in the reservoir flow simulator:

- Viscosity of live oil, brine and gas.
- Formation volume factor of live oil and gas.
- Solution gas to oil ratio of live oil.

All these parameters are provided as a function of pressure, in order to ensure realistic behaviour of the physical properties during the simulation. The temperature dependence is

ignored, and the reservoir temperature is assumed to be a constant 60°C – corresponding to a temperature gradient of 29°C/km (Parnell *et al.*, 1999).

5.4 Petro-elastic modelling

The petro-elastic properties of the reservoir rock are obtained by substituting the fluid-flow properties into the dry-frame properties of the rock. This procedure is extensively described in Chapter 3. In order to carry out a successful petro-elastic transformation, reliable rock physics models need to be computed to accurately represent the sensitivity of the rock to pressure and saturation. In the present study, pressure and saturation laws described and validated in Chapter 3 are used. Compliance-based laws are also used in order to represent the stress-sensitivity of the shale. Stress-sensitivity parameters for the pressure model of shale and sandstone are presented in Table 5.2, and represent the average pressure-sensitivity of the Foinaven database detailed in Table 3.1. Parameters P_κ, P_μ, S_κ and S_μ derived for sandstone are assumed to be applicable for shale since shale is only present in the non-reservoir part of the model. However, the high-pressure asymptotes κ_∞ and μ_∞ are computed by selecting ultrasonic velocity measurements at high confining pressures, available on shale core plugs from the Foinaven field.

	Sandstone	**Shale**
P_κ (MPa)	5.81	5.81
P_μ (MPa)	7.11	7.11
S_κ	0.52	0.52
S_μ	0.54	0.54
μ_∞ (GPa)	7.94	7.16
κ_∞ (GPa)	10.19	8.14

Table 5.2: Stress-sensitivity parameters for sandstone and shale. These parameters are representative of the average pressure-sensitivity of the Foinaven database. Shale stress-sensitivity parameters are assumed to be comparable to sandstone, except for the high-pressure asymptotes – which are derived from ultrasonic measurements.

To model the sandy-shale mixture, an iso-stress average is used (Postma, 1950). Rock grain properties are assumed to be constant in this model (κ_m = 36.4 GPa and ρ_m = 2.5 g/cm^3). To derive fluid properties dependent on pressure and temperature, the empirical relationships from Batzle and Wang (1992) are used (Appendix B). It should be noted that the fluid characteristics used in the petro-elastic transformation are consistent with the PVT properties inputted in the flow simulator. The outputs of the petro-elastic transformation are the seismic velocities (V_p and V_s) and density in depth at the reservoir simulator scale.

5.5 Time-lapse seismic modelling

In the previous section, elastic properties are representative of what is happening at the reservoir scale (with a vertical resolution of 2 m). In surface seismic, as a result of the frequency of the wavelet and the averaged velocity of the non-reservoir formation, the vertical resolution is poorer than that for the reservoir model. In order to synthesize realistic 4D changes from 3D conventional surface seismic acquisition, a 1D convolutional synthetic modelling procedure is followed. This convolutional modelling is selected because it corresponds to the technique used in elastic inversion packages, and is believed to be robust for simple geology where the effects of internal multiples, mode conversions and wave transmission are negligible (Mallick, 2001). To compute the reflectivity coefficients, the Aki & Richards (1980) approximation is used. Relative contrasts in P-wave velocity, S-wave velocity and density are derived using the outputs of the petro-elastic transformation. Then, reflectivity series are converted from the depth to the time domain, using the averaged velocities (V_p = 2963.8 m/s and V_s = 1829.9 m/s) and density (ρ = 2.14 g/cm^3) for the overburden and underburden formations. Furthermore, time-shifts due to production effects are neglected, and an averaged velocity of 3300 m/s is assumed for the reservoir unit. To obtain the synthetic seismogram, the reflectivity series in the time domain are convolved with a wavelet having a dominant frequency of 45 Hz. Figure 5.10 presents the near (0° degrees) and far (25° degrees) angle stack cross-sections for phase I (base survey) and phase II (monitor survey after four years of production), together with the corresponding time-lapse differences (repeat minus base). Even if there is a better contrast

at the far angle on the static seismic (phases I and II), the oil–water contacts can only be discerned with difficulty, because the size of the water-bearing sand is under or close to the seismic resolution. Here, the seismic resolution is defined using the Rayleigh's criterion (Kallweit and Wood, 1982), which states that the minimum resolvable bed thickness is a quarter of the seismic wavelength. Having a velocity of 3300 m/s and a dominant frequency of 45 Hz, the resulting seismic resolution is equal to 18 metres. After differentiating the seismic, a characteristic trough–peak doublet is observable (MacBeth *et al.*, 2003), and the 4D seismic response can be interpreted. The trough is associated with the original oil–water contact (OOWC), while the peak corresponds to the moved oil–water contact (MOWC). As stated previously, it is notable that the 4D signatures of the OOWC and MOWC are more prominent on the far angle stack. However, the 4D seismic response is predominantly affected by the saturation changes occurring during production, and no apparent pressure effect can be observed.

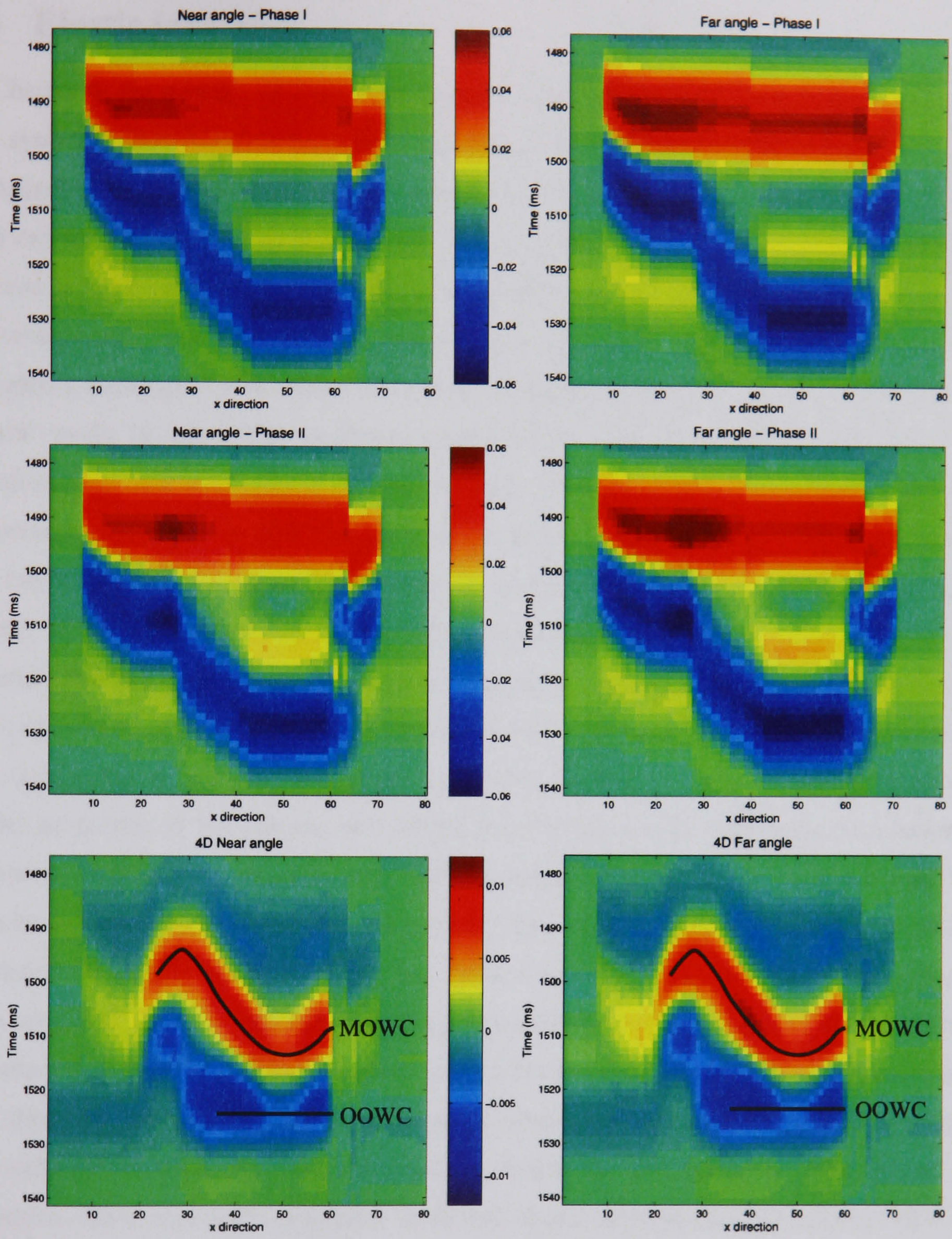

Figure 5.10: Time-lapse synthetic seismic for near angle (left column) and far angle (right column). A cross-section through the model is displayed. The top row shows the base survey; the central row the repeated survey; and the bottom row the time-lapse difference for near and far angles. The original (OOWC) and moved (MOWC) oil–water contact are visible on the 4D sections.

5.6 Elastic inversion

In Chapter 4, the concept of elastic impedance is presented. To derive elastic impedance in this synthetic case, there are two different methods that are implemented in MATLAB and compared to mimic the elastic inversion process. In the first method, the synthetic seismic data can be deconvolved by the wavelet, and the corresponding elastic impedance model derived in order to minimize the difference between the synthetic seismic (input data) and the seismic computed from the impedance model. In general, the elastic inversion workflow includes a calibration step where the elastic impedance model is calibrated with one or several wells. In this study, an elastic impedance log from one well is computed using equation 4.11 and assuming a constant velocity ratio V_P/V_S for the reservoir unit. The impedance model, which provides the best match with this impedance log and minimizes the misfit between the input and computed seismic, is selected as the final impedance model. This leads to the second method: if it is assumed that the calibration at the well is optimal, then the final model should be equivalent to using equation 4.11 with a constant velocity ratio to compute the elastic impedance. Since no difference is noticed between the two approaches in this synthetic case, the second method is used. To upscale reservoir model properties to the seismic wavelength prior to the elastic impedance calculation, a sequential Backus averaging (Backus, 1962) is applied. The Backus technique is modified in order to ensure the preservation of the strong discontinuities (i.e. shale/sand- or oil/brine-bearing sand interfaces), by detecting any large contrast in the properties to be averaged. This modified Backus average effectively upscales reservoir properties to the seismic wavelength. Elastic moduli are averaged using a harmonic mean, while an arithmetic mean was applied to the bulk density. The size of the upscaling window is defined by estimating the temporal wavelength from the wavelet frequency and averaged velocity of the formation. Since upscaling is applied to derive elastic impedance, it is assumed that the achievable vertical resolution of the impedance model is half that of the seismic (i.e. 9 metres). The modified sequential Backus averaging applied assumed a normal incidence of the ray path (Lindsay, 2001); the effect of non-normal incidence is not considered. Figure 5.11 presents the elastic impedance cross-sections pre- and post-production, together with the time-lapse differences at the near and far angles. Figure 5.12 presents the corresponding

cross-sections of the time-lapse pore pressure and fluid bulk modulus changes. The elastic impedance appears to be easier to interpret than the seismic results. In the pre-production state, the oil-bearing sand (blue) and the water-bearing sand (brown) can be identified, whereas, in the post-production state, the light-blue area corresponds to the region where the oil is swept by the upward movement of the water leg due to the reservoir pressure drop. Furthermore, the time-lapse differences reveal more insight into the pressure and saturation fields. As observed in Chapter 4, the elastic impedance is prominently affected by saturation changes and slightly by pressure – particularly if pore pressure goes down. Also, the elastic impedance results reveal a possible qualitative discrimination between pressure- and saturation-related effects. A background increase in elastic impedance appears at the near angle, due to the depletion of the reservoir (Figure 5.11, white arrows). However, no changes appear at the far angles, confirming once again their insensitivity to pressure variations. It can be concluded that elastic impedance provides a better support to qualitatively discriminate between production effects.

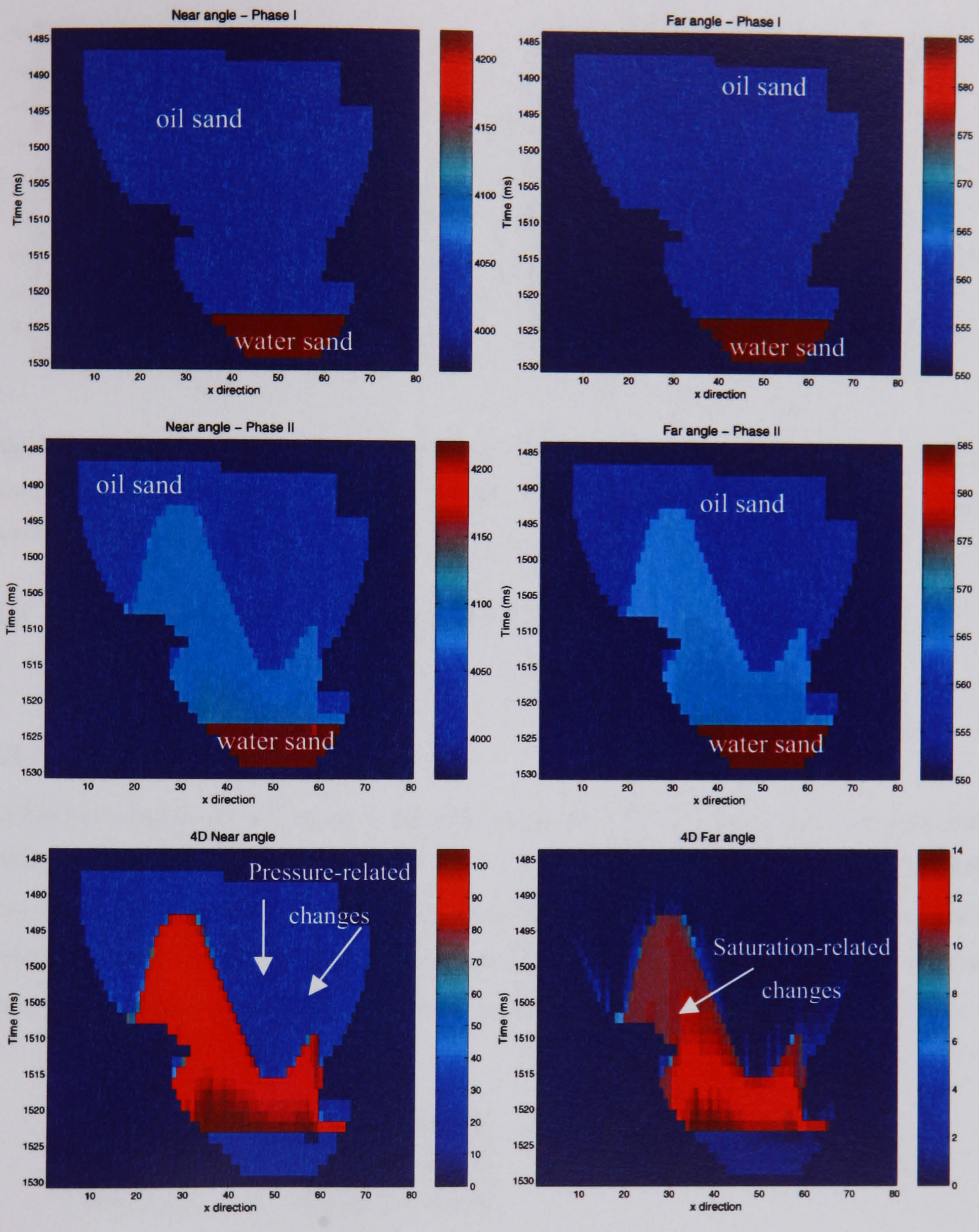

Figure 5.11: Elastic impedance for the near angle (left column) and the far angle (right column). A cross-section through the model is displayed. The top row shows the base survey; the central row the repeated survey; and the bottom row the time-lapse difference for near and far angles. Large 4D signatures related to saturation changes (red anomalies) are visible at near and far angles. Smaller 4D signatures related to pressure depletion (light-blue anomalies) are observed at the near angle.

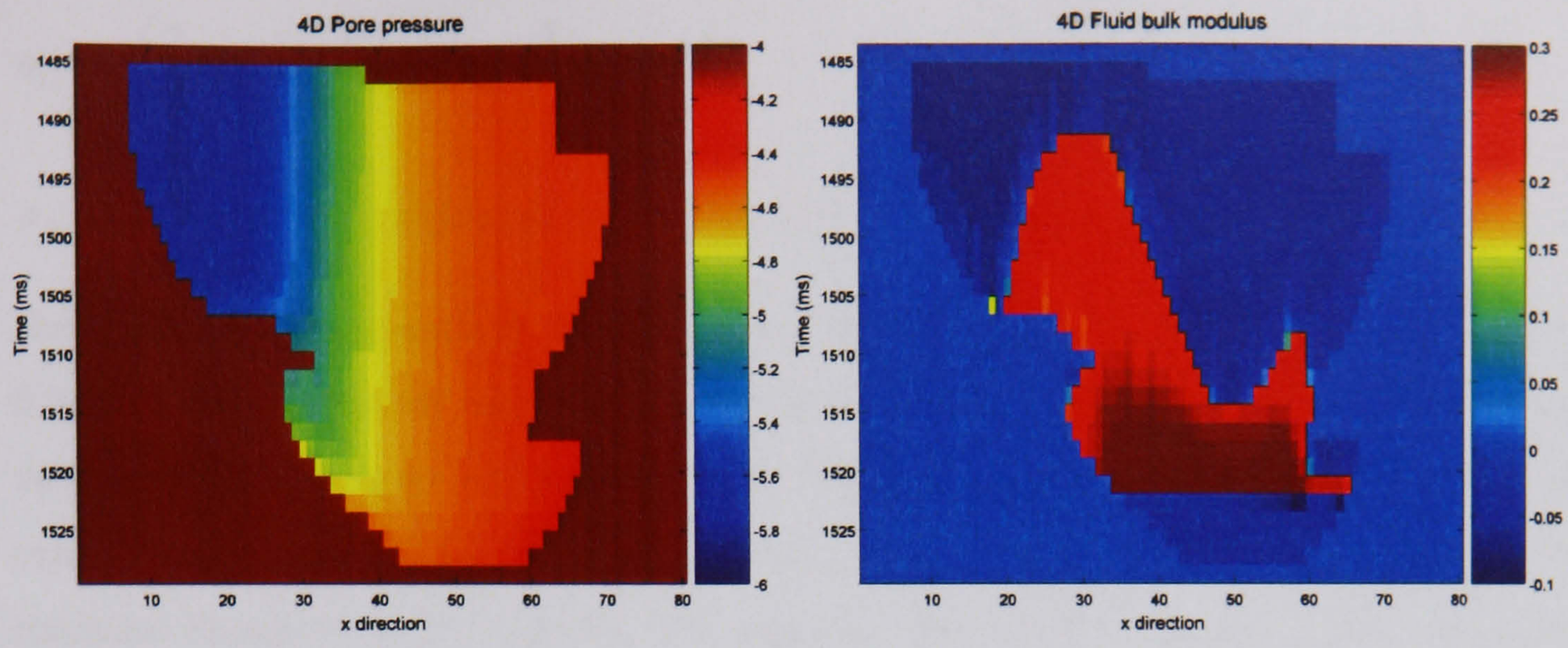

Figure 5.12: Simulated time-lapse pore pressure (left) and fluid bulk modulus (right) changes. The smooth pore pressure variations and region (red area) where the oil is swept by the upward movement of the water leg due to the reservoir pressure drop are visible.

5.7 Estimation of pore pressure and fluid saturation

5.7.1 The inversion process

As has been explained in Chapter 3, the discrimination of pore pressure and fluid saturation effects can be achieved by inverting for the pore pressure and the fluid bulk modulus. The inversion of these attributes is achieved in two steps. Firstly, a minimum of three elastic impedance angle stacks are required to invert the linear system (equation 5.5) in order to retrieve the saturation modulus, χ_s, the shear modulus, μ_d, and the density, ρ_s.

$$\begin{bmatrix} \ln(EI(\theta_{near})) \\ \ln(EI(\theta_{mid})) \\ \ln(EI(\theta_{far})) \end{bmatrix} = \begin{bmatrix} a_{11} & a_{12} & a_{13} \\ a_{21} & a_{22} & a_{23} \\ a_{31} & a_{32} & a_{33} \end{bmatrix} * \begin{bmatrix} \ln(\chi_s) \\ \ln(\mu_d) \\ \ln(\rho_s) \end{bmatrix} \tag{5.5}$$

$$a_{i1} = \left(\frac{1}{2} - \left(\frac{2}{3} + \frac{b}{2} \right) \gamma \right) sec^2 \theta_i$$

$$a_{i2} = \gamma\left(\frac{2}{3}\sec^2\theta_i - 4\sin^2\theta_i + \frac{b}{2}\sec^2\theta_i\right)$$

$a_{i3} = \left(1 - \frac{1}{2}\sec^2\theta_i\right)$, where i stands for the type of angle stack (i.e. near, mid or far).

Note that the linear system is inverted, assuming that the parameter b is a constant, equal to 0.7, and that the elastic impedance calibration with the well is optimal, so the constant velocity ratio chosen to model the synthetic impedance logs can be used. In this synthetic case, a least-squares minimization technique is used. Then, the pressure model for the shear modulus (equation 3.27) and the rock physics relationship (equation 3.26) are used to derive the pore pressure and fluid bulk modulus changes. To compute the pore pressure changes, stress-sensitivity parameters used for the petro-elastic transformation are selected. However, the calculation of the fluid bulk modulus changes requires the critical porosity of the sand, which is an unknown. To obtain the critical porosity representative of the Foinaven rock physics database, the critical porosity model (equation 5.6) for the dry bulk modulus (Mavko *et al.*, 1998) is used:

$$\kappa_d = \kappa_m\left(1 - \frac{\phi}{\phi_c}\right) \tag{5.6}$$

where κ_m, κ_d and ϕ_c stand for the mineral bulk modulus, the dry bulk modulus and the critical porosity, respectively. Laboratory dry bulk modulus and porosity measurements are used, and the bulk mineral modulus is assumed to be equal to 36.4 GPa. Calculated critical porosity is plotted against the corresponding sample porosity (Figure 5.13); the resulting critical porosity for sandstone with a porosity of 24% is equal to 33% and is used in equation 3.26.

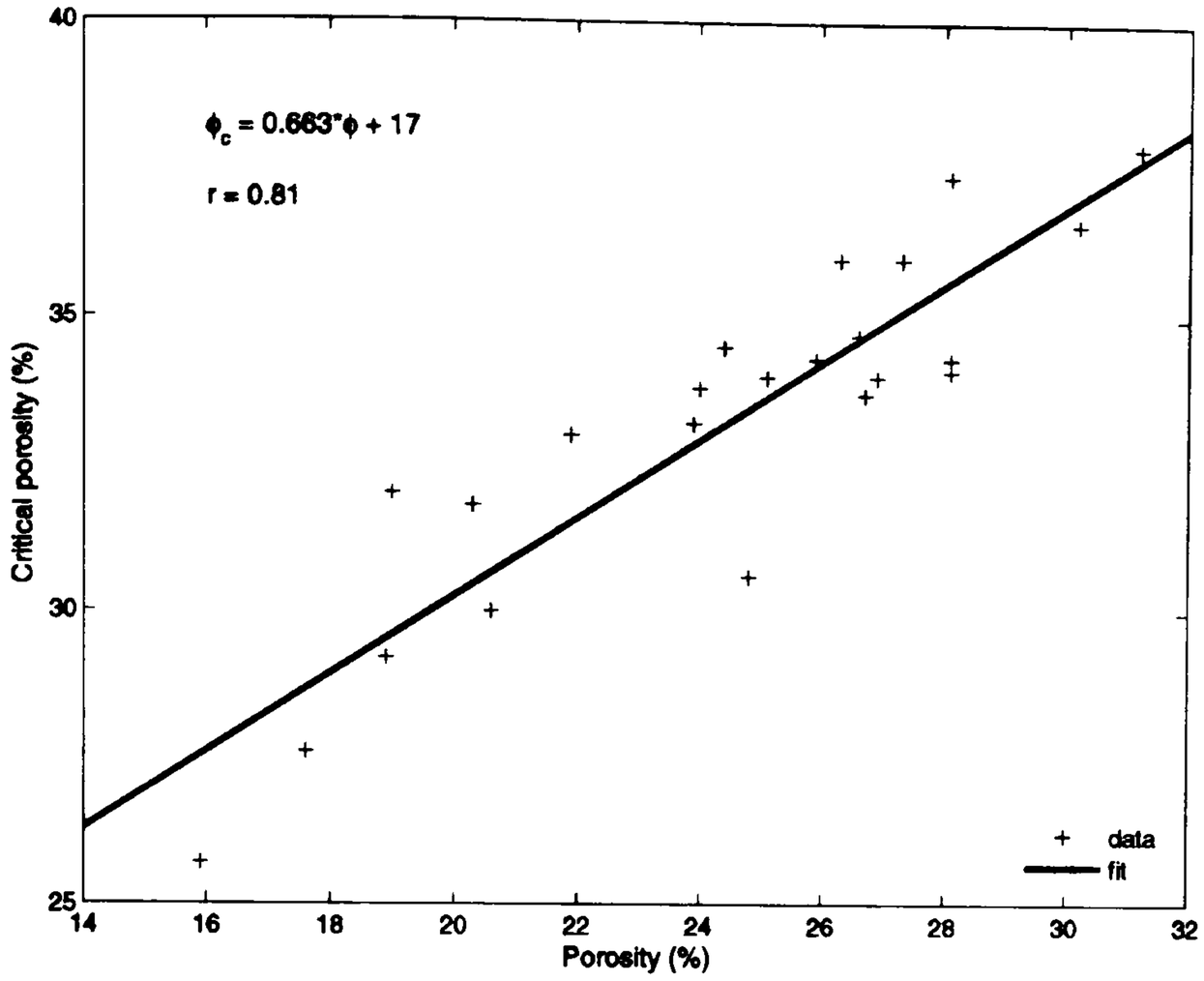

Figure 5.13: Plot of critical porosity against sample porosity. Data points are shown by the + symbols, while the line indicates their least-squares linear fit. A correlation coefficient of 0.81 is obtained between ϕ and ϕ_c.

Figure 5.14 and Figure 5.15 present the fluid bulk modulus and pore pressure changes obtained after inversion of the linear system (equation 5.5) and application of the rock physics approximations (equations 3.26 and 3.27). It can be observed that the estimated results compared well with the outputs from the flow simulator and there is no cross-talk occurring between the attributes. In fact, the smooth fluid pressure gradient and sharp saturation changes inside the reservoir channels are recovered. Changes ranging from 0.2 to 0.30 GPa are observed (Figure 5.14) for the fluid bulk modulus in the zone where the oil has been swept, whereas small changes appear in the rest of the reservoir. Pressure changes ranging from 4.4 to 6 MPa are visible (Figure 5.15) throughout the reservoir. This synthetic case shows the potential to discriminate between pressure and saturation effects, using an alternative form for the elastic impedance.

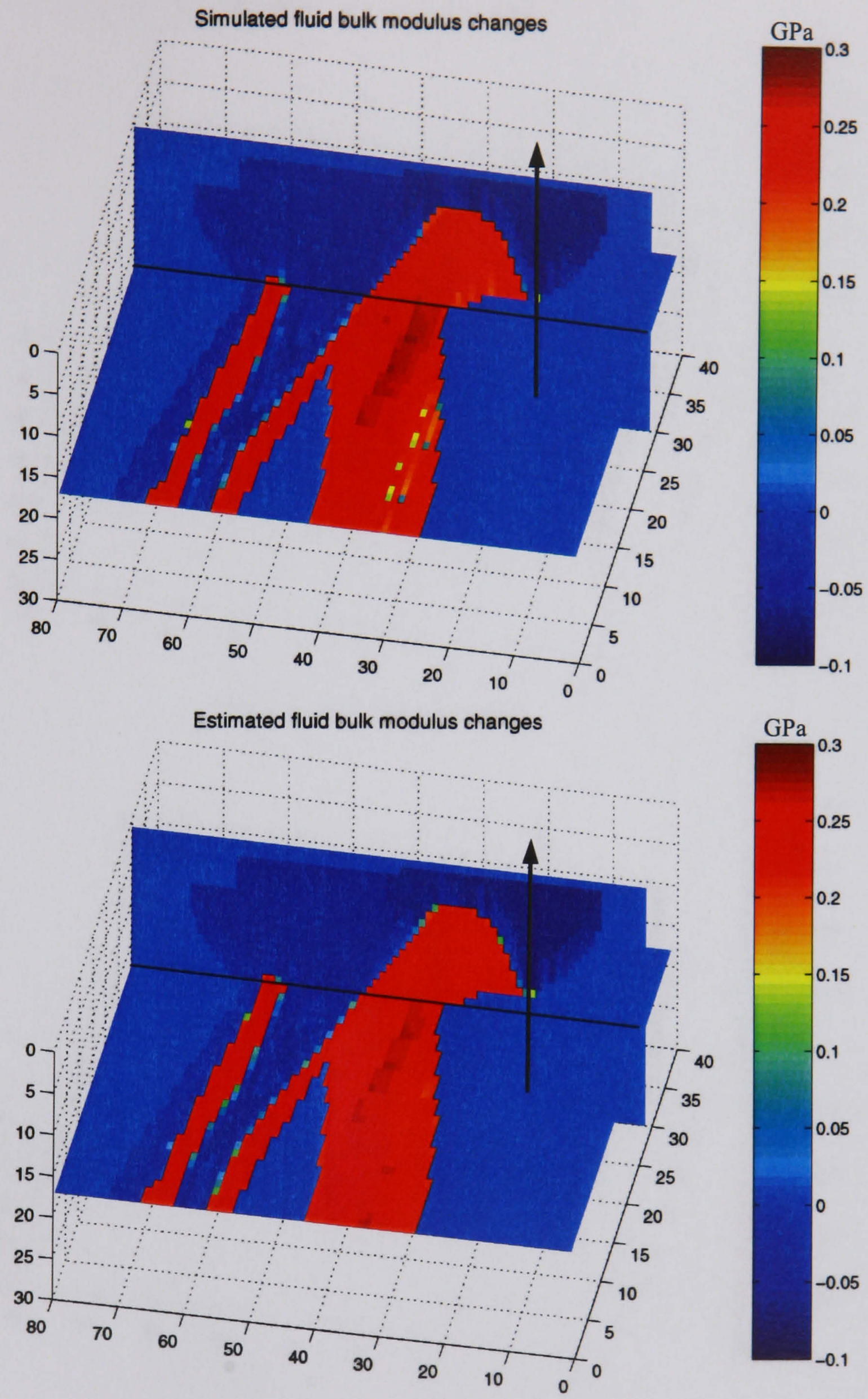

Figure 5.14: 3D display of the fluid bulk modulus changes from the simulator (top) and the inversion (bottom). The κ_f changes related to variations in brine saturation range from 0.2 to 0.3 GPa, and are in good agreement with the flow simulator predictions. The black arrow highlights the location of the producer.

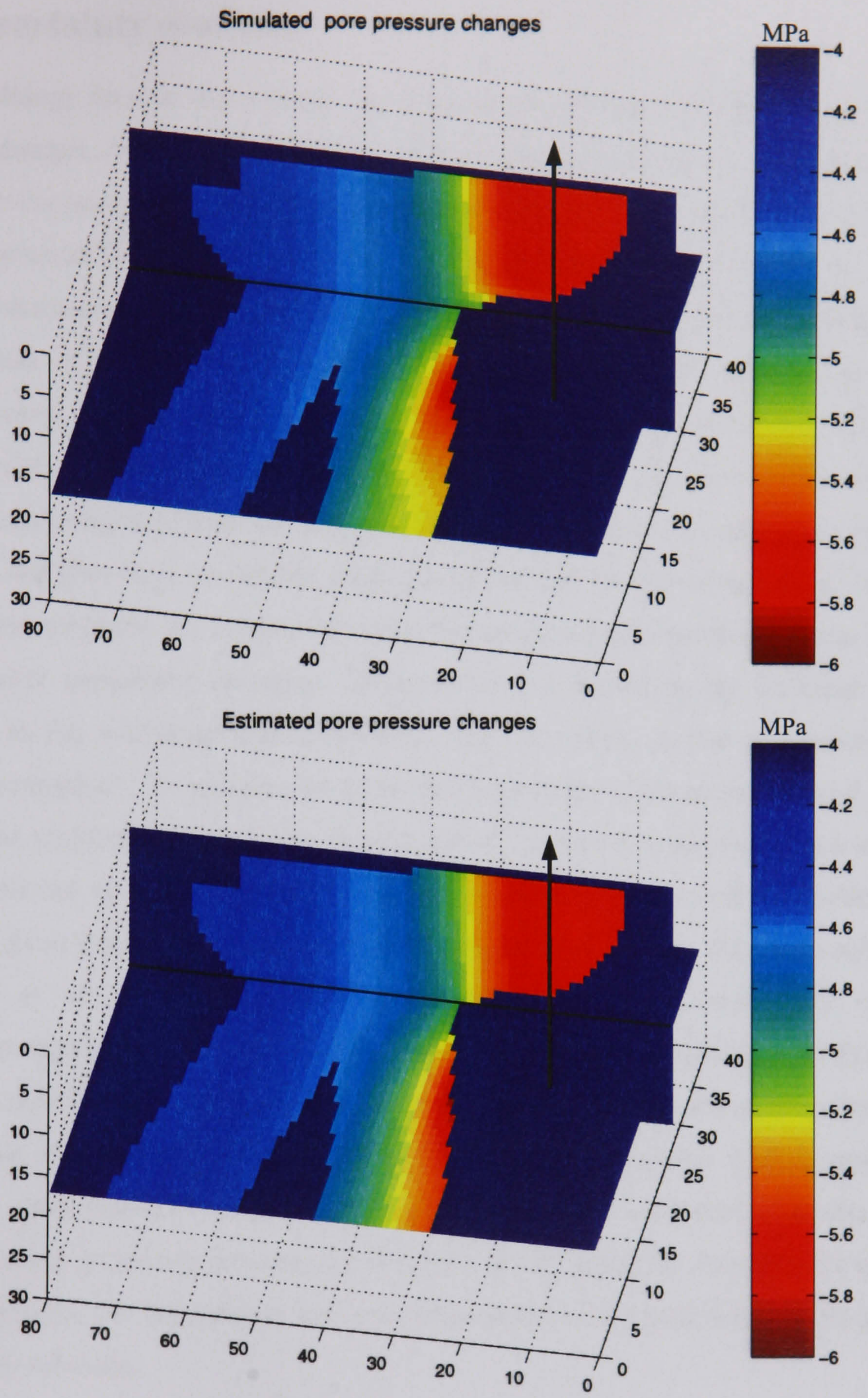

Figure 5.15: 3D display of the pore pressure changes from the simulator (top) and the inversion (bottom). P_p changes related to pressure depletion in the reservoir range from 4.4 to 6 MPa, and are in good agreement with the flow simulator predictions. The black arrow highlights the location of the producer.

5.8 Uncertainty analysis

The methodology presented previously has enabled an accurate estimation of pressure and saturation changes. Accuracy is defined as the true value or the location of the peak (Figure 5.16), while the precision is defined as the width of the bell curve (Kimminau, 1994). The deviation between the true value and the estimate is defined as the bias. In the previous section, the estimation was unbiased, because the elastic impedance values corresponded to the true values. With real data, estimation will generally contain a bias that is corrected for by a calibration step. Uncertainty analysis aims to measure the precision, also called standard deviation of the estimates, by taking into consideration all sources of errors. In this study, the errors originate from the rock physics approximations (uncertainty in the fitting procedure), and also from the seismic attributes (shear and saturation modulus). The errors in the seismic attributes are comparable with the magnitude of impedance errors obtained after an elastic impedance inversion. These errors are related to the inversion process (variability in the solution), angle estimation and, of course, to the uncertainty in the seismic measurements. To estimate the combined uncertainty in the saturation and pressure attributes, the previous errors need to be propagated. A stochastic approach such as Monte Carlo analysis can be used to generate the mean, standard deviation and distribution in the estimates – given that the distributions of each parameter are known. This approach is used by Lumley *et al.* (2003) to generate pressure and saturation uncertainty maps. A deterministic approach can also be used to compute combined uncertainties. In this case, a propagation model is derived by differentiation of the pressure and saturation relations. By assuming that all parameters are independent of each other, Landrø (2002) applied this approach to study the error propagation in his pressure and saturation estimates. In the following section, an uncertainty analysis is carried out by using the deterministic approach and by considering the dependency and non-dependency of the parameters in the pressure and saturation relations.

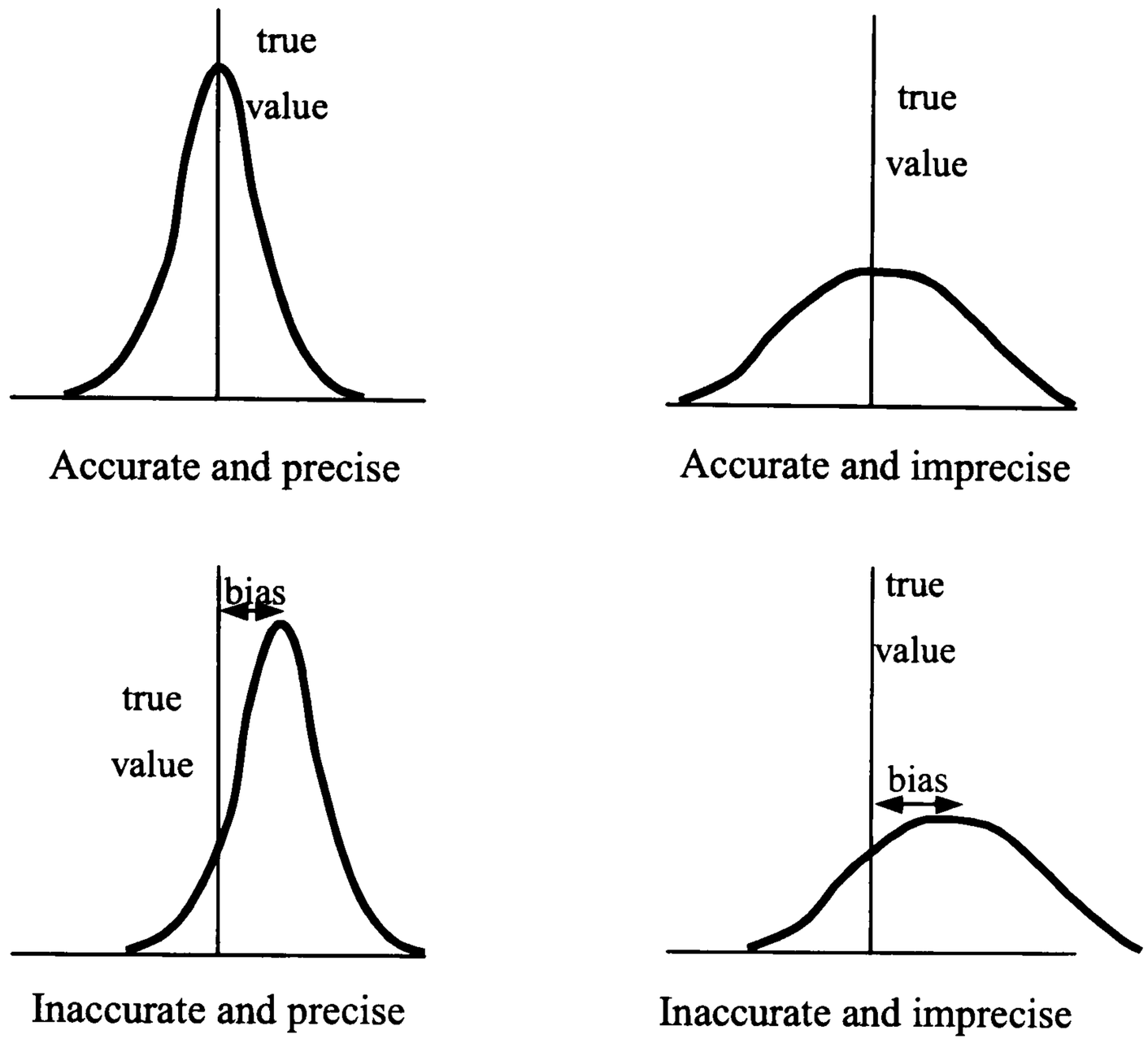

Figure 5.16: Illustration of accuracy and precision for four different distributions (Kimminau, 1994). True value and bias are also shown.

5.8.1 The propagation model

Assuming a physical entity y depending on n variables, $x = (x_1,\ldots, x_n)$ i.e. $y = f(x)$, it can be shown using a first-order Taylor expansion for $y = f(x_i)$, that the combined standard deviation $u(y)$ can be written as follows:

$$u(y) = \sqrt{\sum_{i=1,n} c_i^2 u(x_i)^2 + 2 * \sum_{\substack{i,k=1,n \\ i \neq k}} c_i c_k u(x_i, x_k)} \qquad (5.7)$$

where:

$$c_i = \frac{\partial y}{\partial x_i}$$

$u(x_i)$, $u(x_i, x_k)$ stand for the standard deviation of the parameter x_i and the covariance of x_i and x_k, respectively. The partial derivatives c_i represent the sensitivity coefficients of the entity y, and can be scaled to dimensionless quantities (equation 5.8).

$$C_i = \frac{\partial y}{\partial x_i} * \frac{x_i}{y} \tag{5.8}$$

It can be noted that $u(x_i, x_k) = u(x_i)u(x_k)r_{i,k}$ where $r_{i,k}$, the correlation coefficient, takes on a value between -1 and 1, depending on the degree of correlation between x_i and x_k. The effect of the correlation components can increase or decrease the uncertainty, depending on the sign of $r_{i,k}$. In the special case where it is assumed that the variables are independent, the covariance term in equation 5.7 can be simplified, since the correlation coefficients between the different variables are equal to zero. Equation 5.7 takes the following form, assuming independent variables:

$$u(y) = \sqrt{\sum_{i=1,n} c_i^2 u(x_i)^2} \tag{5.9}$$

From equation 5.7, it can be noted that the standard deviation of each variable x_i is weighted by the appropriate sensitivity coefficient. An analysis of the scaled sensitivity coefficients (equation 5.8) provides a classification of the variables as a function of their significance in the determination of the combined standard deviation $u(y)$.

5.8.2 Sensitivity analysis

Using equations 3.26 and 3.27, the sensitivity coefficients related to the pressure and fluid bulk modulus changes can be derived. The following sensitivity coefficients are obtained for the pressure changes:

$$\frac{\partial \Delta P}{\partial P_\mu} = \ln\left(\frac{\mu_1(\mu_\infty - \mu_2)}{\mu_2(\mu_\infty - \mu_1)}\right)$$

$$\frac{\partial \Delta P}{\partial \mu_\infty} = P_\mu \left(\frac{\mu_1 - \mu_2}{(\mu_\infty - \mu_2)(\mu_\infty - \mu_1)} \right)$$

$$\frac{\partial \Delta P}{\partial \mu_1} = -P_\mu \left(\frac{\mu_\infty}{\mu_1 (\mu_\infty - \mu_1)} \right)$$

$$\frac{\partial \Delta P}{\partial \mu_2} = P_\mu \left(\frac{\mu_\infty}{\mu_2 (\mu_\infty - \mu_2)} \right)$$

and for the fluid bulk modulus changes:

$$\frac{\partial \Delta \kappa_f}{\partial \phi} = -\Delta \chi_s \frac{\phi_c^2}{\phi^2}$$

$$\frac{\partial \Delta \kappa_f}{\partial \phi_c} = 2\Delta \chi_s \frac{\phi_c}{\phi}$$

$$\frac{\partial \Delta \kappa_f}{\partial \Delta \chi_s} = \frac{\phi_c^2}{\phi}$$

where $\Delta\chi_s$ is the saturation modulus changes between the repeat and base cases; μ_1 and μ_2 are the shear moduli for the base and repeat cases; ϕ and ϕ_c are the porosity and the critical porosity, respectively; and μ_∞ and P_μ are the stress-sensitivity parameters of the rock physics model (equation 3.5). The sensitivity coefficients computed are scaled as described previously, and are presented in Table 5.3. The average values of the coefficients are taken along a cross-section going through the producer (cf. Figure 5.14). It can be concluded that the high-pressure asymptote (μ_∞), the base and repeated shear moduli are the main parameters contributing into the uncertainty of the pressure changes. The contribution of P_μ appears to be negligible compared to the other parameters. In fact, this result is expected, since the robustness of the fit of the rock physics model to the laboratory data is more

influenced by a perturbation in the high-pressure asymptote, $\mu_{\infty,}$ than in the rate of pressure increase, P_{μ}. Errors in the determination of the porosity, critical porosity and saturation modulus changes make about the same contribution to the uncertainty of the fluid bulk modulus changes. In summary, sources of error mainly originate from the seismic attributes derived from the inversion process (equation 5.5), and also from the dominant parameter μ_{∞} in the approximation of the pressure changes.

Pressure changes		**Fluid bulk modulus changes**	
$\partial\Delta P/\partial\mu_{\infty}$	30	$\partial\Delta\kappa_f/\partial\phi$	–1
$\partial\Delta P/\partial\mu_1$	25	$\partial\Delta\kappa_f/\partial\Delta\chi_s$	1
$\partial\Delta P/\partial\mu_2$	–55	$\partial\Delta\kappa_f/\partial\phi_c$	2
$\partial\Delta P/\partial P_{\mu}$	1		

Table 5.3: Sensitivity coefficients for the pressure and fluid bulk modulus relationships (equations 3.26 and 3.27). Values are averaged over a cross-section going through the reservoir model and rounded to the nearest integer.

The sensitivity coefficients following the Landrø's approach (2001) for pressure and saturation discrimination introduced in Chapter 2 are computed (cf. Appendix C). Even if the sensitivity coefficient values are not directly comparable between the two approaches because of differences in the absolute values of the parameters involved, nevertheless, the classification of the error sources is still valid. In fact, it can be noted from Table 5.4: that the main factors contributing to the uncertainty of pressure and saturation changes are the input changes in intercept and gradient, which, by analogy, correspond to the shear and saturation modulus. Furthermore, the uncertainty in the pressure changes is also highly affected by the parameter, l_{α}, which represents the slope of the linear approximation between velocities and pressure changes. In comparison, the contributions of the parameters k_{α} and k_{ρ} might be negligible, since they are related to saturation changes and are therefore smaller. However, these parameters are responsible for half the contribution to the uncertainty of the saturation changes, compared to the input changes in intercept and

gradient. These two separate sensitivity analyses classify the origin of the error sources in an equivalent manner. Given a constant known geology, the main factors affecting the uncertainty of the final pressure and saturation estimates are, from the most significant to the least:

- Seismic attribute errors.
- Errors in the fitting parameters for the approximation of the pressure changes.
- Errors in the fitting parameters for the approximation of the saturation changes.

Pressure changes		**Saturation changes**	
$\partial\Delta P/\partial\Delta R_0$	23	$\partial\Delta S/\partial\Delta R_0$	8
$\partial\Delta P/\partial\Delta G$	34	$\partial\Delta S/\partial\Delta G$	8
$\partial\Delta P/\partial k_\alpha$	3	$\partial\Delta S/\partial k_\alpha$	4
$\partial\Delta P/\partial k_\rho$	–5.5	$\partial\Delta S/\partial k_\rho$	4
$\partial\Delta P/\partial l_\alpha$	23		

Table 5.4: Sensitivity coefficients for the pressure and saturation estimates, computed from Landrø (2002). The data example used in the calculation is introduced in Appendix C.

5.8.3 Uncertainty estimation using independent variables

In this first uncertainty estimation, it is assumed that the seismic attributes and rock physics parameters are weakly or non-dependent. This is equivalent to assuming random errors, meaning that the sign and magnitude of the errors may change randomly over time. Equation 5.9 is used to compute the combined standard deviation in the pressure and fluid bulk modulus changes. Required inputs for the uncertainty analysis are the standard deviations in all the parameters. From the Foinaven rock physics database, standard deviations of 17% (±0.04%) and 9% (±0.03%) are observed for the porosity and the critical porosity, respectively. A standard deviation of 10% (±0.71 MPa) is found for the stress-sensitivity parameters, P_μ, whereas a standard deviation of 3% (±0.24 GPa) is observed for

the high-pressure asymptote, μ_∞. The standard deviation of μ_∞ is derived for different porosity subsets, in order to remove the variability of the μ_∞ values due to porosity dependence (cf. Chapter 3). Since the shear and saturation modulus inversion follow the same inversion process as elastic impedance inversion, an overall standard deviation of 2% is assumed (Personal communication, Deschizeaux, 2005), due to inversion processes, which seems reasonable. To take into account the rock physics approximation error, an additional standard deviation of 3%, corresponding to an oil/brine system, is used for both moduli (cf. Chapter 3). This standard deviation is assumed to be constant, but will vary with the nature of the fluid saturant. For example, the error will increase when gas comes out of solution, because of the degradation in the rock physics approximation (equation 3.21). A cross-section going through the producer (cf. Figure 5.14) is selected in order to present the results from this analysis. Figure 5.17 presents profiles of the pressure and fluid bulk modulus changes, passing through the producer. Pore pressure decreases range from 5.4 MPa to a maximum of 6.4 MPa at the producer location, while the fluid bulk modulus changes are approximately constant (*c.*0.22 GPa) in the area that is water-swept close to the producer, and it abruptly drops to zero in the unswept area. It can be seen that the estimated uncertainties (Figure 5.18) are around three times larger than the pressure estimates, and a quarter of the saturation estimates themselves. These uncertainties, being dependent on the value of the seismic attributes, appear to be larger in the vicinity of the producer. In a real field study, uncertainties will be smaller at the well locations due to the added constraints from well data. Sensitivity coefficients from Table 5.3 show that the error contributions are much larger in the case of pressure than the saturation estimates. If the sensitivity coefficients of Table 5.3 are used in equation 5.9, average standard deviations of 315% (±20 MPa) and 25% (±0.06 GPa) are obtained for the pressure and saturation estimates, respectively. This is in agreement with the observations made previously, and also with another study (Landrø, 2002) where relatively large uncertainties were derived using the same approach. It can be concluded that, in this special case, the assumption of independent variables leads to an overestimation of the uncertainties – particularly for the pressure estimates.

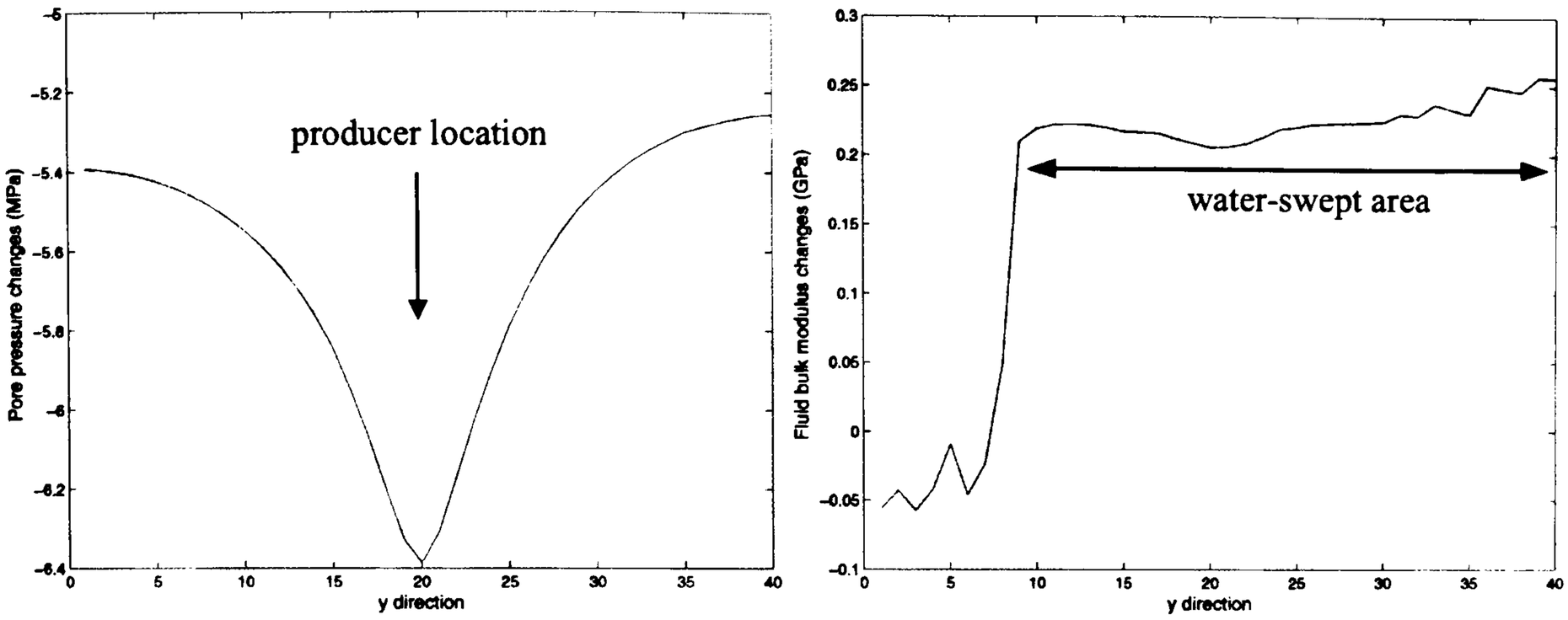

Figure 5.17: Cross-sections of pore pressure change (left) and fluid bulk modulus change (right), going through the producer location.

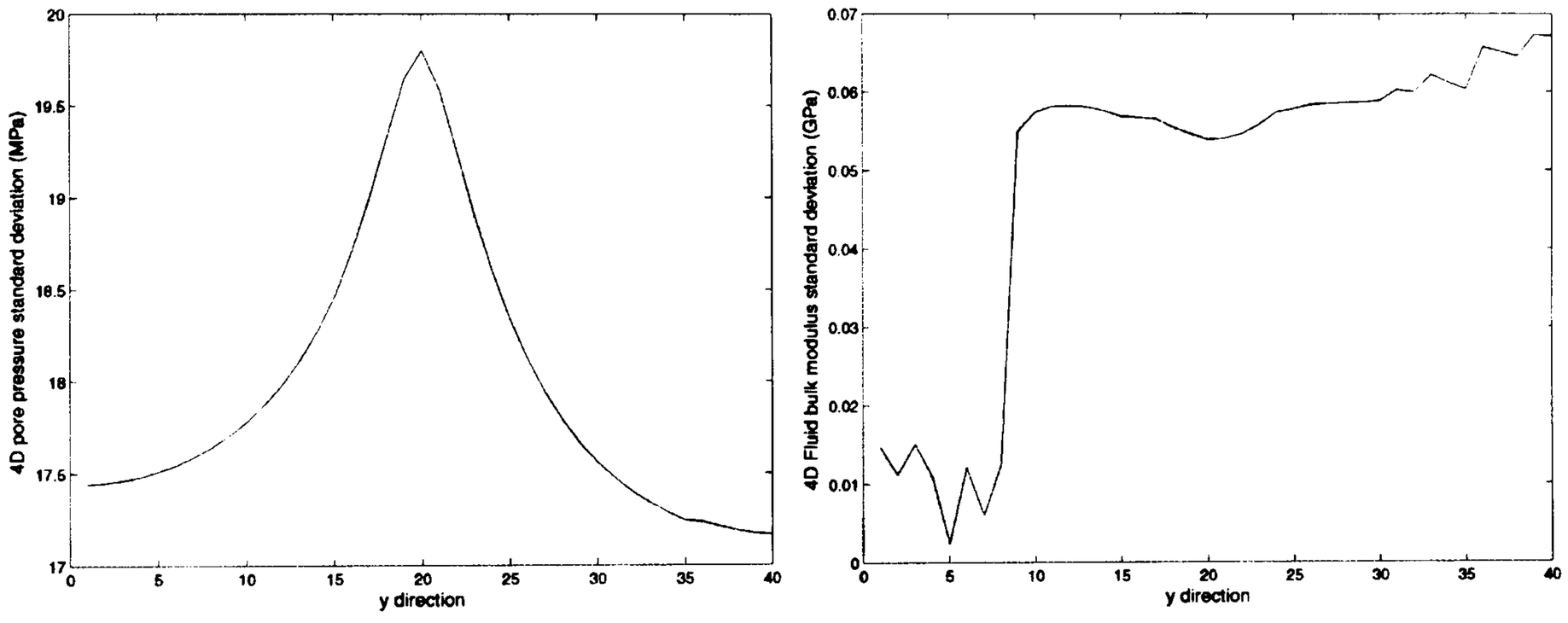

Figure 5.18: Uncertainties in the estimated pore pressure change (left) and fluid bulk modulus change (right), assuming independent variables.

5.8.4 Uncertainty estimation using interdependent variables.

This approach includes uncertainty due to systematic errors, meaning that the sign and magnitude of the errors remain fixed over time and are therefore predictable. The correlation coefficients (equation 5.7) of the different parameters are derived from the rock physics database. It is observed that there is a correlation of 0.90 between μ and μ_∞; and 0.81 between the porosity and the critical porosity. No evident correlation is observed between P_μ and μ_∞ as well as P_μ and μ. A correlation of 0.95 between the time-lapse

seismic attributes μ_1, μ_2 is also observed. The correlations between the saturation modulus changes and the different porosities are assumed to be negligible, since saturation modulus is independent of porosity. A summary of the correlations between the different variables is presented in Table 5.5.

	μ_1	μ_2	μ_∞	ϕ	ϕ_c	P_μ
μ_1	1	0.95	0.9	*N/A*	*N/A*	0
μ_2	0.95	1	0.9	*N/A*	*N/A*	0
μ_∞	0.9	0.9	1	*N/A*	*N/A*	0
ϕ	*N/A*	*N/A*	*N/A*	1	0.81	*N/A*
ϕ_c	*N/A*	*N/A*	*N/A*	0.81	1	*N/A*
P_μ	0	0	0	*N/A*	*N/A*	1

Table 5.5: Correlation coefficients between the different variables from the combined standard deviation expression (equation 5.7).

Figure 5.19 demonstrates that including the covariance term in equation 5.7 significantly reduces the standard deviations in the estimated pressure and saturation attributes. The uncertainties are approximately 100% (±6.4 MPa) and 18% (±0.04 GPa) for the pressure changes and fluid bulk modulus changes, respectively. The negative sensitivity coefficients associated with the porosity (Table 5.3) are the cause of the reduction of the standard deviation of fluid bulk modulus changes. In the case of the pressure changes, μ_1, μ_2 and μ_∞ are nearly fully correlated, but the sensitivity coefficient of μ_2 (–55) shows an opposite sign compared to μ_1 and μ_∞ (25 and 30, respectively). This explains the large decrease in uncertainty related to the pressure changes.

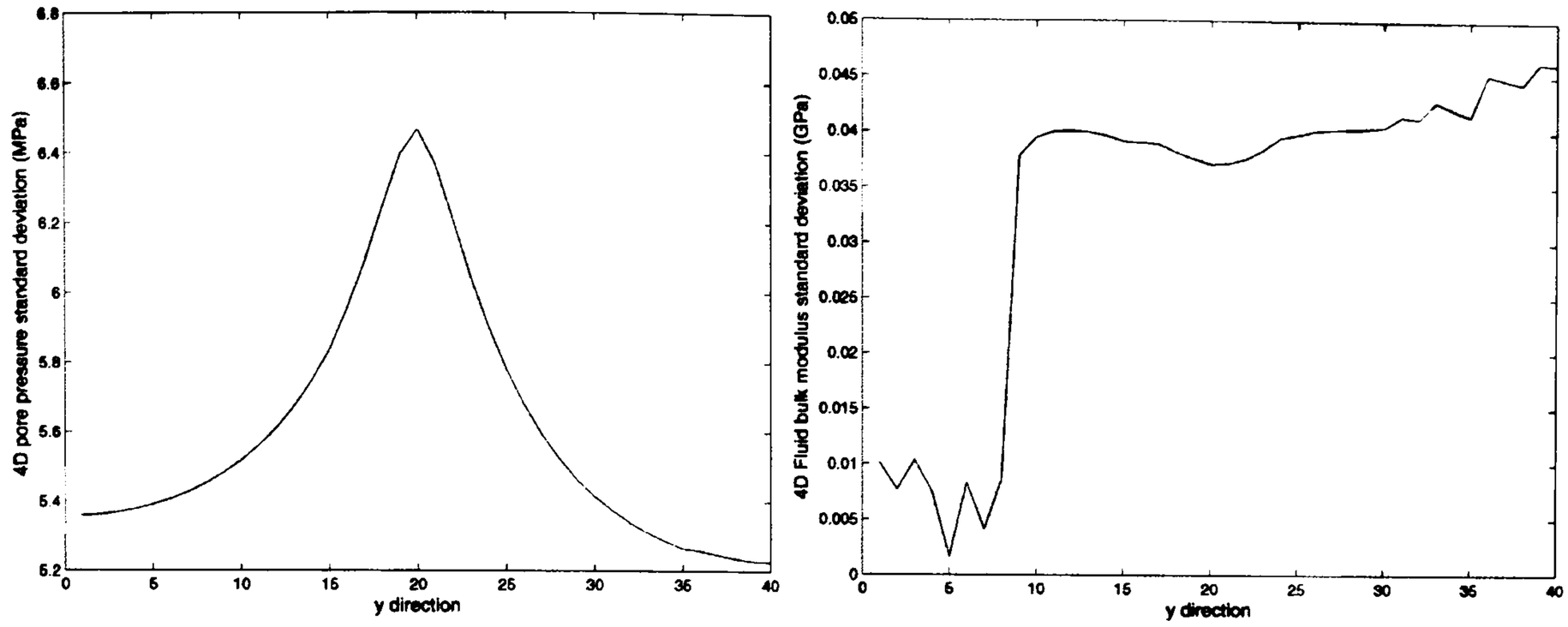

Figure 5.19: Uncertainties in estimated pore pressure changes (left) and fluid bulk modulus changes (right), assuming dependent variables.

By including the dependence between parameters in the estimation of the uncertainty, it is shown that the precision of the pressure and fluid bulk modulus estimates can be improved. Figure 5.20 presents the pore pressure and fluid bulk modulus uncertainty estimates in two channels from the flow simulation models. A further improvement would be to include the spatial correlation between the parameters. The approach where random errors are assumed does not take into account for the time-lapse aspect of the data into the uncertainty analysis. Therefore, the systematic errors that occur between the different surveys are ignored.

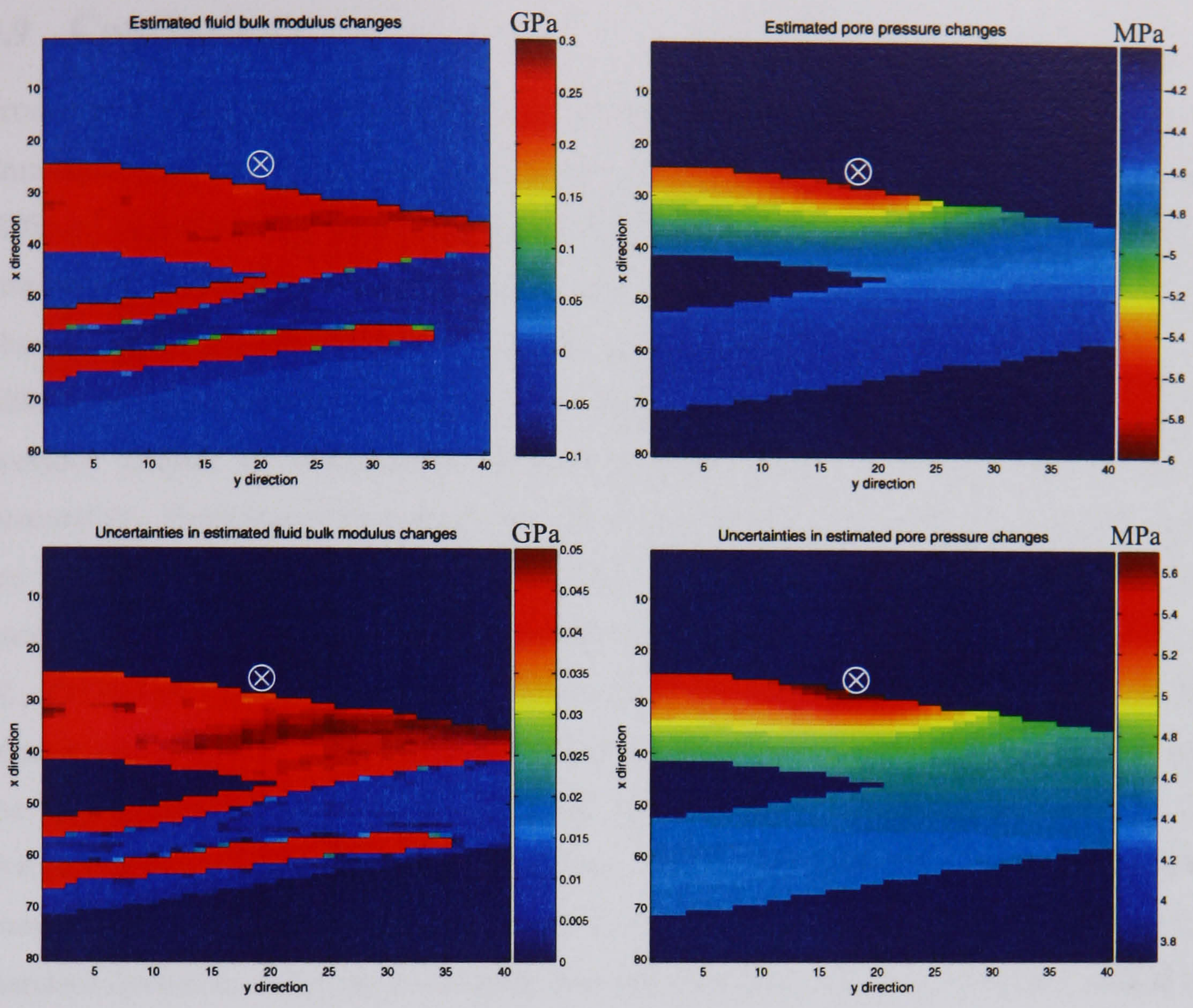

Figure 5.20: Estimated fluid bulk modulus (top left) and pore pressure (top right) changes, together with uncertainties in the respective estimates. The ⊗ symbol stands for the location of the producer well.

5.9 Conclusions

From a reservoir simulation study carried out on a turbidite channel system, the synthetic time-lapse changes in the seismic and elastic impedance domains are modelled. The difficulty of interpreting 4D seismic data when both pressure and saturation effects occur is emphasized. In fact, the saturation changes are found to dominate the 4D signature and to obscure the 4D signature caused by pressure changes. In order to provide an alternative to differentiating between the two types of signature, the new methodology, introduced in the previous chapter to discriminate between saturation and pressure effects, is tested successfully. Estimates of pore pressure changes and fluid bulk modulus changes over time are found to be in good agreement with the outputs from the reservoir simulator. The uncertainty analysis shows results comparable to previous work (Landrø, 2001; Lumley *et al.*, 2003), and also demonstrates that pressure changes are more sensitive to errors in the seismic attributes and fitting parameters than saturation changes. It can be concluded that the assumption of independent variables in the uncertainty analysis leads to an overestimation of the standard deviation. The magnitude of these uncertainties compromises their use for further analysis (i.e. risk management). An estimation of the standard deviation, using the covariance term between interdependent variables, should be preferred in order to gain benefit from the time-lapse aspect of the data. Amplitudes in time-lapse seismic after state-of-the-art processing are highly repeatable and their errors are expected to be highly predictable. Cross-coupling between the parameters is largely reduces the combined standard deviation on the pressure and saturation estimates.

Chapter 6

A case study from the west of Shetland

In the previous chapter, a methodology was applied to a synthetic case study to discriminate between pressure and saturation effects. From a reservoir model-based study, it was shown that the pore pressure and the fluid bulk modulus attributes could be inverted successfully. In the current chapter, this methodology is applied to the deep-water Palaeocene sandstones of the Foinaven field, west of Shetland. A geological and exploration history of the area to the west of Shetland is presented. This is followed by a description of the time-lapse parallel processing and 4D stratigraphic inversion applied to two seismic surveys, in order to obtain the required inputs for pressure and saturation inversion. Finally, an independent estimation of pressure and saturation is carried out and compared with the prediction from the reservoir flow simulator provided by the operators.

6.1 The Foinaven field

The Foinaven field lies 190 km west of the Shetland Isles (Figure 6.1), in a water depth of 500 metres. In 1992, this field, which is operated by BP, was the first oil discovery to be developed in the deep water in the area to the west of Shetland.

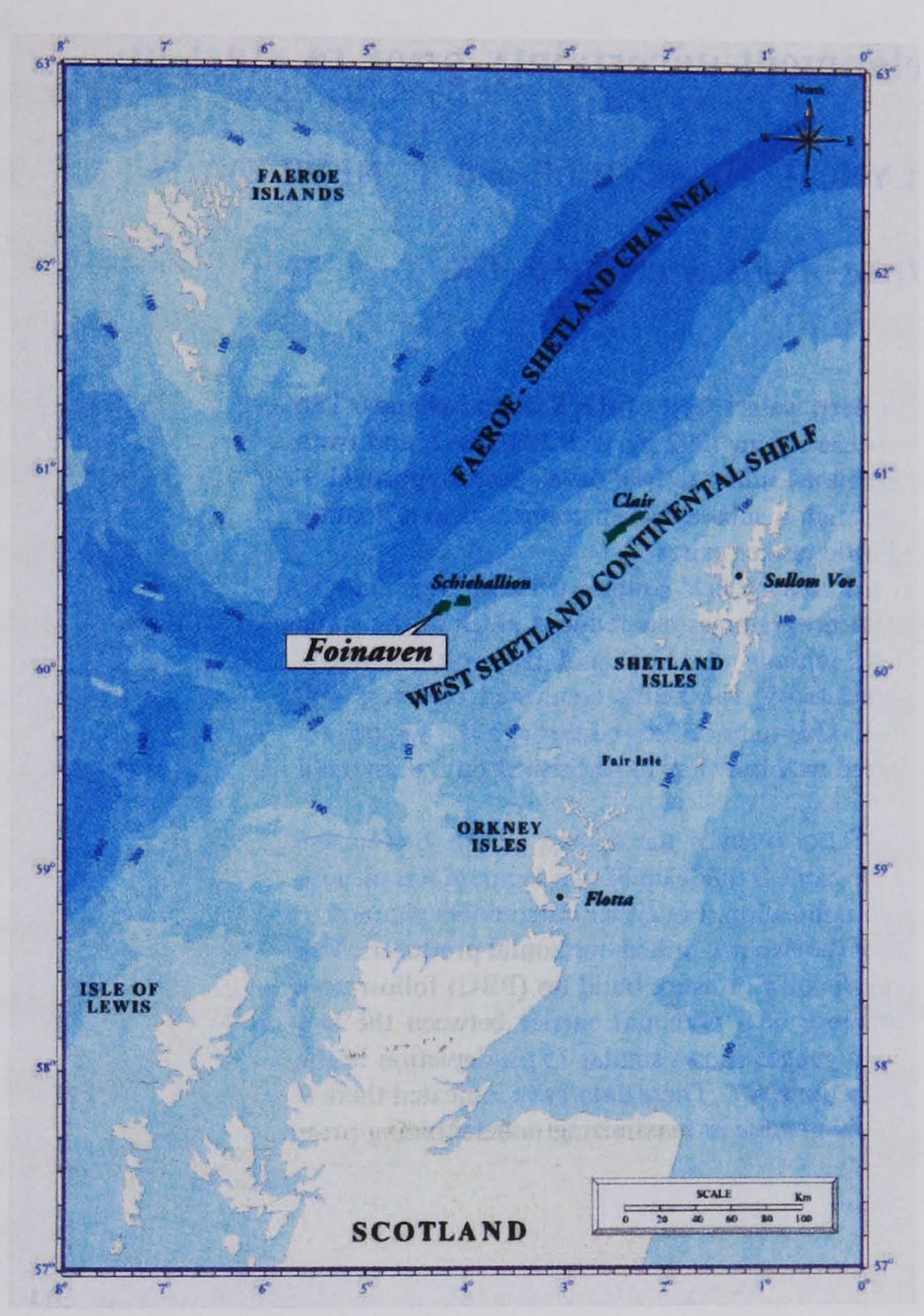

Figure 6.1: Map showing the location of the Foinaven field (from Cooper, 1999a).

6.1.1 Geological setting

The region of potential interest for hydrocarbon exploration to the west of Shetland is located in the Faeroe–Shetland Basin. This basin is divided into two main areas: the Flett Sub-basin in the north-east, and the Foinaven Sub-basin in the south-west (Figure 6.2).

During the Palaeocene, these two sub-basins were fed mainly by sediment from the south-east (Shetland platform), with rare volcanic materials derived from a basaltic source to the north-east. At sea-level lowstands, these sediments were eroded from the shelf sandstone in the south-east, and deposited as slope or basin-floor turbidites in the deep water of the Foinaven and Flett Sub-basins. In the case of the Foinaven field, these turbiditic sands represent the actual reservoir plays (Lamers *et al.*, 1999). Figure 6.3a illustrates the depositional environment of the middle Palaeocene. These reservoir sands are of late Palaeocene age, and are assigned to the T30 sequence. The 'T' stratigraphic sequence is used in the area to the west of Shetland to subdivide the Palaeocene sequence into distinct bio-events (Ebdon *et al.*, 1995; Figure 6.3b). In the late Cretaceous, a large amount of mudrock covered the basin, and this helped to bury the Jurassic source rocks to depths sufficient for hydrocarbon generation. The hydrocarbons then migrated via the Lower Cretaceous sandstones to form palaeo-accumulations. At the end of the Palaeocene–early Eocene, the Cretaceous mudrock seals fractured due to the sedimentation conditions, and the trapped palaeo-accumulations were released, allowing the hydrocarbons to migrate towards the present deep-water reservoir traps. The last event in this sedimentation cycle was of a pyroclastic nature, forming the Balder Tuff. This event was widespread in the area, and represents a reference marker that will be used in the time-lapse survey matching (Section 6.2). Structurally, the Foinaven field is subdivided into five panels defined by the faulting pattern of the area (Figure 6.4). The T30 Palaeocene sands are also further divided into three layers (T31, T32, T34), which make up the main reservoir sands of the field (Cooper *et al.*, 1999a).

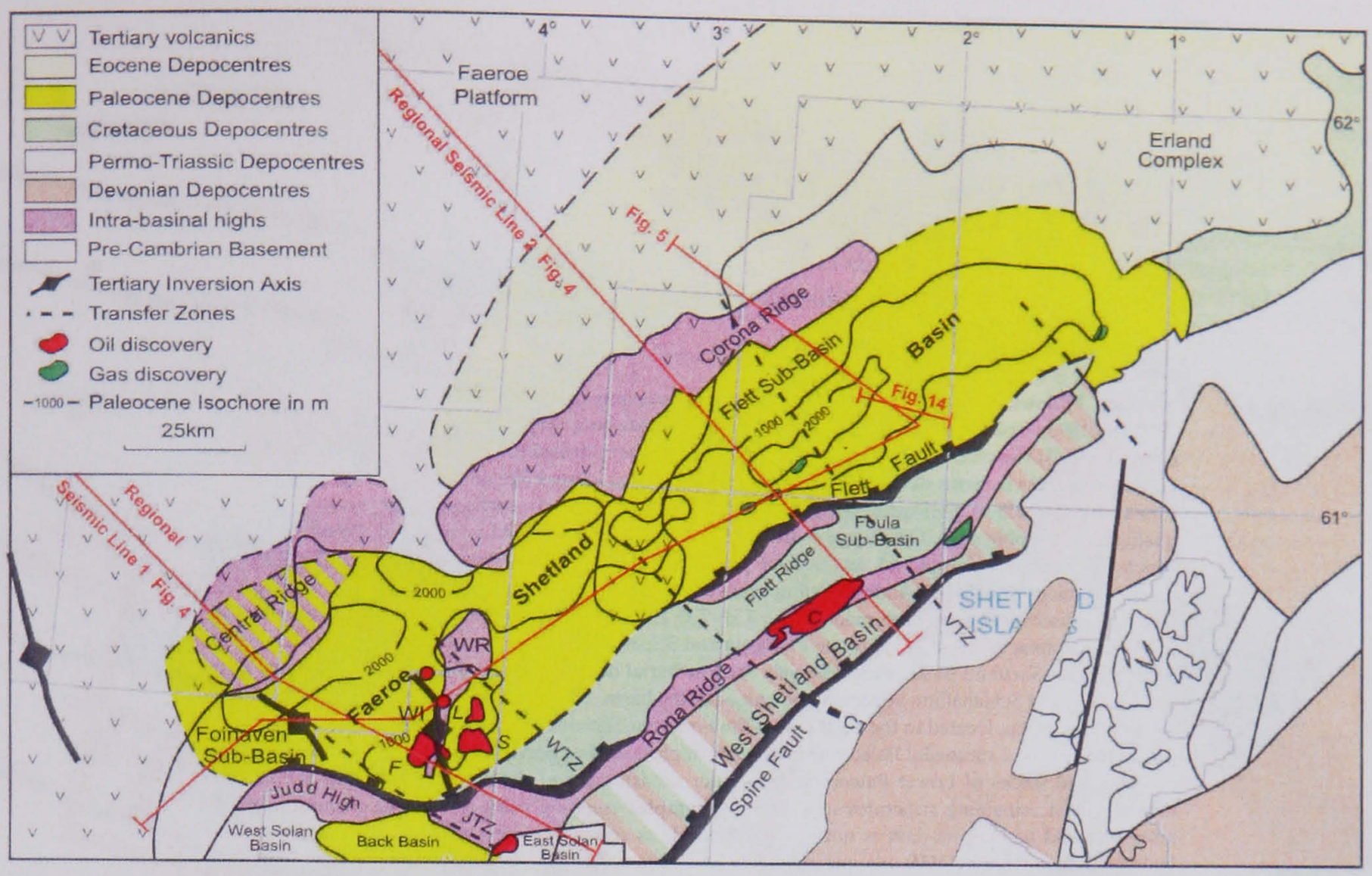

Figure 6.2: Faeroe–Shetland basin structural map. WR = Westray Ridge; WI = Westray Inversion; JTZ = Judd Transfer Zone; WTZ = Westray Transfer Zone; CT= Clair Transfer Zone; VTZ = Victory Transfer Zone (from Lamers *et al.*, 1999).

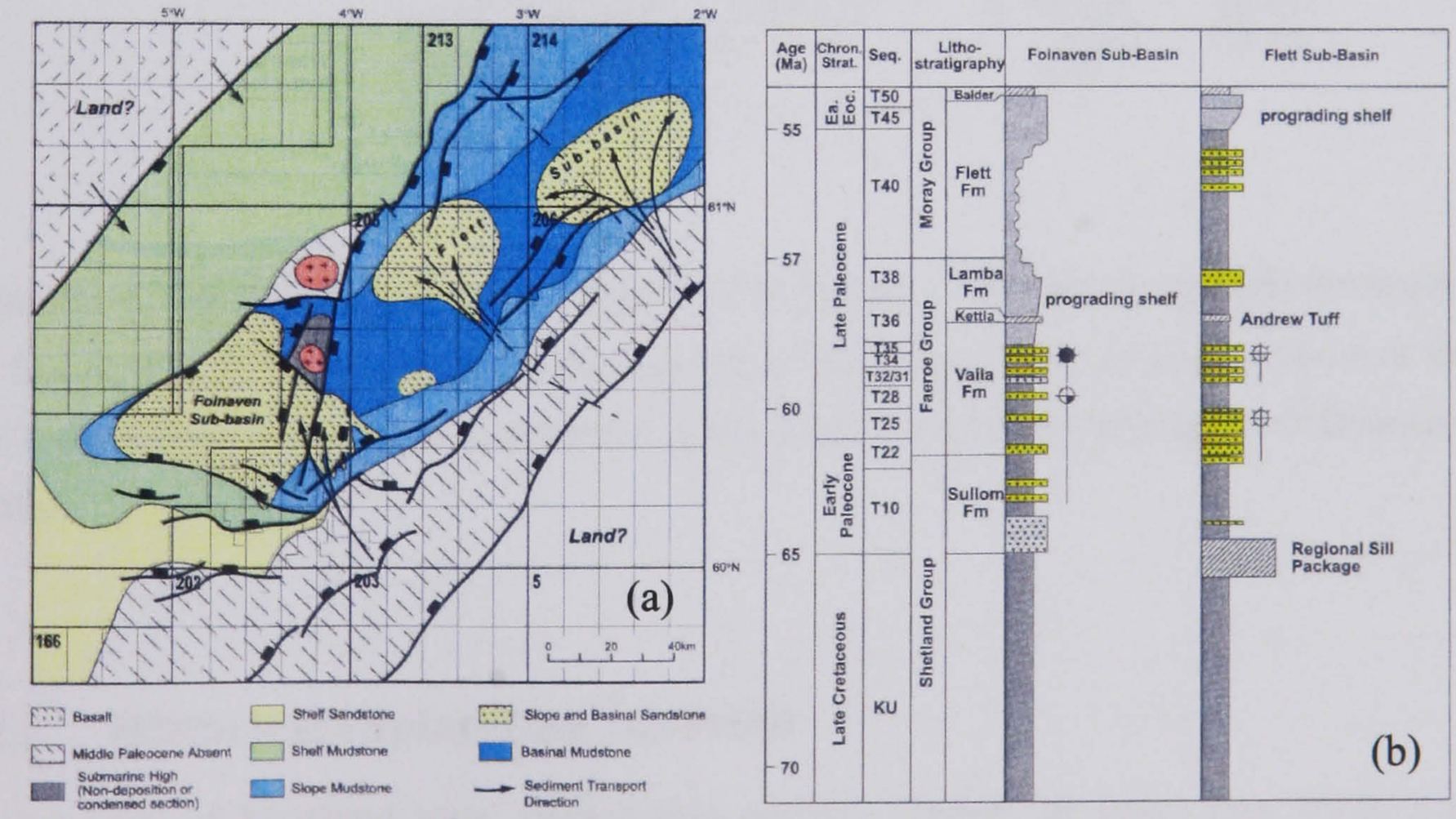

Figure 6.3: (a) Middle Palaeocene depositional environments and (b) T30 sequence stratigraphy (from Lamers *et al.*, 1999).

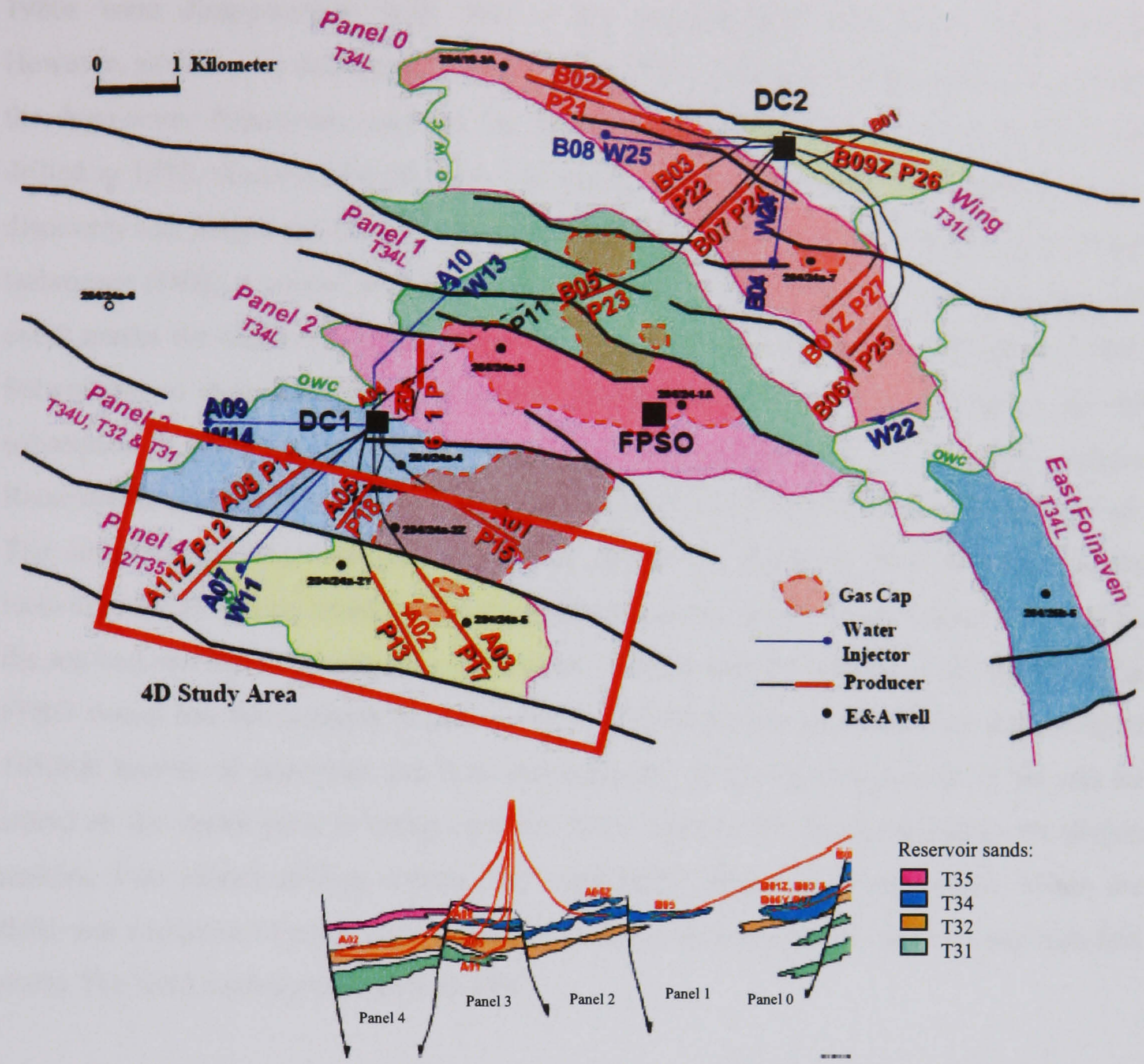

Figure 6.4: Partition of the Foinaven field and distribution of the Palaeocene turbidite sands within the five panels. A map (top) shows the location of the injector and producer wells over the field. The cross-section presents the distribution in depth of the different sands (from O'Donovan *et al.*, 2000).

6.1.2 Historical exploration overview

In the west of Shetland area, exploration activity started 30 years ago. First, the Clair oilfield was discovered by BP in 1977, but, due to its complex structure (a highly fractured reservoir), it is only recently that the technology became available to exploit it fully. The

1980s were disappointing, with only a few sub-economic discoveries being made. However, advances in drilling technology in the 1990s provided the opportunity to explore the deep-water Palaeocene sand of the Foinaven Sub-basin. The first exploration well, drilled in 1990, discovered a 10-metre oil and gas column (Cooper *et al.*, 1999a), but the discovery was judged too risky to continue. Thanks to the application of direct hydrocarbon techniques (DHI), a second well was drilled in 1992, encountering a 50-m oil column. This event marks the discovery of the Foinaven field, which started to be developed in 1994. Subsequent to this discovery, exploration increased in the west of Shetland, with the subsequent discovery of the Schiehallion and Loyal (Figure 6.1) fields, among others. Recoverable reserves are predicted to be in the order of 250 to 600 million barrels of oil. The actual development programme carried out in the Foinaven field is based on the recovery of 200 million barrels of oil through the completion of subsea wells positioned on the sea-bed and linked to a floating production, storage and off-loading vessel (FPSO). The FPSO vessel has the capacity to process up to 95,000 barrels of oil per day and to inject 165,000 barrels of sea-water per day. Furthermore, up to 300,000 barrels of oil can be stored on the vessel prior to being exported to the west of the Shetland Islands via shuttle tankers. Two subsea drilling centres (DC1 and DC2) (Figure 6.4) are present within the field, and comprise 14 production wells, seven water-injection wells, and two gas-injection wells. The field started production in 1997.

6.2 Time-lapse seismic in the Foinaven field

The first 3D seismic survey was acquired over the Foinaven area in 1993. This survey was used to study the geometry of the turbidite channel complex, and also to delineate the location of the oil–water contact. With the development of time-lapse seismic in the early 1990s, the Foinaven Active Reservoir Monitoring (FARM) project was carried out in order to assess the advantage of using 4D towed steamer surveys compared to permanently installed cables (Cooper *et al.*, 1999b). Two surveys for each installation were shot in 1995 and 1998 over the Panel 4 segment and a part of the Panel 3 – both located in the southern part of the field (Figure 6.4, rectangular area). Both towed streamer and sea-bed data

showed an improvement in the delineation of the oil–water contact and also the resolution of the gas–oil contact. Baseline surveys were used to update fluid contacts and faulting in the reservoir model (Cooper *et al.*, 1999c). Predictions from the new model were then favourably compared with the time-lapse signal (Cooper *et al.*, 1999d). The FARM project turned out to be a successful experience that proved the potential of time-lapse seismic to improve the qualitative interpretation of reservoir changes and to impact reservoir management strategy. Furthermore, the study showed that sea-bed installation had the potential to provide a clearer time-lapse signal, due to the better receiver repeatability (Kristiansen *et al.*, 2000). However, to date, the Foinaven field has been subject to four repeated towed streamer surveys (1999, 2000, 2002 and 2004), but so far no attempt to deploy a permanent sea-bed installation has been reported. This preference for the use of towed streamer surveys is probably due to the lower cost and higher turnaround of seismic surveys due to improvements in technology, as compared to the more costly subsea installation. In this chapter, Panel 1 is selected to carry out an independent estimation of pressure and saturation effects, because no major gas cap is present in this area, thus slightly simplifying the study. The survey of 1993 (before the first oil) and the repeated survey of 2002, are chosen as baseline and repeated vintages, respectively.

6.2.1 Time-lapse parallel processing

The 4D pre-stack processing was carried out by CGG (Compagnie Générale de Geophysique) at the Dedicated Processing Centre at BP Exploration, Aberdeen, while the post-stack processing was modified for the purpose of the current work. The objective of the 4D parallel processing was to improve the repeatability of the dataset and the time-lapse signature compared to previous similar processing (CGG, 2002).

A Survey description and acquisition

The 1993 and 2002 seismic surveys are part of the world's largest 4D survey acquired across three producing fields: Schiehallion, Loyal and Foinaven. In order to obtain a satisfying repeatability, acquisition geometry and equipment tend to be made as similar as

possible between surveys. However, due to the improvements in technology occurring between the elapsed time of the baseline and the last survey, some parameters have been found to be different. Table 6.1, Table 6.2 and Table 6.3 present the detailed acquisition characteristics of the different vintages. It should be noted that, due to the FPSO installation present in Panel 1, an area could not be shot. This area was undershot during the 2002 acquisition.

Survey	**1993 survey**	**2002 survey**
Location	Quad 204 west of Shetland	Quad 204 west of Shetland
Survey carried out by	PGS	PGS
Total number of lines	MV Nordic Explorer	MV Ramform Viking
Number of traces per shot	960	240
Bin size	6.25 × 30 m	6.25 m × 25 m
Stacking fold	40	40
Type of operation	Single-vessel operation	Single-vessel operation, except undershoot
Filters		
• Low cut	8 Hz, 18 dB/oct	3 Hz, 6 dB/oct
• High cut	218 Hz, 484 dB/oct	218 Hz, 484 dB/oct
Record length	4600 ms	5120 ms
Sample interval	2 ms	2 ms

Table 6.1: Survey characteristics for the 1993 and 2002 acquisitions.

Survey	**1993 survey**	**2002 survey**
Type of energy source	Sleeve airguns	G guns
Shotpoint interval	18.75 m flip-flop	18.75 m flip-flop
Number of sources	2	2
Source volume	2620	3090
Source pressure	2000	2500
Source depth	6 m ± 0.5m	7 m ± 0.5 m
Source separation	50 m	50 m

Table 6.2: Energy source parameters for the 1993 and 2002 acquisitions.

Survey	1993 survey	2002 survey
Number of cables	4	10
Nominal cable interval	120 m	100 m
Cable length	3000 m	3000 m
Number of groups	4 × 240	10 × 240
Group interval	12.5 m	12.5 m
Cable depth	9 m ± 1 m	8 m ± 1 m

Table 6.3: Streamer parameters for the 1993 and 2002 acquisitions.

B Pre-stack processing sequence

In order to obtain an optimal time-lapse signature, the three datasets are processed in parallel with an identical processing sequence. The advantage of parallel processing comes from the reduction of acquisition and processing artefacts that conventionally arises because of a different choice of processing parameters (Harris and Henry, 1998). Table 6.5 gives an overview of the processing sequence applied to the entire dataset prior to stacking. Some key features in this processing sequence are needed in order to better tackle the problems inherent in this unique deep-water time-lapse project. Multiple energies are very strong in the area to the west of Shetland, and these tend to mask the reservoir unit. High-resolution radon demultiple techniques (Hugonnet *et al.*, 2000), which take advantage of the difference in move-out between primary and secondary energies, are applied prior to and after dip move-out (DMO) correction. However, because of their similarity in move-out compared with the primary events, peg-leg multiples are not optimally attenuated and could damage the 4D signal in some areas. Static correction is also required in order to correct for the time shift due to sea-water velocity variations (Bertrand and MacBeth, 2005) in this deep-water environment. Even if seismic surveys are generally shot in the same seasonal period, water velocity variation due to ocean currents will occur. These velocity variations of the water layer cause an observable time shift between 4D surveys, and also between prime and infill data. Those time shifts, if not corrected, decrease the coherence between surveys and can also have a large impact on the derivation of AVO attributes or AVO-based techniques used to discriminate fluid and lithological properties (Bertrand *et*

al., 2004). A cold-water static correction is applied to the data in order to minimize these effects. Furthermore, a final time-shift correction is applied to the data in order to remove the time differences between surveys due to different cable depth, source depth or navigation errors. This robust process, called trim static correction, also makes it possible to remove the jitter within a common depth point (CDP) gather without causing a deterioration in the residual normal move-out. These last two processing steps, which are described above, are essential in order to ensure time consistency between the two vintages. Prior to stacking, a global matching procedure is applied to compensate for the mismatch in the amplitude and phase between surveys. Phase-only and amplitude-only matching filters are computed on a time window of 1.5 s, using superline gathers for each survey. The superline gathers consist of in-line gathers at 1500-m intervals. Figure 6.5 shows the convergence obtained in amplitude and phase between the repeated surveys (2002) and the baseline (1993).

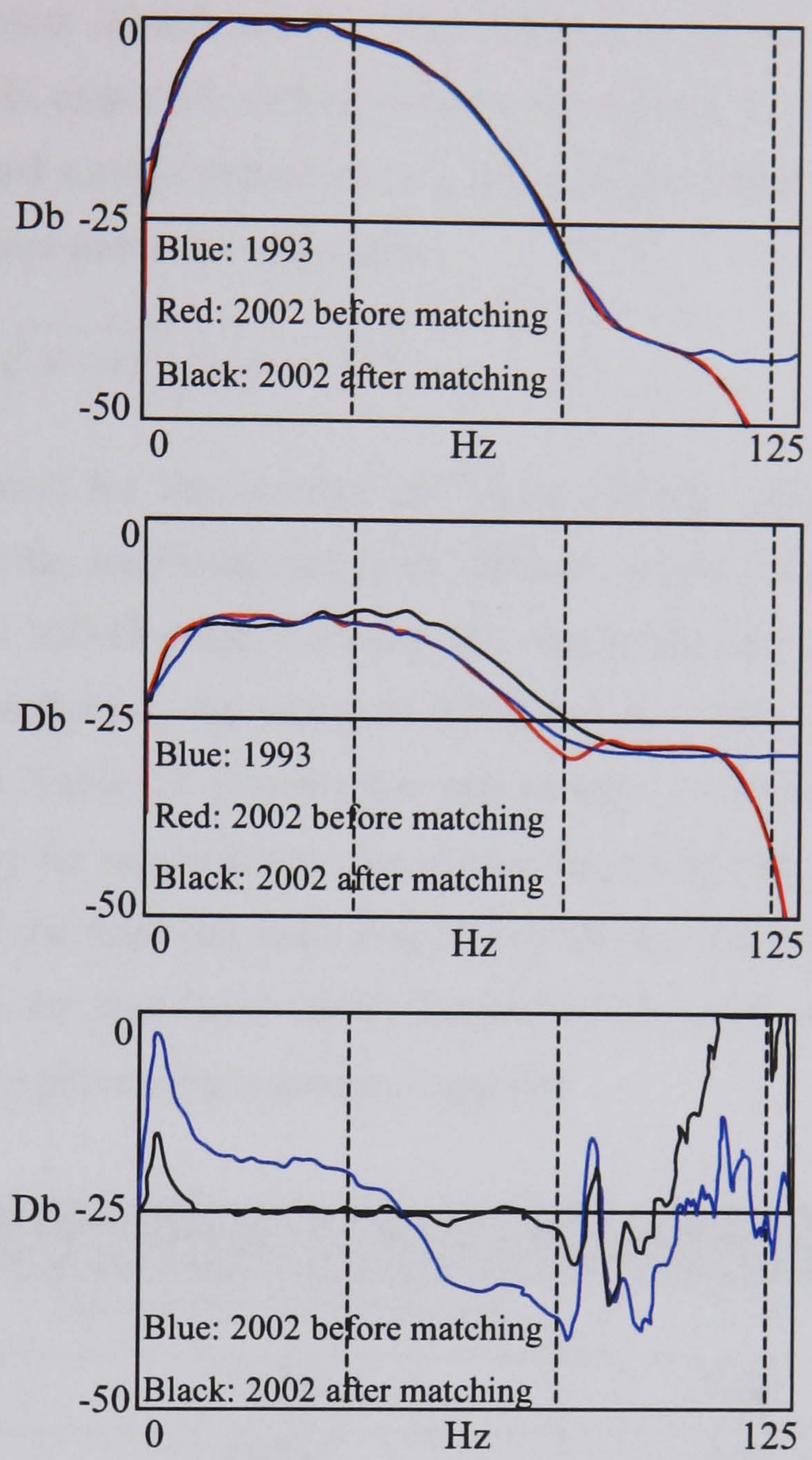

Figure 6.5: Pre-stack amplitude and phase matching applied to correct for the global mismatch in amplitude and phase between repeated and baseline surveys. The signal (top) and noise (middle) spectrum of the repeated data match the baseline spectrum. The phase spectrum (bottom) shows that phase shifts between surveys are removed after application of the phase filter.

Finally, to check the output results of each processing step, quality control (QC) is carried out in order to check the improvement in quality and repeatability of the data. Spectral coherence analysis is used to control the bandwidth and signal-to-noise ratio for each dataset, but the time and phase shift are also monitored between the different surveys. The degree of convergence between datasets is accessed by deriving repeatability

measurements. The normalized root-mean-squared (NRMS) measurements are used as repeatability indicators (Kragh and Christie, 2002). The NRMS is simply defined as the quotient of the RMS amplitude difference over the average of the RMS amplitude of the baseline and repeated surveys (equation 6.1). These measurements are generally made over a survey-wide horizon above the target area.

$$NRMS = \left(2\sqrt{(A-B)^2}\right) \Big/ \left(\sqrt{A^2} + \sqrt{B^2}\right) \qquad (6.1)$$

where A and B stand for the baseline and repeat surveys, respectively. The NRMS is sensitive to time shifts, amplitude and phase differences, and also to the noise level of the data. The lower the NRMS value, the better the repeatability between the baseline and the repeated data. By definition, the values of NRMS range from 0 to 2, with 2 representing anti-correlated data. Table 6.4 presents the improvement in repeatability between the 2000 and the 1993 survey for selected steps throughout the processing flow. It can be noted that the repeatability of the final full-stack data is low (0.22), and demonstrates the benefit of parallel processing for time-lapse study. These NRMS values are representative of the 2002, since the same processing sequence is applied.

Processing step	NRMS value
Navigation/seismic merge	1.14
DMO	0.43
PSTM	0.37
Full stack	0.32
Migrated full stack	0.25
Cross-matched full stack	0.22

Table 6.4: NRMS repeatability measurements at different stages of the processing sequence (CGG, 2002). Those measurements are carried out outside the target area.

1	Navigation	8	DMO (bin size 25*25m)
2	Swell noise removal	9	3D pre-stack time migration
3	Radon anti-multiple (first pass)	10	Cold-water statics
4	Zero phase/de-bubbling filter	11	Radon anti-multiple (second pass)
5	Q compensation	12	Trim-statics
6	Tidal statics	13	Pre-stack matching (amplitude and phase)
7	Random noise attenuation	14	3D steep dip migration

Table 6.5: Pre-stack processing sequence used for the parallel processing of the 1993 and 2002 seismic surveys. The main processing steps are shown by order of application from 1 to 14.

C Post-stack processing

The methodology applied in the previous chapter to discriminate between pore pressure and saturation effects required a minimum of three angle stacks. In order to obtain these stacks, the following incidence angle ranges are used for the summation: near-angle stack equivalent to 8° (range 1–15°); mid-angle stack equivalent to 21° (range 16–26°); and far-angle stack equivalent to 32° (range 27–37°). Primarily, since residual multiple energies coming from the Balder peg-leg are visible in some areas, a predictive deconvolution demultiple method is tested. A great deal of residual energy is removed, but, on the other hand, a large amount of artefact energy appeared to affect the target area. It is concluded that the multiple problem could not be resolved post-stack, and no additional demultiple is applied. Secondly, the pre-stack data are migrated in time with a constant velocity, so a post-stack time migration is applied to each angle stack, using a vertical velocity law to obtain a more accurate image of the subsurface. Finally, an amplitude matching is applied in order to correct for the amplitude differences between the two surveys. Ratio maps of amplitudes along the Balder horizon were computed, and scalar maps were created in order to correct for the systematic RMS amplitude difference between the surveys. Figure 6.6 (left) shows an RMS ratio map for the near-angle stack between 1993 and 2002, before correction; we can observe the low-frequency stripes due to the different seismic swath direction. In order to attenuate the low-frequency striping effects, prior to the correction the

scalar maps are heavily smoothed in the in-line direction in order to preserve the swath limits and avoid spreading the low-frequency stripes in the cross-line direction. The 1993 survey is used as a reference, because it appears to be less affected by low-frequency swaths. Figure 6.6 (right) shows the same RMS ratio map, but after correction; it can be seen that the low-frequency stripes are successfully attenuated. It is important to note that a mask is used over the undershoot area (blue anomaly – Figure 6.6), and additional RMS amplitude map are created over the target area in order to check the preservation of the amplitude at the reservoir level. It is also noteworthy that the undershoot area in 2002 is affecting the amplitude – particularly for the near and mid offset classes. However, the same correction was not applicable in order to compensate for these amplitudes, since the undershoot anomaly varies with offset and depth. A correction design over a 400-ms window over the target is used to successfully attenuate the undershoot imprint (Figure 6.7), but the amplitude might not be truly represented. Special attention needs to be given to this area, in order to exclude it from the final matching step and subsequent quantitative analysis.

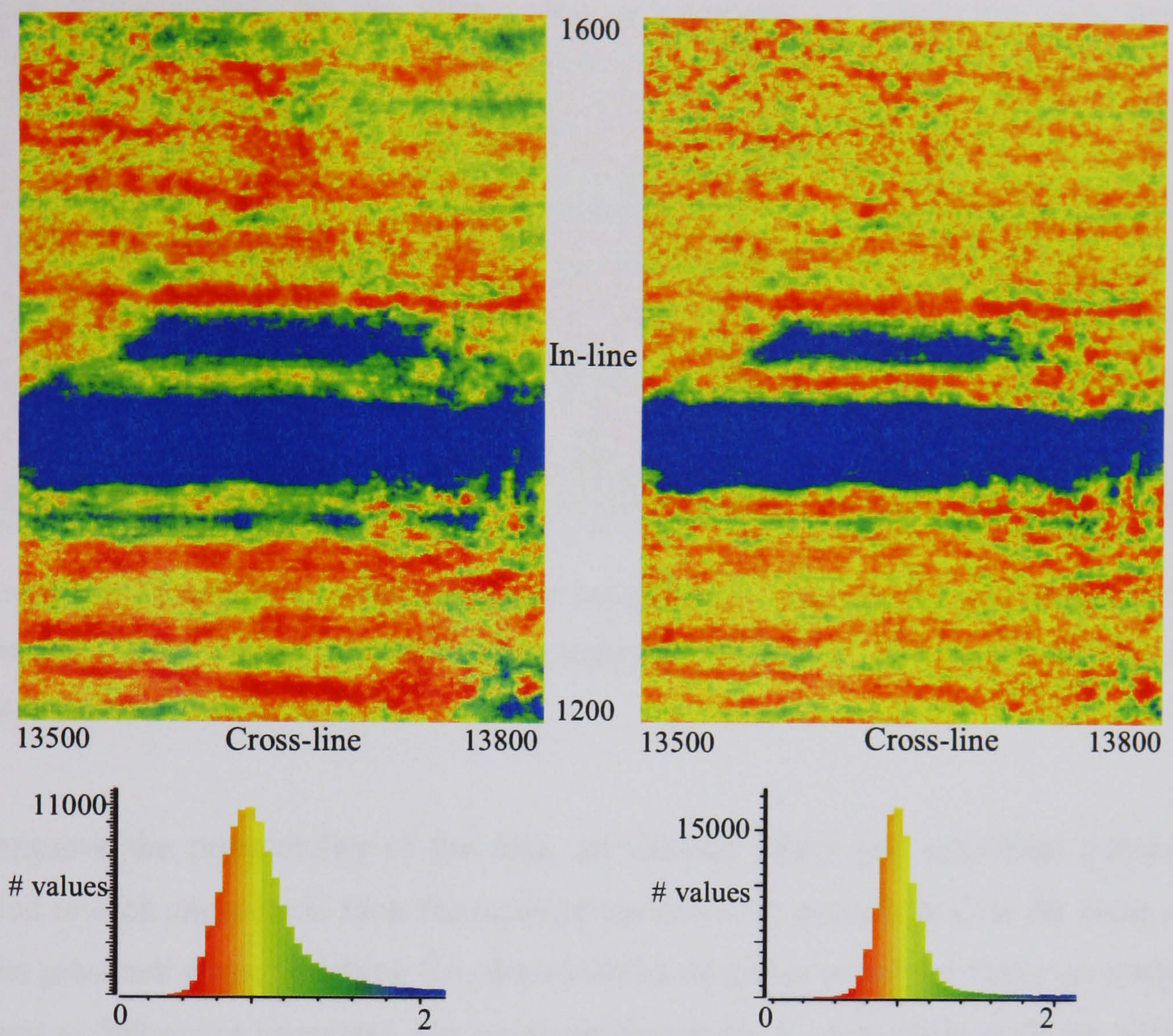

Figure 6.6: RMS ratio maps computed between 2002 and 1993 surveys. The map before correction (left) is smoothed heavily in the in-line direction, in order to avoid a spreading of the low-frequency swath stripes in the cross-line direction. After correction (right), the stripes are attenuated successfully. No correction is applied over the undershoot area (blue anomaly).

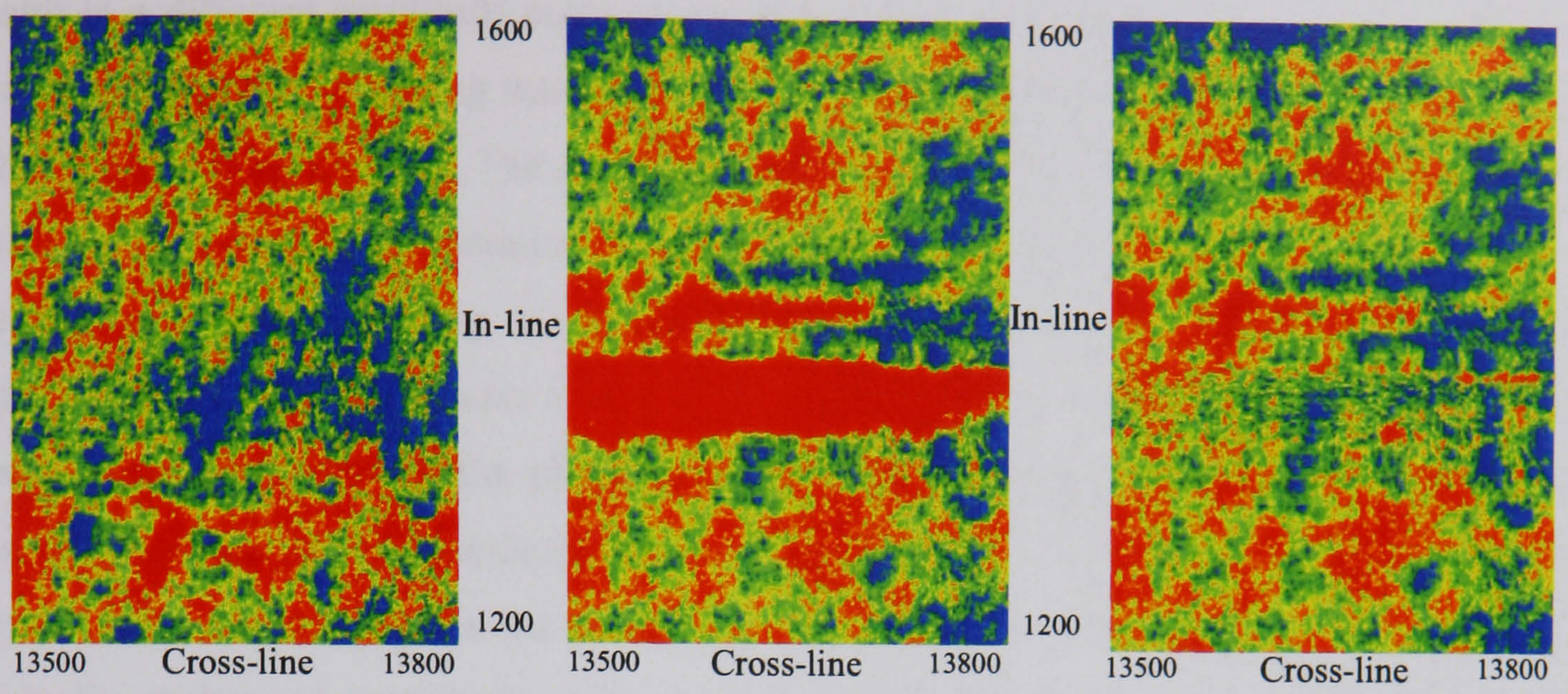

Figure 6.7: RMS maps over a 400-ms window centred on the target for the 1993 vintage (left) and the repeated 2002 vintage (middle), before undershoot correction. After correction (right), the undershoot imprint is attenuated.

To improve the repeatability of the data, an ultimate phase and amplitude matching is applied to each angle stack from the repeated surveys. The process used is the same as that for the pre-stack phase matching (i.e. derivation of the phase matching filters on a selection of lines at 500-metre intervals). The phase shifts applied to each angle stack are presented in Table 6.6.

Angle stack	Phase shift 2002
Near	4.4°
Mid	8.0°
Far	10.7°

Table 6.6: Residual phase shifts present between repeated and baseline surveys prior to final matching. Filters are applied to each angle stack in order to remove the observed phase rotations.

The Balder horizon, used as a reference reflector, is very rugose due to its basaltic nature, and is temporally distant from the reservoir. The difference in illumination of the Balder – caused by variation in survey geometries, together with the rugosity of the horizon – might

result in a different amplitude mismatch at the reservoir and Balder level. After testing, it was concluded that a running matching procedure is a better alternative than a single global filter designed on superline. The amplitude running matching applied consists of computing the amplitude matching operator on a single-trace basis between the two surveys at the Balder level, and averaging those operators on a box of 1000 × 1000 metres before application. Figure 6.8 presents a 4D (1993–2002) time-slice over the target area at the far angle, after application of the phase and amplitude matching procedure described above. An improvement in the time-lapse signature continuity can be observed, meaning that the repeatability has increased in the area where the time-lapse signal is enhanced, and remains virtually unchanged outside this area. As a final QC, NRMS maps are produced for each individual angle, to ensure that a sufficient time-lapse repeatability is achieved. Figure 6.9 presents the NRMS maps between the 1993 and 2002 vintages for the same area as Figure 6.8. It can be noted that most of the NMRS values vary from 0.1 to 0.3 and increase from near to far offset stack due to the better removal of multiple energies and lower frequency content (Landrø, 1999b) at long offset. Furthermore, comparing the time-lapse signal from Figure 6.8 (right) and the corresponding NRMS map (Figure 6.9c) confirms that this observed signal is genuine and relates to production. With the level of convergence obtained between the different surveys, it is feasible to apply time-lapse elastic inversion to derive meaningful seismic attributes.

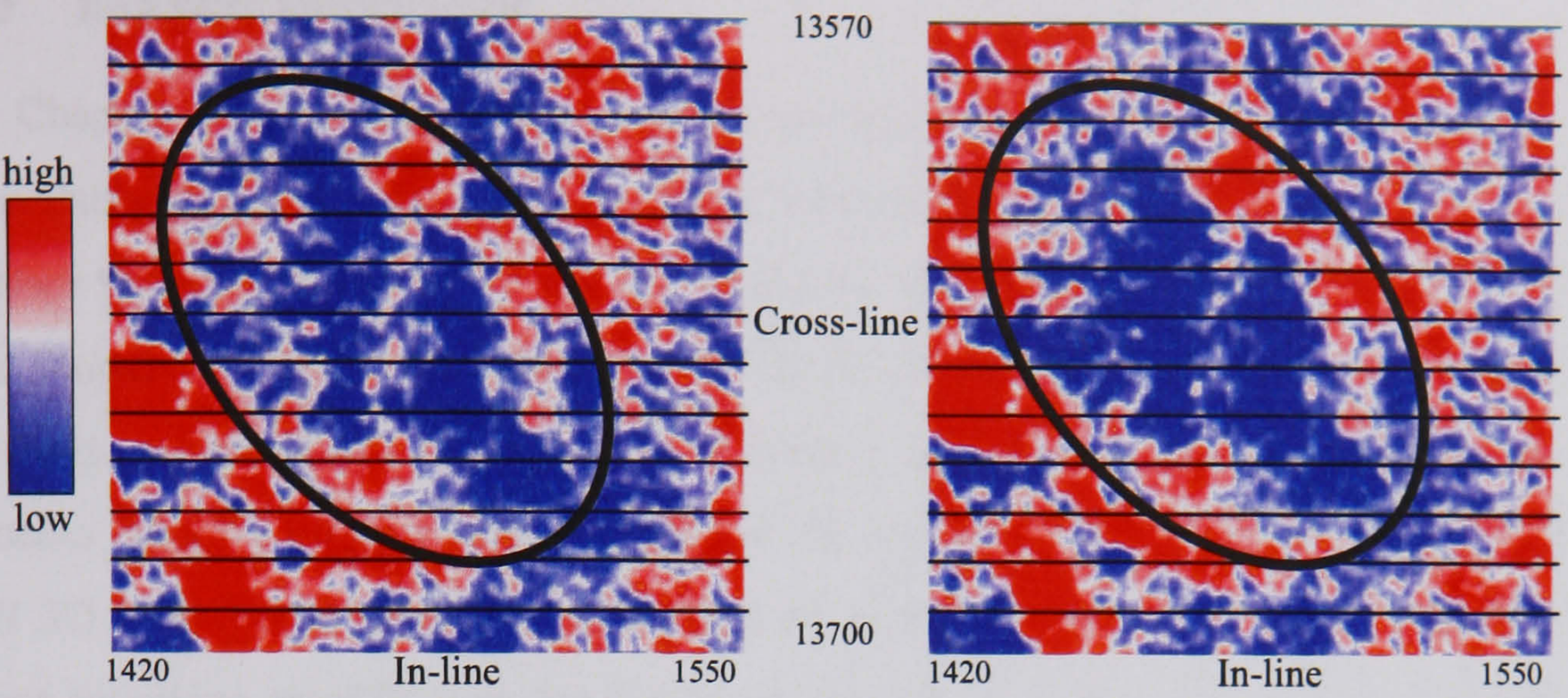

Figure 6.8: Time slice at the reservoir level for the seismic difference between the 1993 and 2002 vintages. A better continuity and delineation of the 4D signal can be noted after the final matching procedure (right) compared to the initial difference (left).

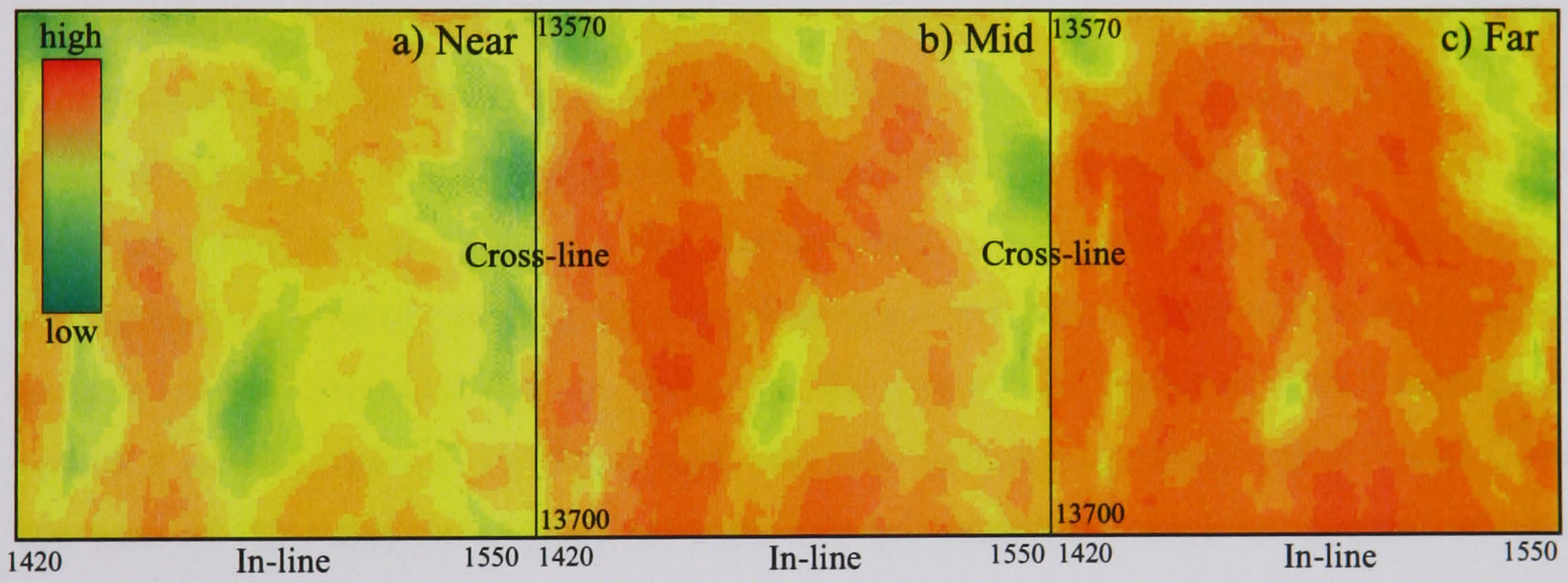

Figure 6.9: NRMS map computed over the same area as Figure 6.8 for near (a), mid (b), and far (c) angles. One can observe an increase in the repeatability with offset. The far-angle NRMS map emphasizes the confidence in the 4D signal, which is located in the highest repeatability area.

6.3 Elastic inversion

In Chapter 4, reflectivity was defined as being generated by the contrast of elastic impedance at the interface of two layers. In other words, the reflectivity can be seen as a surface property of the layers contact, while the elastic impedance can be directly related to the property of each individual layer. Therefore, elastic impedance is a more intuitive quantity, which makes it possible to efficiently interpret the data. Elastic inversion is the process whereby seismic data are inverted for impedance (cf. Section 4.2). In this section, a full 3D layer-based algorithm developed by Gluck *et al.* (1997) is used to apply a time-lapse inversion workflow to the Foinaven dataset. A description of the algorithm and its application to the field data is presented in the following section.

6.3.1 3D Stratigraphic inversion of post-stack seismic data

The main idea of elastic inversion is to perturb an initial impedance model and compute the corresponding seismic response by conventional convolutional modelling. This process is repeated iteratively until convergence is reached between the synthetic seismic response and the actual seismic data. In the current case, the inversion process used a 3D stratigraphic inversion, meaning that both impedance and time are updated in the iterative process. In this inversion process, there are three necessary inputs: an initial impedance model, a seismic wavelet, and the seismic data to be inverted. A macro-model is built from the time of the main geological horizons, and an impedance value is assigned to each macro-interval (Figure 6.10A). The impedance value corresponds to the low-frequency trend derived from synthetic impedance computed from well-log measurements. The macro-model is also called an initial or an a priori impedance model. During the inversion, the initial model is interpolated in time to include micro-layers within each macro-interval (Figure 6.10B). The thickness of the micro-layers is defined by a percentage of the central lobe of the seismic wavelet, which is extracted from the seismic data around a well. This now stratified 3D initial impedance volume is perturbed in the time and impedance domains (Figure 6.10C). Then the seismic wavelet is convolved with the reflectivity from the perturbed model, to generate the synthetic seismic (Figure 6.10D). This step is repeated

until the misfit between the real data and the synthetic seismic is minimized (Figure 6.10E). To minimize this misfit function, a simulated annealing optimisation technique is required to find the global minimum. In fact, the main feature of simulated annealing is its ability to optimally converge, as compared with other methods that can be trapped at local minima. The simulated annealing algorithm employs a random search method that will not only allow changes (in time and impedance) to reduce the misfit function, but also changes to increase it – permitting it to escape from local minima. An overview of simulated annealing is presented in the next section 6.4.2. Furthermore, an impedance corridor can be derived from the well, in order to constrain the solution interval minimizing the misfit function and to avoid any possible divergence. Depending on the weighting factor used for the lower and upper impedance bounds, the corridor can be seen as a soft or hard constraint. Another interesting feature of this inversion is the possibility of defining the degree of confidence of the position and impedance value of the micro-layers. This is allowed to constrain the time and impedance perturbations as a function of the degree of confidence on the a priori model (Gluck *et al.*, 1997). Figure 6.10 summarizes the methodology to invert post-stack seismic data for elastic impedances.

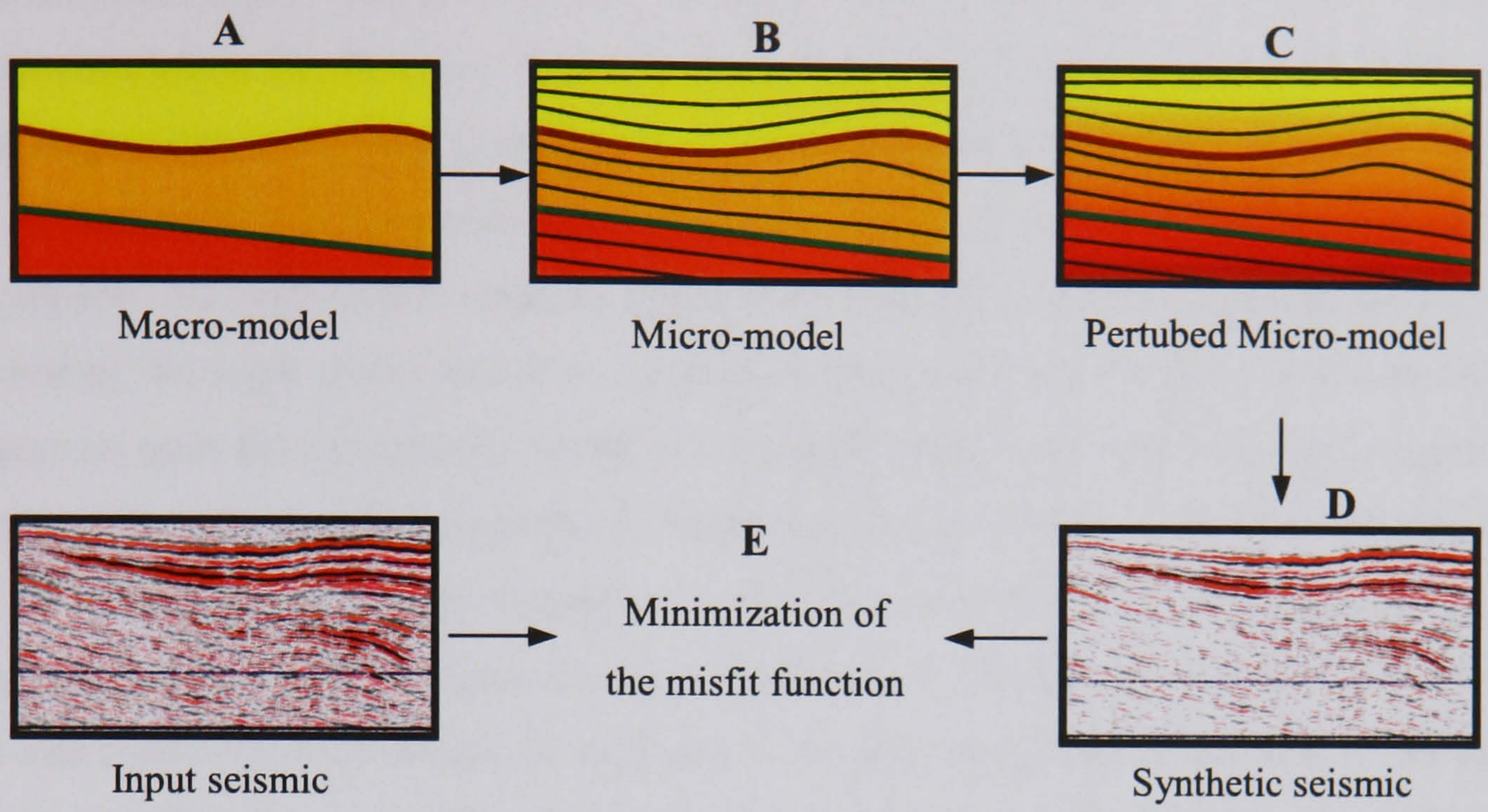

Figure 6.10: 3D stratigraphic elastic inversion methodology. A: Macro-model derived from main seismic horizons and low-frequency impedance at the well. B: Creation of the micro-layers. C: Perturbation of the micro-model in the time and impedance domains. D: Synthetic seismic modelling from perturbed impedance. E: Minimization of the misfit between real and synthetic data.

6.3.2 Data pre-conditioning

Data pre-conditioning for time-lapse surveys aims to optimize the repeatability between vintages prior to the inversion, in order to obtain a high-quality 4D elastic impedance difference (Kirstetter *et al.*, 2004). In fact, 4D time misalignments should be small in order to preserve the consistency between the time of the macro- or micro-layers of the different inverted impedance angles. Residual time shifts between surveys will reduce the quality of the 4D signal, while residual move-out between angle stacks leads to erroneous AVO attributes post-inversion. Therefore, the time misalignments between surveys for each angle stack, and the AVO time misalignments for each survey, need to be computed in order to check that they are within a reasonable range. To compute the time shifts, a complex cross-

correlation (also called generalized cross-correlation) is performed. This cross-correlation has the advantage of being insensitive to phase rotation as compared to the conventional cross-correlation. Furthermore, it also makes it possible to compute the instantaneous phase and control that no residual phase rotations are present between the data. It is observed that all 4D and AVO misalignments are smaller than the sample rate (4 ms) and are considered negligible. No significant residual phase rotations are noticed. Furthermore, prior to inversion, the angle stacks had to be spectrally harmonized to a reference angle, in order to ensure an equivalent frequency content for all angle stacks. Spectral whitening is applied to each angle stack in order to match the frequency content of the near-angle stack spectrum of the 1993 baseline survey chosen as a reference because it had the largest frequency bandwidth. Figure 6.11 presents the signal spectrum of the different angle stacks for 1993 (a) and 2002 (b). A characteristic decrease in the frequency bandwidth with offset can be observed. This pre-conditioning step makes up for the loss of high frequency with offset, and will improve the stratigraphic resolution of the inverted impedances (Freudenreich *et al.*, 2004). This process also provides the opportunity to use a single wavelet in the inversion workflow, instead of deriving a wavelet for each angle stack.

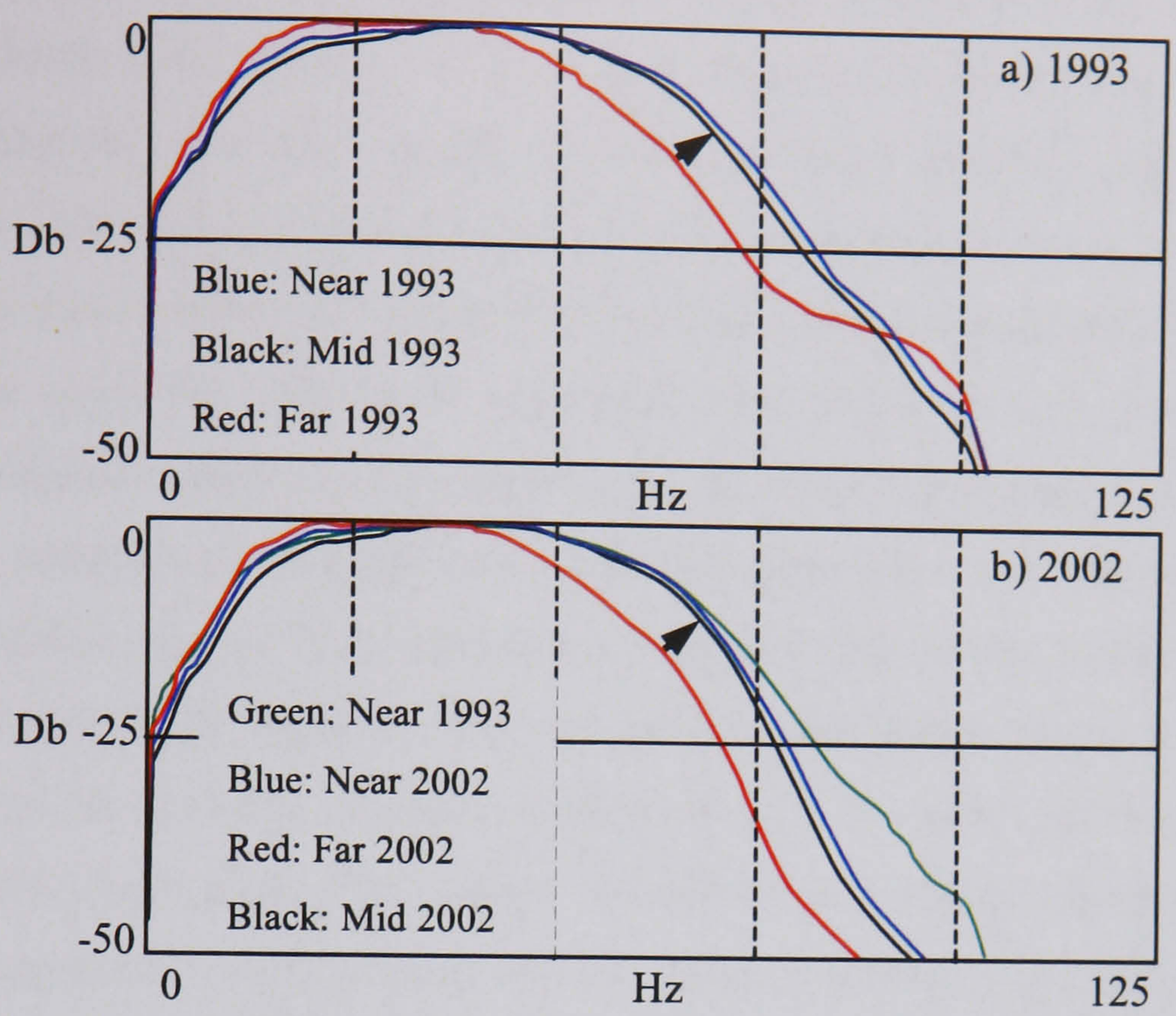

Figure 6.11: Spectral harmonization of the signal spectrum of all angle stacks from the 1993 (a), and 2002 (b), surveys to the near-angle stack of 1993 survey. One can note that the frequency bandwidth of all angles is enhanced in order to match the frequency content of the signal spectrum of the near-angle base survey.

6.3.3 4D elastic inversion

A A 4D workflow

There are several ways to carry out elastic impedance inversion on time-lapse seismic data. Due to the non-uniqueness of inversion techniques, it is important to select a suitable workflow that minimizes this effect. Three different inversion workflows are applicable: the uncoupled inversion, the coupled inversion, and the time-lapse changes inversion. Let us consider the inversion of a repeated and a baseline angle stack. Furthermore, let us assume that the stacks are spectrally balanced to use the same seismic wavelet. The uncoupled inversion consists of separately inverting the two angle stacks with different initial models, and the elastic impedance changes are obtained by differentiation of the individual results. The coupled inversion is equivalent to the previous one, but the final

impedance model of the baseline inversion is used as the initial model in the monitor inversion (Gluck *et al.*, 2000). The time-lapse changes inversion consists of inverting the seismic difference, and will directly provide impedance changes. Furthermore, the last inversion is less time consuming, since it consists of only one inversion. Sarkar *et al.* (2003) show that coupling is necessary for the inversion of time-lapse seismic data, in order to minimize erroneous time-lapse impedance changes. Since only pre-production sonic measurements are available in the present case, the coupled inversion workflow is preferred in order to make direct comparison of synthetic impedance log with inverted impedance from the baseline survey. Time restriction is not an issue in this study, and, furthermore, coupled and time-lapse changes inversion lead to similar results (Sakar *et al.*, 2003). Figure 6.12 presents the coupled inversion workflow used to invert the baseline (1993) and repeated (2002) angle stack. This original workflow is a two-pass inversion process. Firstly, an initial impedance model is built, and the baseline survey is inverted. In this first step, constraints are not applied to the micro-layers in time and impedance, but only soft constraints are used on the impedance corridor. Secondly, the result from this inversion is used as a second initial model for the baseline and repeated data. In this second inversion, the a priori model is believed to be already close to the solution, so the micro-layers are frozen in time and impedance outside the reservoir and slightly constrain inside by applying a taper. On the same basis, harder constraints are applied to the impedance corridor. This highly constrained second pass permits an increase in the resolution of the inverted impedance at the reservoir level, because of the solution space refinement.

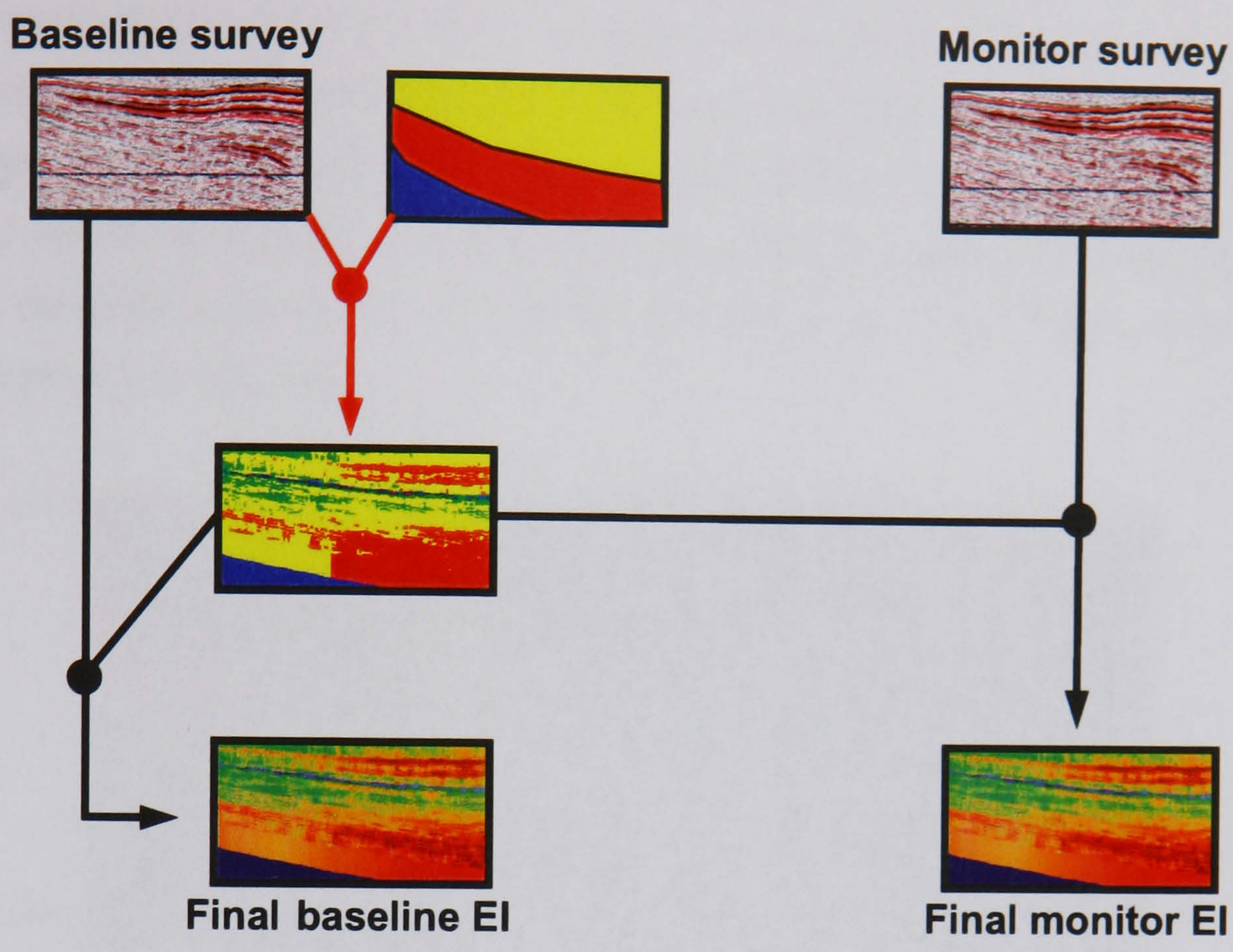

Figure 6.12: Time-lapse elastic inversion workflow applied to each angle stack. The workflow is composed of two steps. Firstly, the baseline survey is inverted, with an initial model having constant impedance value for each macro-layer. Secondly, the result from the previous inversion is used as an input model to invert the baseline and repeated surveys.

B Application to the Foinaven field

In Panel 1 of the Foinaven field, gas is absent prior to production. The reservoir plays are composed of Upper Palaeocene turbidite sandstones, which are subdivided into two stratigraphic sequences: T32 and T34 (Cooper *et al.*, 1999a). Hydrocarbons are produced via five horizontal wells, three producers and two injectors, which maintain pore pressure in the reservoir above or close to the bubble point pressure (21–22 MPa). All the wells are completed into the T34 sand, which is also subdivided into an upper and lower part. However, in some areas, from the seismic data, it appears to be difficult to distinguish between the lower and upper sand units. Figure 6.13 presents the structural map of the base

reservoir, colour-coded as a function of the two-way vertical travel time. The faulting delimiting the areal extension of Panel 1 is shown. The reservoir dips from east to west and can reach up to approximately 40-metre thickness. The producer P1 is completed in the upper sand, while producers P2 and P3 produce hydrocarbons from the lower sand. The two wells, I1 and I2, both inject water into the upper and lower sands. Since necessary shear logs for the elastic inversion are not available in Panel 1, well A (cf. Figure 6.13) from the adjacent panel 2 is selected.

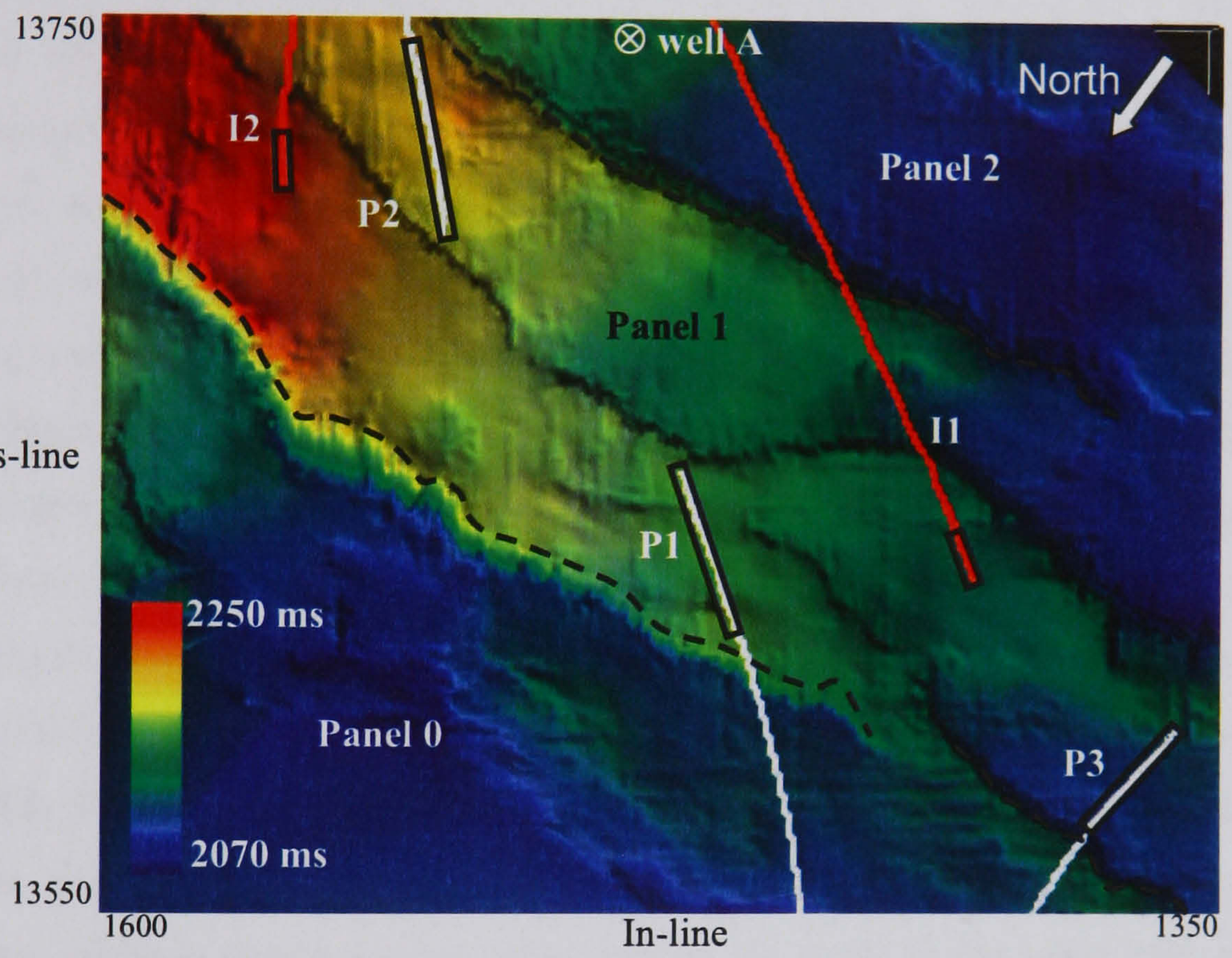

Figure 6.13: Structural map of the base reservoir, colour-coded as a function of the two-way vertical travel time. The producers P1, P2 and P3 (white paths), as well as injectors I1 and I2 (red paths), are displayed. Well A stands for the vertical well used in the elastic inversion. The main faults (black dashed curves) separating the area in three different panels (Panels 0, 1 and 2) are also highlighted and the well completions indicated (black rectangles).

A seismic wavelet is extracted from a selection of traces around well A. The FFT of the amplitude spectrum of those traces is computed to derive the zero-phase wavelet. Synthetic seismic is then computed at the well location and compares favourably with the

neighbouring traces. The synthetic seismograms are modelled by using the Aki & Richards formulation (equation 4.4), assuming a velocity ratio γ of 0.25 and an approximation for small angle (i.e. $\sin^2\theta = \tan^2\theta$). These assumptions are valid, since the average reservoir velocity ratio derived from the well is approximately equal to 0.25, and, furthermore, in this inversion angles below 32 degrees are used. Figure 6.14 shows the good agreement between the synthetic and real seismic at the location of well A, however some differences are visible in the lower part of the display that might be due to residual multiple energies. Stretch and squeeze is not applied on the synthetic seismic but could be an alternative to improve the well-tie. The seismic wavelet presented in Figure 6.14 is input into the inversion process in order to convert the inverted impedance into the seismic domain. As presented previously, an initial impedance model is built from the impedance trend extracted from synthetic impedance computed at well A. A first inversion is run on the baseline, and then the result is used as an input model to run the second inversion (Figure 6.12). Optimal parameters are chosen in order to obtain a good fit between the final inverted elastic impedance and the synthetic impedance at the well. Synthetic impedances are filtered to the seismic frequency prior to comparison. Figure 6.15 presents the comparison between the synthetic elastic impedance and the inverted impedance after the first and second inversion pass at the near, mid and far angles. One can observe an excellent correlation between the modelled and inverted data. The signature at the reservoir level, and also the dynamics of the data, are accurately reproduced. However, a limestone inclusion, which is below seismic resolution, is measured by the sonic tool, explaining the mismatch just above the reservoir.

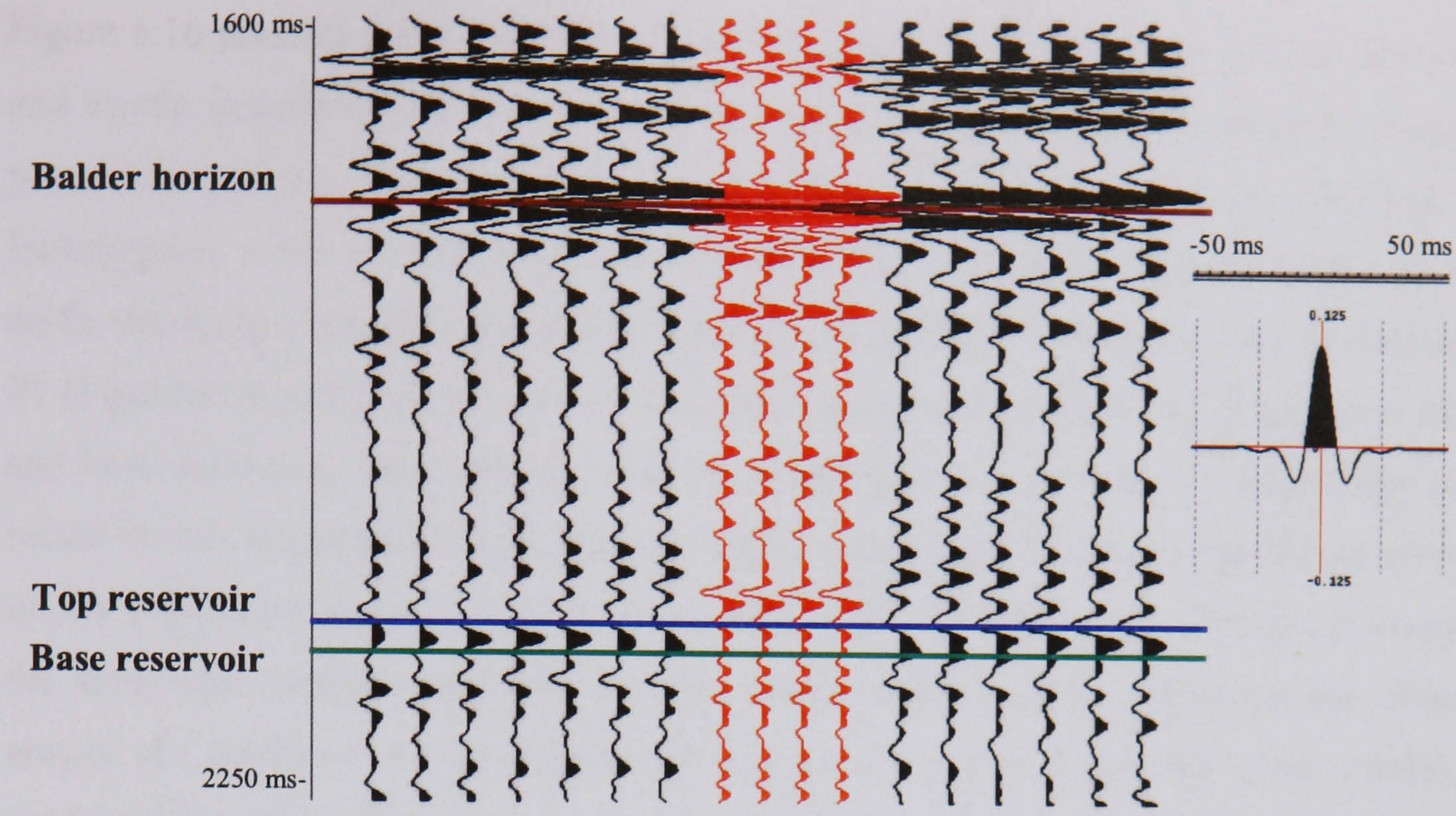

Figure 6.14: Extracted wavelet at the well location (right) and comparison in the cross-line direction of the synthetic (red traces) and actual seismic (black traces), for selected traces at the well position. Synthetic traces are duplicated.

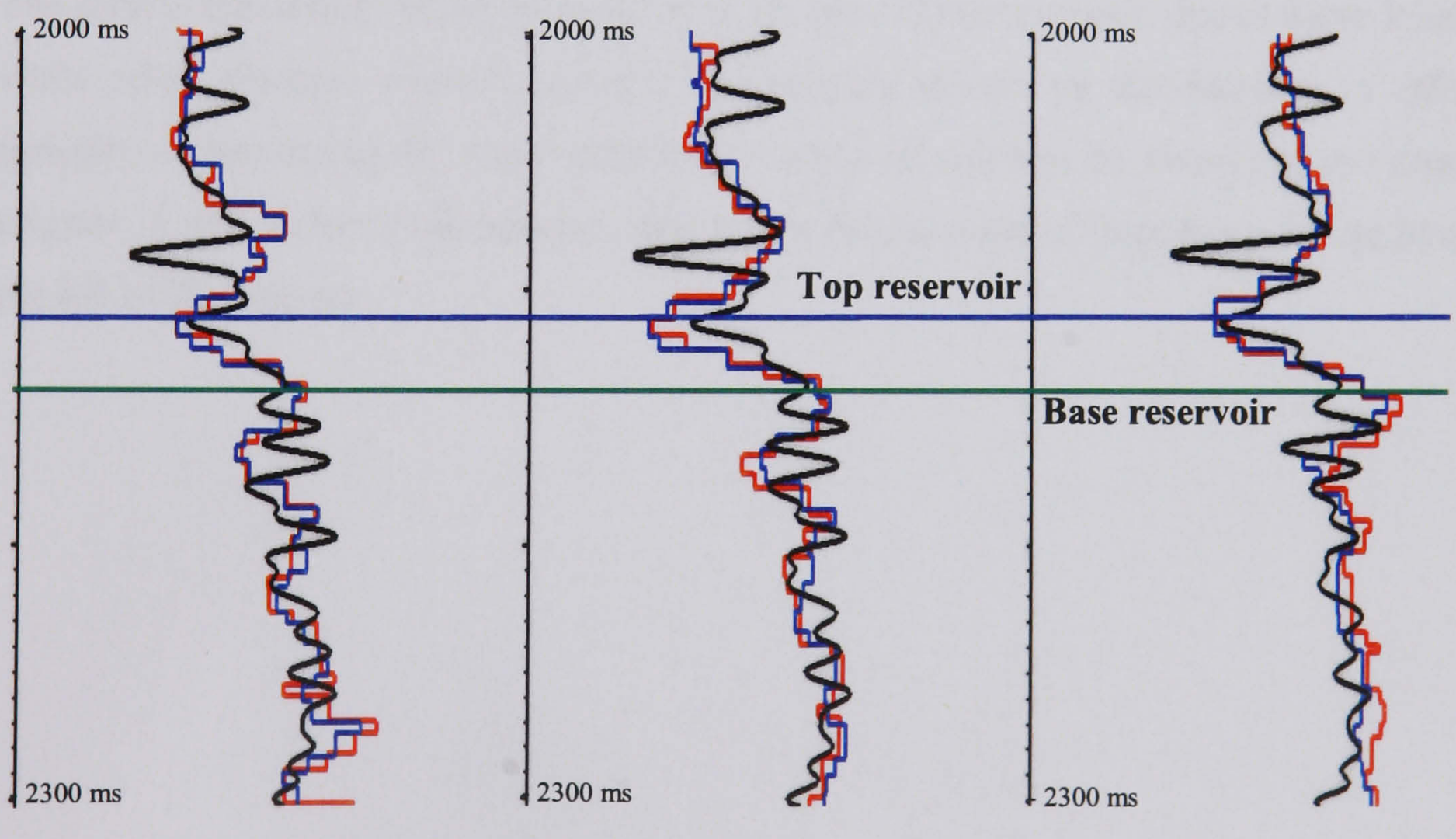

Figure 6.15: Comparison of the synthetic impedance log at seismic frequency (black) with the impedance results from the first inversion (first pass: blue) and second inversion (second pass: red). The impedances are displayed for the near (left), mid (middle) and far (right) angle of the baseline vintage.

Figure 6.16 presents a cross-section of the base and repeat surveys, as well as the seismic and elastic impedance difference at the far angles. Large time-lapse signatures related to production effects are observable in the vicinity of injector I1 and producer P1. Furthermore, a 4D ghost is observable below injector I1 which is probably due to time-shifts variations caused by production induced changes in the reservoir. At the location of P1 (Figure 6.16: white circle), a decrease and increase in amplitude are observed at the top and base reservoir. This variation can be explained by a decrease of impedance in the reservoir, due to gas exsolution. The fluid effect seems to have a more significant influence on the impedance around P1 than the increase in effective pressure. This is corroborating the time-lapse elastic impedance results, where mainly negative changes are observed around the producer. At the location of injector I1 (Figure 6.16: light-green circle), the interpretation of the 4D signal is more complicated. In fact, the gamma-ray log shows the presence of a shale layer between the upper and lower sand units. As a result, the existence of an oil–water contact in each sand is expected. However, the dimensions of these oil and water columns are below the detection limit of the seismic, and thus cannot be observed. The elastic impedance shows an increase at the base of the reservoir, due to water injection; while small changes occurred around I1, probably caused by the decrease in effective pressure counteracting the water substitution effect. It can also be noted that gas seems to migrate in proximity of the injector, judging by the decrease of impedance taking place on the left of the injector.

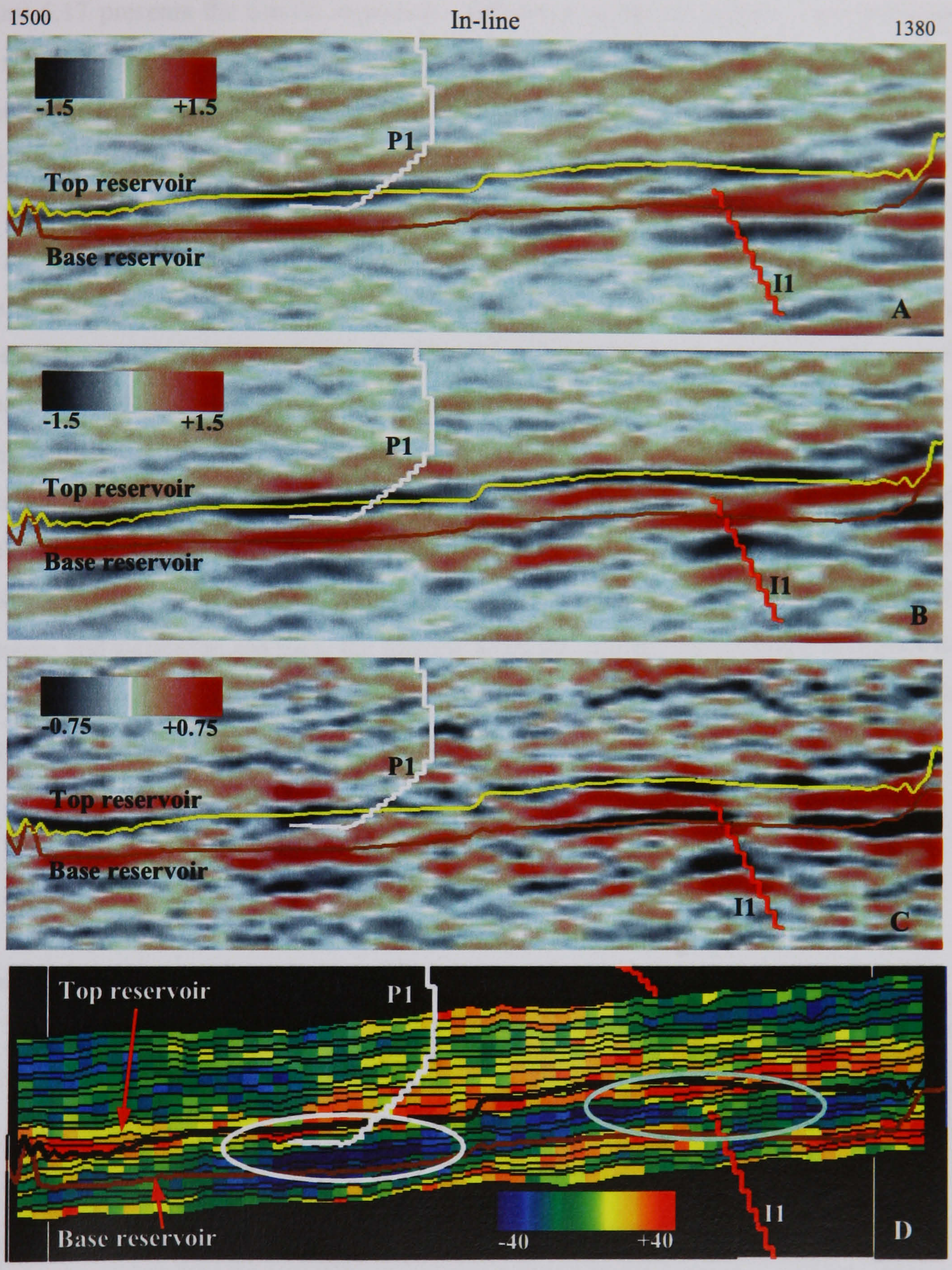

Figure 6.16: Seismic cross-sections at the far angle for the 1993 (A) and 2002 (B) surveys are displayed for cross-line 13626. The differences between the repeat and base surveys are also shown for the seismic (C) and the elastic impedance (D) at the far angle. The paths of the injector I1 (red curve), producer P1 (white curve) and top and base reservoir, are highlighted.

Figure 6.17 presents the elastic impedance difference at the far angles. Two micro-layers are selected from the stratigraphic inversion grid, which are representative of the general behaviour of the eastern part (layer 23) and the western part (layer 18) of the field. The layering of the elastic impedance model is shown on Figure 6.16D. Both these micro-layers are used in subsequent plots. One can observe an increase in impedance in the vicinity of the two water injectors, while a decrease is noticed around the producers. The undershoot area displayed on Figure 6.17 (top – Layer 18) might be at the origin of the large time-lapse anomalies observed. As explained in Chapter 4, far angles are mostly sensitive to fluid effects. Therefore, the positive anomalies at the injectors are interpreted as an effect of brine substituting for oil, while the negative anomalies are related to gas coming out of solution. One can also notice that smaller changes take place around I2 than I1, which could be due to a lower amount of injected water or the greater sensitivity of the rock to pressure effects. In order to get a feeling for a possible qualitative interpretation of the pressure and saturation changes, the seismic attributes $\lambda\rho$ and $\mu\rho$ are computed prior to the pressure-saturation inversion. Following the assumptions made above, the elastic impedance formulation (equation 4.8) can be rewritten as:

$$\ln(EI) = \ln(Ip) + [2\ln(Ip/Is) - \ln(Ip)]\sin^2\theta \qquad (6.2)$$

where: $I\mathrm{p} = \rho V_\mathrm{p}$

$I\mathrm{s} = \rho V_\mathrm{s}$

$\rho\mu = I\mathrm{s}^2$

$\rho\lambda = I\mathrm{p}^2 - 2I\mathrm{s}^2$

From equation 6.2, the $\lambda\rho$ and $\mu\rho$ values can be derived by linear regression of the logarithm of the elastic impedance against the incidence angles ($\sin^2\theta$). These two attributes, $\lambda\rho$ and $\mu\rho$, are commonly used to interpret lithology and fluid effects from seismic data. By definition (equations 3.13 and 3.14), $\lambda\rho$ and $\mu\rho$ are more sensitive to saturation and pressure changes, respectively. The interpretation of fluid effects from the

$\lambda\rho$ changes (Figure 6.18) is equivalent to the observation from the time-lapse elastic impedance at far angles. However, the interpretation of the pressure effect from the $\mu\rho$ changes (Figure 6.19) is difficult. It appears that the two attributes are highly correlated and that leakage occurred from the $\lambda\rho$ into $\mu\rho$ attributes. A possible explanation is the interference of these two attributes to the pressure and saturation effects, which might be the cause of the cross-talk in the estimation process.

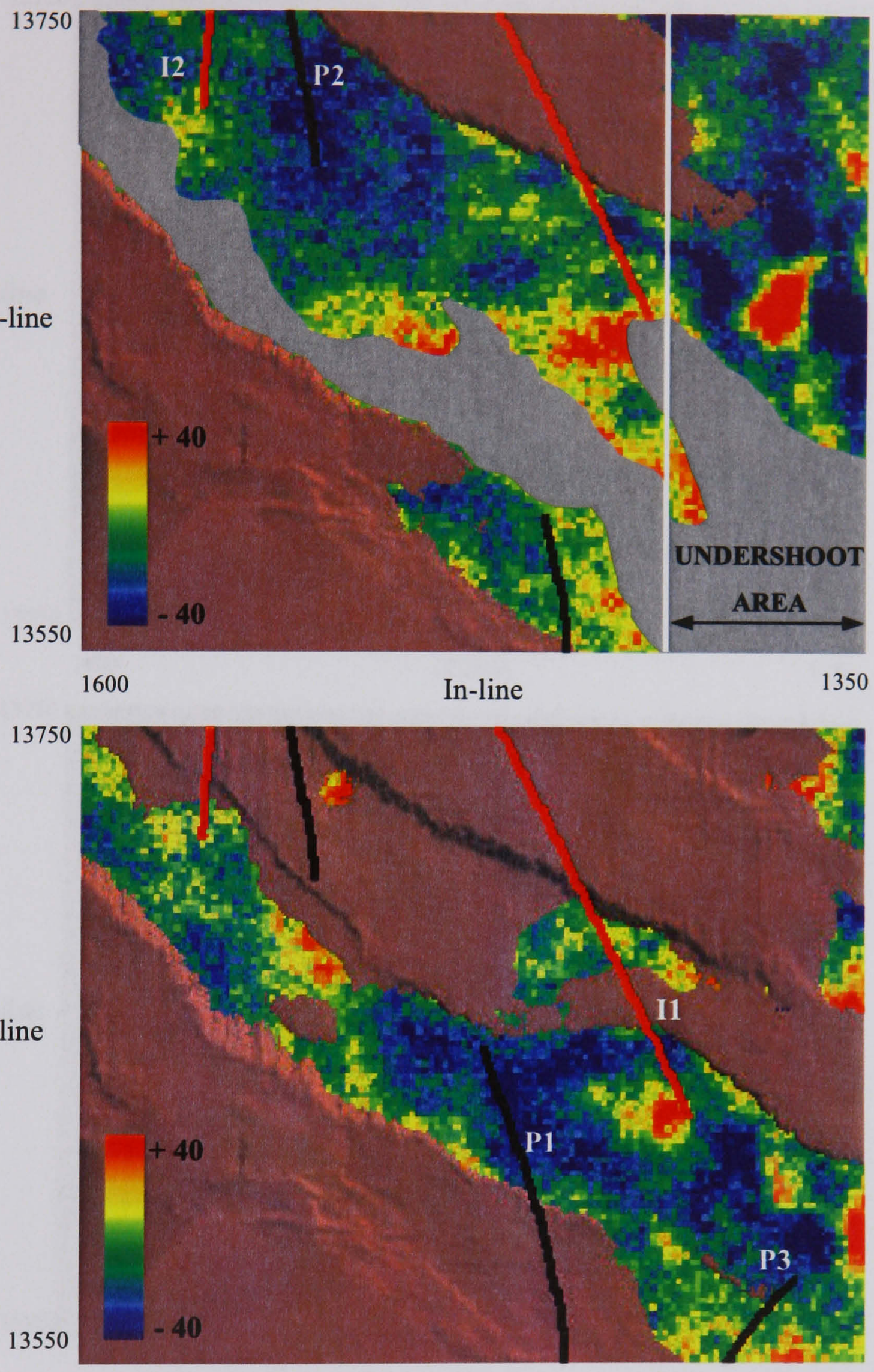

Figure 6.17: Elastic impedance difference at the far angles for layer 18 (top) and layer 23 (bottom) of the stratigraphic inversion grid. Increase of impedance related to water injection is observable in the vicinity of injectors I1 and I2, while a decrease in impedance occurred around the producers (P1, P2 and P3), due to gas exsolution. The brown and grey surfaces stand for the base and top of the reservoir, respectively. The different injectors (red paths) and producers (black paths) located in the area are shown.

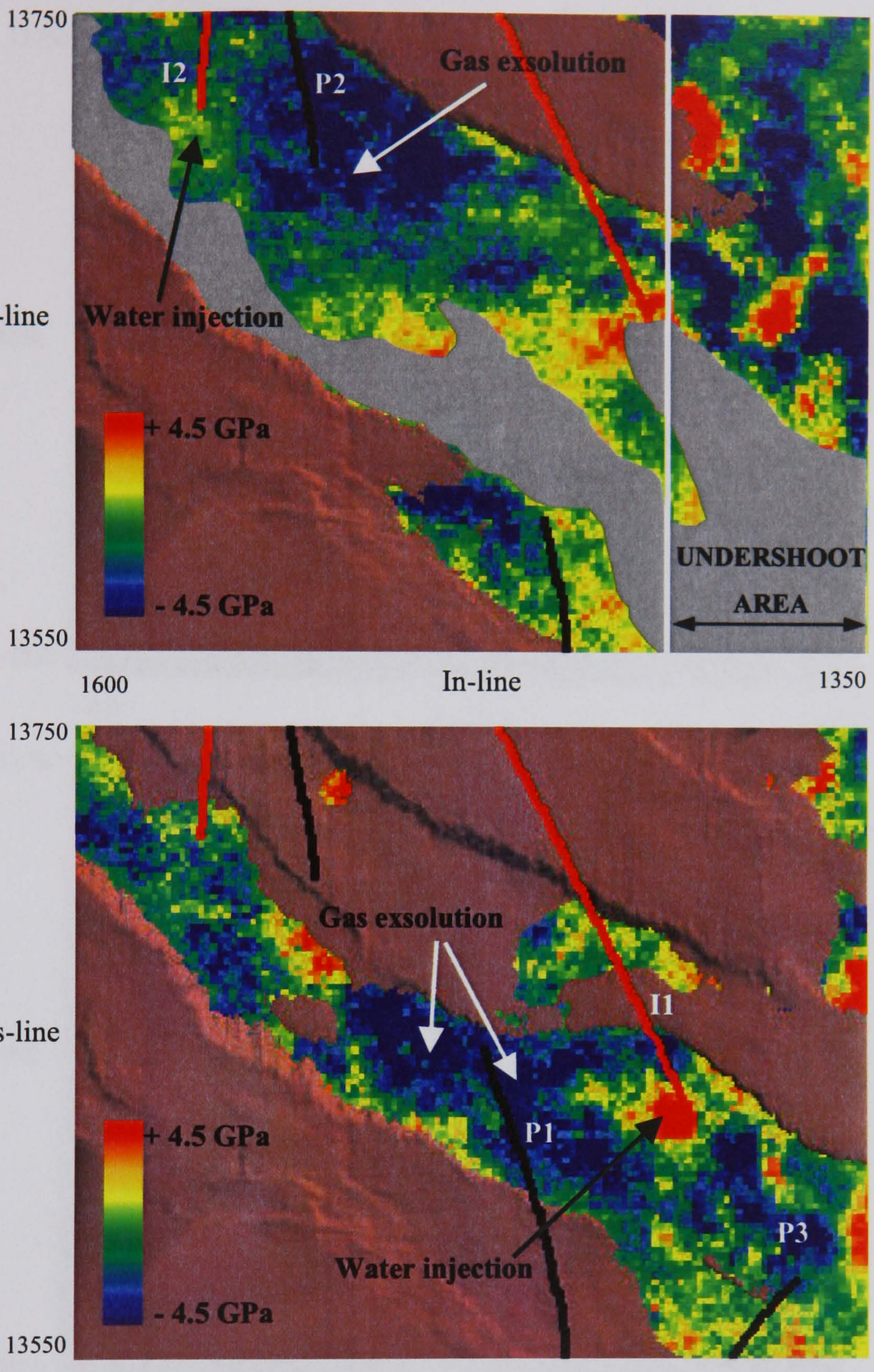

Figure 6.18: The $\lambda\rho$ difference for layer 18 (top) and layer 23 (bottom) of the stratigraphic inversion grid. An increase related to water injection is visible in the vicinity of injectors I1 and I2, while a decrease occurred around the producers (P1, P2 and P3), due to gas exsolution. These observations are in agreement with the interpretation from Figure 6.17. The brown and grey surfaces stand for the base and top of the reservoir, respectively. The different injectors (red paths) and producers (black paths) located in the area are shown.

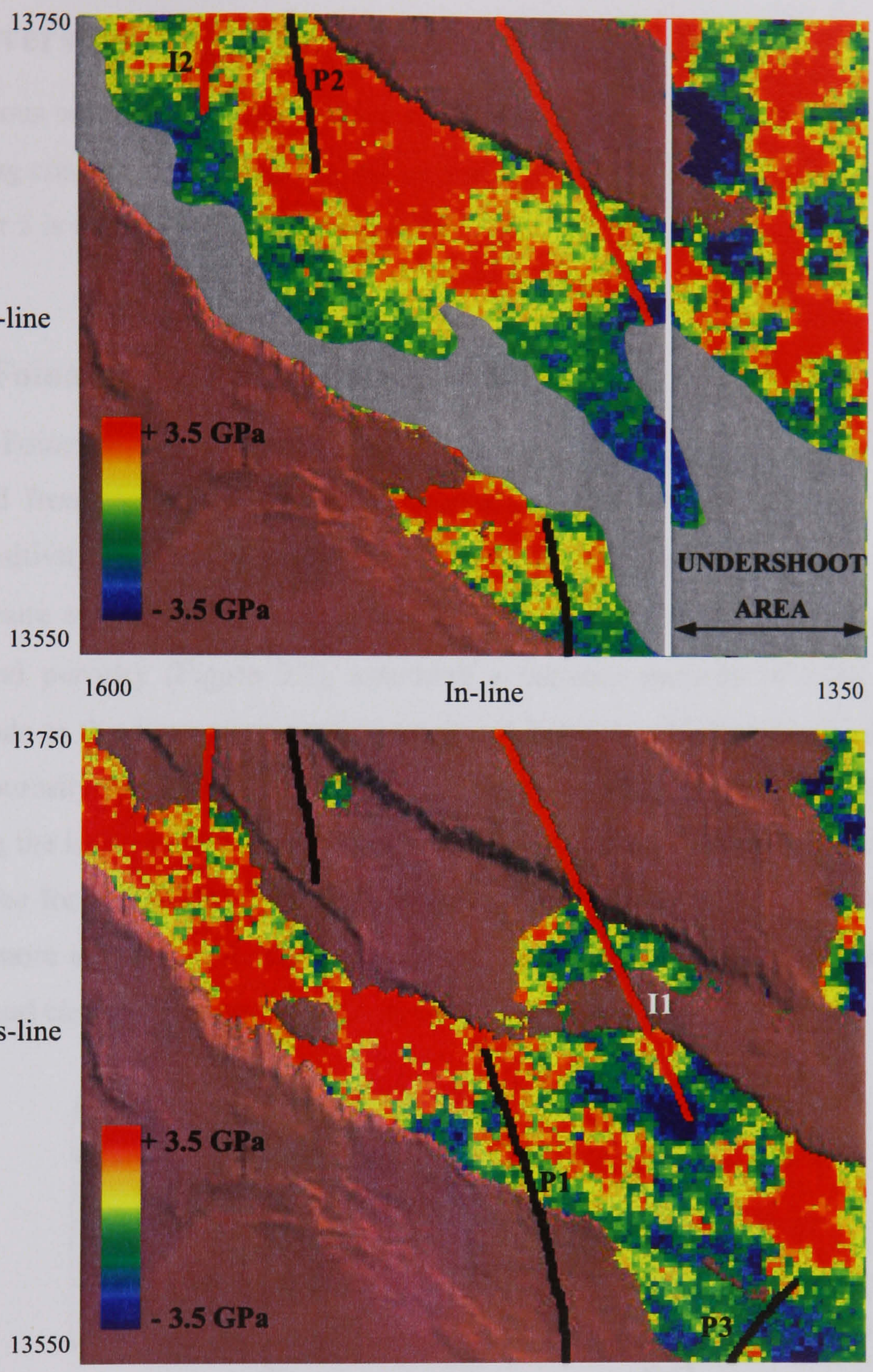

Figure 6.19: $\mu\rho$ difference for layer 18 (top) and layer 23 (bottom) of the stratigraphic inversion grid. The anomalies from this display appear to be highly correlated with the observations made in Figure 6.18. The brown and grey surfaces stand for the base and top of the reservoir, respectively. The different injectors (red paths) and producers (black paths) located in the area are shown.

6.4 Inversion for pressure and saturation changes

The previous section illustrated that the interpretation of pressure and saturation is difficult when using conventional means. In this section, the new technique tested in a synthetic case in Chapter 5 is applied to the Foinaven field.

6.4.1 Foinaven field petro-elastic analysis

From the Foinaven database introduced in Chapter 3, an average pressure-sensitivity model is derived from the stress-sensitivity parameters presented in Table 3.1. The resulting stress-sensitivity parameters are listed in Table 6.7. It should be noted that values for the high-pressure asymptotes μ_∞ and κ_∞ are derived using the relationships obtained between μ_∞, κ_∞ and porosity (Figure 3.7), assuming a constant porosity of 24%. This porosity corresponds to the average reservoir porosity of Panel 1, which approximately equals the average porosity obtained from the reservoir model and the Foinaven database. The effect of clay on the high-pressure asymptotes is neglected, since Figure 3.7 showed only a linear dependence for low-porosity samples, which are not representative of the porosity of the field. A more detailed rock physics analysis is required in order to include the effect of porosity and clay on the stress-sensitivity of the reservoir rock.

	Sandstone
P_κ (MPa)	5.81
P_μ (MPa)	7.11
S_κ	0.52
S_μ	0.54
μ_∞ (GPa)	10.05
κ_∞ (GPa)	12.40

Table 6.7: Stress-sensitivity parameters for the Palaeocene sandstone of the Foinaven field. These parameters are representative of the average pressure sensitivity of the Foinaven database. The high-pressure asymptote values are obtained from relationships derived in Figure 3.7.

From these stress-sensitivity parameters, the dry-frame elastic properties (κ_d and μ_d) computed from equations 3.4 and 3.5, are fluid substituted using the Gassmann's relations and fluid properties from Table 3.5, representative of the reservoir characteristics of this part of the field. The process of fluid substitution is fully explained in section 3.2. To derive similar relationships to those in equations 3.20 and 3.21, a mixture of brine (90%) and live oil (10%) is considered for the fluid substitution. This mixture assumed a residual oil saturation of 10%, which provides the greatest possible change in dry bulk modulus due to saturation. As a result, this saturation scenario represents an upper boundary on the cross-plot of the bulk modulus against the shear modulus (Figure 6.20). A common gradient, *b*, of 0.967, is derived from the dry and saturated cases. The correlation coefficients are approximately 0.8 for both cases, and demonstrate the robustness of the discriminating relationships (equations 3.20 and 3.21). The change in saturation corresponds to the variation in saturation modulus (i.e. the vertical shift between the two fits), while the change in differential pressure occurs along the fits from low (i.e. low μ_d) to high (i.e. high μ_d) pressures. It should be noted that the variations along the fits are also due to porosity changes from low (i.e. high μ_d) to high (i.e. low μ_d) porosities.

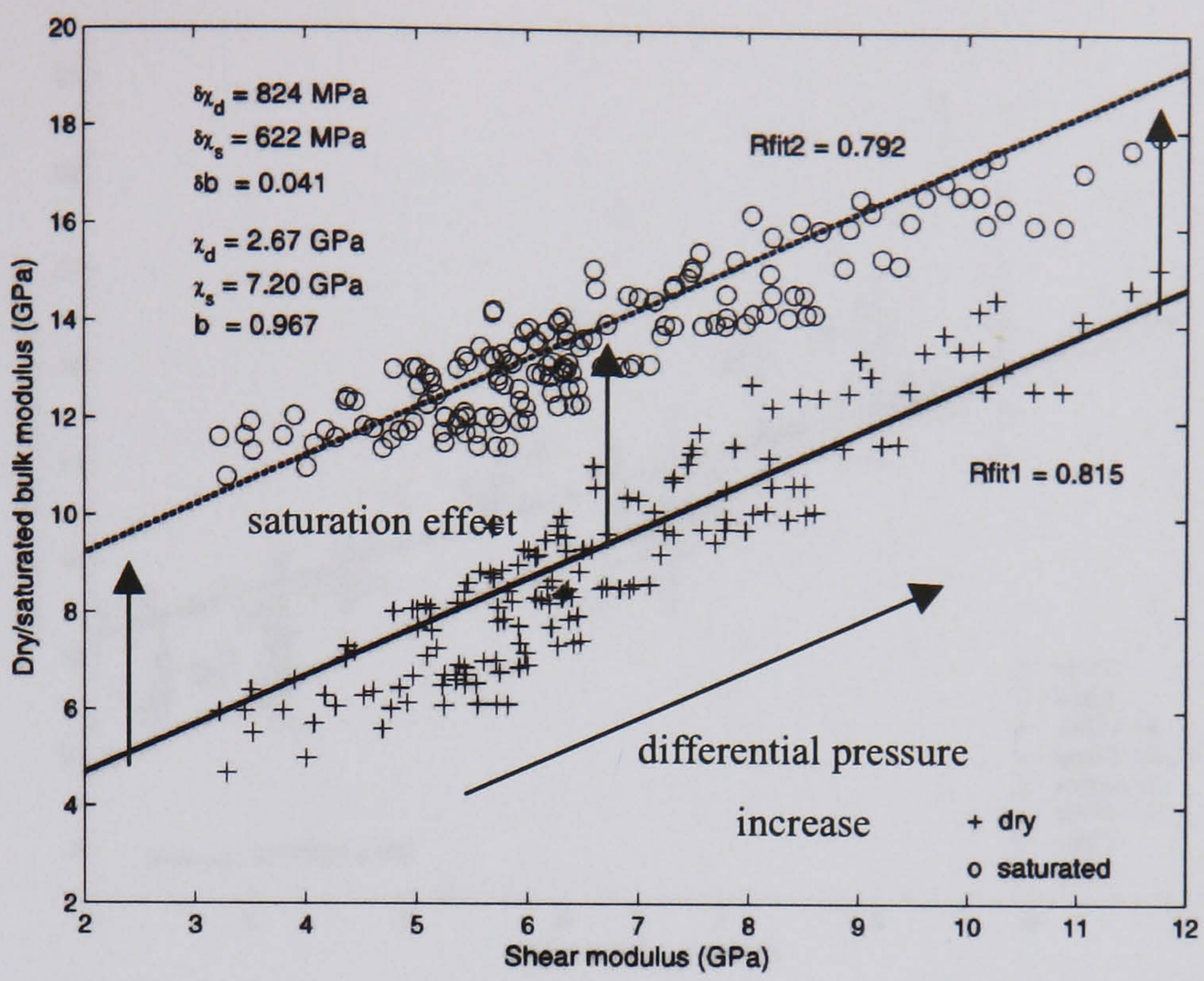

Figure 6.20: Dry/saturated bulk modulus plotted against shear modulus for the Foinaven database. Differential pressures ranging from 5 to 30 MPa are considered. Rfit1 and Rfit2 stand for the correlation coefficients in the dry and saturated cases, respectively. Parameters χ_d, χ_s and b, with their corresponding standard deviations, are provided. Pressure and saturation effects are also illustrated.

The gradient b agrees reasonably well with the sonic measurements. In fact, density, P-wave and S-wave velocities are selected from the wells of the Foinaven field outside Panel 1, since only one shear log is available near this part of the field. Figure 6.21 presents a cross-plot of bulk modulus against shear modulus, where only brine-bearing sands are chosen in order to minimize vertical variation along the bulk modulus axis due to saturation effects. Mean values of bulk and shear modulus at each well are also displayed with their corresponding standard deviation. It can be noted that the linear approximation defined from the laboratory data is still valid at the sonic scale. This approximation can now be used confidently with the elastic impedance models derived in the previous section, to invert for pressure and saturation as explained in Section 5.7.

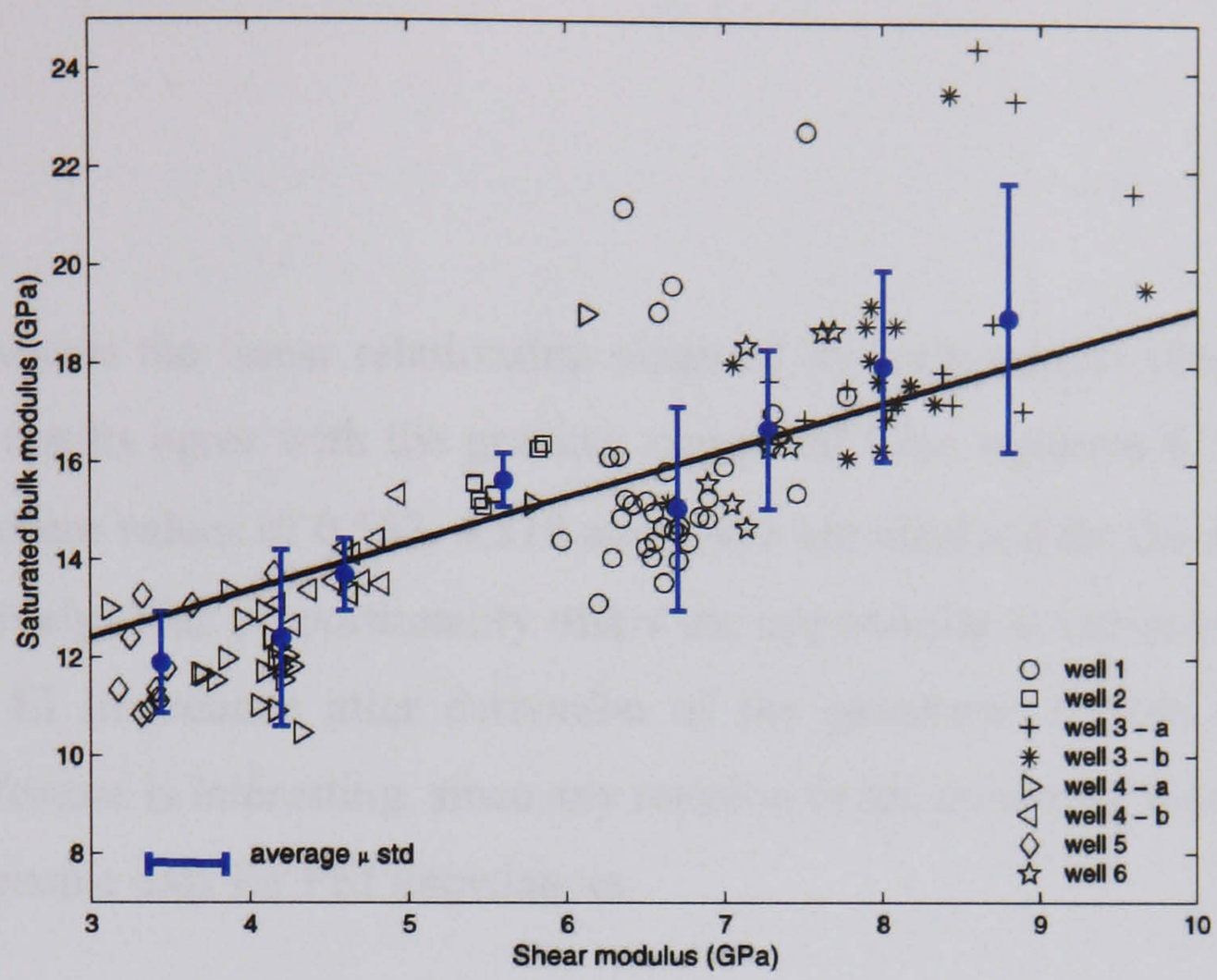

Figure 6.21: Saturated bulk modulus plotted against shear modulus for a selection of wells from the Foinaven field. Bulk and shear modulus are computed from sonic measurements and displayed only for brine-bearing sand. Mean values of the moduli are plotted (blue dots) with their standard deviation. A good correlation is observed between sonic measurements and the linear relationship (Figure 6.20) derived from the rock physics database.

6.4.2 Inversion process

A FEI/EI relationship

It should be noted that a linear relationship is observed between fluid elastic impedance (FEI) and elastic impedance (EI). In fact, one can show that the ratio of FEI to EI is proportional to a function (equation 6.3) dependent on b, the squared velocity ratio γ and incidence angles. These linear relationships can be derived from well logs in order to compute FEI impedance from the previously inverted EI at all angles.

$$\frac{FEI}{EI} = \left[\frac{\left(\gamma^{-1} - c\right)^{-\frac{c}{4}}}{\left[1 + c\left(\gamma^{-1} - c\right)^{-1}\right]} \right]^{\frac{1+\tan^2\theta}{2}} \tag{6.3}$$

where:

$\gamma = V_s^2/V_p^2$

$c = b + 4/3$

Figure 6.22 presents the linear relationship obtained by least-squares fitting between FEI and EI. These results agree with the gradient computed from equation 6.3 with $b = 0.967$ and $\gamma = 0.25$, where values of 0.553, 0.519 and 0.475 are obtained for the near, mid and far angles, respectively. This proportionality offers the opportunity to compute FEI impedance from inverted EI impedance after derivation of the parameter b from the petro-elastic analysis. This feature is interesting, since any revision in the parameter b does not imply re-inverting the seismic data for FEI impedances.

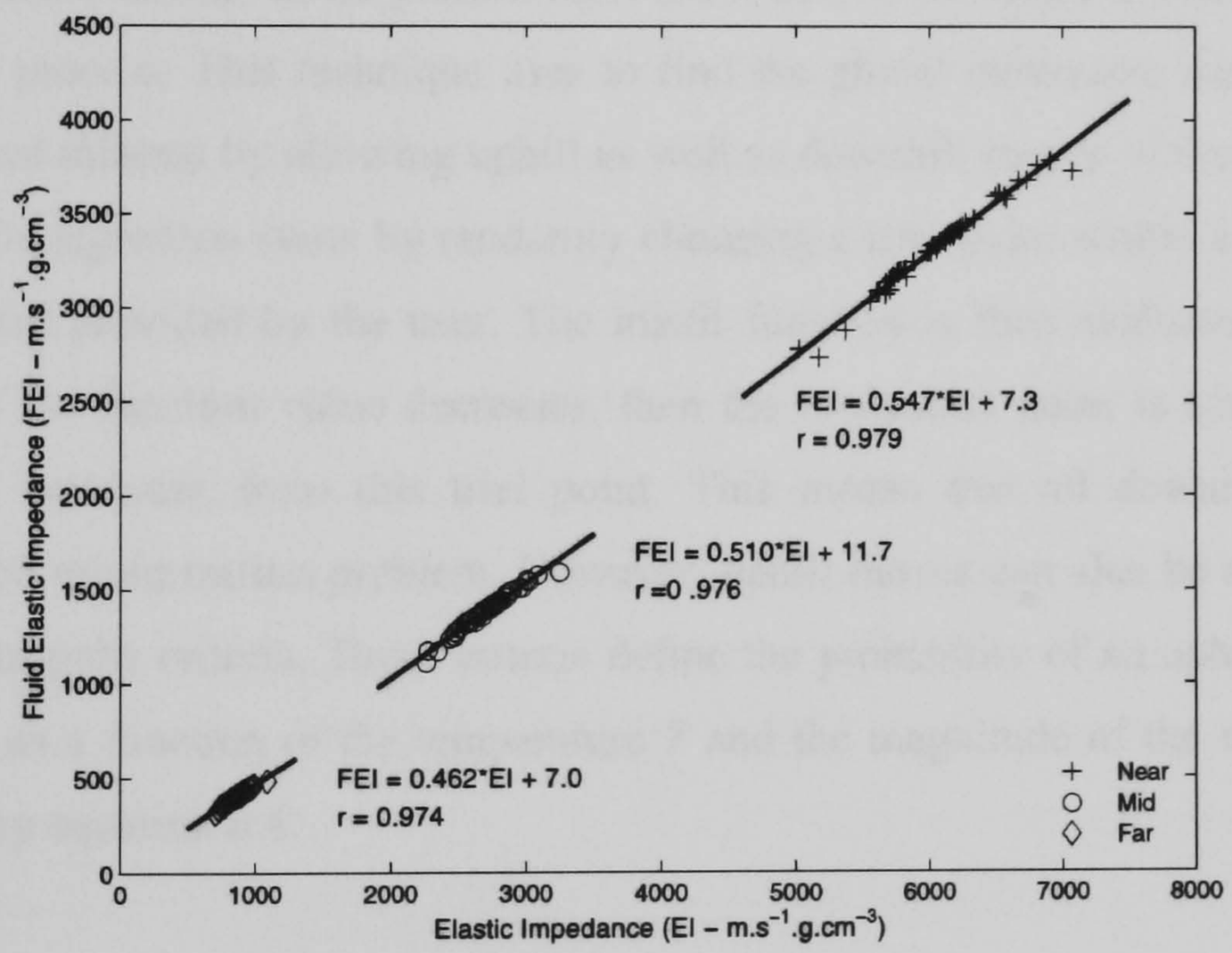

Figure 6.22: Cross-plot of fluid elastic impedance (FEI) and elastic impedance (EI) at the near, mid and far angles. Elastic impedances are computed at the well, using equations 4.8 and 4.11. Least-squares fitting is used to derive linear relationships for each angle. Coefficient correlations higher than 0.97 are obtained for all angles, showing the robustness of the previous fits.

FEI impedance computed using the previous linear relationships (Figure 6.22) can now be input into the linear system presented in equation 5.5, in order to invert for the shear and saturation modulus. In contrast with the synthetic case presented in Chapter 5, a simulated annealing minimization technique is used in this inversion.

B Simulated annealing (SA)

SA is an optimisation technique that is motivated by an analogy with metallurgy (Metropolis, 1953). It simulates the process of cooling a liquefied metal by gradually reducing its temperature. If the rate of temperature decrease is small enough, the resulting crystals reach a minimum-energy crystalline structure and contain no imperfections. This idea was first applied to optimisation problems by Kirkpatrick (1983), in order to converge towards optimal solutions. In the present case, SA is used to minimize the misfit function of the inversion process. This technique tries to find the global minimum, and avoids being trapped in local minima by allowing uphill as well as downhill moves of the function to be optimised. The algorithm starts by randomly choosing a trial point within a step-length of the initial point provided by the user. The misfit function is then evaluated for this trial point, and, if the function value decreases, then the evaluation point is accepted and the minimization continues from this trial point. This means that all downhill moves are accepted in the minimization problem. However, uphill moves can also be allowed if they fulfil the Metropolis criteria. These criteria define the probability of an uphill move being accepted, P_r, as a function of the temperature T and the magnitude of the uphill move, d, and is given by equation 6.4.

$$\mathrm{Pr} = \exp(-d/T) > r \tag{6.4}$$

where r is a random number between 0 and 1. It should be noted that as temperature decreases, the probability of allowing an uphill move is decreased. If the uphill move is rejected, then another trial point is chosen randomly. The starting temperature needs to be hot enough to allow a move to almost any neighbourhood location; otherwise, if the starting

temperature is too low, the final solution will be very close or even the same as the initial solution. To decrement the temperature, proportional cooling is applied ($T(i + 1) = m*T(i)$), where m is generally chosen to be between 0 and 1, and i is the i^{th} iteration. As cooling progresses, uphill moves are less likely to be accepted, and the percentage of rejection increases. In the version of SA used in this inversion (Goffe *et al.*, 1994), the step length is adjusted as the temperature decreases, in such a way that half of all the evaluations are accepted for each model parameter. This process improves the optimisation of the algorithm that focuses on the most promising area as temperature falls. The algorithm stops when the error tolerance of the misfit function is reached. SA is proven to be a reliable global optimisation technique (Gluck *et al.*, 1997; Ma, 2001).

C Methodology

As a starting point for the algorithm, constant values for the shear and saturation moduli derived from well A (Figure 6.13) are chosen. An average density value of 2.29 g/cm^3 is also derived from the well data, and is kept constant during the inversion. Tests showed that the inversion for three parameters appeared to be difficult and unreliable with only three angle stacks. Other attempts to invert for elastic properties have shown that several angle stacks (more than three) larger than 30 degrees are necessary to obtain a meaningful result for the density term (Personal communication, Deschizeaux, 2005). Changes in density due to saturation effects are computed in order to quantify their magnitude. One can observe from Figure 6.23 that the variation in density reaches a maximum of 0.03 due to fluid substitution, which represents a change of around 1%. It can be concluded that, for the purpose of the present inversion, density changes are assumed to be negligible in first approximation. It is demonstrated in Chapter 3 that the same conclusion is also valid for a change in density due to pressure effects.

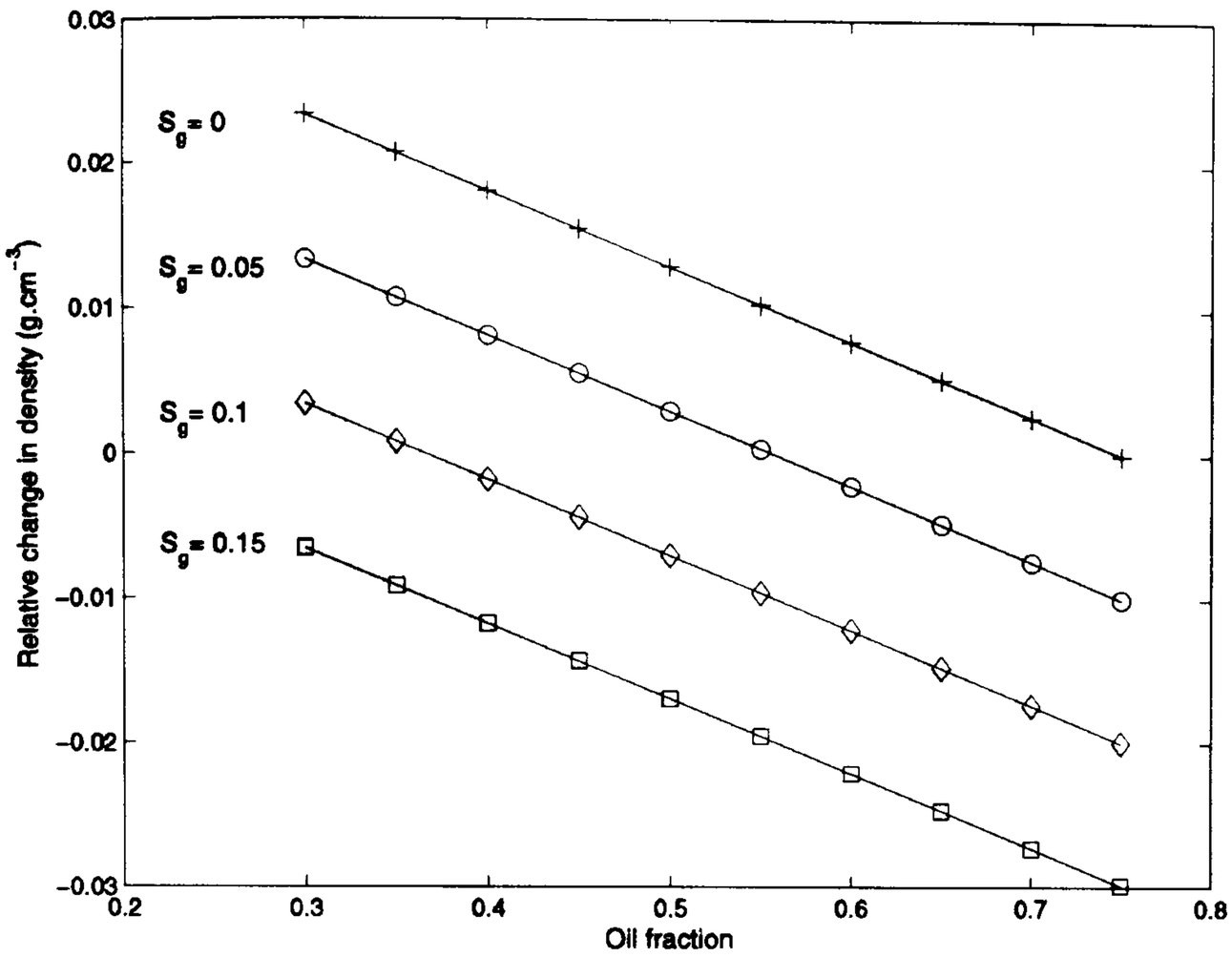

Figure 6.23: Change in density versus oil fraction relative to $S_o = 0.75$ for different gas saturations S_g. Saturated densities are computed using equations 3.15 and 3.17, with $\rho_m = 2.66$ g/cm^3 at a differential pressure of 25 MPa. Fluid characteristics and reservoir conditions from Table 3.5 are considered. Connate water of 25% and residual oil saturation of 30% are assumed in this display, that can be related to the different scenario of a primary gas cap. The dependence of density on fluid saturation appears to be relatively small in this case.

Outputs from the optimization algorithm are the shear and saturation moduli for each survey. These inverted results are used in equations 3.26 and 3.27 in order to derive the pore pressure and fluid bulk modulus changes. Since equation 3.26 is obtained from an approximation of Gassmann's relation (equation 3.13), which is relevant to seismic frequencies, the fluid bulk modulus changes do not require calibration. An average porosity for the reservoir of 24% and a critical porosity of 33% (derived in Section 5.7.1) are used. However, equation 3.27, which is based on ultrasonic measurements, required a calibration step. Furthermore, a preliminary inversion trial showed an overestimation of the pore pressure changes using the pressure-sensitivity model described in Table 6.7. This overestimation is attributed to core damage effects (cf. Section 3.1.5), which enhance the stress-sensitivity of the rock at low differential pressures, due to the closing of internal damage created during the unloading of the core samples from the *in situ* formation. In

order to take into account the core damage effect prior to the calibration with the seismic data, a new pressure-sensitivity model is derived by fitting the laboratory data (as in Figure 3.3), but for a differential pressure larger than 15 MPa. It would be preferable to choose a pressure threshold corresponding to the initial differential pressure of the reservoir (*c.*23 MPa), but the lack of ultrasonic measurements at high pressure justifies the present choice. The resulting stress-sensitivity model of the shear modulus is presented in Figure 6.24, and shows a more gradual increase in the shear modulus with differential pressure. The updated stress-sensitivity parameters are: μ_∞ = 12 GPa, E_μ = 1.22 and P_μ = 17.3 MPa. It should be noted that a number of samples had to be ruled out because they were not tested up to sufficient confining pressure. This explains the difference between the original and the corrected core damage models. To calibrate this model, the inverted shear modulus changes at the location of injector I1 and producer P1 are chosen, with the pore pressure changes predicted from the flow simulation provided by the operators. The predicted pore pressure changes are assumed to be fairly accurate around the wells, since the simulation is calibrated to the production data. These calibration points are displayed on Figure 6.24, together with the calibrated pressure-sensitivity model. Calibrated stress-sensitivity parameters are: μ_∞ = 10.7 GPa, E_μ = 1.61 and P_μ = 17.3 MPa. The calibrated model is used in the next section to estimate pore pressure changes.

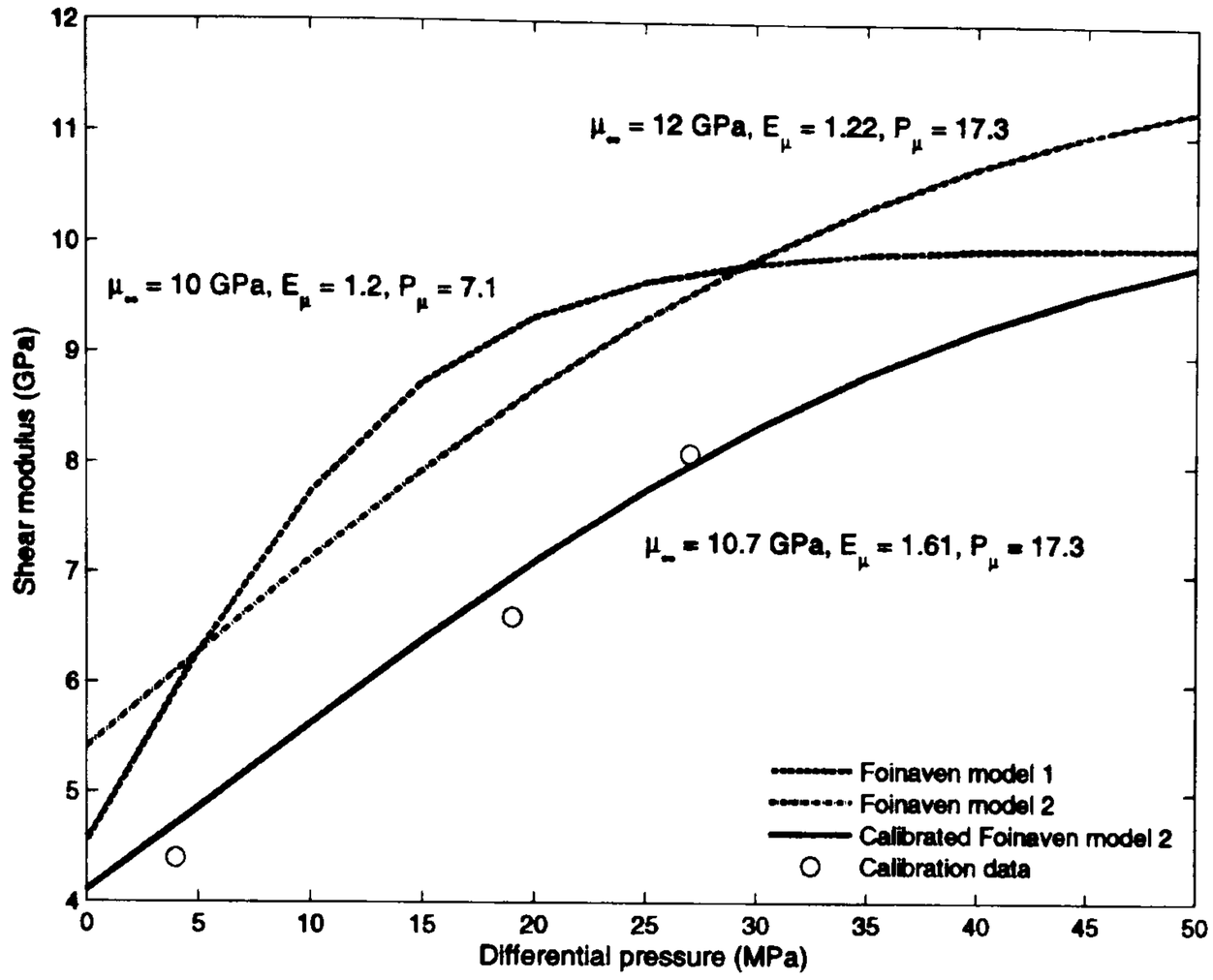

Figure 6.24: Pressure dependence of the shear modulus from the Foinaven database. Original (from Table 6.7: dotted curve), corrected (dashed curve) and calibrated (plain curve) pressure-sensitivity models are displayed. The circles stand for the calibration points derived from the inverted shear modulus and pore pressure from the flow simulation at the injector I1 and producer P1 locations. The calibrated model fits the calibration data reasonably well.

6.4.3 Independent interpretation of pressure and fluid effects

Inverted pore pressure changes and inverted fluid bulk modulus changes from the previously described inversion procedure are presented in this section. Figure 6.25 presents the inverted fluid bulk modulus changes for two micro-layers, as in Figure 6.17. Increases in fluid bulk modulus changes are noticeable in the vicinity of injectors I1 and I2. Changes reach up to +650 MPa at I1, while smaller changes are once again observed at I2 (*c.*+500 MPa). Large changes up to –650 MPa and over are present around the producers. These large variations are caused by the high sensitivity of the fluid bulk modulus to a small degree of gas saturation (cf. Figure 3.24). Gas appears to be coming out of solution close to the producers which is confirmed by measurements, but also in the neighbourhood of the injector I1 where the initial pore pressure (*c.*23 MPa) is presumably not maintained above the bubble point. In order to compare these results with the prediction from the flow

simulation, fluid bulk modulus changes are computed for homogeneous and heterogeneous mixtures (equations 3.16 and 3.18) at the reservoir scale, based on the predicted fluid saturation. The dimensions of the flow simulation model are 100 by 100 metres horizontally and approximately 5 metres vertically. Figure 6.26 and Figure 6.27 present the homogeneous and heterogeneous κ_f changes, respectively. Layers representative of the general behaviour of the top and base sands are displayed. It is notable that the inverted $\Delta\kappa_f$ compares favourably with the predicted results around I1, even if the aerial extension of the fluid saturation changes is larger. However, it seems that the predicted $\Delta\kappa_f$ is overestimated in the vicinity of injector I2. These observations are valid for the homogeneous and heterogeneous κ_f changes. In the case of patchy saturation distribution (Figure 6.27), the effect of the gas is not visible; however, in the homogeneous case (Figure 6.26) large decreases of the same magnitude as the inverted results are observable. It can be concluded from the previous remark that the gas phase coming out of solution is homogeneously distributed in the fluid mixture saturating the pores. Furthermore, the areal extension of the gas exsolution from the inverted and predicted results is in good agreement. In addition to the previous observation, a fault shown just below producer P3 (Figure 6.13) appears to be sealed, since no communication is discernible between P3 and P1. It should be restated that the estimated κ_f changes in the presence of gas are also dependent on the pressure changes, as shown in Section 3.3.2. Therefore, the uncertainty in κ_f changes will increase as gas is released from the live oil. The interpretation of the κ_f changes demonstrates that the fluid is likely to be homogeneously distributed even in the presence of gas. This conclusion is in agreement with the results from (Sengupta and Mavko, 2003), who show that the homogeneous saturation model is a valid approximation for most water-flooding and primary production scenario with gas exsolution.

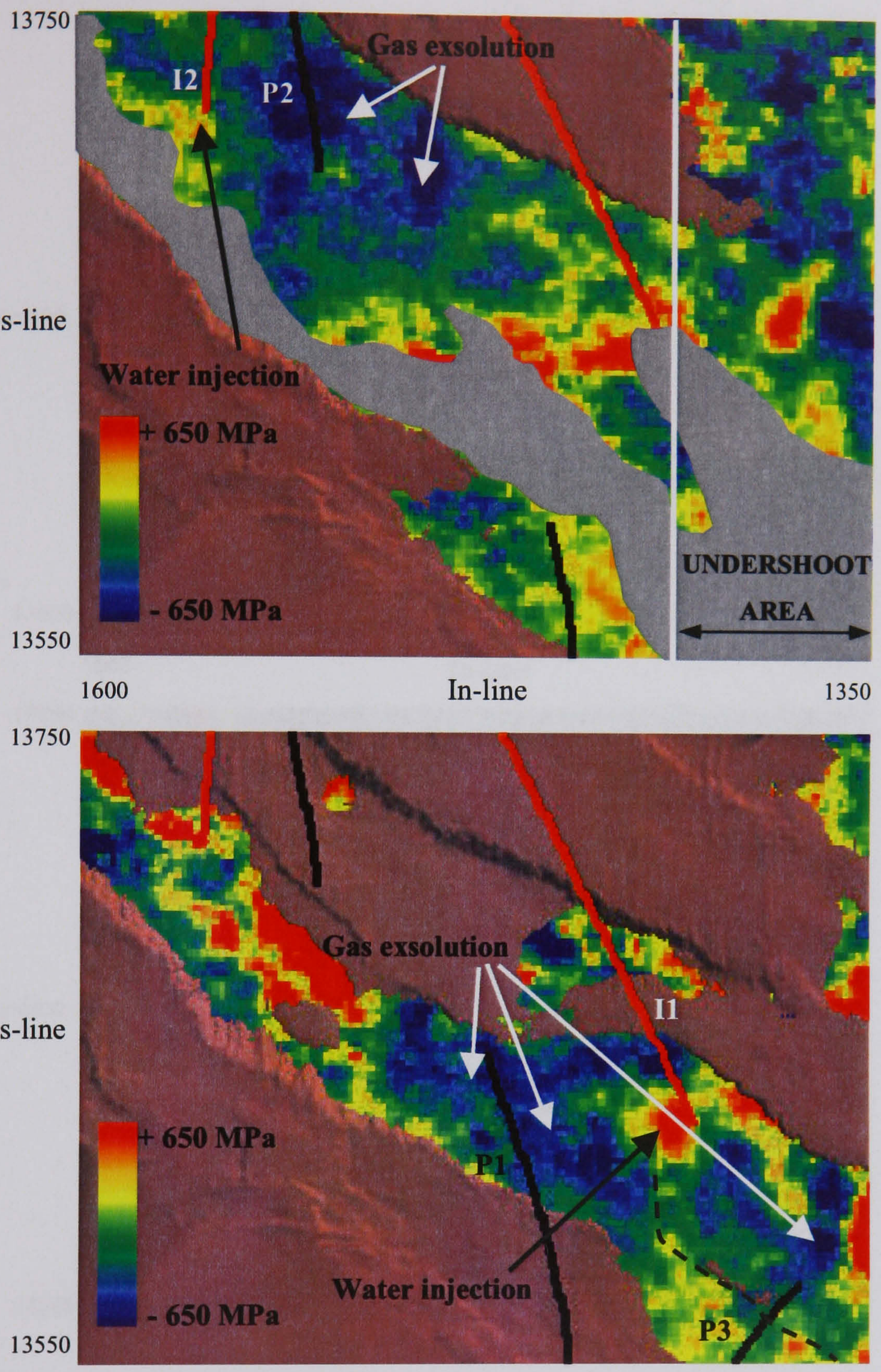

Figure 6.25: Inverted fluid bulk modulus changes for layer 18 (top) and layer 23 (bottom) of the stratigraphic inversion grid. The brown and grey surfaces stand for the base and top of the reservoir, respectively. The different injectors (red paths) and producers (black paths) located in the area are shown. In the bottom right-hand corner, a possible sealing fault is highlighted.

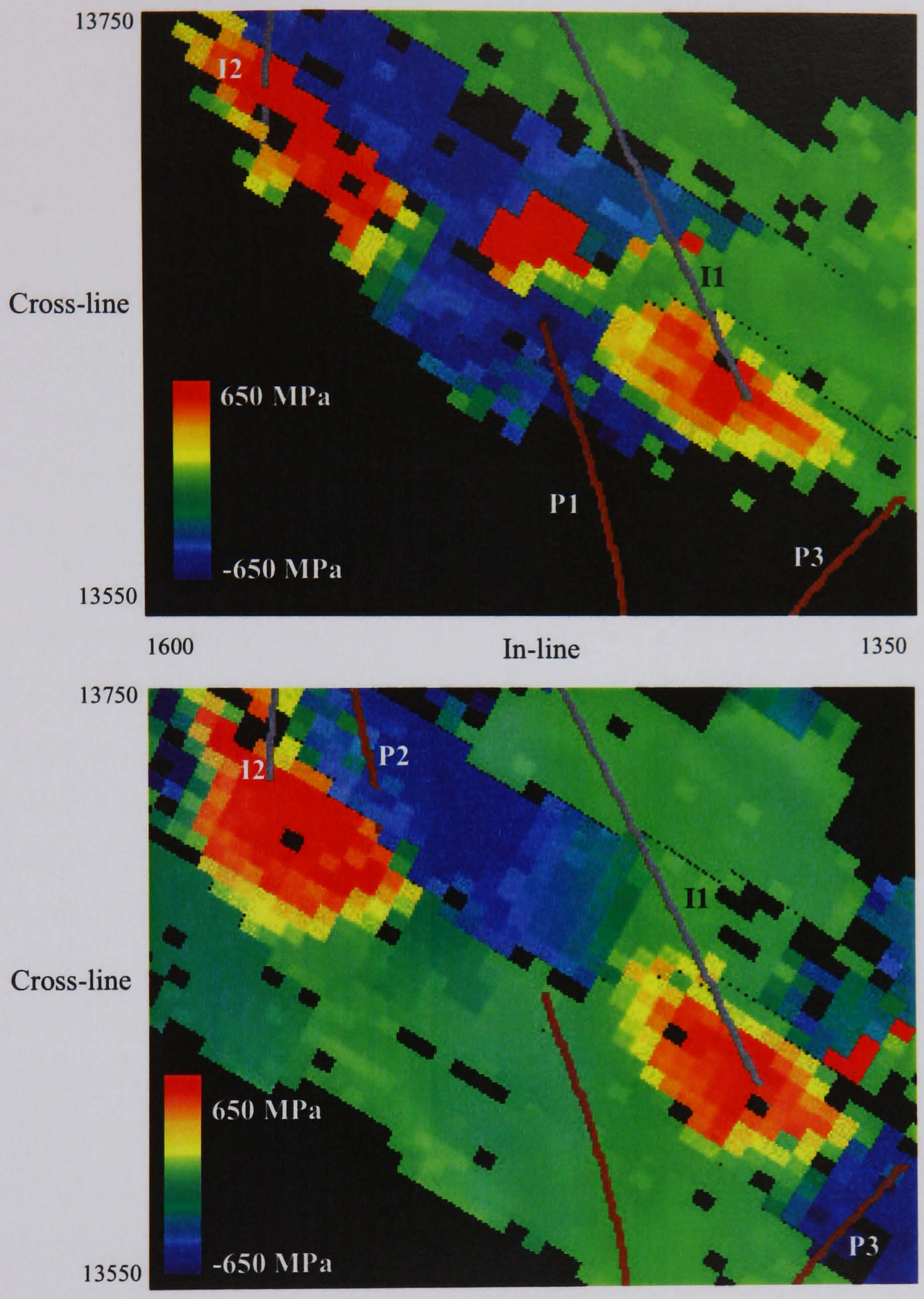

Figure 6.26: Predicted homogeneous fluid bulk modulus changes in the top sand (top) and base sand (bottom). The different injectors (grey paths) and producers (brown paths) located in the area are shown.

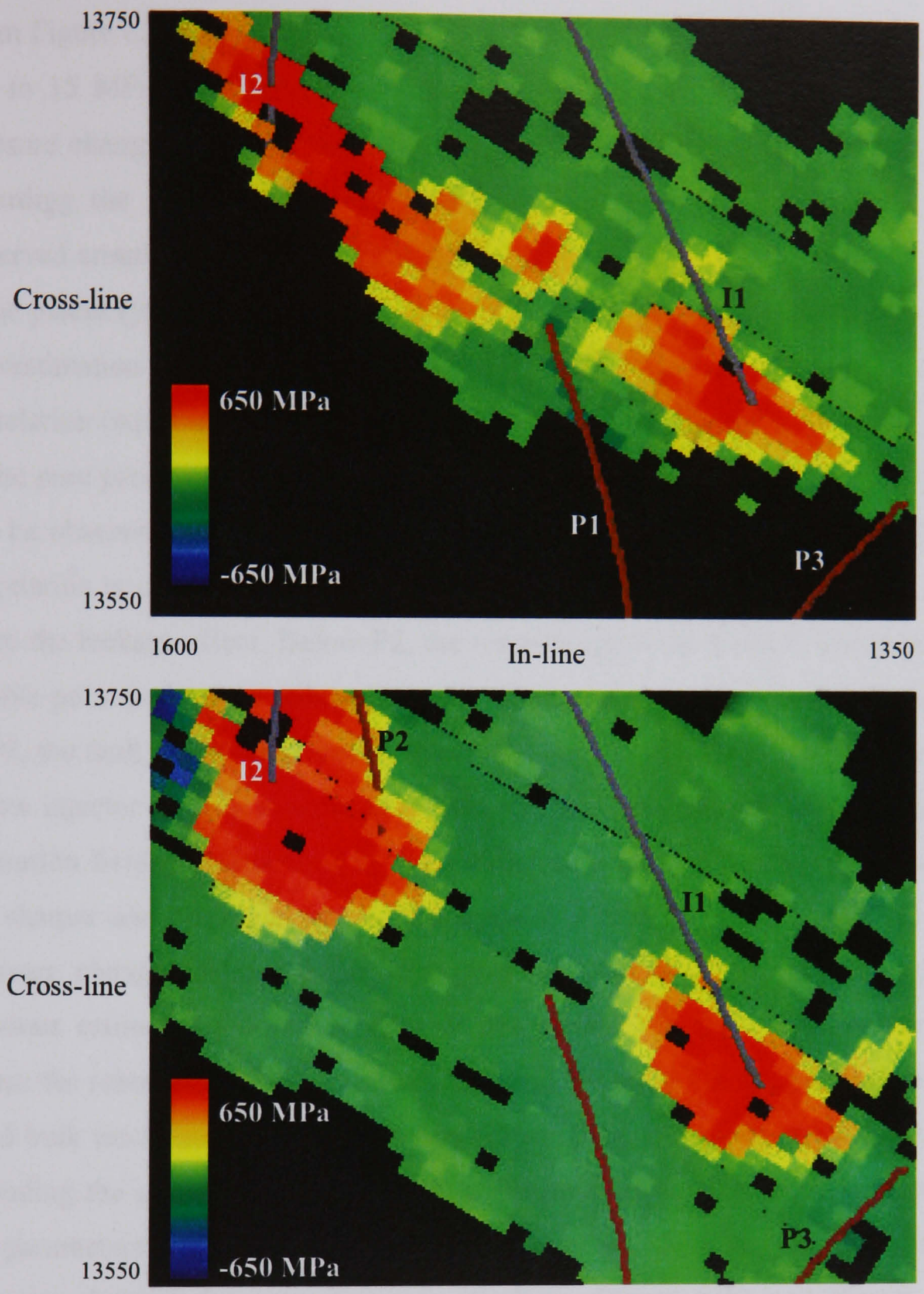

Figure 6.27: Predicted heterogeneous fluid bulk modulus changes in the top sand (top) and base sand (bottom). The different injectors (grey paths) and producers (brown paths) located in the area are shown.

From Figure 6.28, increases in the inverted pore pressure changes are visible at injector I1 (up to 15 MPa) and injector I2 (*c.*4–5 MPa). These results confirm the predicted pore pressure changes from the flow simulation (Figure 6.29). There is also a good agreement regarding the decreases in pore pressure around the producers, with higher variations observed around P1 (*c.* –8 MPa) compared to P2 (*c.* –5 MPa). However, it appears that in some places (yellow circle: Figure 6.28) the pore pressure changes are overestimated. This overestimation is caused by the possible presence of gas, which weakens the rock physics correlation (equation 3.21), and, as result, introduces leakage from the fluid bulk modulus to the pore pressure change maps. By comparing Figure 6.25 and Figure 6.28, a correlation can be observed between the two attributes where gas comes out of solution, however no correlation is observed between Figure 6.26 and Figure 6.29 in these areas showing once more the leakage effect. Below P2, the reservoir pressure remains above or just below the bubble point and only a reduced amount of gas comes out of solution (Figure 6.25). Close to P3, the fault noted earlier seems to act as a barrier, which helps to maintain pore pressure below injector I1. It is interesting to note that the behaviour of the pore pressure and fluid saturation fields are described by the estimated results, where fluid bulk modulus changes are sharper and contained around the wells (Figure 6.25, wells I1 and I2) while the pore pressure changes exhibit a smoother gradient (Figure 6.28, wells I1 and I2). However spurious estimated production changes are obtained in the undershoot area. In order to assess the robustness of the estimates, standard deviations in the pore pressure changes and fluid bulk modulus changes are computed using the method presented in section 5.8.1 by including the correlation between the model parameters. The same standard deviations in the parameters and coefficient correlations are used as in sections 5.8.3 and 5.8.4, since they are derived from the Foinaven database. Figure 6.30 and Figure 6.31 show the uncertainty in the fluid bulk modulus and pore pressure estimates, respectively. The standard deviation in $\Delta\kappa_f$ can reach up to 100 MPa for a change in κ_f of ±650 MPa near I1, P2 and P3. Smaller standard deviations are observed around I2 (±50 MPa) and P1 (below 100 MPa). Regarding the uncertainty in the pore pressure changes, one can note an average standard deviation of 1 MPa in areas where variations in pressure are small. Larger standard deviations (up to 2 MPa and over) are observed near the producer I1, and also in

the area where pore pressure changes are believed to be overestimated. In fact, it should be noted that in this uncertainty analysis, the standard deviations in the model parameters are held constant, regardless of the type of saturants. However, it was shown previously that the presence of gas in the system can produce leakage between the saturation and pressure domains. In order to take this effect into account, the standard deviation should be updated as a function of the fluid saturation. As a result, in the present study, standard deviations are likely to be underestimated in the presence of gas. The inversion procedure presented here used fluid elastic impedance (FEI) to invert for pressure and saturation estimates. However, an alternative method to obtain these estimates is to use the $\lambda\rho$ and $\mu\rho$ attributes with the rock physics relationship (equation 3.21), and a constant-density term as previously assumed, to retrieve the shear and saturation modulus. The production estimates from this method are not reliable, since they are highly contaminated by the large amount of leakage occurring between $\lambda\rho$ and $\mu\rho$ as stated in this section. Therefore, the use of FEI for independent estimation of pressure and saturation effects is recommended.

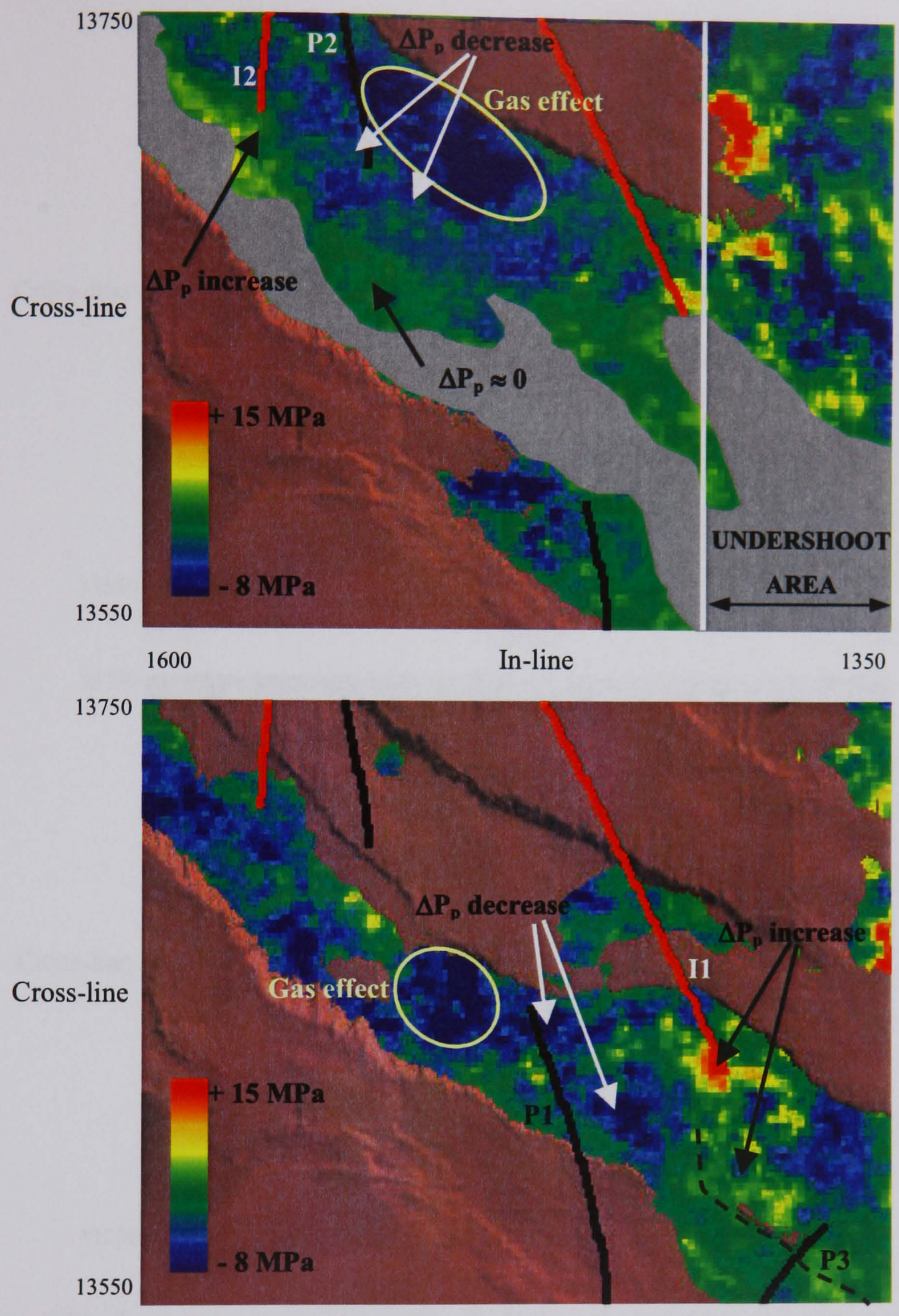

Figure 6.28: Inverted pore pressure changes for layer 18 (top) and layer 23 (bottom) of the stratigraphic inversion grid. The brown and grey surfaces stand for the base and top of the reservoir, respectively. The different injectors (red paths) and producers (black paths) located in the area are shown.

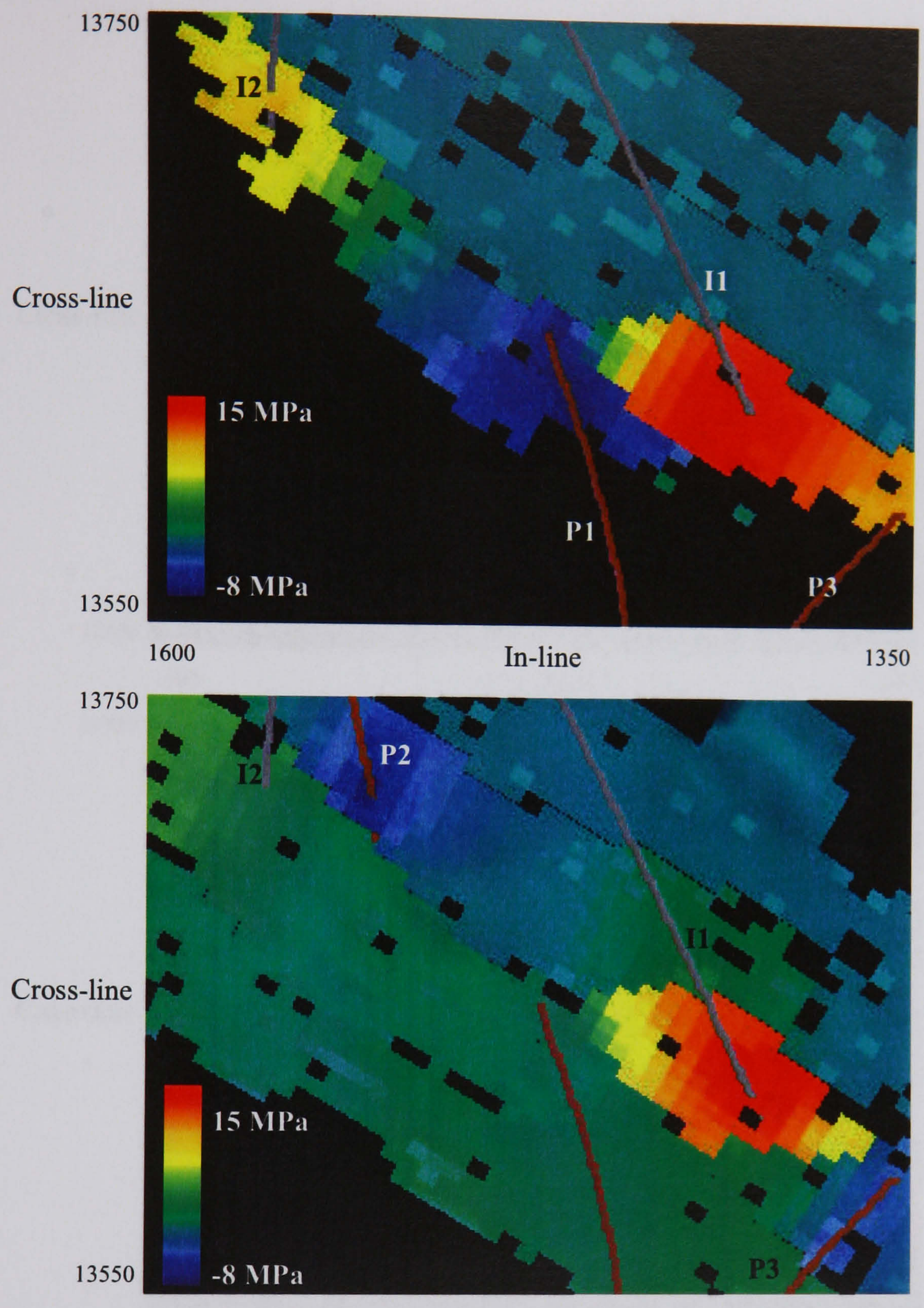

Figure 6.29: Predicted pore pressure changes in the top sand (top) and base sand (bottom). The different injectors (grey paths) and producers (brown paths) located in the area are shown.

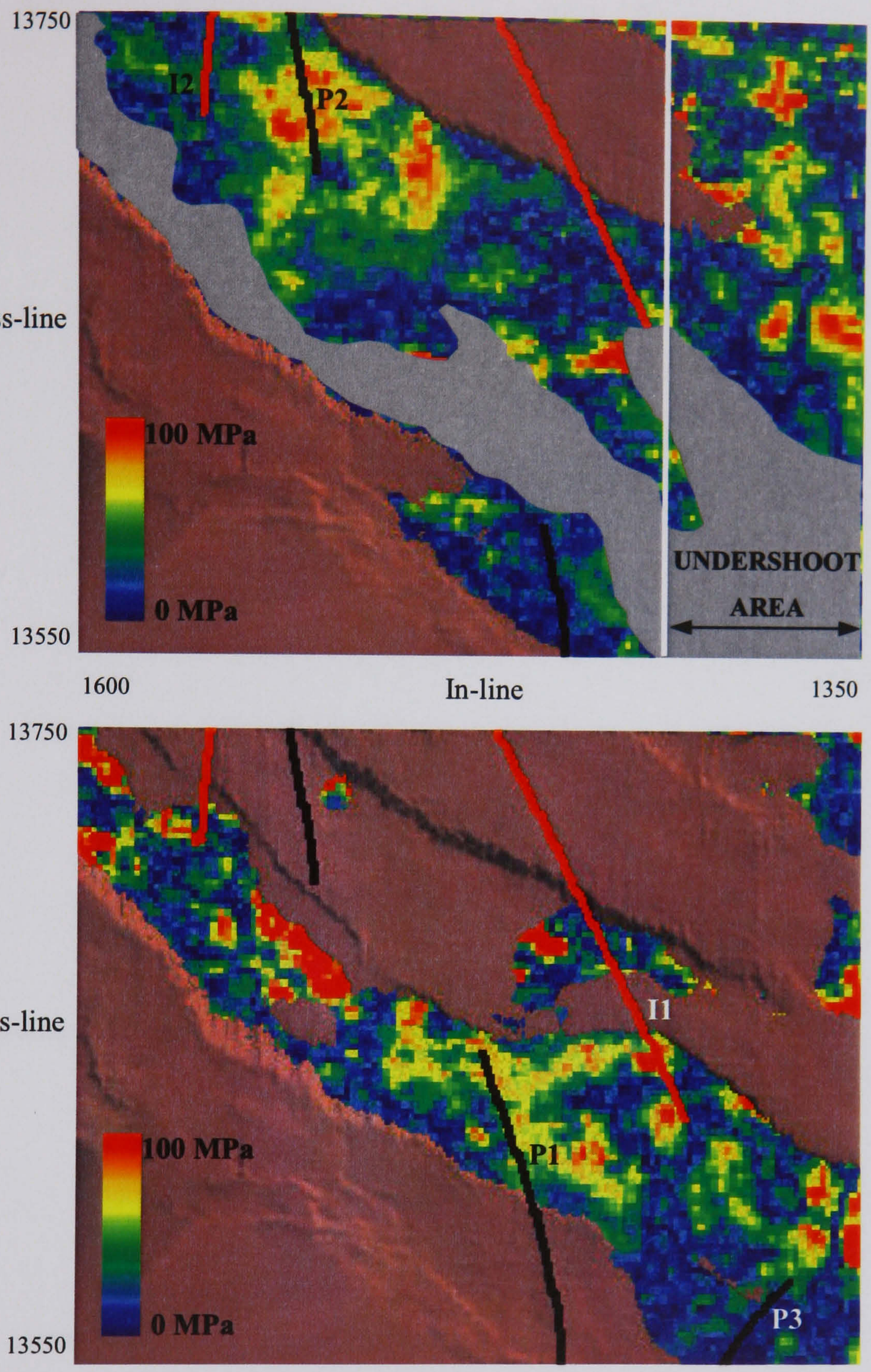

Figure 6.30: Estimated uncertainty in the fluid bulk modulus changes for layer 18 (top) and layer 23 (bottom) of the stratigraphic inversion grid, including correlation between the inversion parameters. The brown and grey surfaces stand for the base and top of the reservoir, respectively. The different injectors (red paths) and producers (black paths) located in the area are shown.

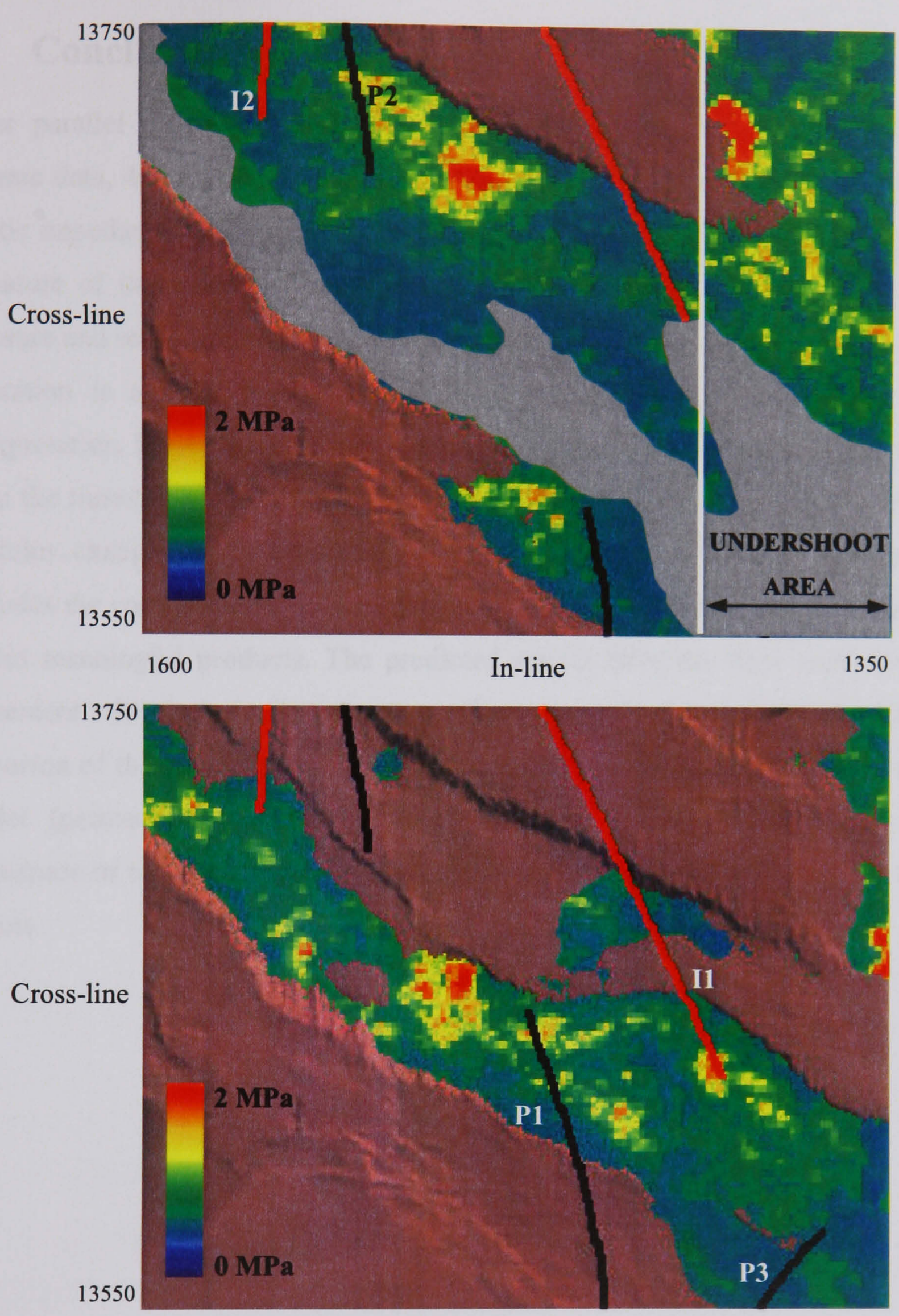

Figure 6.31: Estimated uncertainty in the pore pressure changes for layer 18 (top) and layer 23 (bottom) of the stratigraphic inversion grid, including correlation between inversion parameters. The brown and grey surfaces stand for the base and top of the reservoir, respectively. The different injectors (red paths) and producers (black paths) located in the area are shown.

6.5 Conclusions

After parallel processing and appropriate pre-conditioning of the Foinaven time-lapse seismic data, 4D stratigraphic elastic inversion is applied. Qualitative interpretation of the elastic impedance highlighted the main factors contributing to the origin of the time-lapse signature of the reservoir, but failed to provide any insight into the distribution of the pressure and saturation fields. A new methodology to independently invert for pressure and saturation is applied to the data in order to enhance the quantitative aspect of the interpretation. Elastic properties of the rock (i.e. shear and saturation modulus) are inverted from the time-lapse elastic impedance, and are converted into pore pressure and fluid bulk modulus changes using calibrated rock physics relationships. The calibration procedure includes the correction of the core damage effect on the stress-sensitivity model in order to obtain meaningful products. The predicted results from the flow simulation are in good agreement with the seismic estimation. However, differences observed between the aerial extension of the estimated and predicted changes suggest potential updates to the reservoir model (permeability and porosity adjustments). The uncertainty analysis shows the robustness of the proposed methodology for discriminating between these two production effects.

Chapter 7

Conclusions and recommendations for further work

In this dissertation, a new petro-elastic-based approach has been presented to independently estimate reservoir pressure and saturation from 4D seismic data. In this chapter, the main conclusions drawn in the course of this study are summarized and recommendations made to extend the present research.

7.1 Conclusions

Petro-elastic analysis of sandstones

Ultrasonic measurements – from the literature and the rock physics database at Heriot-Watt Institute of Petroleum Engineering – have enabled a petro-elastic study to be made of reservoir sandstones from the North Sea and the Gulf of Mexico. A rock physics correlation observed between the shear modulus and the dry/saturated bulk modulus constitutes the basis for the definition of a new elastic property called the saturation modulus. The main result of this analysis demonstrates that the effect of pressure and fluid saturation can be isolated into two rock physics attributes. One is dependent on the pressure effect (shear modulus), and the other is dependent on the fluid-saturation effect (saturation modulus). This separation of the production effects represents a general result valid for a variety of reservoir sandstones. The principal factors affecting the reliability of this new rock physics correlation are found to be the porosity and clay content. Relationships are proposed to include porosity and clay content changes in the stress-sensitivity of the rock. Approximations are presented to estimate pore pressure and fluid bulk modulus changes from time-lapse variations in shear and saturation moduli in homogeneously and

heterogeneously saturated sandstones for an oil–brine system. Fluid bulk modulus is preferred to fluid saturation in this work, because it does not presume any hypothesis regarding the distribution of the fluid saturant in the rock. The core damage effect is also highlighted as a possible factor impacting on the quality of the pressure changes relationship.

The first part of this dissertation shows that pore pressure and fluid saturation can be accurately discriminated at the rock physics scale.

From the rock physics to the seismic domain

In the second part of this thesis, the interpretation of pressure and saturation effect from seismic attributes are investigated. The new rock physics relationships are implemented and new forms for the AVO equation and elastic impedance (called fluid elastic impedance – FEI) are developed and validated against existing approximations. The new formulations offer a more intuitive interpretation of the pressure and saturation effect compared to Aki & Richards or Connolly's forms for reflectivity and elastic impedance.

From a variety of offset-dependent reflectivity and elastic impedance formulations, the discriminating power of several seismic attributes (i.e. P-wave velocity, S-wave velocity, shear modulus, saturation modulus and bulk modulus) is studied on synthetic data. It is shown that conventional seismic attributes are highly interdependent in terms of pressure and saturation, and that the shear and saturation moduli lead to a better discrimination of these production effects. Seismic inversion for shear and saturation moduli emerges as the best alternative to estimate pore pressure and fluid bulk modulus changes, and optimally reduces the cross-talk between the estimates.

Time-lapse seismic inversion for reservoir pressure and saturation

In this dissertation, the application of a new methodology to discriminate between the pressure and saturation effects is illustrated using synthetic and real case studies. This methodology consists of estimating pore pressure and fluid bulk modulus changes from the

inversion of multi-angle near, mid and far elastic impedance stacks from a baseline and repeat vintages. From the inverted elastic impedance, shear and saturation moduli are obtained and converted to production effects. Elastic impedance is favoured to reflection amplitudes in this multi-angle inversion, because it overcomes problems encountered by AVO analysis and, furthermore, forms a more intuitive basis for the integration of pressure and saturation estimates with static or dynamic reservoir simulation. Additionally, a deterministic uncertainty analysis, including the correlation and non-correlation of the different error sources, is performed.

For the synthetic case, the Ainsa II turbidite-filled channel complex (southern Pyrénées – Spain) is used as analogue in a reservoir model-based study. The inverted pore pressure and fluid bulk modulus changes from the synthetic seismogram show a good agreement with the outputs from the reservoir flow simulator, and demonstrate the accuracy of this petro-elastic-based approach. The precision in the estimates is derived from a deterministic uncertainty analysis, where all sources of errors are propagated via the differentiation of the pressure and saturation change relations. The combined effect of these errors on the estimates is examined for two scenarios: interrelated and unrelated errors. In addition, a sensitivity study is carried out and shows that the largest factor affecting the uncertainty of the final results is errors in the seismic attributes; followed by errors in the pressure model and errors in the approximation of the saturation change. The assumption of unrelated errors leads to an overestimation of the combined standard deviation in the estimates. The magnitude of the standard deviation in the pore pressure and fluid bulk modulus changes are significantly reduced by the introduction of the correlation between input errors.

For the real case study, the methodology is applied to the deep-water Palaeocene turbidite sandstones of the Foinaven field, west of the Shetland Isles. Pre-stack towed-streamer data from a baseline and a repeat survey are selected after parallel seismic processing, and are converted to angle stacks (i.e. near, mid and far). These angle stacks are cross-matched and preconditioned to ensure a high repeatability of the products from the time-lapse stratigraphic inversion. A qualitative interpretation of the data from time-lapse seismic

attributes (i.e. $\lambda\rho$ and $\mu\rho$) highlights the aerial extension of the 4D signature related to the injector and producer activities, but fails to show accurately any features from the pressure or saturation fields. The cross-talk in terms of pressure and saturation between $\lambda\rho$ and $\mu\rho$ is at the root of the difficulties arising in the interpretation. By applying the new methodology, the understanding of the change in pressure and saturation across the field can be largely improved. In order to obtain meaningful results for the pressure attribute, a correction for the core damage effect is derived in the calibration of the pressure-sensitivity model. In the presence of gas, leakages from the saturation to the pressure map are observed, due to the degradation of the rock physics correlation. However, the magnitude of these leakages is dependent on the initial pressure of the reservoir and pressure changes. Overall, the predictions from the reservoir flow simulation are in good agreement with the estimations of the production effects, and emphasize some possible update to the reservoir model. The uncertainty analysis shows the robustness of the proposed methodology for independently estimating pressure and saturation effects.

7.2 Recommendations for further work

The following items are suggested as possible topics for future research to strengthen the rock physics foundation and enhance the quantitative aspect of the proposed time-lapse pressure-saturation inversion.

- A detailed investigation of the stress-sensitivity of unsaturated shaley sandstones is recommended. It is found that the current data did not allow for a definitive conclusion of this topic. SEM (scanning electron microscopy) analysis of the sandstone samples is necessary to understand the distribution of the clay (i.e. framework, interstitial and laminar clay deposits), and to enable the derivation of appropriate micro-mechanical pressure-sensitivity models. This lack of knowledge of the clay distribution also affects possible conclusions regarding the effect of porosity on certain stress-sensitivity parameters.

- Core damage effects increase the stress-sensitivity of the rock at low effective pressure, and can have a dramatic impact on the reliability of the pore pressure estimates. Even if a correction is proposed to remove this effect – by considering ultrasonic measurements made above the initial effective pressure in the Foinaven field – it remains a fact that alternative methods are required, particularly in fields exhibiting high effective pressure, where such a correction is not applicable. Sonic measurements performed at different stages of reservoir production might provide the opportunity to use the reservoir as a laboratory and to derive a rock physics model from logs.

- In Chapter 3, a linear approximation is used to relate the shear modulus to the saturated bulk modulus. It should be noted that the use of a non-linear function might be more appropriate in particular cases.

- It is observed that gas saturation causes leakage between the saturation and the pressure domains. In fact, the pressure dependence of the fluid bulk modulus changes cannot be neglected in the presence of gas, especially at high pore pressure. To reduce the interference between the production estimates, pressure dependence could be included in the fluid bulk modulus changes for partially gas-saturated rock.

- To further evaluate the new inversion method, a more challenging geological model could be selected together with advanced seismic modelling algorithm.

- In the real case study, the average porosity of the reservoir is considered and the effect of clay is neglected. If reliable rock physics models are available, porosity and net-to-gross information from the reservoir model can be used to constrain the pressure-saturation inversion. However, the integration of net-to-gross information in the inversion via the rock physics models is not straightforward. In fact, different rock physics models might be available, depending on the distribution of the clay, but only net-to-gross information which is independent of the clay distribution.

- The quantitative aspect of the new methodology can be further developed by implementing the technique in a simultaneous inversion scheme where direct estimation of shear modulus, saturation modulus and density could be performed. This implementation will involve the direct inversion of the new form for reflectivity presented in Chapter 4. The inversion for the density term (instead of a fixed constant) and implicit inversion for the squared velocity ratio γ offer the potential to improve the accuracy of the production estimates. The acquisition of time-lapse pressure (e.g. permanent pressure gauges, Repeat Formation Tester – RFT) and saturation (e.g. resistivity logs, Reservoir Saturation Tool – RST) at well locations could also be useful to constrain the inversion. The benefit of including time-shifts analysis could also be investigated.

- A natural extension of this work is the study of subseismic resolution fluid distribution in order to accurately estimate fluid-saturation variations from the inverted fluid bulk modulus changes provided the new pressure-saturation inversion. To understand how saturation scales influence seismic properties, fine-grid (e.g. 1-metre cell) reservoir simulations are necessary to avoid the artificial averaging of saturation output from a coarse-grid (e.g. 10-metre cell) model. Upscaling of fine-grid models should provide some insights into the factors affecting fluid distribution (Sengupta and Mavko, 2003; Kirstetter, 2002) and also derivation of alternative saturation laws (i.e. between uniform and non-uniform models). Refined downscaling techniques for reservoir simulation might be another option to improve knowledge of the fluid distribution.

Appendix A: Elastic properties versus stiff and compliant porosities

In this appendix, pressure-sensitivity models are derived for the dry bulk and shear moduli using the stress dependencies of the stiff and compliant porosities (Shapiro, 2003).

By separating the total porosity ϕ into two components:

$$\phi = \phi_{co} + \phi_{s} \qquad \text{A.1}$$

where ϕ_{co} stands for the compliant porosity supported by micro-cracks and grain–grain contacts and ϕ_{s} for the stiff porosity supported by the pores. Shapiro (2003) showed that the dry compressibility of a rock is provided by:

$$C_{d}(\phi_{s}, \phi_{co}) = C_{ds}\left[1 + \theta_{s}\phi_{s} + \theta_{c}\phi_{co}\right] \qquad \text{A.2}$$

where C_{ds} is the drained compressibility of a rock with a closed compliant porosity (i.e. $\phi_{co} = 0$) and a stiff porosity corresponding to zero confining pressure. Furthermore,

$$\theta_{s} = \frac{1}{C_{ds}}\frac{\partial C_{d}}{\partial \phi_{s}} \text{ and } \theta_{c} = \frac{1}{C_{ds}}\frac{\partial C_{d}}{\partial \phi_{co}} \qquad \text{A.3}$$

where the derivatives are taken at $\phi_{co} = \phi_{s} = 0$. By assuming that the compressibility depends mainly on changes in the compliant porosity rather than stiff porosity, i.e.

$$\theta_{s}\phi_{s} << \theta_{c}\phi_{co}$$

and also by assuming that compliant porosity decreases exponentially with pressure:

$$\phi_{co} = \phi_{co}(0)\exp(-\theta_{c}P_{c}C_{ds}) \qquad \text{A.4}$$

where $\phi_{co}(0)$ is the compliant porosity at zero confining pressure and P_c is the confining pressure. It can be shown that the compressibility or bulk modulus ($C_d = 1/\kappa_d$) can be written as:

$$\kappa_d = \frac{\kappa_{ds}}{1+\theta_c\phi_{co}(0)\exp\left(-P_c \,\partial C_d / \partial\phi_{co}\right)} \qquad \text{A.5}$$

A similar expression can be derived for the shear bulk modulus:

$$\mu_d = \frac{\mu_{ds}}{1+\theta_{c\mu}\phi_{co}(0)\exp\left(-P_c \,\partial C_d / \partial\phi_{co}\right)} \qquad \text{A.6}$$

where μ_{ds} is the shear modulus of a rock with a closed compliant porosity (i.e. $\phi_{co} = 0$) and a stiff porosity corresponding to zero confining pressure. Furthermore,

$$\theta_{c\mu} = \frac{1}{\mu_{ds}}\frac{\partial\mu_d}{\partial\phi_{co}} \qquad \text{A.7}$$

By analogy with equations 3.4 and 3.5 in the main text, one can show, for the dry bulk modulus, that:

$$\kappa_\infty = \kappa_{ds}, \qquad \text{A.8}$$

$$E_\kappa = \theta_c\phi_{co}(0), \qquad \text{A.9}$$

$$P_\kappa = \partial\phi_{co} / \partial C_d \qquad \text{A.10}$$

and, for the shear modulus, that:

$$\mu_\infty = \mu_{ds}, \qquad \text{A.11}$$

$$E_{\mu} = \theta_{c\mu}\phi_{co}(0), \qquad \text{A.12}$$

$$P_{\kappa} = {\partial\phi_{co}}/{\partial C_{d}} \qquad \text{A.13}$$

This analogy show that the stress-sensitivity parameters P_κ and P_μ in equations 3.4 and 3.5, correspond to a gradational change of compliant porosity cause by compressibility changes.

Appendix B: Pore fluid properties

From a combination of thermodynamic relationships and empirical trends derived from laboratory data, Batzle and Wang (1992) established expressions to compute the P-wave velocities and densities of fluids as a function of their composition, temperature and pressure. In the following sections, expressions for gas, brine, dead and live oil are presented.

Gas properties

Density

Gas density ρ_g (g/cm^3) is given by:

$$\rho_g \cong \frac{28.8GP}{ZRT_a},$$

where $T_a = T + 273.15$ (absolute temperature), P is the pore pressure, T is the temperature (°C), G is the specific gravity of the gas and R is the gas constant (8.31441 J/g.mole.°C).

The compressibility factor, Z, is given by:

$$Z = \left[0.03 + 0.00527\left(3.5 - T_{pr}\right)^3\right]P_{pr} + \left(0.642T_{pr} - 0.007T_{pr}^4 - 0.52\right) + E$$

$$Z = \left[0.03 + 0.00527\left(3.5 - T_{pr}\right)^3\right]P_{pr} + \left(0.642T_{pr} - 0.007T_{pr}^4 - 0.52\right) + E,$$

where $E = 0.109\left(3.85 - T_{pr}\right)^2 \exp\left\{-\left[0.45 + 8\left(0.56 - 1/T_{pr}\right)^2\right]P_{pr}^{1.2}/T_{pr}\right\}$,

$P_{pr} = P/\left(4.892 - 0.4048G\right)$ (pseudo-reduced pressure),

$T_{pr} = T_a / (94.72 + 170.75G)$ (pseudo-reduced temperature).

Bulk modulus

The adiabatic bulk modulus of the gas K_s (MPa) is given by:

$$K_s \cong \frac{P}{\left(1 - \frac{P_{pr}}{Z}\frac{\partial Z}{\partial P_{pr}}\right)_T}\gamma_0,$$

where $\gamma_0 = 0.85 + \frac{5.6}{(P_{pr}+2)} + \frac{27.1}{(P_{pr}+3.5)^2} - 8.7\exp[-0.65(P_{pr}+1)]$,

$$\left(\frac{\partial Z}{\partial P_{pr}}\right)_T = 1.2E\left\{-\left[0.45 + 8\left(0.56 - \frac{1}{T_{pr}}\right)^2\right]\frac{P_{pr}^{0.2}}{T_{pr}}\right\} + 0.03 + 0.00527(3.5 - T_{pr})^3.$$

Oil properties

Density

Live oil density ρ_{lo} (g/cm^3) is given by:

$$\rho_{lo} = \rho_P / [0.972 + 3.81 \times 10^{-4}(T + 17.78)^{1.175}],$$

where $\rho_P = \rho_G + (0.00277P - 1.71 \times 10^{-7} P^3)(\rho_G - 1.15)^2 + 3.49 \times 10^{-4} P$,

$$\rho_G = (\rho_0 + 0.0012GR_G)/B_0,$$

$$B_0 = 0.972 + 0.00038\left[2.4R_G\left(\frac{G}{\rho_0}\right)^{0.5} + T + 17.8\right]^{1.175},$$

$\rho_0 = \frac{141.5}{\text{API} + 131.5}$, with API being the American Petroleum Institute oil gravity number, and B_0 the formation volume factor (m^3/m^3).

The solution gas–oil ratio R_G (m^3/m^3) is given by the Vasquez–Beggs equation (1980) for oil gravity less than 30.

$$R_G = 6.45 \times 10^{-3} * G\left(P / 0.006895\right)^{1.0937} \times \exp\left(25.724 \times \frac{\text{API}}{(T * 1.8 + 32) + 460}\right)$$

To obtain the dead oil density ρ_{do}, ρ_G needs to be replaced by ρ_0.

P-wave velocity

The P-wave velocity of live oil V_0 (m/s) is given by:

$$V_0 = 2096\left(\frac{\rho'}{2.6 - \rho'}\right)^{0.5} - 3.7T + 4.64P + 0.0115\left[4.12\left(1.08\rho'^{-1} - 1\right)^{0.5} - 1\right]TP$$

where $\rho' = \frac{\rho_0}{B_0}\left(1 + 0.001R_G\right)^{-1}$.

The P-wave velocity of dead oil can obtained by replacing ρ' by ρ_0.

Brine properties

Density

Brine density ρ_0 (g/cm^3) is given by:

$$\rho_b = \rho_w + S\{0.668 + 0.44S + 1 \times 10^{-6}[300P - 2400PS + T(80 + 3T - 3300S - 13P + 47PS)]\}$$

where $\rho_w = 1 + 1 \times 10^{-6}\left(A + 0.016T^2P - 1.3 \times 10^{-5}T^3P - 0.333P^2 - 0.002TP^2\right)$ is the density of pure water.

$A = -80T - 3.3T^2 + 0.00175T^3 + 489P - 2TP$, with S being the salinity (10^{-6} ppm).

P-wave velocity

Brine P-wave velocity V_b (m/s) is given by:

$$V_b = V_w + S\left(1170 - 9.6T + 0.055T^2 - 8.5 \times 10^{-5}T^3 + 2.6P - 0.0029TP - 0.0476P^2\right) + B,$$

$$B = S^{1.5}\left(780 - 10P + 0.16P^2\right) - 820S^2,$$

$V_w = \sum_{i=0}^{4}\sum_{j=0}^{3} w_{ij}T^iP^j$ (P-wave velocity of pure water).

where the coefficients for the water properties' computation are:

$w_{00} = 1402.85$	$w_{02} = 3.437 \times 10^{-3}$
$w_{10} = 4.871$	$w_{12} = 1.739 \times 10^{-4}$
$w_{20} = -0.04783$	$w_{22} = -2.135 \times 10^{-6}$
$w_{30} = 1.487 \times 10^{-4}$	$w_{32} = -1.455 \times 10^{-8}$
$w_{40} = -2.197 \times 10^{-7}$	$w_{42} = 5.230 \times 10^{-11}$
$w_{01} = 1.524$	$w_{03} = -1.197 \times 10^{-5}$
$w_{11} = -0.0111$	$w_{13} = -1.628 \times 10^{-6}$
$w_{21} = 2.747 \times 10^{-4}$	$w_{23} = 1.237 \times 10^{-8}$
$w_{31} = -6.503 \times 10^{-7}$	$w_{33} = 1.327 \times 10^{-10}$
$w_{41} = 7.987 \times 10^{-10}$	$w_{43} = -4.614 \times 10^{-13}$

Appendix C: Pressure-fluid discrimination from 4D – Landrø's approach

The expressions for pressure and saturation changes from AVO attributes can be written as follows (Landrø, 2002), assuming that second-order changes in pressure and saturation (cf. equations 2.1 and 2.2) are negligible:

$$\Delta P = \frac{k_\alpha \Delta R_0 - (k_\alpha + k_\rho)\Delta G}{4\frac{\beta^2}{\alpha^2} l_\beta (k_\alpha + k_\rho) - \frac{1}{2} l_\alpha k_\rho} \qquad \text{C.1}$$

$$\Delta S = \frac{1}{k_\alpha + k_\rho}\left[2\Delta R_0 - l_\alpha \frac{k_\alpha \Delta R_0 - (k_\alpha + k_\rho)\Delta G}{4\frac{\beta^2}{\alpha^2} l_\beta (k_\alpha + k_\rho) - \frac{1}{2} l_\alpha k_\rho} \right] \qquad \text{C.2}$$

where k_α, k_ρ, l_α, l_β stand for the fitting parameters from equations 2.1, 2.2 and 2.3. The ΔR_0 and ΔG represent the intercept and gradient time-lapse changes, whereas $\beta/\alpha = V_S/V_P$ is the velocity ratio. One can note that the uncertainties in the pressure and saturation changes are due to the errors in the parameters k_α, k_ρ, l_α, l_β, ΔR_0, ΔG and V_P/V_S. For many sandstones, the value of V_P/V_S is found to be close to 2, and l_α is equivalent to l_β, leading to the simplifications of equations C.1 and C.2:

$$\Delta P \approx \frac{k_\alpha \Delta R_0 - (k_\alpha + k_\rho)\Delta G}{l_\alpha k_\alpha + \frac{1}{2} l_\alpha k_\rho} \qquad \text{C.3}$$

$$\Delta S \approx \frac{1}{k_\alpha + \frac{1}{2} k_\rho}(\Delta R_0 + \Delta G) \qquad \text{C.4}$$

By considering equations C.3 and C.4, the uncertainties in the pore pressure and saturation changes can be derived, assuming that the controlling parameters in these equations are independent. The uncertainties in pressure changes, $u(\Delta P)$, and saturation changes, $u(\Delta S)$, take the following forms:

$$u(\Delta P)=\sqrt{A^2u(\Delta R_0)^2+B^2u(\Delta G)^2+C^2u(k_\alpha)^2+D^2u(k_\rho)^2+E^2u(l_\alpha)^2} \quad \text{C.5}$$

$$u(\Delta S)=\sqrt{F^2u(\Delta R_0)^2+F^2u(\Delta G)^2+G^2u(k_\alpha)^2+G^2u(k_\rho)^2} \quad \text{C.6}$$

where A, B, C, D and E stand for the partial derivatives of ΔP against ΔR_0, ΔG, k_α, k_ρ and l_α, respectively. The F and G are the partial derivatives of ΔS against ΔR_0 orΔG, and k_α or k_ρ. A, B, C, D, E, F and G represent the sensitivity coefficients used in Table 5.4.

$$A=\frac{k_\alpha}{k_\alpha l_\alpha+\frac{1}{2}k_\rho l_\alpha} \quad \text{C.7}$$

$$B=\frac{k_\alpha+k_\rho}{k_\alpha l_\alpha+\frac{1}{2}k_\rho l_\alpha} \quad \text{C.8}$$

$$C=\frac{(\Delta R_0-\Delta G)\left(k_\alpha l_\alpha+\frac{1}{2}k_\rho l_\alpha\right)-l_\alpha\left(k_\alpha\Delta R_0-(k_\alpha+k_\rho)\Delta G\right)}{\left(k_\alpha l_\alpha+\frac{1}{2}k_\rho l_\alpha\right)^2} \quad \text{C.9}$$

$$D=\frac{-\Delta G\left(k_\alpha l_\alpha+\frac{1}{2}k_\rho l_\alpha\right)-\frac{1}{2}l_\alpha\left(k_\alpha\Delta R_0-(k_\alpha+k_\rho)\Delta G\right)}{\left(k_\alpha l_\alpha+\frac{1}{2}k_\rho l_\alpha\right)^2} \quad \text{C.10}$$

$$E = \frac{\left(k_\alpha \Delta R_0 - \left(k_\alpha + k_\rho\right)\Delta G\right)}{\left(k_\alpha + \frac{1}{2}k_\rho\right)l_\alpha^2} \qquad \text{C.11}$$

$$F = \frac{1}{k_\alpha + \frac{1}{2}k_\rho} \qquad \text{C.12}$$

$$G = \frac{\Delta R_0 + \Delta G}{\left(k_\alpha + \frac{1}{2}k_\rho\right)^2} \qquad \text{C.13}$$

The following values of fitting parameters and AVO attributes changes are assumed (Landrø, 2002) to calculate the sensibility coefficients (Table 5.4):

$k_\alpha = 0.1$

$l_\alpha = 0.035$

$k_\rho = 0.05$

$\Delta R_0 = 0.05$

$\Delta G = 0.01$

References

Aki, K., and Richards, P. G. (1980). Quantitative seismology: Theory and methods. New York, USA, W. H. Freeman and Co.

Almaskeri, Y., and MacBeth, C. (2005). Location and evaluation of flow barriers using 4D seismic. SEG International Exposition and 75th Annual Meeting, Houston, Texas.

Alvarez, P., Malcotti, H., and Ortega, A. (2002). Estimacion de los cambios de presion y saturacion de fluido del yacimiento a traves del analisis de atributos AVO4D. XI Congreso Venezolano de Geofisica, Caracas, Venezuela.

Archer, J. S., and Wall, C.G. (1986). Petroleum Engineering - Principles and Practice. London, UK, Graham & Trotman.

Bachrach, R., Dvorkin, J., and Nur, A. M. (2000). Seismic velocities and Poisson's ratio of shallow unconsolidated sands. Geophysics 65: 559-564.

Backus, G. E. (1962). Long-wave elastic anisotropy produced by horizontal layering. Journal of Geophysical Research 67: 4427-4440.

Barkved, O. I., Kommedal, J. H., and Thomsen, L. (2004). The role of multi-component seismic data in developing the Valhall field, Norway. EAGE 66th Conference & Exhibition, Paris.

Batzle, M., and Wang, Z. (1992). Seismic properties of pore fluids. Geophysics 57: 1396-1408.

Berryman, J. G. (1999). Origin of Gassmann's equations. Geophysics 64: 1627-1629.

Bertrand, A., Ribeiro, C., and MacBeth, C. (2004). Uncertainties in the 4D seismic signatures due to seawater velocity variations. EAGE 66th Conference & Exhibition, Paris, France.

Bertrand, A., and MacBeth, C. (2005). Repeatability enhancement in deep-water permanent seismic installations: a dynamic correction for seawater velocity variations. Geophysical Prospecting 53: 229-242.

Biot, M. A. (1941). General theory of three-dimensional consolidation. Journal of Applied Physics 12: 155-164.

Brandt, H. (1955). A study of the speed of sound in porous granular media. Journal of Applied Mechanics 22: 479-486.

Brevik, I. (1999). Rock model-based inversion of saturation and pressure changes from time-lapse seismic data. SEG International Exposition and 69th Annual Meeting, Houston, Texas.

Bruce, B., and Bowers, G. (2002). Pore pressure terminology. The Leading Edge 21: 170-173.

Cambois, G. (2000). Can P-wave AVO be quantitative? The Leading Edge 19: 1246-1251.

Cambois, G. (2001). AVO processing: Myths and reality. EAGE 63rd Conference & Exhibition, Amsterdam, The Netherlands.

Capello de P., M. A., and Batzle, M. (1997). Rock physics in seismic monitoring. The Leading Edge 16: 1255-1260.

Carcione, M. J., and Helle, B. H. (2002). Rock physics of geopressure and prediction of abnormal pore fluid pressures using seismic data. CSEG Recorder 27: 8-32.

Castagna, J. P., Batzle, M. L., and Eastwood, R. L. (1985). Relatioships between compressional-wave and shear-wave velocities in clastic silicate rocks. Geophysics 50: 571-581.

Castagna, J. P., Batzle, M. L. and, Kan, T. K. (1993). Rock physics - the link between rock properties and AVO response. In offset-dependent reflectivity - theory and practice of AVO analysis. Castagna, J. P and Backus, M. M. (eds). Tulas, USA, Soc. of Explo. Geo.

Castagna, J. P., and Swan, H. W. (1997). Principles of AVO crossplotting. The Leading Edge 16: 337-342.

CGG (2002). Final processing report: West of Shetland 4D, Compagnie Générale de Géophysique

Christensen, N. I., and Wang, H. F. (1985). The influence of pore pressure and confining pressure on dynamic elastic properties of Berea sandstone. Geophysics 50: 207-213.

Clark, J. D. (1995). Detailed section across the Ainsa II Channel complex, south central Pyrenees, Spain. Atlas of Deep Water Environments: architectural style in turbitite systems. K. T. In: Pickering, Hiscott, R. N., Kenyon, N. H., Ricci Lucchi, F., and Smith, R. D. A. (eds). London, Chapman & Hall: 139-144.

Clifford, P. (2005). Reservoir management challenges and solutions in North Sea waterfloods. Internal presentation, Heriot-Watt Institute of Petroleum Engineering.

Cole, S., Lumley, D., Meadows, M., and Tura, A. (2002). Pressure and saturation inversion of 4D seismic data by rock physics forward modeling. SEG International Exposition and 72nd Annual Meeting, Salt Lake City, Utah.

Connolly, P. (1999). Elastic impedance. The Leading Edge 18: 438-452.

Cooper, M. M., Evans, A. C., Lynch, D. J., Neville, G., and Newley, T. (1999a). The Foinaven field: managing reservoir development uncertainty prior to start-up. Petroleum Geology of Northwest Europe: Proceedings of the 5th conference. A. J. a. B. Fleet, S. A. R. (eds). London, Geological Society: 675-682.

Cooper, M. M., Westwater, P., Thorogood, E., Kristiansen, P., and Christie, P. (1999b). Foinaven active reservoir management: Towed streamer and buried sea-bed detectors in deep water for 4D seismic. SEG International Exposition and 69th Annual Meeting, Houston, Texas.

Cooper, M. M., Westwater, P., Thorogood, E., Probert, T., Kristiansen, P., and Christie, P. (1999c). Foinaven active reservoir management: The benefits from the baseline surveys. SEG International Exposition and 69th Annual Meeting, Houston, Texas.

Cooper, M. M., Thorogood, E., O'Donovan A., Kristiansen, P., and Christie, P. (1999d). Foinaven active reservoir management: The time-lapse signal. SEG International Exposition and 69th Annual Meeting, Houston, Texas.

Dake, L. P. (1978). Fundamentals of reservoir engineering. Amsterdam, Elsevier.

Dasgupta, S. N. (2004). Reservoir monitoring with permanent borehole seismic sensors: Ghawar field Arab-D reservoir. SEG International Exposition and 74th Annual Meeting, Denver, Colorado.

De Waal, H., and Calvert, R. (2003). Overview of global 4D seismic implementation strategy. Petroleum Geoscience 9: 1-6.

Digby, P. J. (1981). The effective elastic moduli of porous granular rocks. Journal of Applied Mechanics 48: 803-808.

Domenico, S. N. (1976). Effect of brine-gas mixture on velocity in an unconsolidated sand reservoir. Geophysics 41: 882-894.

Dvorkin, J., Moos, D., Packwood, J. L., and Nur, A. M. (1999). Identying patchy saturation from well logs. Geophysics 64: 1756-1759.

Ebdon, C. C., Granger, P. J., Johnson, H. D., and Evans, A. M. (1995). Early Tertiary evolution and sequence strtigraphy of the Faeroe-Shetland basin: implications for

hydrocarbon prospectivity. The tectonics, sedimentation and palaeoceanography of the North Atlantic region. R. A. Scrutton, et al. (eds). London, Geological Society: 51-69.

Eberhart-Phillips, D., Han, D-H., and Zoback, M. D. (1989). Empirical relationships among seismic velocity, effective pressure, porosity, and clay content in sandstone. Geophysics 54: 82-89.

Fatti, J. L., Vail, P. J., Smith, G. C., Strauss, P. J., and Levitt, P. R. (1994). Detection of gas in sandstone reservoirs using AVO analysis: A 3-D seismic case history using the Geostack technique. Geophysics 59: 1362-1376.

Fetrl, W. H. (1976). Abnormal Formation Pressures. Amsterdam, The Netherlands, Elsevier.

Fjaer, E., and Holt, R. (1999). Stress and stress release effects on acoustic velocities from cores, logs and seismics. SPWLA 40th Annula Logging Symposium.

Floricich, M., MacBeth, C., and Staples, R. (2005). An engineering-driven approach for separating pressure and saturation using 4D seismic: Apllication to a Jurassic reservoir in the UK North Sea. SEG International Exposition and 75th Annual Meeting, Houston, Texas.

Freudenreich, Y., Reiser, C., Sognnes, H. I., and Bjerkebaek, E. (2004). Optimised data preconditioning for improved 3D stratigraphic inversion of the Gudrun field. EAGE 66th Conference & Exhibition, Paris, France.

Freund, D. (1992). Ultrasonic compressional and shear velocities in dry clastic rocks as a function of porosity, clay content and confining pressure. Geophysical Journal International 108: 125-135.

Gardiner, A. (2003). Field excursion to the southern Pyrenean and Ebro foreland basins, Spain. Field trip notes, Heriot-Watt Institute of Petroleum Engineering.

Gassmann, F. (1951). Elastic waves through a packing of spheres. Geophysics 16: 673-685.

Gluck, S., Juve, E., and Lafet, Y. (1997). High-resolution impedance layering through 3-D stratigraphic inversion of the poststack seismic data. The Leading Edge 16: 1309-1315.

Gluck, S., Deschizeaux, B., Mignot, A., Pinson, C., and Huguet, F. (2000). Time-lapse impedance inversion of post-stack seismic data. SEG International Exposition and 70th Annual meeting, Calgary, Canada.

Goffe, W. L., Ferrier, G. D., and Rogers, J. (1994). Global optimization of statistical functions with simulated annealing. Journal of Econometrics 60: 65-100.

Goodway, B., Chen, T., and Downton, J. (1997). Improved AVO fluid detection and lithology discrimination using Lame petrophysical parameters; ??? fluid stack from P and S inversions. SEG International Exposition and 67th Annual Meeting, Dallas, Texas.

Goodway, B. (2001). AVO and lame constants for rock parameterization and fluid detection. CSEG Recorder 26: 39-60.

Gray, F., Chen, T., and Goodway, W. (1999). Bridging the gap: Using AVO to detect changes in fundamental elastic constants. SEG International Exposition and 69th Annual meeting, Houston, Texas.

Gregory, A. R. (1976). Fluid saturation effects on dynamic elastic properties of sedimentary rocks. Geophysics 41: 895-921.

Gurevich, B. (2004). A simple derivation of effective stress coefficient for seismic velocities in porous rocks. Geophysics 69: 393-397.

Han, D.-H. (1986). Effect of porosity and clay content on acoustic properties of sandstones and unconsolidated sediments. Department of Geophysics, Stanford University. PhD thesis.

Han, D.-H., Nur, A. M., and Morgan, D. (1986). Effect of porosity and clay content on wave velocity in sandstones. Geophysics 51: 2093-2107.

Han, D.-H., and Batzle, M. (2004). Estimate shear velocity based on dry P-wave and shear modulus relationship. SEG International Exposition and 74th Annual Meeting, Denver, Colorado.

Harris, P. E., and Henry, B. (1998). Time-lapse processing: A North Sea case study. SEG International Exposition and 68th Annual Meeting, New Orleans, Louisiana.

He, N., Inderwiesen, P., and Condon, P. (2004). Pressure and saturation inversion from 4D seismic constrained by production data. EAGE 66th Conference & Exhibition, Paris, France.

Hofmann, R., Xu, X., Batzle, M., and Tshering, T. (2004). Which effective pressure coefficient do you mean? SEG International Exposition and 74th Annual meeting, Denver, Colorado.

Holt, R., Fjaer, E., and Furre, A-K., Ed. (1996). Laboratory simulation of the influence of earth stress changes on wave velocities. Seismic anisotropy, Soc. Explor. Geophys.

Hoversten, G. M., Gritto, R., Washbourne, J., and Daley, T. (2003). Pressure and fluid saturation prediction in a multicomponent reservoir using combined seismic and electromagnetic imaging. Geophysics 68: 1580-1591.

Hugonnet, P., Herrmann, P., and Ribeiro, C. (2001). High Resolution Radon - a Review. EAGE 63rd Conference & Exhibition, Amsterdam, The Netherlands.

Jackson, S., and Jacquot, J. (2004). 4-D and full-wave imaging of Rulison field, Field trip guidebook.

Johnston, D. H. (1987). Physical properties of shale at temperature and pressure. Geophysics 52: 1391-1401.

Kallweit, R. S., and Wood, L. C. (1982). The limits of resolution of zero-phase wavelets. Geophysics 47: 1035-1046.

Khaksar, A., Griffiths, C. M., and McCann C. (1999a). Compressional- and shear-wave velocities as a function of confining stress in dry sandstones. Geophysical Prospecting 47: 487-508.

Khaksar, A., Griffiths, C. M., and McCann, C. (1999b). Effective stress coefficient for P- and S-wave velocity and quality factor in sandstone, Example from the Cooper Basin-Australia. SEG International Exposition and 69th meeting, Houston, Texas.

Khan, M., Waggoner, J.R., and Hughes, J.K. (2000). 4D Cause and Effect: What do reservoir fluid changes look like on seismic? SPE Annual Technical Conference and Exhibition, Dallas, Texas.

Kimminau, S. (1994). Traceability - making decisions with uncertain data. The Log Analyst.

King, M. S. (1966). Wave velocities in rocks as a function of changes in overburden pressure and pore fluid saturants. Geophysics 31: 50-73.

Kirkpatrick, S. G., C. D., and Vecchi, M. P. (1983). Optimization by Simulated Annealing. Science 220: 671-680.

Kirstetter, O. H., and MacBeth, C. (2001). Compliance-based interpretation of the dry frame pressure sensitivity in shallow marine sandstone. SEG International Exposition and 71st Annual Meeting, San Antonio, Texas.

Kirstetter, O. H. (2002). The integration of laboratory data with flow simulation for application to seismic reservoir monitoring. Institute of Petroleum Engineering. Edinburgh, Heriot-Watt University. PhD thesis.

Kirstetter, O. H., Reiser, C., Lecerf, D., McInally, A., Conway, P., and Flanagan, K. (2004). Data pre-conditioning for 4D stratigraphic inversion, a case study: the Gryphon field. EAGE 66th Conference & Exhibition, Paris, France.

Kragh, E., and Christie, P. (2002). Seismic repeatability, normalized rms, and predictability. The Leading Edge 21: 640-647.

Kristiansen, P., Christie, P., Bouska, J., O'Donovan, A., Westwater, P., and Thorogood, E. (2000). Foinaven 4D: Processing and analysis of two designer 4Ds. SEG International Exposition and 70th Annual meeting, Calgary, Canada.

Kuster, G. T., and Töksöv, M. N. (1974). Velocity and attenuation of seismic waves in two-phase media: Part I. Theoretical formulations. Geophysics 39: 587-606.

Lamers, E., and Carmichael, S. M. M. (1999). The Paleocene deep water sandstone play West of Shetland. Petroleum Geology of Northwest Europe: Proceedings of the 5th conference. A. J. a. B. Fleet, S. A. R. (eds). London, Geological Society: 645-649.

Landrø, M. (1999a). Discrimination between pressure and fluid saturation changes from time-lapse seismic data. SEG International Exposition and 69th Annual Meeting, Houston, Texas.

Landrø, M. (1999b). Repeatability issues of 3-D VSP data. Geophysics 64: 1673-1679.

Landrø, M. (2001). Discrimination between pressure and fluid saturation changes from time-lapse seismic data. Geophysics 66: 836-844.

Landrø, M., Digranes, P., and Strønen L. K. (2001). Mapping reservoir pressure and saturation changes using seismic methods - possibilities and limitations. First Break 19: 671-677.

Landrø, M. (2002). Uncertainties in quantitative time-lapse seismic analysis. Geophysical Prospecting 50: 527-538.

Landrø, M., Veire, H., H., Duffaut, K., and Najjar, N. (2003). Discrimination between pressure and saturation changes from marine multicomponent time-lapse seismic data. Geophysics 68: 1592-1599.

Lindsay, R., and Van Koughnet, R. (2001). Sequential Backus averaging: Upscaling well logs to seismic wavelengths. The Leading Edge 20: 188-191.

Lumley, D., Behrens, R. A., and Wang, Z. (1997). Assessing the technical risk of a 4-D seismic project. The Leading Edge 16: 1287-1291.

Lumley, D., Adams, D., Meadows, M., Cole, S., and Ergas, R. (2003). 4D seismic pressure-saturation inversion at Gullfaks field, Norway. First Break 21: 49-56.

Lumley, D., Meadows, M., Cole, S., and Adams, D. (2003). Estimation of reservoir pressure and saturations by crossplot inversion of 4D seismic attributes. EAGE 65th Conference & Exhibition, Stavanger, Norway.

Ma, X. Q. (2002). Simultaneous inversion of prestack seismic data for rock properties using simulated annealing. Geophysics 67: 1877-1885.

MacBeth, C. (2002). Compliance-based laws fro the dry-frame pressure sensitivity of sandstone. EAGE 64th Conference & Exhibition, Florence, Italy.

MacBeth, C., Stephen, K.D., and McInally, A. (2003). 4D Modelling of OWC movement in low NTG areas of the Nelson field. EAGE 65th Conference & Exhibition, Amsterdam, The Netherlands.

MacBeth, C., Stephen, K.D., and McInally, A. (2005). The 4D signature of OWC movement due to natural production in a stacked turbidite reservoir. Geophysical Prospecting 53: 182-203.

MacBeth, C. (2004). A classification for the pressure-sensitivity of a sandstone rock frame. Geophysics 69: 497-510.

MacBeth, C. (2004). Deconvolving permeability from time-lapsed seismic data. SEG International Exposition and 74th Annual meeting, Denver, Colorado.

MacBeth, C., Soldo, J., and Floricich, M. (2004). Going quantitative with 4D seismic analysis. EAGE 66th Conference & Exhibition, Paris, France.

MacBeth, C., and Ribeiro, C. (2005). The stress sensitivity of unsaturated shaley sandstones. Geophysical Prospecting In Press.

Mallick, S. (2001). AVO and elastic impedance. The Leading Edge 20: 1094-1104.

Marion, D., Nur, A., Yin, H., and Han, D-H. (1992). Compressional velocity and porosity in sand-clay mixtures. Geophysics 57: 554-563.

Marsh, M. J., Whitcombe, D. N., Raikes, S. A., Parr, R. S., and Nash. T. (2003). BP's increasing systematic use of time-lapse seismic strategy. Petroleum Geoscience 9: 7-13.

Mavko, G., and Mukerji, T. (1998). Bounds on low-frequency seismic velocities in partially saturated rocks. Geophysics 63: 918-924.

Mavko, G., Mukerji, T., and Dvorkin, J. (1998). The rock physics handbook: tools for seismic analysis in porous media. Cambridge, UK, Cambridge University Press.

Meadows, M. (2001). Enhancements to Landrø's method for separating time-lapse pressure and saturation changes. SEG International Exposition and 71st Annual Meeting, San Antonio, Texas.

Meadows, M., Adams, D., Wright, R., Tura, A., Cole, S., and Lumley, D. (2002). Rock physics analysis for time-lapse seismic at Schiehallion Field, North Sea. SEG International Exposition and 72nd Annual Meeting, Salt Lake City, Utah.

Metropolis, N., Rosenbluth, A. W., Rosenbluth, M. N., Teller, A. H., and Teller, E. (1953). Equation of State Calculation by Fast Computing Machines. Journal of Chemical Physics 21: 1087-1092.

Mindlin, R. D. (1949). Compliance of elastic bodies in contact. Journal of Applied Mechanics 16: 259-268.

Morrow, N. R. and Melrose, J. C. (1991). Application of capillary pressure measurements to the determination of connate water saturation. In interfacial phenomena in petroleum recovery. Morrow, N. R. (ed.). New York, Marcel Dekker Inc.: 257-287.

Murphy, W. F., Schwartz L. M., and Hornby, B. (1991). Interpretation physics of V_P and V_S in sedimentary rocks. SPWLA 32nd Annual Logging Symposium.

Mutti, E., and Lucchi, F (1972). Le torbiditi dell'Appennino Strentrionale: introduzione all'analisi di facies. Mem. Soc. Geol. It. 11: 161-199.

Mutti, E., and Ghibaudo, G. (1972). Un esempio di torbiditi di conoide esterna: le Arenarie di S. Salvatore (Formazione di Bobbio, Miocene) nell' Appennino di Piacenza. Mem. Acc. Sci. Torino, Cl. Sci. Fis. Mat. Nat. 16: 1-40.

Mutti, E., Remacha, E., Tinterri, R., Mavilla N., Angella, S., and Fava, L. (2000). An introduction to the analysis of ancient turbidite basins from an outcrop perspective. PESGB Turbidite training course.

O'Donovan, A. R., Smith, S. G., and Kristiansen, P. (2000). Foinaven 4D seismic - Dynamic reservoir parameters and reservoir management. SPE Annual Technical Conference and Exhibition, Dallas, Texas.

Parnell, J., Carey, P. F., Grenn, P., and Duncan, W. (1999). Hydrocarbon migration history, West of Shetland: integrated fluid inclusion and fission track studies. Petroleum Geology of Northwest Europe: Proceedings of the 5th conference. A. J. a. B. Fleet, S. A. R. (eds). London, Geological Society: 613-625.

Prasad, M., and Manghnani, M. H. (1997). Effects of pore and differential pressure on compressional wave velocity and quality factor in Berea and Michigan sandstones. Geophysics 62: 1163-1176.

Reuss, A. (1929). Berechnung der fliessgrenzen von mischkristallen auf grund der plastizitatsbedingung fur einkritalle. Zeitschrift fur angewandte mathematik und mechanik 9: 49-58.

Ribeiro, C., and MacBeth, C. (2004). A petroelastic -based approach to pressure and saturation estimation using 4D seismic. EAGE 66th Conference & Exhibition, Paris, France.

Rutherford, S. R., and Williams, R. H. (1989). Amplitude-versus-offset variations in gas sands. Geophysics 54: 680-688.

Sams, M., and Andrea, M. (2001). The effect of clay distribution on the elastic properties of sandstones. Geophysical Prospecting 49: 128-150.

Sarkar, S., Gouveia, W. P., and Johnston, D. H. (2003). On the inversion of time-lapse data. SEG International Exposition and 73rd Annual Meeting, Dallas, Texas.

Sayers, C. M., and Kachanov, M. (1995). Microcrack-induced elastic wave anisotropy of brittle rocks. Journal of Geophysical Research 100: 4149-4156.

Sayers, C. M. (2002). Stress-dependent elastic anisotropy of sandstones. Geophysical Prospecting 50: 85-95.

Selley, R. C. (2000). Applied Sedimentology. San Diego, California, Academic press.

Sengupta, M., and Mavko, G. (2003). Impact of flow-simulation parameters on saturation scales and seismic velocity. Geophysics 68: 1267-1280.

Sengupta, M., Mavko, G., and Mukerji, T. (2003). Quantifying subresolution saturation scales from time-lapse seismic data: A reservoir monitoring case study. Geophysics 68: 803-814.

Shapiro, S. A. (2003). Elastic piezosensitivity of porous and fractured rocks. Geophysics 68: 482-486.

Shuey, R. (1985). A simplification of Zoeppritz equations. Geophysics 50: 609-614.

Smith, G. C., and Gidlow, P. M. (1987). Weighted stacking for rock property estimation and detection of gas. Geophysical Prospecting 35: 993-1014.

Smith, T., Sondergeld, C. H., and Rai, C. S. (2003). Gassmann fluid substitutions: A tutorial. Geophysics 68: 430-440.

Stendahl, T. (2000). Consolidation of core samples: adjusting porosity, permeability and pore geometry by means of "The silica-lock-method". NTNU Norwegian university of science and technology website.

Stephen, K. D., Clark, J.D., and Gardiner, A.R. (2001). Outcrop-based stochastic modeling of turbidite amalgamation and its effect on hydrocarbon recovery. Petroleum Geoscience 7: 163-172.

Stephen, K. D. (2002). Channel modelling software, Heriot-Watt Institute of Petroleum Engineering.

Stovas, A., Landrø, M., and Avseth, P. (2004). Estimation of net-to-gross and fluid saturation in a fine-layered sand-shale sequence - tested on offshore Brazil data. SEG International Exposition and 74th Annual Meeting, Denver, Colorado.

Stovas, A., and Landrø, M. (2004). Optimal use of PP and PS time-lapse stacks for fluid-pressure discrimination. Geophysical Prospecting 52: 301-312.

Stovas, A., and Landrø, M. (2004). Pressure-fluid discrimination versus net-to-gross for finely layered reservoir units. EAGE 66th Conference & Exhibition, Paris, France.

Terrell, M. J., Davis, T. L., Brown, L., and Fuck, R. (2002). Seismic monitoring of a CO_2 flood at Weyburn field, Saskatchewan, Canada: demonstrating robustness of time-lapse seismology. SEG International Exposition and 72nd Annual Meeting, Salt Lake City, Utah.

Terzaghi, K. (1936). The shearing resistance of saturated soils and the angle between the planes of shear. Proceedings of the International Conference on Soil Mechanics and Foundation Engineering, Harvard University Press, Cambridge, Mass.

Todd, T., and Simmons, G. (1972). Effect of pore pressure on the velocity of compressional waves in low-porosity rocks. Journal of Geophysical Research 77: 3731-3743.

Tura, A. C., and Lumley, D. (1999). Estimating pressure and saturation changes from time-lapse AVO data. SEG International Exposition and 69th Annual Meeting, Houston, Texas.

Vasco, D. W. (2004). Seismic imaging of reservoir flow properties: Time-lapse pressure changes. Geophysics 69: 511-521.

Vasquez, M., and Beggs, H.D. (1980). Correlations for fluid physical property prediction. Journal of Petroleum Technology: 968-970.

Veire, H., Borgos, H., and Landrø, M. (2003). Stochastic inversion of pressure and saturation changes from time-lapse seismic data. SEG International Exposition and 73rd Annual Meeting, Dallas, Texas.

Verm, R., and Hilterman, F. (1995). Lithology color-coded seismic sections: The calibration of AVO crossplotting to rock properties. The Leading Edge 14: 847-853.

VerWest, B., Masters, A., and Sena, A. (2000). Elastic impedance inversion. SEG International Exposition and 70th Annual meeting, Calgary, Canada.

Voigt, W. (1928). Lehrbuck der kristallphysik. Leipzig, Teubner.

Walton, K. (1986). The effective elastic moduli of a random packing of spheres. Journal of Mechanics and Physics Solids 35: 213-226.

Wang, Z. (2000). Fundamentals of seismic rock physics. Geophysics 66: 398-412.

Whitcombe, D. N. (2002). Elastic impedance normalization. Geophysics 67: 60-62.

Whitcombe, D. N., Connolly, P. A., Reagan, R. L., and Redshaw T. C. (2002). Extended elastic impedance for fluid and lithology prediction. Geophysics 67: 63-67.

Wood, A. B. (1941). A textbook of sound. New York, The Macmillan Company.

Wyllie, M. R. J., Gregory, A. R., and Gardner, G. H. F. (1958). An experimental investigation of factors affecting elastic wave velocities in porous media. Geophysics 23: 459-493.

Xu, S., and White, R. (1995). A new velocity model for clay-sand mixtures. Geophysical Prospecting 43: 91-118.

Yilmaz, O. (2001). Seismic data analysis: processing, inversion and interpretation of seismic data. Tulsa, USA, Soc. of Explo. Geo.

Zhang, J. J., and Bentley, L. R. (1999). Change of bulk and shear moduli of dry sandstone with effective pressure and temperature, CREWES Research report.

Zimmerman, R. W. (1991). Compressibility of sandstones. New York, USA, Elsevier.

Zoeppritz, K. (1919). Erdbebenwellen VIII B, On the reflection and penetration of seismic waves through unstable layers. Goettinger Nachr.: 66-84.